A GLOBAL IONOSPHERIC F2 REGION PEAK ELECTRON DENSITY MODEL USING NEURAL NETWORKS AND EXTENDED GEOPHYSICALLY RELEVANT INPUTS

A thesis submitted in fulfilment of the

requirements for the degree of

DOCTOR OF PHILOSOPHY

of

RHODES UNIVERSITY

by

Elijah Oyedola Oyeyemi

November 2005

Abstract

This thesis presents my research on the development of a neural network (NN) based global empirical model of the ionospheric F2 region peak electron density using extended geophysically relevant inputs. The main principle behind this approach has been to utilize parameters other than simple geographic co-ordinates, on which the F2 peak electron density is known to depend, and to exploit the technique of NNs, thereby establishing and modeling the non-linear dynamic processes (both in space and time) associated with the F2 region electron density on a global scale. Four different models have been developed in this work. These are the foF2 NN model, M(3000)F2 NN model, short-term forecasting foF2 NN, and a near-real time foF2 NN model. Data used in the training of the NNs were obtained from the worldwide ionosonde stations spanning the period 1964 to 1986 based on availability, which included all periods of calm and disturbed magnetic activity. Common input parameters used in the training of all 4 models are day number (day of the year, DN), Universal Time (UT), a 2 month running mean of the sunspot number (R2), a 2 day running mean of the 3-hour planetary magnetic index a_p (A16), solar zenith angle (CHI), geographic latitude (θ), magnetic dip angle (I), angle of magnetic declination (D), angle of meridian relative to subsolar point (M).

For the short-term and near-real time foF2 models, additional input parameters related to recent past observations of foF2 itself were included in the training of the NNs.

The results of the foF2 NN model and M(3000)F2 NN model presented in this work, which compare favourably with the IRI (International Reference

Ionosphere) model successfully demonstrate the potential of NNs for *spatial* and *temporal* modeling of the ionospheric parameters foF2 and M(3000)F2 globally. The results obtained from the short-term foF2 NN model and near-real time foF2 NN model reveal that, in addition to the *temporal* and *spatial* input variables, short-term forecasting of foF2 is much improved by including past observations of foF2 itself. Results obtained from the near-real time foF2 NN model also reveal that there exists a correlation between measured foF2 values at different locations across the globe. Again, comparisons of the foF2 NN model and M(3000)F2 NN model predictions with that of the IRI model predictions and observed values at some selected high latitude stations, suggest that the NN technique can successfully be employed to model the complex irregularities associated with the high latitude regions.

Based on the results obtained in this research and the comparison made with the IRI model (URSI and CCIR coefficients), these results justify consideration of the NN technique for the prediction of global ionospheric parameters. I believe that, after consideration by the IRI community, these models will prove to be valuable to both the high frequency (HF) communication and worldwide ionospheric communities.

Acknowledgements

Firstly, I would like to express my special thanks to my supervisor, Prof Allon Poole, for his encouragement of this research, and for inspiring and supporting my interest in the field of Ionospheric Physics. Many thanks to Dr. Lee-Anne McKinnell for her untiring assistance at all times. Words alone cannot express my sincere appreciation.

My sincere appreciation goes also to both the Hartebeesthoek Radio Observatory (HartRAO), a national facility of the National Research Foundation (NRF), and GrinTek Ewation (GEW) for their financial support during 2004 and 2005 respectively. Many thanks to University of Lagos, Nigeria, for granting me study leave. I will always be grateful to the institution.

Many people have helped in different capacities to make this research a reality. I cannot mention them, as I do not want to offend any one. I appreciate you all. I appreciate the supports of every staff member (both the academic and non-academic) of the Physics and Electronic Department, Rhodes University. Special thanks to Mr Anthony Sullivan for his untiring assistance.

I am grateful to all my friends, who are too numerous to mention, for their encouragement during the course of this program. Many thanks to my brother, Mr Gabriel Oyeyemi and my mother, Mrs Ruth Oyeyemi for their understanding and support. I appreciate the supports of my in-laws, brothers and sisters.

But first, last and always, I would like to thank my wife, Mrs Olufunke Oyeyemi, and my children, Timi, Ife and Dolapo for their endurance and understanding. I will always be grateful to you all.

And finally, Glory to God Almighty for seeing me through this program.

TABLE OF CONTENTS

LIST OF FIGURES

Chapter 1

Chapter 2

Chapter 3

Chapter 4

Chapter 5

LIST OF TABLES

Chapter 1

1 Introduction

This thesis presents my research on the development of a neural network (NN) based global empirical model of the ionospheric F2 region peak electron density using extended geophysical relevant inputs. My focus in this region of the ionosphere has been motivated by the important role the maximum electron density (N_e) plays in the study of the ionosphere and its effects on high frequency (HF) radio communications. The use of NNs is generally motivated by their principal ability to describe non-linear phenomena, a principal characteristic of the F2 region due to its non-linear dynamic processes arising from global themospheric circulation. Also, a NN has the ability to generalise from a set of training patterns when presented with input patterns that are similar, but not identical to that with which the NN was trained. Various groups (Altinay et. al., 1997; McKinnell, 1996, 2002; Williscroft and Poole, 1996; Lamming and Cander, 1999; Tulunay et. al., 2000; Wintoft, 2000) have shown the methods of NNs to be successful when employed to model the non-linear behaviour of the ionosphere, especially the critical frequency of the F2 region (foF2).

A brief description of the ionospheric structure and F2 region variability is summarised in the following sections. Details can also be found in Rishbeth and Garriott, 1969; McNamara, 1994 and various articles (e.g. Forbes et al., 2000; Rishbeth and Mendillo, 2001)

1.1 The Earth's Ionosphere

The ionosphere is that region of the Earth's upper atmosphere extending from a height of about 50 km up to about 1000 km. This region is the ionised part of the upper atmosphere that is formed by photoionisation due to solar extreme ultraviolet (EUV) and x-radiation (Rishbeth and Garriott, 1969; Hargreaves, 1979; McNamara, 1994). This process may also be caused by solar wind particles and cosmic rays but their effect is small in comparison with the EUV radiation. Within the ionosphere free ions and electrons exist in sufficient abundance to influence the propagation of radio frequency electromagnetic waves that are propagated within and through it, giving the ionosphere much of its practical importance. This region is an important region of the atmosphere, because these charged particles and free electrons are responsible for the reflection or bending of radio waves occurring between certain critical frequencies, which vary with the degree of ionisation. Due to the changes in the sources of ionisation (i.e. the sun activity), and also because the ionosphere responds to the changes in the neutral part of the upper atmosphere (i.e. the thermosphere), the structure and peak densities of the ionosphere vary with time (i.e. 11-year solar cycle, diurnally, and seasonally), with geographical location (i.e. geographic latitude and longitude), and with solar-related ionospheric disturbances (i.e. sporadic E, sudden ionospheric disturbances (SID), and ionospheric storms) (McNamara, 1994). This variability is known to cause distortion effects on satellite and HF communications, navigation and altimetry.

1.1.1 Structure of the Ionosphere

The ionosphere is vertically divided into three main regions, namely, D, E and F regions. These regions are classified according to their chemical composition, sources of ionisation, level of variability and dynamic nature. An example of the daytime electron density variation of the ionospheric layers and their predominant ion populations as a function of height above the ground is illustrated in Figure 1-1.

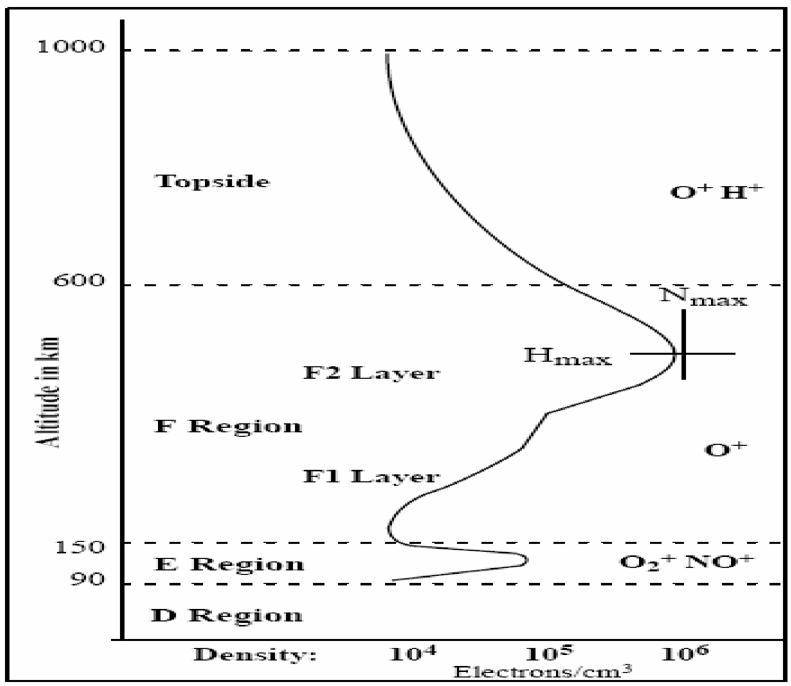

Figure 1-1. Electron density profile of ionospheric layers with their predominant ion populations as a function of height. (Figure from Space Environment Center (SEC) and Space Oceanic and Atmospheric Administration (NOAA) by Anderson and Fuller-Rowell, 1999).

The lowest part of the ionosphere between an altitude of about 50 and 90 km is the D region. This region is characterised by relatively weak ionisation, which is responsible for the absorption of HF radio waves, particularly those frequencies below 7MHz. Hard x-rays are the major source of ionisation in this region. The region just above the D region from about 90 to 150 km is the E region. Ionisation in this region is due to soft x-rays (1-10 nm) and far ultraviolet (UV) solar radiation ionisation of molecular oxygen (O_2). The E layer can only reflect radio waves with frequencies less than 10MHz and has a negative effect on higher frequencies due to its partial absorption of these higher frequency radio waves. The E-layer is a daytime phenomenon because it develops shortly after sunrise and disappears a few hours after sunset, with maximum ionisation around midday. Within the E region, a very thin region of extremely dense ionisation that is different from the normal E layer ionisation can form. This region is called the sporadic E region (E_S) and is capable of reflecting radio frequencies from about 30 to 300MHz. Sporadic E appears mostly during summer months, and less during winter, with the peak during early summer.

The F region, which is the subject of this research, lies above the E region between about 150 and 300 km, and is the most important region for the purpose of HF radio propagation. Extreme ultraviolet radiation from the Sun is the main source of ionisation in this region. This region is much thicker than the E region and heavily ionised. The peak height of the F region is a function of the season, latitude, time of day, and level of solar activity. During the day, the F region can divide into two regions, F1 and F2, depending on the diurnal and seasonal variations. The F1 region, which lies between about 150 and 210 km altitude, has its maximum ionisation near midday and merges with the F2 region after sunset to reform the F region. The lower part of the F region is dominated by NO^+, while the upper part is dominated by O^+. The F2 region extends from about 250 km above the Earth surface to well over 300 km depending on the time of the day and level of solar activity. The peak daytime electron density in the F2 region is usually reached one hour after midday around 300 km and typically decreases after sunset. The F2 region is the most variable region of the ionospheric layers due to the complicated non-linear dynamical processes, arising from temporal and geographical variabilities in the upper atmospheric chemistry, ionisation production and loss mechanisms, particle diffusion and electrodynamical phenomena. In spite of the fact that much of the ionospheric variability can be explained from the basic principles of physics, the F2 layer is so complex that its critical frequency does not behave in the manner of a simple Chapman layer (Rishbeth and Garriott, 1969, McNamara, 1994). Unlike the D, E and F1 regions, the F2 region is subjected to more short term (a few hours) variations, with greater critical frequency often during the equinoxes. The complex nature of the F2 region is a limiting factor for terrestrial and Earth-space communications (Rush, 1975; Tulunay et al., 2000; Richard et al., 2004). However, this upper part of the F region is the most important region for HF communications (Nisbet, 1971; Bent et al., 1978; Rush et al., 1983, 1984) because its altitude allows the longest communication paths, and it is always present (24 hours of the day), and it can refract the highest frequencies in the HF range. The maximum electron density of this region is quantified by the critical frequency, foF2, and determines the maximum usable frequency (MUF). The critical frequency, foF2, which is defined as the highest cutoff frequency at which the F2 region reflects electromagnetic waves, is related to the maximum ionospheric electron density, N_e, according to

$$N_e/\mathrm{m}^{-3} = 1.24 \times 10^{10} \left(f / \mathrm{MHz}\right)^2 \qquad (1.1)$$

The maximum usable frequency, MUF(3000), defined as the highest frequency at which radio waves can propagate from a given point over a distance of 3000 km, is expressed as

$$\mathrm{M(3000)F2} = \frac{\mathrm{MUF(3000)}}{f_o\mathrm{F2}} \qquad (1.2)$$

where M(3000)F2 is the propagation factor closely related to the height of the F2-peak (hmF2) (Shimazaki, 1955; Bilitza et al., 1979), and also, proportional to the secant of the ray zenith angle. Both ionospheric parameters, foF2 and M(3000)F2, are essential for HF planning for radio communication applications (Xenos, 2002). As a result, prediction of these parameters is of fundamental importance in ionospheric modelling (Rush, 1975).

Based on the significance of the F2 region to HF communications and its high level of variability due to solar activity and magnetic activity, the subject of this research is therefore centred on the development of an ionospheric model for the peak density of this region.

1.2 Variations in the F2 region

The F2 region of the ionosphere is subject to a number of influences because its existence is directly related to the changes resulting from the interaction of solar radiations, solar wind and the geomagnetic field. The structure of the F2 region at any geographical location and time is complex and depends on the amount of solar radiation from the sun and the electron density arising from the processes of photoionisation and recombination. Due to the Earth's tilt and rotation around the sun, the path of the atmosphere through which the solar radiation passes varies with the time of the day and month of the year. As a result, the F2 region electron density varies with time of the day (diurnally) and with season (seasonally) due to the change in solar zenith angle, and over the ~11-year cycle (Rishbeth and Garriott, 1969; Hargreaves, 1979; Forbes et al., 2000). Because of these variations, a frequency which may provide successful propagation at one geographical location may not do so at another, and even from one hour to the next hour within the same location. These variations are the result of the non-linear dynamical processes in the ionopshere, and can be grouped into two categories: those which are more or less regular and occur in cycles, and those which are irregular in their behaviour (irregular disturbances) due to disturbances in the atmosphere arising from solar-related ionospheric disturbances. These two classes of variations are briefly discussed in the next section.

1.2.1 Regular variations

Regular variations occur as a result of the rotation of the Sun and the Earth about their own axes. There are four types of regular variations: diurnal, seasonal, 27-day and solar cycle variations. An example of such variations has been performed on foF2 measured at the Grahamstown (33.3 ^{o}S, 26.5 ^{o}E) station over a period of 27 years (1973-2000) using Fourier transform (FT) techniques, see Figure 1-2. The powerful FT technique makes it possible to show the extent to which periodicities in the secular variation of foF2 follow the solar activity. As can be observed in Figure 1-2, the results of the FT show the changes of foF2 in duration of day (diurnal and semidiurnal variations), season (annual and semiannual variations), 27-day and 11-year variations. Three of these variations (diurnal, seasonal and solar cycle variations) that are used in this research are discussed briefly in this section, with more detail to be found in (Rishbeth and Garriott, 1969; Torr and Torr, 1973; Hargreaves, 1979; McNamara, 1994; Millward et al., 1996; Forbes et al., 2000; Rishbeth and Mendillo, 2001). The fourth variation (27-day) has not been considered for the purpose of this research because its power amplitude (< 10 x 10^5) (Figure 1-2) is much smaller in comparison with other variations and therefore considered of no practical significance. The weak 12.42 hr gravitational lunar periodicity is also not considered for the same reason.

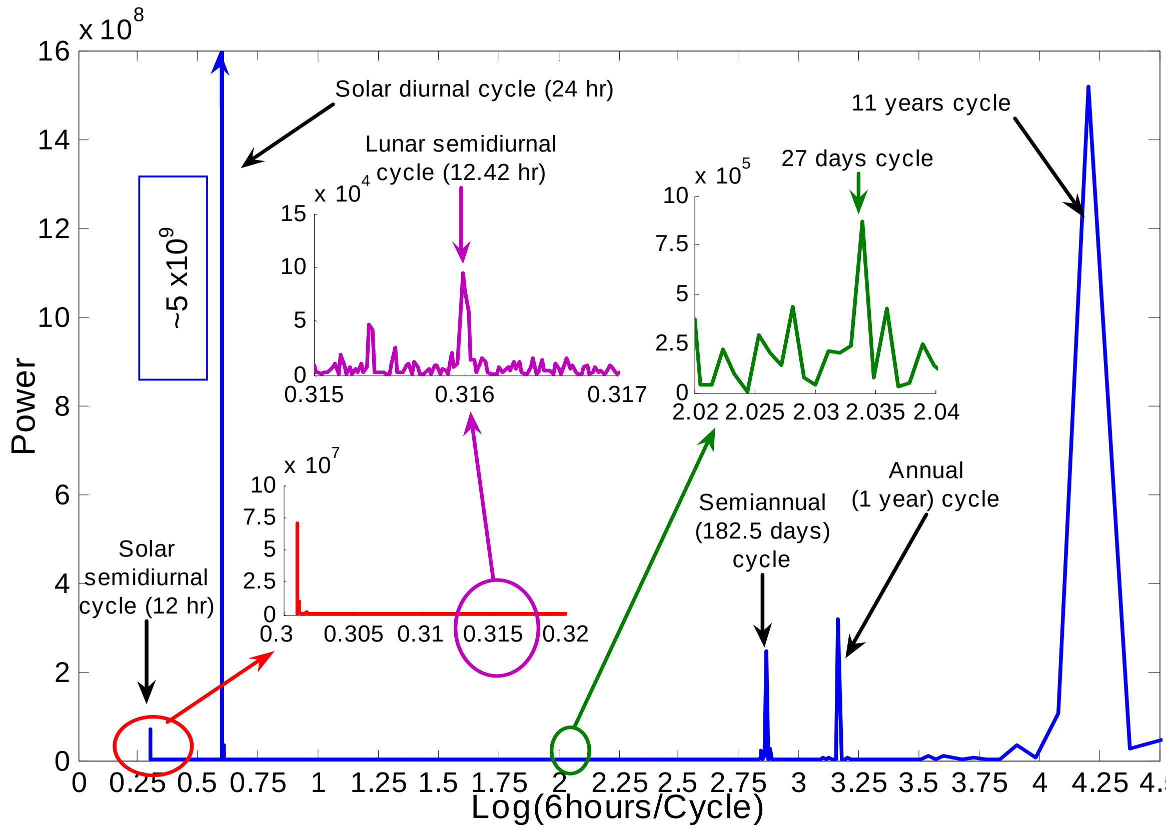

Figure 1-2. The result of Fourier transform (FT) of Grahamstown foF2 for the interval January 1973 through December 2000 (a total of 27 years). The sampling period is an average of 6 hours per cycle.

1.2.1.1 Diurnal variations

Diurnal variations are caused as a result of the daily rotation of the Earth about its own axis following the apparent movement of the sun. The rotation of the Earth around the sun causes sunrise and sunset on a daily basis, which can be described by the solar zenith angle. As a result, the atmosphere undergoes a regular variation of the solar day (24 solar hour) due to the combined gravitational and thermal effects of the sun on the Earth. Since the formation of the ionosphere is itself directly related to the sun's activity, this suggests that the F2 region peak electron density will vary with the time of day according to the solar zenith angle over a particular geographical location (McNamara, 1994). Figure 1-2 illustrates the diurnal effect of the solar activity on foF2 (i.e. solar diurnal (24 hour) and solar semidiurnal (12 hour) cycles). The effect of this is only noticeable during the day in the D, E and F1 regions. At night these layers vanish leaving only the F2 region. HF communication during the night is therefore via the F2 region, since absorption of radio waves is lower due to the absence of the D region. These characteristics make the F2 region the most important region for long distance HF communications. Another daily regular variation is the lunar day (24.83 hour) due to the gravitational attraction between the moon and the Earth as the moon revolves around the Earth. This has a period of the lunar semidiurnal cycle of 12.42 hour (half of lunar day, 24.84 hour), Figure 1-2.

1.2.1.2 Seasonal variations:

Seasonal variations are caused by the tilt and rotation of the Earth on its axis. In this case the Earth revolves around the sun such that the relative position of the sun moves from one hemisphere to the other with changes in seasons. This brings about seasonal variations in the angle of the sun (solar zenith angle) and its intensity at any geographical location on the surface of the Earth. As expected, the critical frequencies of the D, E and F1 regions are always greater in summer than in winter because ionisation is greatly enhanced during the summer period (McNamara, 1994; Hargreaves, 1979). The F2 region ionisation at noon is sometimes greater in winter than in summer, the reverse of what is expected (Rishbeth and Setty, 1961). This is called the winter anomaly. The winter (or seasonal) anomaly of the F2 region is caused as a result of seasonal changes in the chemical composition of the atomic-to-molecular ratio (i.e. ratio of $[O]/[N_2]$ higher in winter than summer) of the neutral atmosphere due to vertical and horizontal winds associated with the global thermospheric circulation (Rishbeth and Setty, 1961; King and Smith, 1968; Duncan, 1969; Wright, 1963; Torr and Torr, 1973; Torr et al., 1980; Rishbeth, 1998). In addition, there are annual (1 year) and semiannual anomalies, in that electron densities are 20% greater in December than in June in the former and also, abnormally high at the equinoxes in the latter case (Rishbeth and Setty, 1961; Rishbeth, 1969; Torr and Torr, 1973; Hargreaves, 1979).

1.2.1.3 Variations with solar activity:

Various groups (Kane, 1992; Williscroft and Poole, 1996; Kouris et al., 1998; Bilitza, 2000; Forbes et al., 2000; Richard, 2001; Rishbeth and Mendillo, 2001; Sethi et al., 2002; Liu et al., 2003) have shown the dependence of the F2 region peak electron density on solar cycle activity. The electron density concentration in the F2 region of the ionosphere is primarily due to the ionisation of atmospheric constituents O, O_2 and N_2 by the solar extreme ultraviolet (EUV) radiations (Gupta and Lakha, 2001).

Solar cycle activity is associated with the appearance and disappearance of dark spots on the surface of the sun. These dark spots, which are responsible for variations in the ionisation level of the ionosphere, are called sunspots. A regular cycle of the sunspot activity known as the solar cycle has periods of minimum and maximum levels that occur approximately every 11 years. In reality, these 11-year sunspot cycles are the two halves of a 22-year quasi-sinusoidal cycle characterised by a change in the polarity of the magnetic fields associated with the sunspots (because the solar magnetic dipole orientation changes after every cycle) (Russell, 1974; Russell and Mulligan, 1995). By the application of the FT, values of foF2 recorded at the Grahamstown station (33.3 ^{o}S, 26.5 ^{o}E) have been used to illustrate the 11-year periodicity of the F2 region critical frequency (foF2) over a period of two solar cycles (Figure 1-2). During solar maximum, and especially during periods of high sunspot activity, the amount of ionising radiation (EUV) reaching the ionosphere increases substantially. This results in an increase in ionisation density of all ionospheric layers. Because of this increase absorption in the D region is high during the day, which leads to higher critical frequencies in the E, F1 and F2 regions. This is one of the geophysical conditions leading to successful propagation of only higher operating frequencies of the HF band during solar maximum, while the ionosphere can only support lower frequencies at solar minimum.

1.2.2 Irregular disturbances

As the name implies, these variations occur randomly in such a way that make them difficult to model. The major source of these irregular disturbances is solar flares, which affect radio communication at all latitudes. Solar flares are huge explosions on the surface of the sun, caused by a sudden release of magnetic energy that has built up over time in the active sunspot region of the solar atmosphere (Rishbeth and Garriott, 1969; Hargreaves, 1979; McNamara, 1994). Ionospheric disturbances associated with solar flares include sudden ionospheric disturbance (SID), polar cap absorption (PCA) and ionospheric and magnetic storms. They are classified according to the kind of emissions and effects they have on HF communications. For the purpose of this research I have familiarised myself with those that have greater effects on the F2 region of the ionosphere (particularly on foF2), which is the subject of this research. These are ionospheric and magnetic storms. They are briefly discussed below and details can be found in Rishbeth and Garriott (1969), Hargreaves (1979) and McNamara (1994).

1.2.2.1 Ionospheric storms

Ionospheric storms are disturbances in the ionosphere resulting from the delayed effect of the solar flares. This effect can occur throughout the solar cycle and is caused when a cloud of plasma ejected from a large flare strikes the earth (McNamara, 1994). Ionospheric storms may prevail for several days and mostly affect mid and high latitudes. Lower regions of the ionosphere are not appreciably affected by this effect unless the disturbance is great. At any geographical location, the effect of an ionospheric storm on the F2 region critical frequency (foF2) (either high or low) depends on the time of occurrence of the storm such as the time of the day and season, and on the geographic latitude and duration of occurrence (McNamara, 1994). This effect usually affects the HF communicators in their selection of maximum and lower usable frequencies (MUF and LUF).

1.2.2.2 Geomagnetic storms

Geomagnetic storms are disturbances in the Earth's magnetic field, arising from the effects of solar disturbances (solar flares) (Rishbeth and Garriott, 1969; McNamara, 1994, Hargreaves, 1979). During geomagnetic storms, the F2 region of the ionosphere becomes unstable, which may result in rapid fading of HF radio waves. The effects of a geomagnetic storm on the ionosphere are more severe over the auroral zone than the lower latitudes (Rishbeth and Garriott, 1969). These effects usually lead to a decrease in the maximum usable frequency (MUF) and an increase in the lowest usable frequency (LUF) of the F2 region, thereby resulting in a much smaller range of frequencies that can be used for HF communications. The severity of a geomagnetic disturbance at any time is represented by the magnetic indices K (a three-hourly quasi-logarithmic local index of geomagnetic activity) and A (a daily index of geomagnetic activity) (Rishbeth and Garriott, 1969; McNamara, 1994). Geomagnetic indices such as a_p, A_p, C_p and C9, which are related to K_p (a planetary three-hour average of the K index) have also been used to classify storms as weak or strong. Reports have shown that at any geographic location, the effect of a geomagnetic storm on the F2 region peak electron density depends on a number of factors such as Universal Time (UT), season of the year and the level of solar activity itself (Wrenn et al., 1987; Rodger et al., 1989; Field and Rishbeth, 1997; Duncan, 1969). Details on the causes and effects of geomagnetic storms can be found in Rishbeth and Garriott (1969), McNamara (1994) and Hargreaves (1979).

1.3 The International Reference Ionosphere (IRI) model

The success of HF communications depends on the ability to predict ionospheric conditions, and requires up-to-date information on the state of the ionosphere. As mentioned earlier, the key characteristics of particular concern for radio propagation conditions via the ionosphere are the maximum plasma frequency, foF2, and propagation factor M(3000)F2 for a distance of 3000 km. Over the years a large number of global, regional and station-specific models (Leftin et al., 1967; Jones and Obitts, 1970; Ching and Chiu, 1973; Chiu, 1975; Fox and McNamara, 1988; Rush et al., 1989; Mikhailov et al., 1994; Mikhailov et al., 1996; Bradley, 1999; Hanbaba, 1999; Poole and McKinnell, 2000; Bilitza, 1990, 2001; Bilitza et al., 1997; Tulunay et al., 2001; Liu et al., 2004) have been developed to predict ionospheric parameters. A comprehensive review of many of these ionospheric models has been provided by Bilitza (2002). Among these the International Reference Ionosphere (IRI) model is the most widely used. The IRI model has been developed to produce a global reference model, which is able to reproduce a number of ionospheric parameters. This model plays a significant role in application areas where radio signals are involved, such as ionospheric radio propagation and estimating the ionospheric effects on satellite signals. Significant efforts have been made in recent times to improve the IRI model. Recently, due to the work of Fuller-Rowell et al. (2000), a storm-time correction model has been a major development for the updating of the F2 peak electron density incorporated into the IRI model. Others include the works of Fox and McNamara (1988), Rush et al. (1989) and Bilitza (2001), which are based on improving worldwide maps of the monthly median foF2. The motivation behind these efforts has been the significant role that the F2 region peak electron density plays in the study of the ionosphere and its effects on radio communications. The IRI model is recognized as a standard specification of ionospheric parameters by the Committee on Space Research (COSPAR) and the International Union of Radio Science (URSI). The IRI is an international project jointly sponsored by COSPAR and URSI. The CCIR and URSI coefficients provide alternative maps of parameters, and are based on Fourier analysis and Legendre functions (spherical harmonic formulations) using monthly median values or worldwide values of foF2 for predicting foF2 (Fox and McNamara, 1988; Bilitza, 1990; Bradley, 1990; Zolesi and Cander, 2000). These organizations formed a Working Group in the late 1960s to produce an empirical standard model of the ionosphere. While COSPAR's prime interest is in a general description of the ionosphere as part of terrestrial environmental effects on spacecraft and experiments in space, URSI's prime interest is in the electron density part of IRI for defining the background ionosphere for radiowave propagation studies and applications (Bilitza, 2004). The IRI Working Group meets on an annual basis to discuss and implement improvements to the IRI model as new data and models become available and as old databases are fully evaluated and exploited. Later in this thesis, the IRI model (URSI and CCIR coefficients) are used as a benchmark to assess the success of the NN model.

1.4 Motivation for this present work

Recent studies (Balan et al., 1994; Richards, 2001; Sethi et al., 2002; Liu et al., 2003; Liu et al., 2004) have established the non-linear solar cycle dependence of the F2 peak electron density. It has also been well established that the most vulnerable region of the ionosphere to variability both on temporal and spatial scales is the F2 region due to the effect of the vertical and horizontal winds associated with global thermospheric circulation (Dougherty, 1961; King et al., 1967; Rishbeth, 1967, 1972, 1998; Kohl and King, 1967; Kohl et al., 1968). A comprehensive review on the effect of thermospheric winds on the ionospheric F2 region can be found in Rishbeth (1972) and Titheridge (1995). Most of the existing models (Jones and Gallet, 1962, 1965; Leftin et al., 1967; Jones and Obitts, 1970; Fox and McNamara, 1988; Rush et al., 1983, 1984; Rush et al., 1989) were developed by numerical mapping methods using theoretical formulations (i.e. spherical harmonic analysis) to describe the global distribution of the F2 region peak electron density. Numerical methods were employed to generate artificial values of foF2 for areas where measurements were not available, especially the ocean areas and southern hemisphere, and then combined with measured values of foF2 to develop global maps of the F2 region critical frequency (Bilitza, 2002). Bradley et al. (2004) have explained in detail the limitations and potential for updating the existing long-term global models due to an increase in the latest data and analysis techniques. These models provide a better reflection of the northern hemisphere than the southern hemisphere due to the disproportionate global distribution of ionosonde stations. The International Radio Consultative Committee (CCIR) and URSI coefficients are based on the worldwide ionosonde data for epochs 1954 and 1964 (Bradley, 1990; Zolesi and Cander, 2000). Also, Rush et al. (1983, 1984) coefficients were based on data from July 1975 to June 1976 and July 1978 to July 1979. These periods were considered representative of solar minimum and solar maximum conditions respectively, and may not accurately represent periods of solar maximum and minimum observed over a number of years. These models are based on geographical coordinates, Universal Time (UT), 12-month running mean of monthly sunspot number (R12) and modified-dip latitude (Modip). Models that use geographical coordinates as their basis have the problem that ionospheric data is not available for the vast areas occupied by the oceans. Again, there is some evidence of long-term ionospheric changes over greater time scales than a single solar cycle as a possible indicator of the atmospheric green house effect (Bremer, 1992). In view of these considerations, the primary motivation for this research is to develop a new global model for the prediction of foF2 and M(3000)F2, based on the application of Neural Networks (NNs), which exploits their ability to deal with non-linear behaviour thereby establishing and modelling the non-linear dynamical processes (both in space and time) associated with F2 region electron density on a global scale. Also investigated are parameters other than geographical coordinates on which the ionosphere is known to depend, and which are more evenly spread over the available data grid points. Unlike the classical methods, the NN technique provides an empirical model that can describe non-linear phenomena and requires no artificial data points in order to be able to generalise. The applications of NNs as an alternative to classical methods for predicting the non-linear behaviour of ionospheric parameters, both on a station and regional basis, have been well demonstrated (McKinnell, 1996, 2002; Wintoft and Cander, 1999; Poole and McKinnell, 2000; Wintoft, 2000; Tulunay et al., 2000; Xenos, 2002). The subject of this research is to apply the NN technique to model global F2 peak electron density using relevant geophysical input parameters.

The next chapter describes NNs and their basic elements. Chapter 3 describes in detail the process of developing each model and the results. These include sections on the relevant input parameters used for developing each model, sources of data, followed by NN architectures and comparisons of results with the IRI model. High latitude regions are known to have problems of unpredictability due to the effects of thermospheric winds, which usually limit the accuracy of the predictions of ionospheric parameters such as foF2 in these regions (Rishbeth and Garriott, 1969).

Chapter 4 describes the results obtained from some high latitude stations by NN models and compared with the IRI model predictions and the observed values. Finally, I discuss the justification of these techniques for modelling the foF2 and M(3000)F2 ionospheric parameters on a global scale and compare the results with the current IRI model.

Chapter 2

2 Neural Networks

2.1 Introduction

A Neural Network is an information-processing system that has certain performance characteristics in common with biological neural networks and is modeled after the human brain, which computes some relationship between its input(s) and output(s) (Fausett, 1994; Haykin, 1994).

The history of Neural Networks dates back to the early 1940s when McCulloch and Pitts (1943) developed simple models of biological neurons and their interaction systems. This was later followed by Rosenblatt (1959), whose work was based on single layer feed-forward networks. The use of single layer networks was later explored by many researchers in the 1950s and 1960s (Widrow and Hoff, 1960). There was a significant decline in interest in using NNs in the 1970s when Minsky and Papert (1969) demonstrated that single layer networks were not capable of learning classes of linearly inseparable functions. It was later discovered in the 1980s by researchers (Rumelhart et al., 1986b; McClelland and Rumelhart, 1988) that the limitations posed by single layer networks could be resolved if more layers (hidden layers) were added to the networks. This discovery played a major landmark in the recent resurgence of interest in the applications of NNs (most especially the generalized delta rule for learning by backpropagation) as a tool for solving a wide variety of problems in various fields. The backpropagation NN otherwise known as the *multilayer perceptron* or *multilayered feed-forward networks* has become the most commonly used NN for various applications in many fields because of its capability to solve complex problems. Examples of areas in which NNs have been successfully applied are: medicine, speech production, pattern recognition, control systems, speech recognition, business and ionospheric predictions (Fausett, 1994). Very simply a NN is a computer program that is trained to learn the relationship between a given set of inputs and the corresponding output(s). The applications of the NN technique have been found to be successful for solving problems in ionospheric predictions, due to the ability of this technique to provide empirical models that can describe non-linear phenomena by extracting patterns and detecting trends that are too complex to be noticed by classical methods and even humans when trained on real observed data (Williscroft and Poole, 1996; Altinay et al., 1997; Lamming and Cander, 1999; Tulunay et al., 2001). The following sections detail the basic elements of a NN, followed by the NN architecture and learning algorithm that are used throughout this research.

2.1 Basic Elements of Neural Networks

The basic element of a typical NN is shown in Figure 2-1. A NN is made of three basic components: weights, an activation function and a bias.

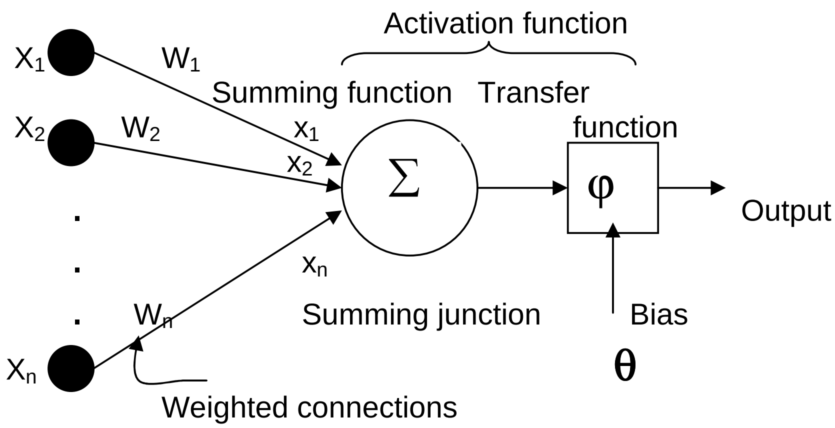

Figure 2-1 Basic elements of a network neuron.

Illustrated in figure 2-1, the values of W_1, W_2, …., W_n are weights associated with each unit (or neuron or node or cell as the case may be) which determine the strength of the output signals (x_1, x_2, …., x_n) from n input units, X_1, X_2, …., X_n according to

$$x_n = X_n W_n$$

The activation function is made up of the *combination function* and the *transfer function*. While the *combination function* sums up all the inputs into a single value, usually as a weighted summation, the *transfer function* calculates the output value from the result of the combination function, usually between 0 and 1. The bias, which is connected to each of the hidden and output nodes in a network, provides a threshold for the activation of nodes.

2.3 Multilayer feedforward networks

A NN architecture is made up of a large number of interconnected processing elements called units (or nodes), which respond in parallel to a set of input signals each with an associated weight (Fausett, 1994). Based on this simple definition, a NN is thought of as consisting of four main parts: (a) processing units each having a certain activation level at any point in time, (b) weighted interconnections between various processing units which determine how the activations of one unit leads to input for another unit, (c) an activation function which acts on inputs to compute the output signal and (d) a learning rule which specifies how the weights are being adjusted for a given input and output pair. The capability of the multi layer network stems from the non linearities used within the nodes. A typical example of a multilayer feedforward network architecture is shown in figure 2-2. This network has *i* input units, two hidden layers with *j* and *k* units respectively and one unit in the output layer. For the purpose of this discussion the inputs are not considered as an additional layer since the input units do not perform any of the functionality of a unit. This may not be the case in some applications.

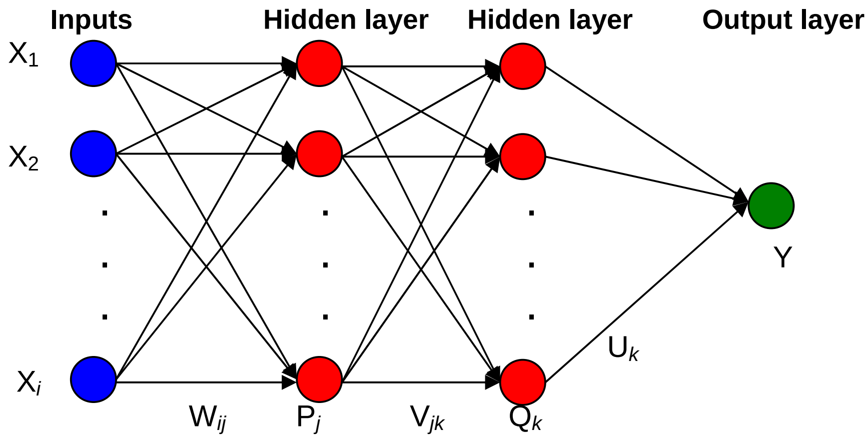

Figure 2-2. A two layer feedforward neural network

From figure 2-2 W_{ij} denotes the weight from a unit *i* in the network inputs to a unit *j* in the first hidden layer, V_{jk} denotes the weight from unit *j* to a unit *k* in the second hidden layer and U_k denotes the weight from a unit *k* in the second hidden layer to the unit of the output layer.

The basic operation of a NN involves summing its weighted input signal and applying an output, or activation function. Three common classes of transfer functions are the sigmoid, linear and hyperbolic functions. The choice of any of these functions depends on the type of problem to be solved by the network. The most widely used of these functions is the sigmoid function (also known as the logistic function) or "squashing" function, because the function is both continuous and differentiable (i.e. it provides *linear, near-linear,* and *non-linear approximations* for a given set of inputs) (Berry and Linoff, 1997). The binary sigmoid function has the following form:

$$a(n) = \frac{1}{1+\exp(-\alpha n)}, \qquad 0 \le a(n) \le 1 \qquad 2.1$$

Another common transfer function is the bipolar sigmoid, which has the form:

$$a(n) = \frac{2}{1+\exp(-\alpha n)} - 1, \qquad -1 \le a(n) \le 1 \qquad 2.2$$

The bipolar sigmoid function is closely related to the function

$$\tanh(n) = \frac{e^n - e^{-n}}{e^n + e^{-n}} \qquad 2.3$$

where α ($\alpha > 0$) is a slope parameter (learning rate) which can be used to modify the shape of the sigmoid function.

These functions are as illustrated in figures 2-3a and 2-3b respectively.

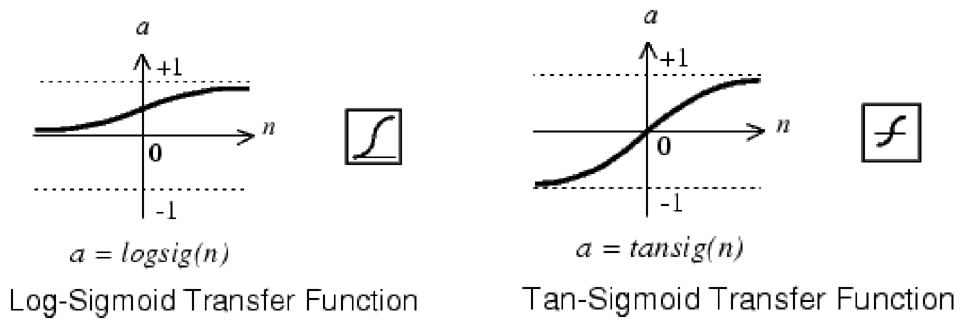

(a) (b)

Figure 2-3 A representation of (a) logistic sigmoid function and (b) bipolar sigmoid function.

2.4 Learning mechanism

The learning mechanism of a particular NN is usually determined by the type of problem needing to be solved. NN learning algorithms can be divided into two major groups. These are supervised (associative learning) and unsupervised (Self-Organisation) learning (Haykin, 1994; and Fausett, 1994). In the supervised learning algorithm both input vectors and target vectors are specified. During training the network compares the outputs with the desired target value. After training the NN can then be used for predictions when presented with input that is similar, but not identical to that used in training. One of the most commonly used supervised algorithms is the backpropagation learning algorithm. A self-organising NN is provided with input vectors without target vectors. As the name implies, it self-organises data presented to the network and detects their emergent collective properties. That is, during training the network modifies the weights and learns the distribution of the patterns so that similar input patterns are assigned to the same output cluster (Fausett, 1994). Once the training is completed and a new pattern is presented, one of the output neurons will detect the category a particular input belongs to. For the purpose of this work a supervised backpropagation learning algorithm has been employed throughout using the NN software package version 4.2 of the Stuttgart Neural Network Simulator (SNNS, 1995a). The software was developed by the University of Stuttgart Institute for Parallel and Distributed High Performance Systems and is available via the Internet (SNNS, 1995b). The backpropagation algorithm is briefly discussed as follows and details can be found in Haykin (1994) and Fausett (1994).

2.5 Backpropagation learning algorithm

As mentioned earlier, a backpropagation algorithm is a supervised training network. It involves using a gradient-descent approach to minimize the squared error between generated output values and target output values (Fausett, 1994). A backpropagation algorithm consists of two major stages. The first stage is referred to as the **forward pass,** which involves network weights initialization to reasonably small random values, propagation of input signals layer-by-layer to the outputs and the predicted outputs calculated. The second stage is the **backward pass,** which involves propagation of the error backward to all the units in the previous layer (i.e. the hidden units that are connected to the output layer) followed by an adjustment of the weights from hidden units to the output units according to the gradient descent rule. These processes are repeated until the actual output is moved closer to the desired output (i.e. when stopping criterion is satisfied). The stopping criterion is usually applied to prevent overfitting whereby a trained NN performs very well on the training set but not as well as it could when presented with unseen patterns. The backpropagation learning algorithm is illustrated as follows using figure 2-4. The network has *i* input units, one hidden layer with *j* units and a unit output layer. W_{ij} represent the weights.

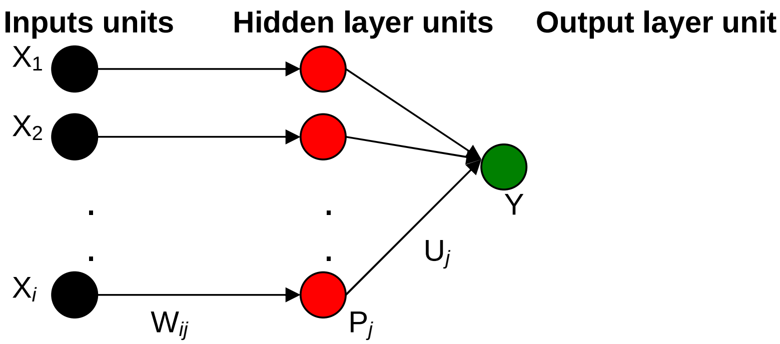

Figure 2-4. Backpropagation NN with one hidden layer

In the forward pass

Step 1. Initialize all weights to small random numbers in the network.

Step 2. While terminating condition is not satisfied, repeat steps 3 to 6

Step 3. Each input signal x_i is propagated to all the units of the hidden layer.

Step 4. All input signals are summed up in each of the hidden units into a single value according to

$$P_j = \sum_{i=1}^{n} x_i W_{ij} \ , \qquad 2.4$$

the output signal of each unit is computed using an appropriate activation function according to

$$P_{j(out)} = f_{hidden}\left(\sum_{j=1}^{m} x_i W_{ij}\right), \qquad 2.5$$

where f_{hidden} is the hidden layer transfer function.

This is followed by summing up all the output signals from the hidden units at the output unit according to

$$Y = \sum_{j=1}^{m} p_{j(out)} U_j \qquad 2.6$$

Eventually, the output is calculated as:

$$Y_{out} = f_{output} Y \qquad 2.7$$

where f_{output} is the output layer transfer function.

Backward pass

Step 5. Starting from the output layer, an error term is computed as:

$$\delta_{output} = f^{/}_{output} \left(T - Y_{out} \right) \qquad 2.8$$

where $f^{/}_{output}$ is the derivative of the output unit transfer function, T is the desired network output and Y_{out} is the computed network output.

The error signal is propagated to each unit in the hidden layer and the error is computed as:

$$\delta_j = f^{/}_{hidden} \delta_{output} U_j \qquad 2.9$$

This is followed by an adjustment of the weights

For hidden units

$$\Delta W_{ij} = \alpha \delta_j x_i \qquad 2.10$$

and for the output unit

$$\Delta U_j = \alpha \delta_{output} p_j \qquad 2.11$$

where α is the network learning parameter.

The new weights for the hidden and output units respectively are

$$W_{ij(new)} = W_{ij(old)} + \Delta W_{ij} \qquad 2.12$$

and

$$U_j = U_{j(old)} + \Delta U_j \qquad 2.13$$

Step 6. At this step the stopping criterion is tested.

2.6 Generalization

The aim of applying NNs is generally to produce acceptable results when presented with input patterns it has not previously seen. In other word, a NN is trained to achieve a balance between the ability to respond correctly to the input patterns that are used for training (memorization) and good responses to new input patterns that are similar, but not identical to that on which the network was trained (generalization) (Fausett, 1994). One of the major problems that impedes generalization during NN training is called overfitting. Overfitting occurs when the error on the training data set is driven to a very low value for too long such that the network performs very well on the training data, but not as well as it could on unseen data. In this case the network is said to have memorized the training examples, but it has not learned to generalize new situations. In order to achieve generalization, Hecht-Nielsen (1990) suggested the use of two sets of data during training. The first subset is the training set, which is used for computing the gradient and updating the network weights, while the second subset is the testing set, which is used to check whether the network has learnt the structure held within the training set. Firstly, the network is trained for different numbers of epochs (each run through all the training data is called an epoch). During training, the error on the testing set will normally decrease during the initial phase of training, as does the error on the training set. However, when the network starts to overfit the data (memorizing), the error on the testing set begins to rise. The point at which the error on the testing set begins to rise is estimated and the network is trained for this number of epochs (i.e. stopping criterion). Once the network has been trained, it can now be used for the purpose for which it has been trained. The next chapter is centered on the application of this backpropagation learning algorithm for predictions of foF2 and M(3000)F2 ionospheric parameters and their results.

Chapter 3

3 GLOBAL MODEL: F2 REGION

3.1 Introduction

Ionospheric predictions are an important guide for the planning and frequency management of HF communications, HF automatic link establishment and global positioning systems (GPS). In the past much effort has been expended in the quest for global, regional and station-specific ionospheric models to predict the F2 region critical frequency (foF2) and propagation factor M(3000)F2. Authors such as Shimazaki, 1955; Jones and Gallet, 1962, 1965; Leftin et al., 1967; Jones and Obitts, 1970; Bradley and Dudeney, 1973; Bilitza et al., 1979; Fox and McNamara, 1988; Rush et al., 1983, 1984; Rush et al., 1989; Bradley, 1999; Hanbaba, 1999; Fuller-Rowell, 2000; Bilitza, 1990, 1997, 2001; Zolesi and Cander, 1998 have used the standard approach of fitting mathematical functions to a mixture of measured and theoretical ionospheric data. Various ionospheric models have been employed in different capacities such as HF propagation studies (Barghausen et al., 1969; Jones and Obitts, 1970; Nisbet, 1971), and transionospheric propagations models (Bent et al., 1978). Variations (both temporal and spatial) of many of the key ionospheric parameters, especially the F2 region critical frequency, are complex due to the complicated non-linear dynamical processes arising from temporal and geographical variabilities in the upper atmospheric chemistry, ionisation production and loss mechanisms, particle diffusion and electrodynamical phenomena. In order to take care of these complex variations in ionospheric predictions for practical applications with an acceptable minimum error, fast and robust techniques are required. As a result, the techniques of neural networks (NNs), which are explained in chapter 2, have been employed in this research to develop global empirical models for the peak electron density of the F2 region of the ionosphere. The next section discusses the results of the application of NNs to global modelling of the F2 peak electron density, followed by sections on the four categories of models namely, the foF2 model, M(3000)F2 model, short-term foF2 model and the near real time foF2 model developed in this research. Details on the source of data, NN architectures, input and output space, training procedure and testing on each model are discussed in this chapter.

3.2 Initial attempts: foF2 NN model

3.2.1 foF2

In the last decade, much attention has been given to the use of NNs in many different applications where there is a need to find a non linear dependence between variables (Fausett, 1994). NNs have been employed for various ionospheric modeling applications such as the prediction of the noon value of foF2 (Williscroft and Poole, 1996; Francis et al., 1998), short-term prediction of foF2 (Altinay et al., 1997; Cander and Lamming, 1997; Wintoft, 2000; Wintoft and Cander, 1999; McKinnell and Poole, 2000, 2001), temporal and spatial forecasting of foF2 (Kumluca et al., 1999; Wintoft and Cander, 2000; Tulunay et al., 2000), prediction of the monthly median of foF2 (Lamming and Cander, 1999), prediction of geomagnetic activity (Hernandez et al., 1993; Lundstedt and Wintoft, 1994; Wu and Lundstedt, 1996; Wintoft and Cander, 2000) and prediction of long-term trends in foF2 (Poole and Poole, 2002). For the purpose of global modeling, which is the main focus of this research, a preliminary investigation was carried out in order to decide on the input parameters to NNs that could best describe the output parameter foF2 on a global scale. The inputs to the IRI model for predicting foF2 are geographic latitude and longitude, modified dip latitude, Universal time (UT), day number of the year, 12-month running mean of monthly sunspot number (R_{12}) or Global ionospheric index based on ionosonde foF2 data (IG_{12}) (Bilitza, 2002). Within the IRI, R_{12} = 0 and 100 are taken as representative of low and high levels of solar activity respectively for foF2 predictions, while intermediate values of foF2 are assumed to have linear variation with R_{12}. In the case where R_{12} is greater than 150, foF2 is taken to be the same at all locations and time. The saturation effect on the foF2 for R_{12} greater than 150 was observed by Kane (1992). The accuracy of most of the available models, including the IRI, is dependent upon the geographical distribution of the data that were used in the generation of their coefficients due to the uneven global distribution of ionosonde stations across the globe. King and Slater (1973) reported that the accuracy of CCIR predicted foF2 values is quite reasonable in the areas where data were available for the inclusion in the analysis that generated the coefficients (especially the northern hemisphere), while the accuracy is questionable for the areas where data is not available, for example, with the vast areas occupied by the oceans and sparsely distributed data areas (especially in the southern hemisphere). Because of this, predictions of foF2 in the northern hemisphere are often more accurate than in the southern hemisphere.

3.2.2 Database

The primary source of data in this research is the long data record of daily hourly values of foF2 and M(3000)F2 accumulated by the worldwide network of ground ionosondes located ionospheric stations across the globe. The database covers the years from 1964 to 1986, which include all periods of calm and disturbed magnetic activities, and is spread across three ionospheric regions covering low, mid and high latitudes. Although not all the stations have data that are equally distributed within these years, efforts have been made to ensure that the best use is made of the available data from each station within this period. For example, some stations have data from 1964 to 1976 while some have data from 1976 to 1978, and some stations did not have data for a complete solar cycle. As long as a station can provide up to at least seven years of data within a solar cycle, such a station is considered in the training process. A major problem with most stations, if not all, is that there are a lot of missing data points due to one reason or another. This problem has been partially overcome with the use of NNs because this technique does not require evenly distributed data points in the training procedure and there is no need to generate artificial data for the missing points. In the initial attempts measured values of foF2 from 36 ionospheric stations (Tables 1a and 1b) have been used to train NNs. The performance of the initial NNs was verified with measured foF2 data from ionospheric stations in Table 1b and compared with the IRI model (URSI and CCIR coefficients). Figure 3-1 illustrates a map of coordinates of training and verification stations.

Table 1a. Ionospheric stations used for training of the foF2 NNs (initial attempts)

	Station name	Latitude ^oN	Longitude ^oE
1	Kiruna	67.8	20.4
2	Narssarssuaq	61.2	314.6
3	Uppsala	59.8	17.6
4	Moscow	55.5	37.3
5	Kaliningrad	54.7	20.6
6	Juliusruh/Rugen	54.6	13.4
7	Goose Bay	53.3	299.2
8	Slough	51.5	359.4
9	Dourbes	50.1	4.6
10	Winnipeg	49.8	265.6
11	Lannion	48.5	356.7
12	Ottawa	45.4	284.1
13	Wakkanai	45.4	141.7
14	Rome	41.8	12.5
15	Boulder	40.0	254.7
16	Akita	39.7	140.1
17	Wallops Is	37.9	284.5
18	Yamagawa	31.2	130.6
19	Grandbahama	26.6	281.8
20	Okinawa	26.3	127.8
21	Maui	20.8	203.5
22	Raratonga	-21.2	200.2
23	Brisbane	-27.5	152.9
24	Mundaring	-32.0	116.3
25	Canberra	-35.3	149.0
26	Concepcion	-36.6	287.0
27	Hobart	-42.9	147.2
28	Port Stanley	-51.7	302.2
29	Campbell Is	-52.5	169.2
30	Argentine Is	-52.5	169.2
31	Halley Bay	-75.5	333.4

Table 1b. Ionospheric stations used for verification of foF2 NNs (initial attempts).

	Station name	Latitude ^oN	Longitude ^oE
1	Grahamstown	-33.3	26.5
2	Norfolk Is	-29.0	168.0
3	Tomsk	56.6	84.9
4	Point Arquello	34.6	239.4
5	Irkutsk	52.4	101.0

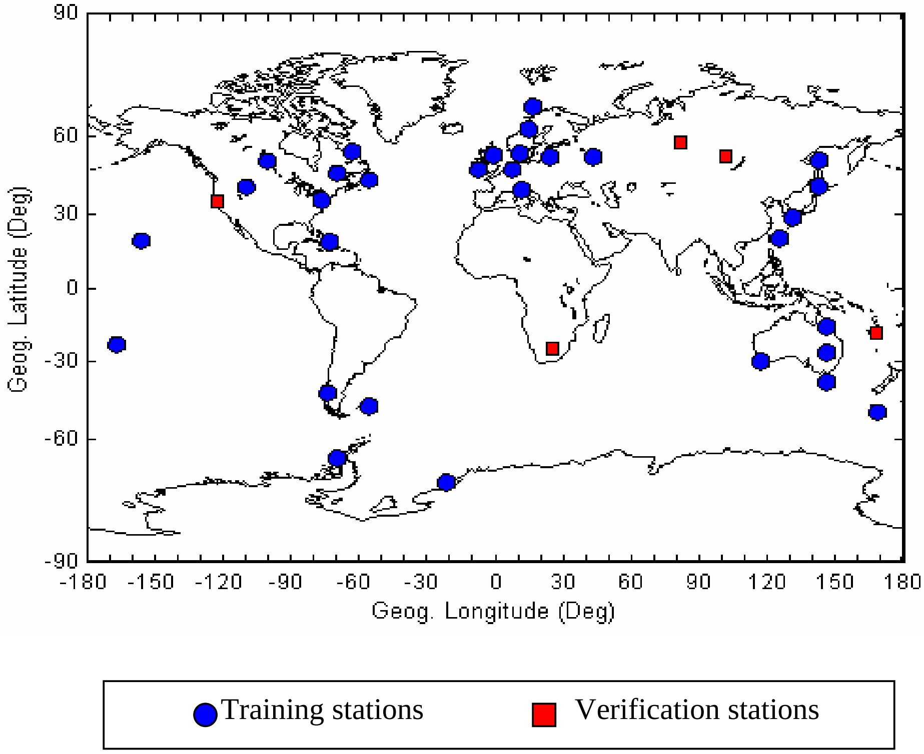

Figure 3-1. Map of coordinates of training and verification stations used for the initial foF2 NNs.

3.2.3 NN input space

As a requirement for the training of a NN, input parameters representing the variables that the output responds to are required. As mentioned earlier, the F2 region ionosphere is subject to a number of influences since its existence is directly related to the changes resulting from the interaction of solar radiations, solar wind and the geomagnetic field. The choice of input parameters to the NN is based on previous findings by many researchers as well as on sources that are known to cause variations in foF2. Various groups (Rishbeth and Setty, 1961; Wright, 1963; Rishbeth, 1967, 1972, 1998; Kohl and King, 1967; Rishbeth and Garriott, 1969; Hargreaves, 1979; McNamara, 1994; Forbes et al., 2000; Rishbeth and Mendillo, 2001) have discussed in detail the variability of the F2 region maximum electron density with latitude, solar activity, magnetic activity and solar wind. The relative importance of these sources and their contributions to the prediction of foF2 have also been established (Kane, 1992; McKinnell, 1996; Williscroft and Poole, 1996; Jones and Obitts, 1970; Kumluca et al., 1997; Kouris et al., 1998; Kumluca et al., 1999; Wintoft and Cander, 1999; McKinnell and Poole, 2000, 2001; Bilitza, 2000; Chen et al., 2000; Liu et al., 2003; Liu et al., 2004). The result of the Fourier transform (FT) of foF2 (Grahamstown) for the interval January 1973 through December 2000 (a total of 27 years) is illustrated in Figure 1-2. As can be observed in Figure 1-2, the spectral analysis of foF2 temporal variation (given in behaviour of amplitude) shows pronounced changes within a duration of 24 hour (diurnal), 1 year (annual) and 11-years (solar). The input space to the NN for the purpose of this research is discussed as follows.

3.2.3.1 Diurnal variation

Earlier studies (Rishbeth and Setty, 1961; Rishbeth and Garriott, 1969; Hargreaves, 1979) of the diurnal F2-region variation showed that its critical frequency, foF2, reaches its lowest level in the early hours of the morning, rises rapidly after sunrise due to photoionization during the day and starts to fall to low values again at sunset due to recombination. As a result, the hour number, HR (in Universal Time, UT) was considered to represent the diurnal variation of foF2 in the inputs to the NN. The choice of solar diurnal cycle (24 hour) (i.e. solar day) as a representative of diurnal variation (HR) of foF2 is based on the fact that its power amplitude (order of 5×10^9) is much higher when compared with that of solar semidiurnal cycle (12 hour) (order of 7.5×10^7) and lunar semidiurnal cycle (12.42 hour) (order of 10×10^4) (see figure 1-2). The HR is an integer in the range 0 < HR < 23. Following Williscroft and Poole, (1996), in order to see 00h00UT and 23h000UT as two adjacent hours, HR input is split into its cyclic components according to

$$\mathrm{HRS} = \sin\left(\frac{2\pi \text{ x UT}}{24}\right) \tag{3.1a}$$

$$\mathrm{HRC} = \cos\left(\frac{2\pi \text{ x UT}}{24}\right) \tag{3.1b}$$

The 24-hour variation takes care of its harmonics (i.e. 12-, 8-, 6-hour, etc.).

3.2.3.2 Seasonal variation

The solar zenith angle (χ) dependence of diurnal and seasonal variations in the F2 region of the ionosphere has been well established (Wright, 1963; Rishbeth and Garriott, 1969; Hargreaves, 1979; McNamara, 1994; Forbes et al., 2000). The inclusion of the solar zenith angle as an input to the NN, rather than only geographic latitude and longitude, eliminates the huge "holes" in the input data that may arise from the geographical clustering of the ionospheric data. As a result this parameter has been included as an input to the NN, and its values with respect to each geographical location were generated using the following relation:

$$\mathrm{Cos}(\chi) = \sin(\theta)\sin(\delta) + \cos(\theta)\cos(\delta)\cos(\lambda_s - \lambda_g) \tag{3.2}$$

where λ_s (subsolar longitude) is given as

$$\lambda_s = 15\mathrm{H} - 180$$

δ is the subsolar latitude (i.e. angle between the earth-sun line and the equatorial plane called the declination angle) given as

$$\delta = 23.45\sin\left[\frac{360}{365}\left(\mathrm{N} + 284^0\right)\right] \tag{3.3}$$

λ_g is the geographic longitude, θ is the geographic latitude, H is the hour number and N is the day number of the year.

Using the argument as for the hour number, HR, the solar zenith angle is converted as follows:

$$\mathrm{CHIS} = \sin\left(\frac{2\pi \text{ x CHI}}{360}\right) \tag{3.4a}$$

$$\mathrm{CHIC} = \cos\left(\frac{2\pi \text{ x CHI}}{360}\right) \tag{3.4b}$$

It has also been established (Williscroft and Poole, 1996; Kumluca et al., 1999) that not only the hour of the day but also the day of the year has an effect on the variations of foF2. This variation is due mainly to the response of the maximum electron density to the seasonal changes in the solar zenith angle and global thermospheric circulation. A comparison of the power amplitudes of monthly (27-day), semiannual (182.5 day) and annual (1 year) cycles of Grahamstown (33.3 ^{o}S, 26.5 ^{o}E) foF2 values, which are of the order of 7.7 x 10^5, 2.8 x 10^8 and 3.3 x 10^8 respectively, was carried out using Fourier analysis techniques (Figure 1-2). The results obtained confirmed that foF2 has a strong seasonal dependence. The inclusion of day number of the year, DN, (1 < DN < 365) (1 year cycle), which also represents the seasonal variation of foF2, as an input to NN is based on the fact that its power amplitude is greater than that of 27-day cycle (Figure 1-2). The effect of the semiannual cycle variation has been taken care of by the annual cycle variation. Again, to avoid unrealistic discontinuity between December 31 and January 1, the seasonal variation (DN) is represented by the two quadrature components as follows (Williscroft and Poole, 1996):

$$\mathrm{DNS} = \sin\left(\frac{2\pi \text{ x DN}}{365}\right) \tag{3.5a}$$

$$\mathrm{DNC} = \cos\left(\frac{2\pi \text{ x DN}}{365}\right) \tag{3.5b}$$

Work on the seasonal behaviour of the F2 region of the ionosphere has been carried out by the following groups: Rishbeth and Setty, 1961; Wright, 1963; King and Smith, 1968; Rishbeth and Garriott, 1969; Torr and Torr, 1973; Hargreaves, 1979; Torr et al., 1980; Titheridge and Buonsanto, 1983; McNamara, 1994; Millward and Rishbeth, 1996; Forbes et al., 2000, Rishbeth and Mendillo, 2001. A summary of seasonal variations in the F2 region peak electron density, which are larger in winter than in summer, has been given by Torr et al. (1980) as follows: 1) seasonal changes in neutral composition; 2) an increase in the vibrational temperature of N_2 and hence in the rate coefficient for the reaction

$$O^+\left({}^4S\right) + N_2 \rightarrow NO^+ + N\,;$$

3) an increase in winter in the production of O^+ (^4S) which results in enhanced quenching of electron, O^+ (^2D).

3.2.3.3 Solar cycle variation

Various studies have established dependence of the ionospheric characteristic, foF2, on solar activity (Appleton, 1950; Kane, 1992; Bradley, 1993; Williscroft and Poole, 1996; Kouris et al., 1998; Zakharov and Tyrnov, 1999; Chen et al., 2000; Forbes et al., 2000; Richards, 2001; Rishbeth and Mendillo, 2001; Sethi et al., 2002; Liu et al., 2003). Comprehensive studies on the uniqueness of the connection between foF2 and solar activity during the growth and decay phase of the solar cycle have been carried out (Rao and Rao, 1969; Smith and King, 1981; Triskova and Chum, 1996). An excellent review of the relative importance of the solar indices (the 12-month running mean of sunspot number R_{12}, the solar radio flux F10.7 and the solar EUV (170 – 190 Å) for driving the IRI model has also been presented by Bilitza (2000). Also, as discussed earlier in section 1.2.1.3, the results of FT on measured values of foF2 recorded at the Grahamstown station (33.3 ^{o}S, 26.5 ^{o}E) have been used to illustrate the 11-year periodicity of foF2 over a period of two solar cycles (Figure 1-2). Therefore, as a measure of solar EUV flux which has been established to affect the F2 region critical frequency (foF2), R2 (2-month running mean of the daily sunspot number) has been employed in this research as an input to the NN. The choice of R2 is based on the findings of Williscroft and Poole (1996), where R2 was determined to be the optimum parameter to represent the solar variations for a trained NN to predict foF2. In previous work, McKinnell (1996) explored the possibility of using F10.7 cm solar flux as a measure of the solar activity but no great improvement over the R2 value was found.

3.2.3.4 Short-term variations

In addition to the well-known cyclic variations (i.e. diurnal, seasonal and 11-year variations), F2 region peak electron density is also subject to short-term (noncyclic) (1 to 4 days, typically) variations (Duncan, 1969; Wrenn et al., 1987; Rodger et al., 1989; Fuller-Rowell et al., 1996; Field and Rishbeth, 1997; Poole and McKinnell, 2000). Recently, the work of Fuller-Rowell et al. (2000) has shown the significance of inclusion of a storm-time correction in the prediction of the F2 region peak critical frequency (foF2). Short-term variations occur randomly in such a way that makes them difficult to model. Typical examples of such disturbances that give rise to these variations are the ionospheric and geomagnetic storms that are caused by solar flares (see section 1.2.2). This suggests that a parameter that can predict these noncyclic variations is required as an input to the NN. As a result, a measure of the magnetic activity, A16 (2 day running mean of the 3-hour planetary magnetic index, a_p) has been employed. The choice of A16 is based on the findings of Williscroft and Poole (1996), where A16 was determined to be the optimum magnetic index for the predictions of foF2. The index a_p was obtained from the Space Physics Interactive Data Resource (SPIDR). The service of SPIDR is provided by the World Data Center for Solar-Terrestrial Physics (STP).

3.2.3.6 Inputs related to Earth's magnetic field

It is well known that the effects of thermospheric winds are very important for accurate explanation and modeling of F-region parameters, particularly, the daily hourly variation of peak electron density, and its seasonal anomaly (Rishbeth, 1972). Various groups (Rishbeth, 1967, 1998; King et al., 1967; Kohl et al., 1967, 1968; Kohl and King, 1967) have studied the effects of neutral air winds on the ionospheric F2 region. A comprehensive review can be found in Rishbeth (1972) and Titheridge (1995). The Universal Time (UT) control of F region electron density, particularly at high latitudes, has been suggested to relate to diurnal rotating neutral wind (Kohl et al., 1968; King et al., 1967, King et al., 1968; Duncan, 1969). Several other studies on the effect of magnetic declination and inclination as a consequence of horizontal atmospheric winds have been reported (Eyfrig, 1963; Rishbeth, 1972; King et al., 1968; Challinor and Eccles, 1971). Based on these findings regarding the linkage between ionospheric morphology and themospheric wind theory, both declination and inclination of the Earth's magnetic field were included in the inputs to the NN to model the effects of thermospheric winds. The well-known vertical ion drift equation produced by horizontal neutral air winds is given as

$$W = U\cos(\theta - D)\cos I \sin I \tag{3.6}$$

where *W* is the vertical ion drift velocity, *U* is the horizontal wind velocity blowing at geographic azimuth θ, and *D* and *I* are the magnetic declination and inclination respectively. This vertical ion drift velocity can vary markedly from one place to another. From equation 3.6, one can deduce that

$$W \propto \cos(\theta - D) \text{ and} \qquad (3.7a)$$

$$W \propto \cos I \sin I \qquad (3.7b)$$

This implies that the phase of the diurnal variation of *W* depends on *D* (equation 3.7a) and the amplitude of the diurnal variation of *W* depends on *I* (equation 3.7b) (Challinor and Eccles, 1971). Following the expansion of the vertical ion drift equation, *D* is converted to two cyclic components according to

$$\mathrm{DS} = \sin\left(\frac{2\pi \text{ x } D}{360}\right) \qquad \text{(D is in degrees)} \qquad (3.8a)$$

and

$$\mathrm{DC} = \cos\left(\frac{2\pi \text{ x } D}{360}\right) \qquad (3.8b)$$

while *I* is expressed as

$$\mathrm{IS} = \sin\left(\frac{2\pi \text{ x } 2I}{360}\right) \qquad \text{(I is in degrees)} \qquad (3.9)$$

3.2.3.6 Other inputs to the NNs

As with seasonal variations, the ionosphere is well known to vary considerably with latitude (θ) due to variation in solar zenith angle, and the latitudinal dependence of the neutral wind and its role in blowing ionization up and down the field lines (Rishbeth and Gariott, 1969; McNamara, 1994). As mentioned earlier in section 3.2.3.2, if one uses solar zenith angle as an input to the NN rather than geographic coordinates, the problem of the huge "holes" in the input data arising from the geographical clustering of the ionospheric data is eliminated. But in view of the fact that geographic coordinates are related to solar zenith angle and also because they affect secondary effects such as neutral wind and local time, they are therefore considered to be relevant as inputs to the NN. The Local Time, LT, which is represented as the angle of the meridian relative to subsolar point M (i.e. angular equivalent of the location Local Time), accounts for the persistence of the ionosphere that is evidenced by the asymmetry of foF2 about noon at any geographical location. M is expressed as

$$\mathrm{M} = (\mathrm{UT} - 12)\ \mathrm{x}\ 15 + \lambda_{\mathrm{g}} \tag{3.10}$$

where UT and λ_g are the Universal Time and geographic longitude respectively. Using the same argument as for the hour number HR, M is converted according to:

$$\mathrm{M} = \sin\left(\frac{2\pi\ \mathrm{x}\ \mathrm{M}}{360}\right) \tag{3.11a}$$

$$\mathrm{M} = \cos\left(\frac{2\pi\ \mathrm{x}\ \mathrm{M}}{360}\right) \tag{3.11b}$$

In addition to those input parameters mentioned above, other parameters considered at this initial stage are L-value (i.e. equatorial crossing distance of the magnetic field line in a dipole field), geomagnetic field components (X, Y, Z) and total magnetic field F at each ionospheric station. The input parameters to the NN with the best performance during initial attempts were DNS, DNC, HRS, HRC, CHS, CHC, MS, MC, A16, R2, IS, DS, DC, θ). The NN produces the function F such that

$$f_0\mathrm{F2} = \mathrm{F}(\mathrm{DNS}, \mathrm{DNC}, \mathrm{HRS}, \mathrm{HRC}, \mathrm{CHS}, \mathrm{CHC}, \mathrm{MS}, \mathrm{MC}, \mathrm{IS}, \mathrm{DS}, \mathrm{DC}\ \mathrm{R2}, \mathrm{A16}, \theta)$$

These inputs have their meanings as described above.

3.2.4 Neural network architecture

The basic structure of the foF2 NN is a standard fully connected feed-forward network with back propagation. Figure (3-2) shows the block diagram of the initial foF2 NNs with input and output parameters. The number of inputs and output units are determined by what is considered in section 3.2.3. The output layer has one node of the target parameter foF2 (Figure 3-2). There are no hard and fast rules for choosing the number of hidden layers and the number of nodes in each of the hidden layers. It is generally believed that one hidden layer is sufficient for any network architecture (Fausett, 1994; Haykin, 1994). Various authors have established the use of one hidden layer to be successful for a trained NN (Williscroft and Poole, 1996; Tulunay et al., 2000; Poole and Poole, 2002). Several other authors have employed NNs with more than one hidden layer based on the complexity of their networks (Hirose et al., 1991; Lamming and Cander, 1999; Derong et al., 2002; Xenos, 2000). In order to determine the optimum NN for predicting foF2, I trained several different NNs with different architectures. The best NN architecture obtained in this case was a NN with two hidden layers each having 25 and 20 nodes respectively. The choice of this NN architecture was based on its better performance in terms of RMSE when compared with the results of other configurations. Other configurations that were tested were: one hidden layer with each having 20, 30, 40 nodes, two hidden layers each having 10/10, 20/10, 25/20, 25/25, 30/25, and three hidden layers each having 10/10/10, 20/20/10, 25/20/20 nodes in the middle layers. It should be clearly stated here that the choice of number of nodes for each hidden layer was determined on a trial-and-error basis. The sigmoid transfer function with weight between -1.0 and 1.0 was applied as an activation function.

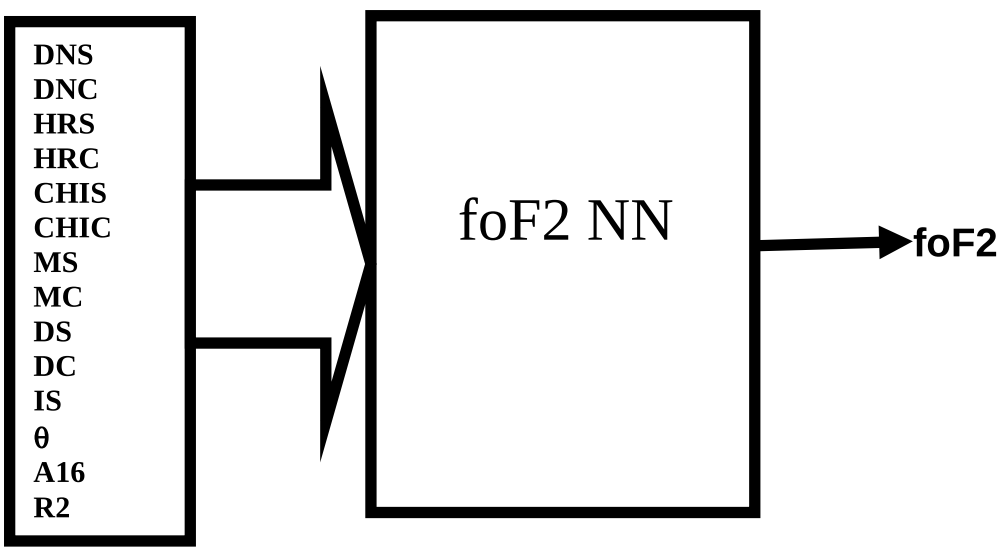

Figure 3-2: A block diagram of the inputs and output to the initial foF2 NNs.

3.2.5 Training, testing and verification of the initial foF2 NNs

The aim of training a NN is to achieve a balance between correct responses to training patterns and good responses to a new testing input pattern that is similar, but not identical, to that used in training. This implies that the performance of a NN strongly depends on the selection of the training data set. In making use of NNs, if the input data are outside the range of the data values used in the training, the reliability of the NN output would be compromised. Thus, the training data set should cover as wide a range of values as possible. As a result, the foF2 NN has been trained with two solar cycles of hourly target foF2 data from 36 ionospheric stations (Tables 1a and 1b) across the globe spanning the period 1964 to 1986. In order to achieve good responses to the testing data set, the whole data set was randomly divided into training data and testing data sets in the ratio 70% and 30% respectively. The NN is trained by means of the training data set, while the testing data set is used during the training process to check that the NN is not being over-trained. This enables the NN to generalize well when presented with an input pattern that was not part of the data set used in training. During training, the NN is presented with input values, which produces one output value, foF2 (Figure 3-2). The backpropagation algorithm selects a training example, makes a forward and a backward pass (i.e. weights adjustment), and then repeats until the RMSE difference does not change by more than some predetermined amount over a certain number of epochs. At this stage the NN is said to have achieved generalization, such that it produces a good performance on unseen input patterns similar to those used in training the NN. After training as described above, a further test of the NN was necessary to test the hypothesis that a NN trained with the inputs described in section 3.2.3 could successfully predict foF2 for regions that are geographically remote. To do this, two NNs (NNA and NNB) were trained. The first NN (NNA) was trained with data from 31 ionospheric stations (Table 1a) without those stations listed in Table 1b (verification stations). The second NN (NNB) was trained with data from all the stations in Tables 1a and 1b. This enables one to compare results from the two NNs and estimate how well a trained NN can predict foF2 for locations where data are not available, for instance, within the ocean areas. Once a NN has been trained, it will provide an estimate of foF2 for any given set of the input parameters DNS, DNC, HRS, HRC, CHS, CHC, MS, MC, IS, DS, DC, θ, A16 and A2, regardless of its geographical location within the input space.

3.2.6 Results and discussion

Since the objective is to develop a global F2 region peak electron density empirical model, observed foF2 data from five ionospheric stations (Table 1b) that were not part of the training stations were used to verify the predictability of the initial NN models developed. These verification stations were chosen for their geographic remoteness from the training stations in order to verify the ability of NNA to predict foF2. In order to estimate the performance of the NNs, daily hourly values of foF2 predicted from NNA and NNB are compared with those determined by the existing IRI model (URSI and CCIR coefficients) and observed values of foF2 obtained from the verification stations and RMSE differences calculated. The performance of the NNs has been evaluated using the RMS error formula expressed as

$$\mathrm{RMSE} = \sqrt{\frac{1}{\mathrm{N}}\sum_{i=1}^{N}\left(foF2_{obs} - foF2_{pred}\right)^2} \qquad (3.12)$$

where N is the number of data points, and $foF2_{obs}$ and $foF2_{pred}$ are the observed and predicted foF2 values respectively.

As shown in Table 2, the observed values of foF2 during 1965, 1969, 1977 and 1980 were used to compute the error differences between the observed and predicted values derived from URSI, CCIR, NNA and NNB models. These years were chosen as representatives of solar minimum (1965, 1977) and solar maximum (1969, 1980) periods. Table 2 shows the RMSE difference in foF2 determined for the five selected ionospheric stations. A closer inspection of the RMSE values (Table 2) obtained for NN models (NNA and NNB), which compare favourably with the IRI models (URSI and CCIR), suggests that the NN can be used successfully to predict foF2 on a global scale. This can be clearly observed in the bar graphs of Figures 3-3a and 3-3b.

Table 2 RMSE (MHz) for the foF2 NNs (initial attempts) and IRI model (URSI and CCIR) for the years 1965, 1969 (Irkutsk) and 1977, 1980 (Grahamstown, Tomsk, Norfolk Island and Point Arquello)

Station name	Lat ^oN	Long ^oE	Solar minimum				Solar maximum			
			1977				1980			
			URSI	CCIR	NNA	NNB	URSI	CCIR	NNA	NNB
Grahamstown	-33.3	26.5	0.781	0.688	0.722	0.679	1.254	0.915	1.376	0.871
Norfolk Is	-29.0	168.0	0.774	0.756	0.799	0.752	1.164	1.122	0.994	0.917
Tomsk	56.6	84.9	0.636	0.719	0.707	0.606	0.984	0.972	1.003	0.864
Point Arquello	34.6	239.4	0.903	0.823	0.812	0.787	1.095	1.006	0.942	0.895
			1965				1969			
Irkutsk	52.4	101.0	0.616	0.559	0.625	0.569	0.882	0.906	1.044	0.860

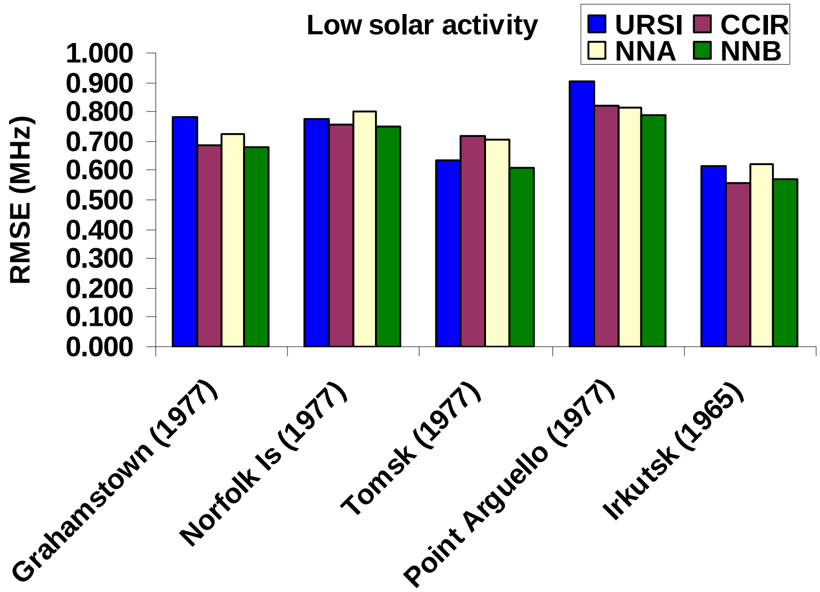

Figure 3-3a. Bar graph illustration of rms differences between measured values of foF2 and predicted values by URSI, CCIR, NNA and NNB for all daily hourly values of foF2 for each station for the year indicated around low solar activity (from Table 2).

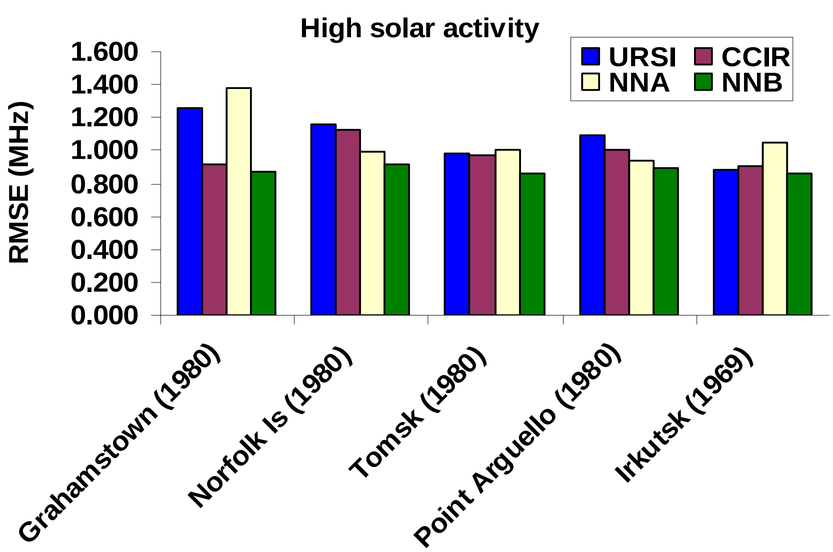

Figure 3-3b. Bar graph illustration of rms differences between measured values of foF2 and predicted values by URSI, CCIR, NNA and NNB for all daily hourly values of foF2 for each station for the year indicated around high solar activity (from Table 2)

Figures 3.4a and 3.4b respectively show examples of diurnal variation of foF2 values predicted by the NN (NNA and NNB) models compared with the IRI model (URSI and CCIR) and the observed values starting at 00h00UT on the first of the days indicated during periods of solar minimum and maximum activity. These days were chosen such that the first day coincides with the spring equinox (northern hemisphere stations) and autumn equinox (southern hemisphere). Also, Figures 3.5a, 3.5b, 3.6a and 3.6b illustrate examples of the seasonal variation of foF2 at 00h00UT and 12h00UT predicted by the NNB model compared with the IRI model (URSI and CCIR) and observed values for 1965 (Irkutsk), 1977 (Grahamstown, Norfolk Is, Tomsk, Point Arguello) (years of solar minimum activity) and 1969 (Irkutsk), 1980 (Grahamstown, Norfolk Is, Tomsk, Point Arquello) (years of solar maximum activity). As can be seen from Figures 3-4, 3-5 and 3-6, the NNs have successfully predicted the average shape both diurnally and seasonally of the F2 peak electron density.

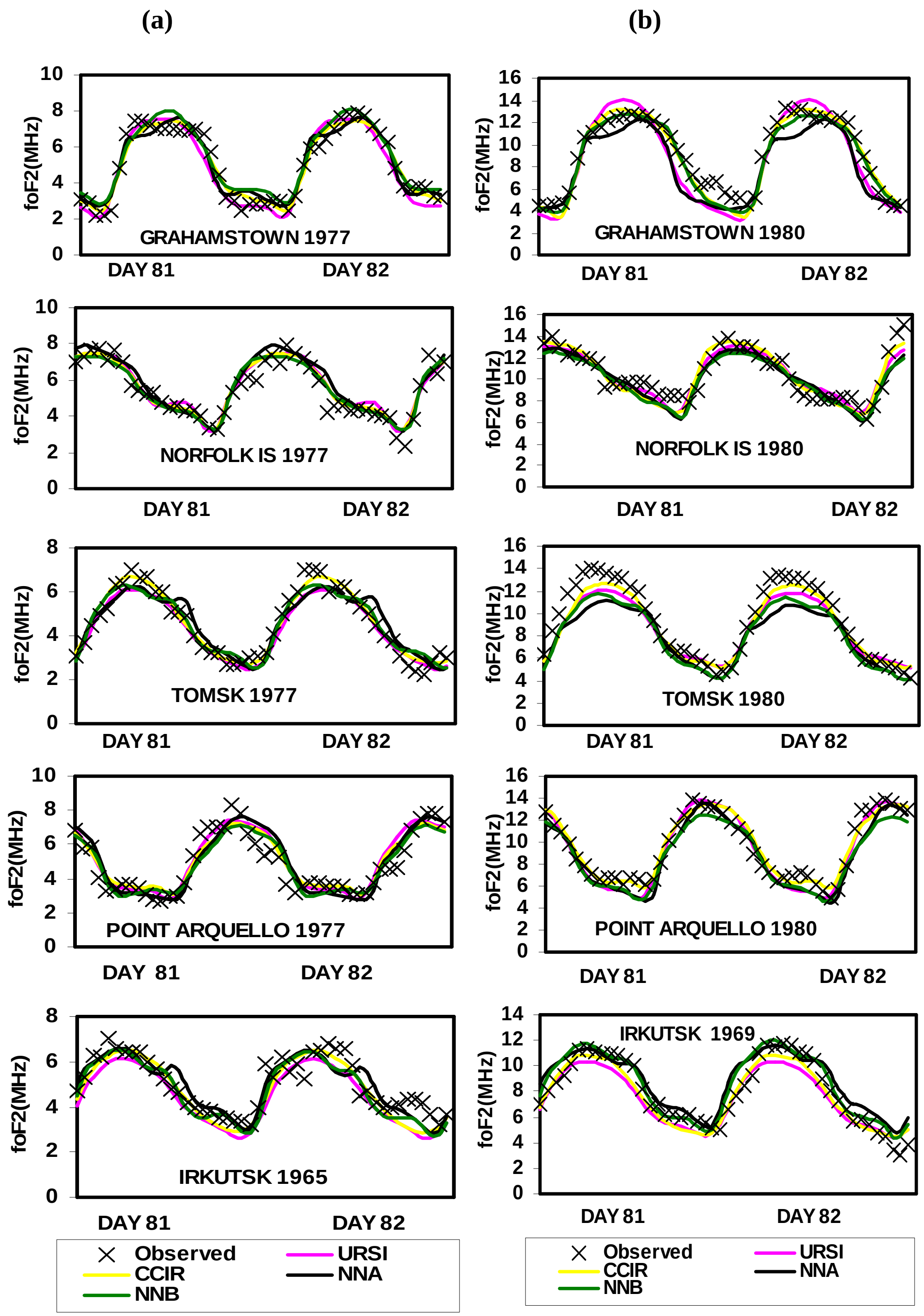

Figure 3-4. Comparisons of the diurnal variation of foF2 predicted values by NNs (NNA and NNB) and IRI model (URSI and CCIR coefficients) with observed values for 2 consecutive days starting at 00h00UT on the first day of the days indicated around (a) solar minimum and (b) solar maximum

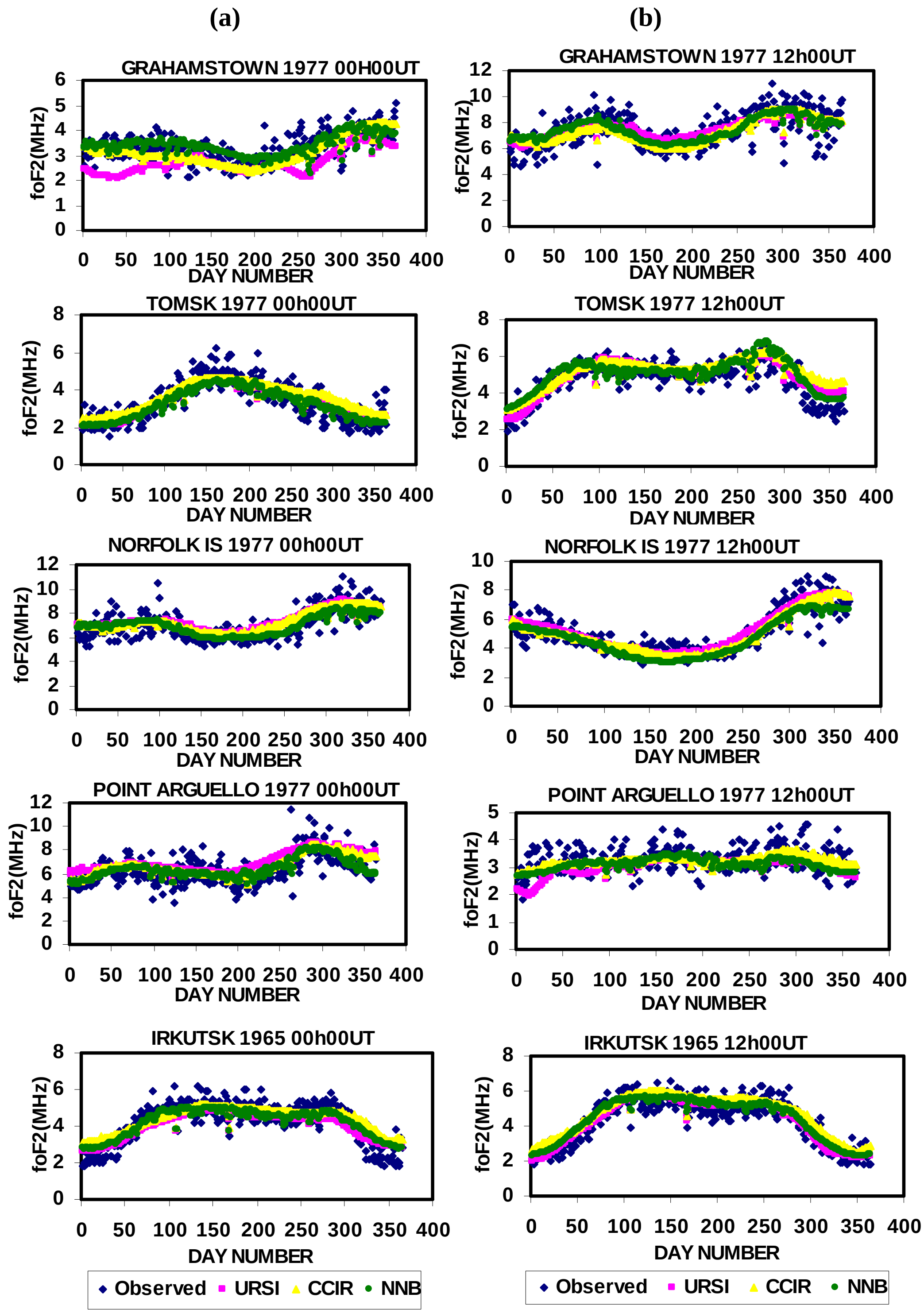

Figure 3-5. These graphs show comparison of the seasonal variations of foF2 predicted values by NNB model (first attempt) with the IRI model (URSI, CCIR) and measured values during low solar activity at (a) 00h00UT and (b) 12h00UT

(a) **(b)**

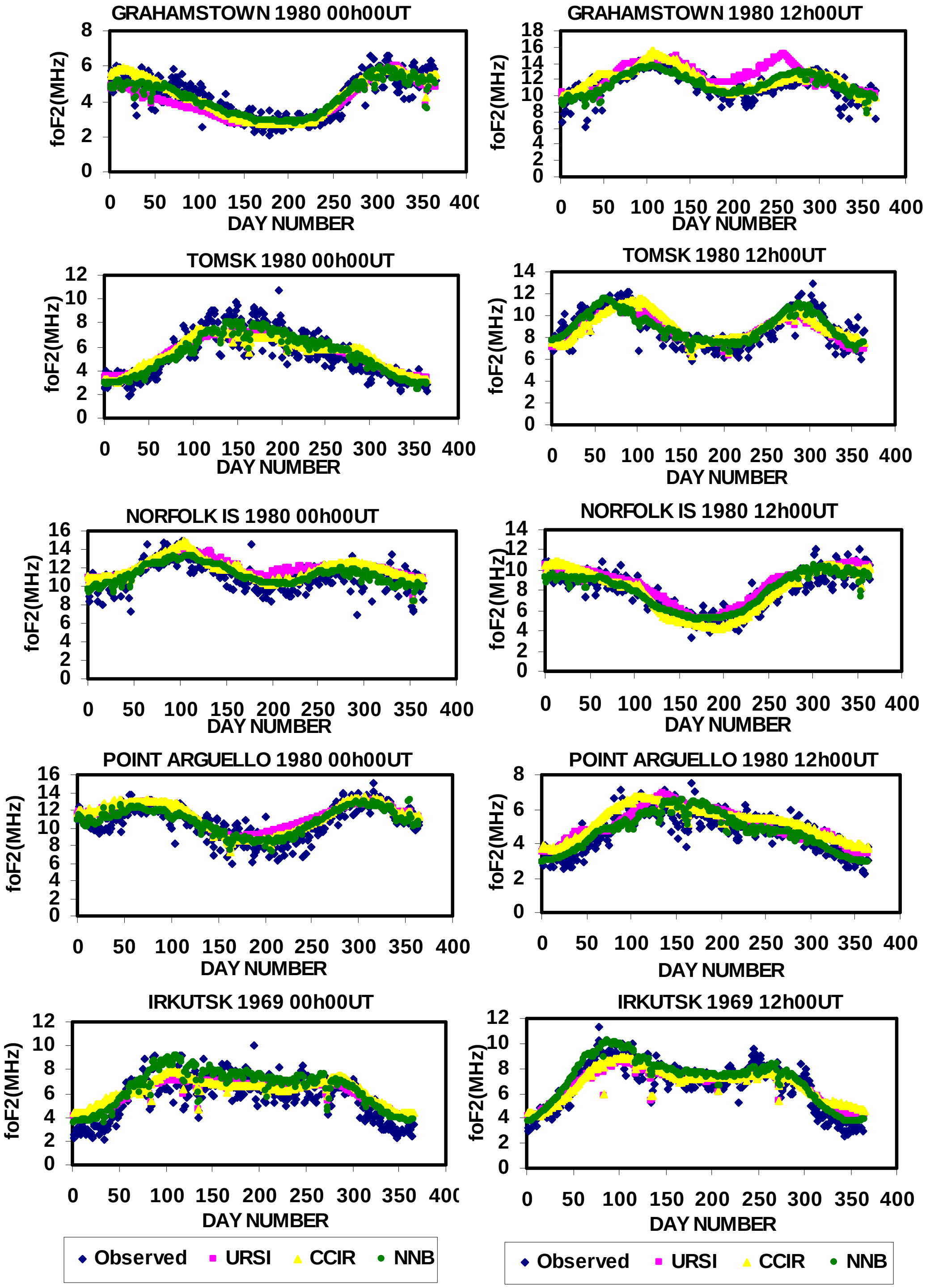

Figure 3-6. These graphs show comparison of the seasonal variations of foF2 predicted values by NNB model (first attempt) with the IRI model (URSI, CCIR) and measured values during high solar activity at (a) 00h00UT and (b) 12h00UT.

3.2.7 Conclusion

The results obtained from this preliminary investigation on the use of NNs for predictions of the F2 region peak electron density, coupled with its successful applications by other researchers (Williscroft and Poole, 1996; Wintoft and Cander, 1999; Lamming and Cander, 1999) show that it is quite possible to develop a NN based global F2 peak electron density empirical model. From these initial attempts, I was able to conclude that a NN trained with the ionospheric parameters day of the year (DN), Universal Time (UT), geographic latitude (θ), magnetic dip angle (I), angle of magnetic declination (D), solar zenith angle (CHI), angle of meridian relative to the subsolar point (M), a 2-month running mean value of the daily SSN (R2) and a two day running mean of the 3-hour planetary magnetic index, a_p (A16), can be used successfully to predict foF2 on a global scale. These results, which are encouragingly similar to that of the IRI, therefore inspire further confidence in the use of NNs as a tool for prediction of the ionospheric parameters foF2 and M(3000)F2 globally. As a result, and with the inclusion of more ionospheric stations where data were available, I, decided to employ NNs for the development of global empirical models for foF2, M(3000)F2, near real time foF2 and short-term foF2 up to five hours ahead. These are discussed in the following sections.

3.3 foF2 NN: Final model

3.3.1 The inputs

The choice of input parameters for this final global foF2 empirical model is based on the results obtained from the initial attempts (i.e. NNB model). It was shown that the optimum input variables for predicting foF2 on a global scale are geographical parameters representing latitude, time, season, solar zenith angle, angle of meridian relative to subsolar point, solar activity, magnetic activity, angles of declination and inclination of the Earth's magnetic field. As earlier explained, HR and DN represent the diurnal and seasonal variations respectively according to equations 3.1 and 3.5. Both the solar activity and magnetic activity are represented by R2 (2-month running mean value of the daily SSN) and A16 (2-day running mean value of the 3-hour planetary magnetic index, a_p) respectively. Similarly, the solar zenith angle and angle of the meridian relative to the subsolar point with respect to each geographical location are represented by equations 3.4 and 3.11 respectively. Following the expansion of equations 3.7a and 3.7b, equations 3.8 and 3.9 were used to represent the Earth's magnetic field declination and inclination respectively.

3.3.2 NN training, testing and verification

Just like the case of the initial attempt, I trained two NNs (NN1 and NN2) but with an expanded data set. The first NN (NN1) was trained with data from 46 ionospheric stations (included in Table 3) without those stations listed in Table 4 (verification stations). The verification stations were chosen for their geographic remoteness from the remaining 46, to be used to verify the ability of NN1 to predict foF2 *spatially*. The second NN (NN2) was trained with data from all the available 59 stations (Table 3).

A block diagram of the NN with input and output variables was the same as for the initial attempts and is shown in Figure 3-2. Figure 3-7 illustrates a map of the geographical locations of the training and verification stations. The same reason as in the case of the initial attempt for two NNs has been considered here (i.e. to compare the results and determine how well the NN can predict foF2 for locations where data are not available). Because of the large volume of the data involved (5.4 million data vectors), and the length of time required to train a NN with such a volume of data, only ten percent (10%) of the total hourly foF2 values randomly chosen from all the available stations were used to train the NNs. The choice of 10% of the total data set was based on the fact that the training of the NN is faster and that there is no significant difference in the errors obtained when 25% and 50% of the total data set was used to train NNs. The 10% data set was again randomly divided into training and testing data sets in the ratio 70% and 30% respectively. The training data set was used to train the network, while the test data set was used to check whether the network has generalized.

In order to determine the optimum NN for predicting foF2, I trained several different NNs with different architectures. Examples of such architectures are: (a) one hidden layer each having 35 and 55 neurons, (b) two hidden layers each having 20/20, 20/15, 25/25 neurons, and (c) three hidden layers each having 10/10/15, 20/15/15, 20/20/15, 25/20/20, 45/30/15, 50/30/20 neurons in the middle layers respectively. The best result was obtained for the architecture with three hidden layers having 45/30/15 neurons respectively. The choice of this configuration is based on the minimization of the RMSE difference between the target and predicted values of foF2 obtained from each configuration.

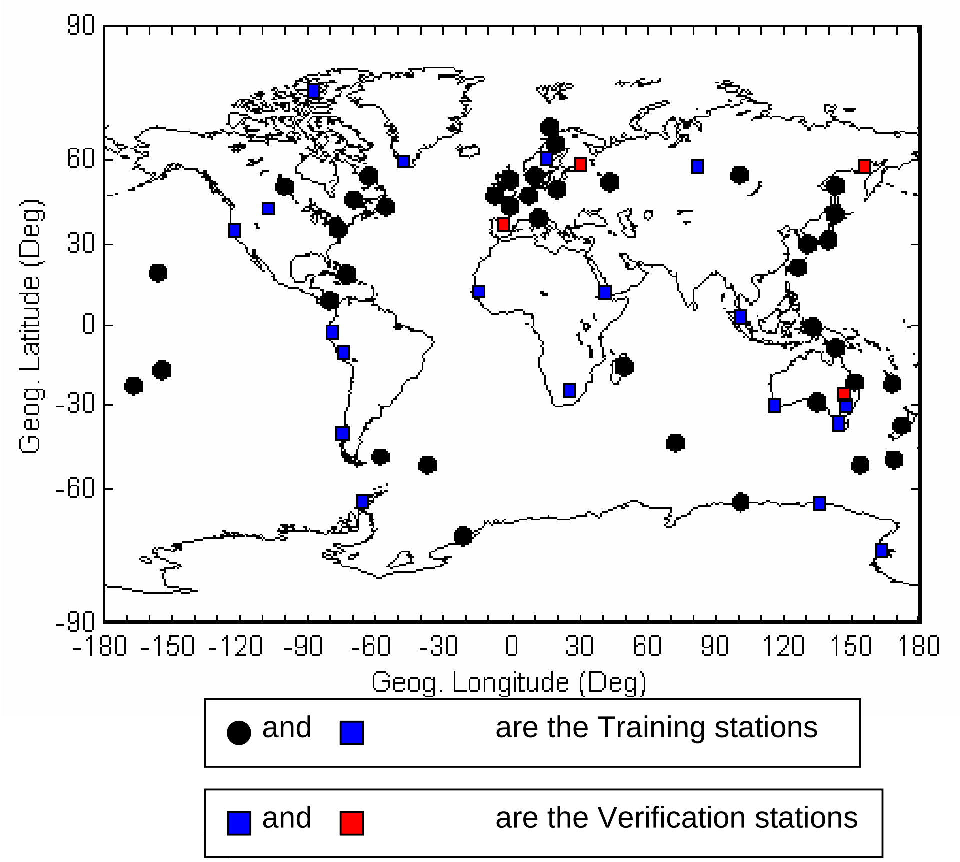

Figure 3-7. Global map of coordinates of training and verification stations for NN1 and NN2.

Table 3. Ionospheric stations used for training of NN1 and NN2 networks

	Station Name	**Latitude °N**	**Longitude°E**
1	Resolute Bay	74.7	265.1
2	Kiruna	67.8	20.4
3	Lycksele	64.6	18.7
4	Narssarssuaq	61.2	314.6
5	Uppsala	59.8	17.6
6	Tomsk	56.5	84.9
7	Moscow	55.5	37.3
8	Kaliningrad	54.7	20.6
9	Juliusruh/Rugen	54.6	13.4
10	Goose Bay	53.3	299.2
11	Irkutsk	52.4	104.0
12	Slough	51.5	359.4
13	Dourbes	50.1	4.6
14	Winnipeg	49.8	256.6
15	Lannion	48.5	356.7

Table 3 continues

	Station Name	Latitude ^oN	Longitude^oE
16	Freiburg	48.1	7.6
17	St Johns	47.6	307.3
18	Poitiers	46.6	0.4
19	Ottawa	45.4	284.1
20	Wakkanai	45.4	141.7
21	Rome	41.8	12.5
22	Boulder	40.0	254.7
23	Akita	39.7	140.1
24	Wallops Is	37.9	284.5
25	Kokubunji	35.7	139.5
26	Point Arguello	34.6	239.4
27	Yamagawa	31.2	130.6
28	Grand Bahama	26.6	281.8
29	Okinawa	26.3	127.8
30	Maui	20.8	203.5
31	Dakar	14.8	341.6
32	Djibouti	11.5	42.8
33	Bogota	4.5	285.8
34	Singapore	1.3	103.8
35	Vanimo	-2.7	141.3
36	Talara	-4.6	278.7
37	Huancayo	-12.0	284.7
38	Tahiti	-17.7	210.7
39	La Reunion	-21.1	55.9
40	Raratonga	-21.2	200.2
41	Brisbane	-27.5	152.9
42	Norfolk Is	-29.0	169.0
43	Mundaring	-32.0	116.3
44	Grahamstown	-33.3	26.5
45	Salisbury	-34.7	138.6
46	Canberra	-35.3	149.0
47	Concepcion	-36.6	287.0
48	Hobart	-42.9	147.2
49	Christchurch	-43.3	172.8
50	Kerquelen	-49.4	70.3
51	Port Stanley	-51.7	302.2
52	Campbell Is	-52.5	169.2
53	South Georgia	-54.3	323.5
54	Macquarie Is	-54.5	159.0
55	Argentine Is	-65.2	295.7
56	Casey	-66.3	110.5
57	Terre Adelie	-66.7	140.0
58	Halley Bay	-75.5	333.4
59	Scott Base	-77.9	166.8

Table 4. Ionospheric stations used for verification of the NN1 and NN2 models.

	Station Name	Latitude ^{o}N	Longitude ^{o}E
1	Singapore	1.3	103.8
2	Dakar	14.8	341.6
3	Huancayo	-12.0	284.7
4	Talara	4.6	278.7
5	Djibouti	11.5	42.8
6	Grahamstown	-33.3	26.5
7	Tomsk	56.5	84.9
8	Terre Adelie	-66.6	140.0
9	Concepcion	-36.6	287.0
10	Narssarssuaq	61.2	314.6
11	Argentine Is	-65.2	295.7
12	Scott Base	-77.9	166.8
13	Resolute Bay	74.7	265.1

3.3.3 Results and Discussion

3.3.3.1 Spatial diversity verification

In order to estimate the performance of the NN models for the prediction of foF2 *spatially*, daily hourly values of foF2 predicted by NN1 and NN2 as well as those determined by the existing IRI model (using both the URSI and CCIR coefficients) are compared with observed values of foF2 obtained from the verification stations (Tables 5a and 5b) and the RMSE differences calculated. All the available observed daily hourly values of foF2 for 365 or 366 days (as the case may be) for each of the years at each station indicated in Tables 5a and 5b are used to evaluate error differences between the observed and URSI, CCIR, NN1 and NN2 predicted values. Because it is difficult to get data for the same years for all the stations considered for verification due to one reason or the other, different years for each station where data are available were used. I made efforts to ensure that there was a good representation for both periods of solar minimum and maximum activities for each of the stations considered. As can be seen from Tables 5a and 5b, there are stations representing low (1 to 5), middle (6 to 11) and high (12 and 13) latitudes. This ensures that the verification stations provide a good global distribution. The root mean square (RMS) error has been used here to evaluate the performance of NN1 and NN2 using the RMS error equation (3.12). The error differences are illustrated in Figures 3-8a and 3-8b respectively using bar graphs. The averages of the RMS error differences for all the years from the verification stations in Tables 5a and 5b for each of URSI, CCIR, NN1 and NN2 were also evaluated using RMSE average equation represented as

$$RMSE_{average} = \frac{1}{k}\sum_{j=1}^{k}\left(RMSE\right)_j \tag{3.13}$$

where k is the total number of stations used for verification (k =13).

The averages of the RMS error differences are illustrated using the bar chart of figure 3-9. Also shown in Tables 5a and 5b are the percentage differences between URSI, CCIR and NN2. The percentage error difference between the IRI model (URSI and CCIR) and NN2 model was evaluated according to equations 3.14 and 3.15 respectively.

$$\left(\frac{URSI_{RMSE} - NN2_{RMSE}}{URSI_{RMSE}}\right)\times 100 \qquad 3.14$$

$$\left(\frac{CCIR_{RMSE} - NN2_{RMSE}}{CCIR_{RMSE}}\right)\times 100 \qquad 3.15$$

Table 5a. The foF2 RMSE difference (MHz) at the verification stations for different years during solar minimum using URSI, CCIR, NN1 and NN2 models.

S/N	Station name	LAT °N	LONG °E	RMSE (MHz)				% Error difference between URSI and NN2	% Error difference between CCIR and NN2	Year
				URSI	CCIR	NN1	NN2			
1	Singapore	1.3	103.8	1.003	1.008	1.101	0.865	13.759	14.187	1964
2	Dakar	14.8	341.6	1.242	1.123	1.244	1.053	15.217	6.233	1976
3	Huancayo	-12.0	284.7	1.078	1.057	0.952	0.931	13.636	11.921	1974
4	Talara	4.6	278.7	1.208	1.685	0.991	0.944	21.854	43.976	1965
5	Djibouti	11.5	42.8	1.162	1.084	1.065	1.022	12.048	5.720	1974
6	Grahamstown	-33.3	26.5	0.781	0.688	0.857	0.684	12.420	0.581	1977
7	Tomsk	56.5	84.9	0.636	0.719	0.653	0.593	6.761	17.524	1977
8	Terre Adelie	-66.6	140.0	0.717	0.784	0.845	0.675	5.858	13.903	1977
9	Concepcion	-36.6	287.0	1.451	1.260	1.228	1.071	26.189	15.000	1965
10	Narssarssuaq	61.2	314.6	0.572	0.594	0.568	0.525	8.217	11.616	1965
11	Argentine Is	-65.2	295.7	0.846	0.916	0.766	0.703	16.903	23.253	1977
12	Scott Base	-77.9	166.8	0.799	0.837	0.771	0.739	7.509	11.708	1977
13	Resolute Bay	74.7	265.1	0.721	0.767	0.695	0.691	4.161	9.909	1977
	RMSE average			**0.940**	**0.963**	**0.903**	**0.807**	**14.080%**	**16.180%**	

Table 5b. The foF2 RMSE difference (MHz) at the verification stations for different years around solar maximum using URSI, CCIR, NN1 and NN2 models.

S/N	Station name	LAT °N	LONG °E	RMSE (MHz)				% Error difference between URSI and NN2	% Error difference between CCIR and NN2	Year
				URSI	CCIR	NN1	NN2			
1	Singapore	1.3	103.8	1.503	1.513	1.531	1.151	23.420	23.926	1958
2	Dakar	14.8	341.6	1.418	1.405	1.504	1.207	14.880	14.093	1971
3	Huancayo	-12.0	284.7	1.273	1.296	1.145	1.124	11.705	13.272	1968
4	Talara	4.6	278.7	1.402	1.670	1.272	1.173	16.334	29.760	1961
5	Djibouti	11.5	42.8	1.290	1.200	1.293	1.230	4.651	-2.500	1978
6	Grahamstown	-33.3	26.5	1.268	0.927	1.134	0.903	28.785	2.589	1979
7	Tomsk	56.5	84.9	1.262	1.166	1.275	0.996	21.078	14.580	1979
8	Terre Adelie	-66.6	140.0	1.203	1.209	1.154	1.092	9.227	9.677	1979
9	Concepcion	-36.6	287.0	1.732	1.539	1.388	1.193	31.120	22.482	1968
10	Narssarssuaq	61.2	314.6	1.061	1.076	1.042	0.965	9.048	10.316	1968
11	Argentine Is	-65.2	295.7	1.418	1.398	1.019	1.000	29.478	28.469	1979
12	Scott Base	-77.9	166.8	1.402	1.319	1.182	1.163	17.047	11.827	1979
13	Resolute Bay	74.7	265.1	1.371	1.374	1.325	1.263	7.877	8.079	1979
	RMSE average			**1.354**	**1.315**	**1.251**	**1.112**	**17.855%**	**15.399%**	

(a)

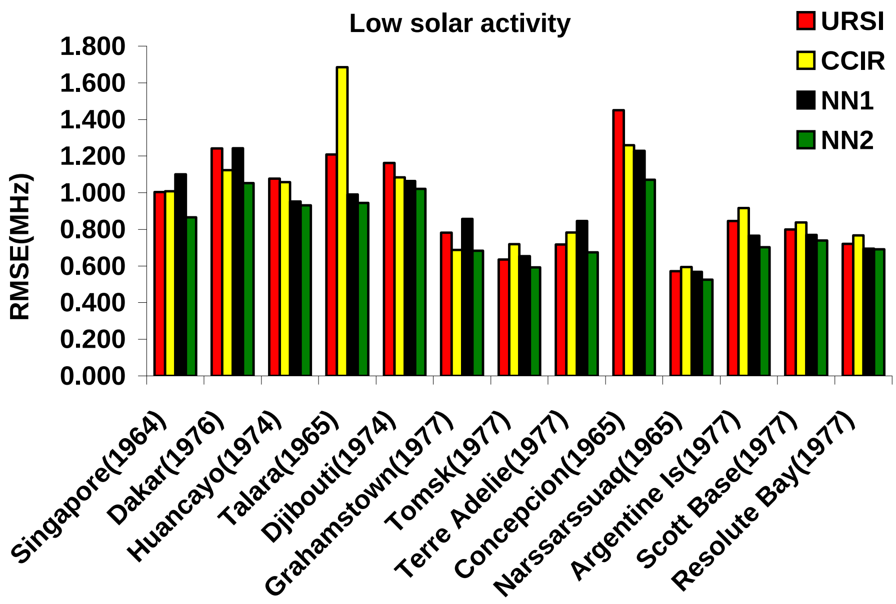

(b)

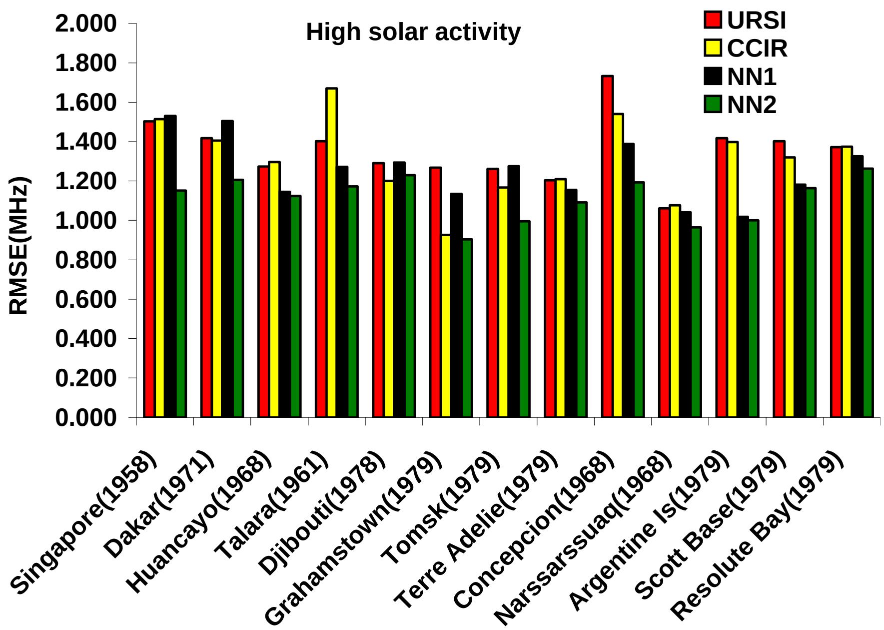

Figure 3-8. Bar graphs illustrating the rms error differences between measured values of foF2 and predicted values by URSI, CCIR, NN1 and NN2 for all daily hourly values of foF2 for each station for the year indicated around (a) low solar activity and (b) high solar activity.

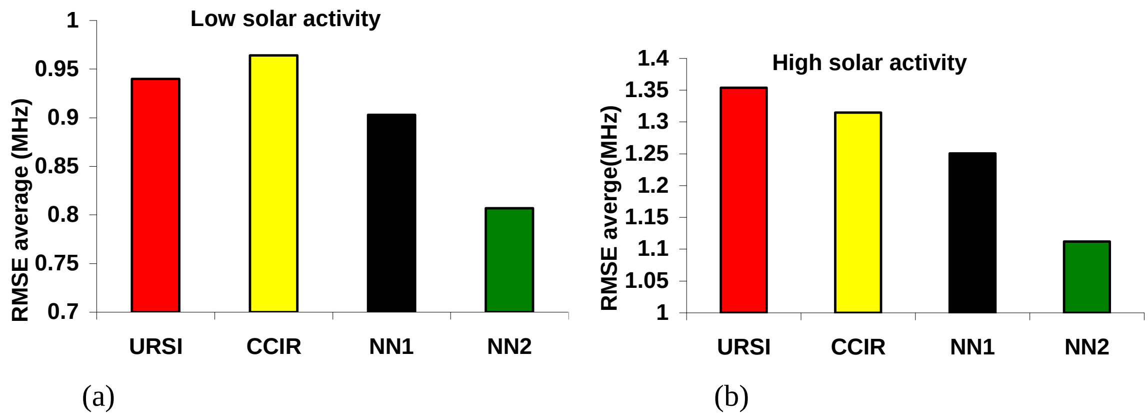

Figure 3-9. Bar graphs illustrating the RMSE average calculated for URSI, CCIR, NN1 and NN2 for (a) Low solar activity and (b) high solar activity, from Tables 5a and 5b respectively.

The overall percentage error difference of the verification stations during solar minimum activity between URSI and NN2 is 14.08%, and between CCIR and NN2 is 16.18% (Table 5a). For solar maximum activity the percentage error differences are 17.86% and 15.40% respectively (Table 5b).

Figures 3-10 and 3-11 show examples of the diurnal variation of foF2 predicted by the NN2 model compared with URSI and CCIR, and the observed values starting at 00h00UT on the first of the days indicated in the month of the year in each case. Figure 3-12 illustrates a similar comparison of the diurnal variation of foF2 for selected stations not included in the training dataset, and for time periods that fell outside the training period. A close observation of these graphs also shows that all three models successfully predict the general diurnal shape of foF2 behaviour. Such differences that do exist are short term (< ~ 3hrs) variations in foF2 which neither the NN models nor the IRI models are designed to predict.

There are cases where each of the models tends to perform better than the others (see error Tables 5a and 5b). A comparison of NN2 results with URSI and CCIR show a very large improvement for Singapore, Talara, Concepcion, Argentine Is and Scott Base (Tables 5a and 5b). NN2 is almost always an improvement on either URSI or CCIR, an exception is Djibouti from Table 5b for which CCIR performs better than NN prediction. It is possible that this exception could be due to a measurement problem in the Djibouti database.

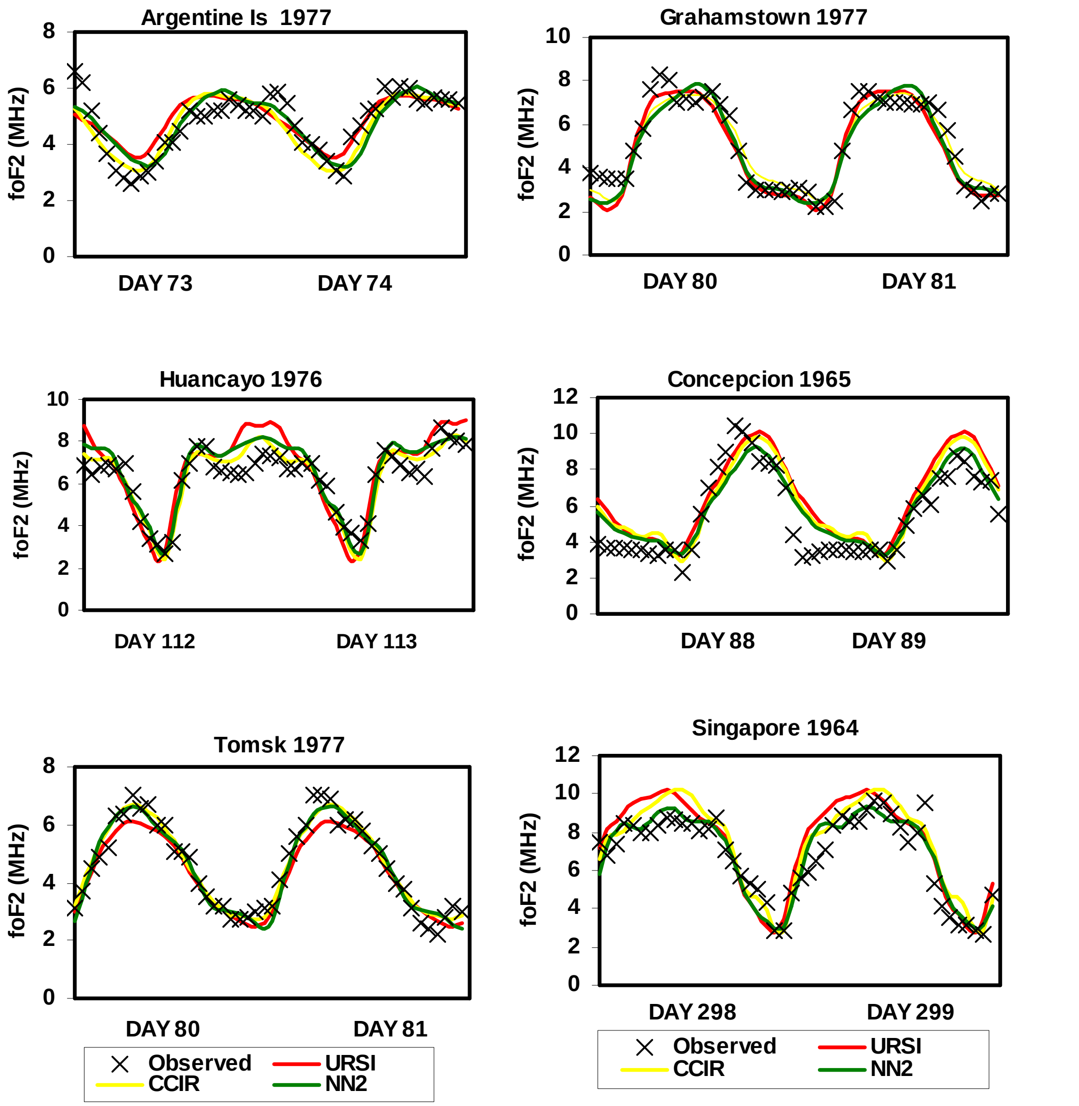

Figure 3-10. Comparisons of the diurnal behaviour of foF2 during a solar minimum period predicted by the NN2, URSI and CCIR with observed values for 2 consecutive days starting at 00h00UT on the first day of the days as indicated.

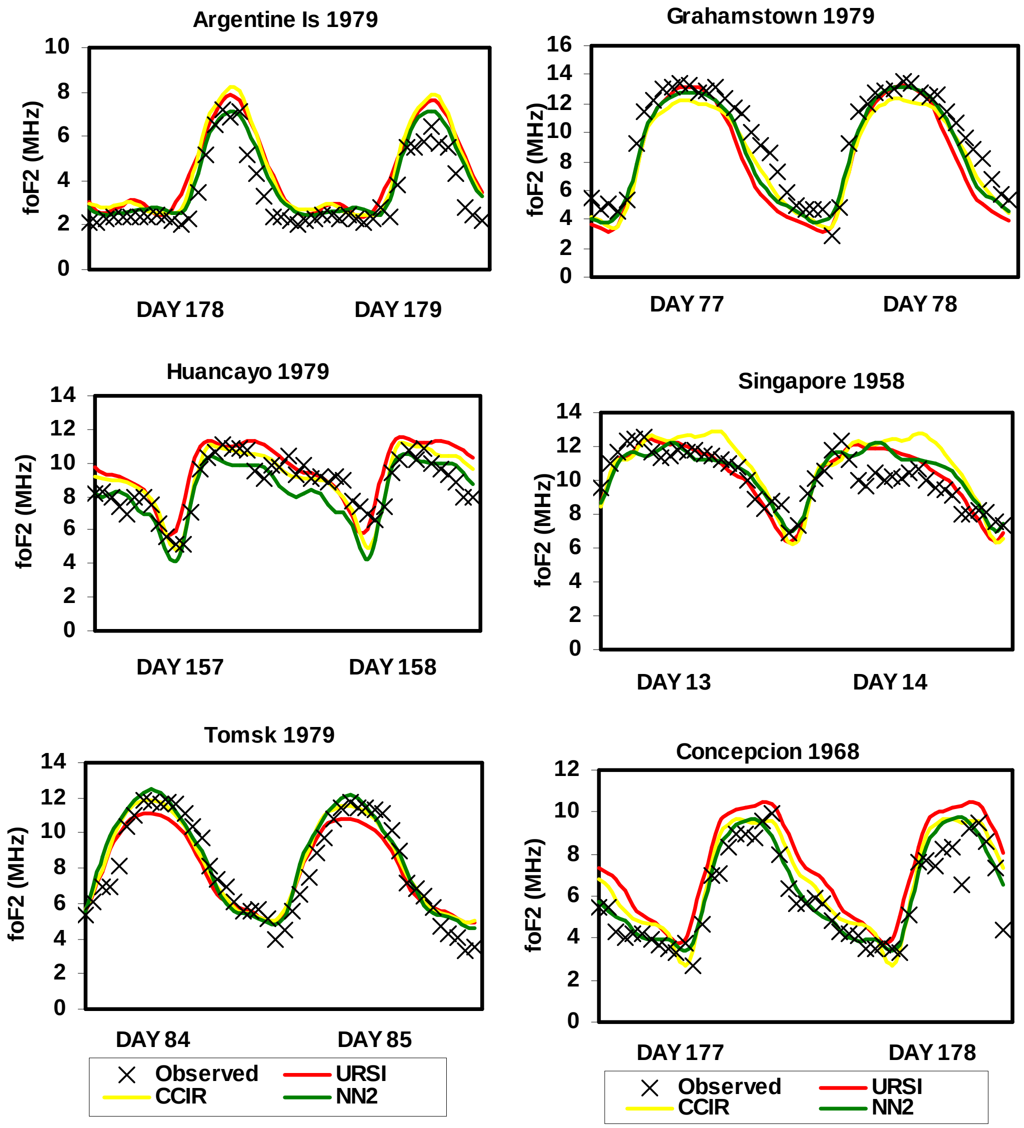

Figure 3-11. Comparisons of the diurnal behaviour of foF2 during solar maximum period predicted by the NN2, URSI and CCIR with observed values for 2 consecutive days starting at 00h00UT on the first day of the days as indicated.

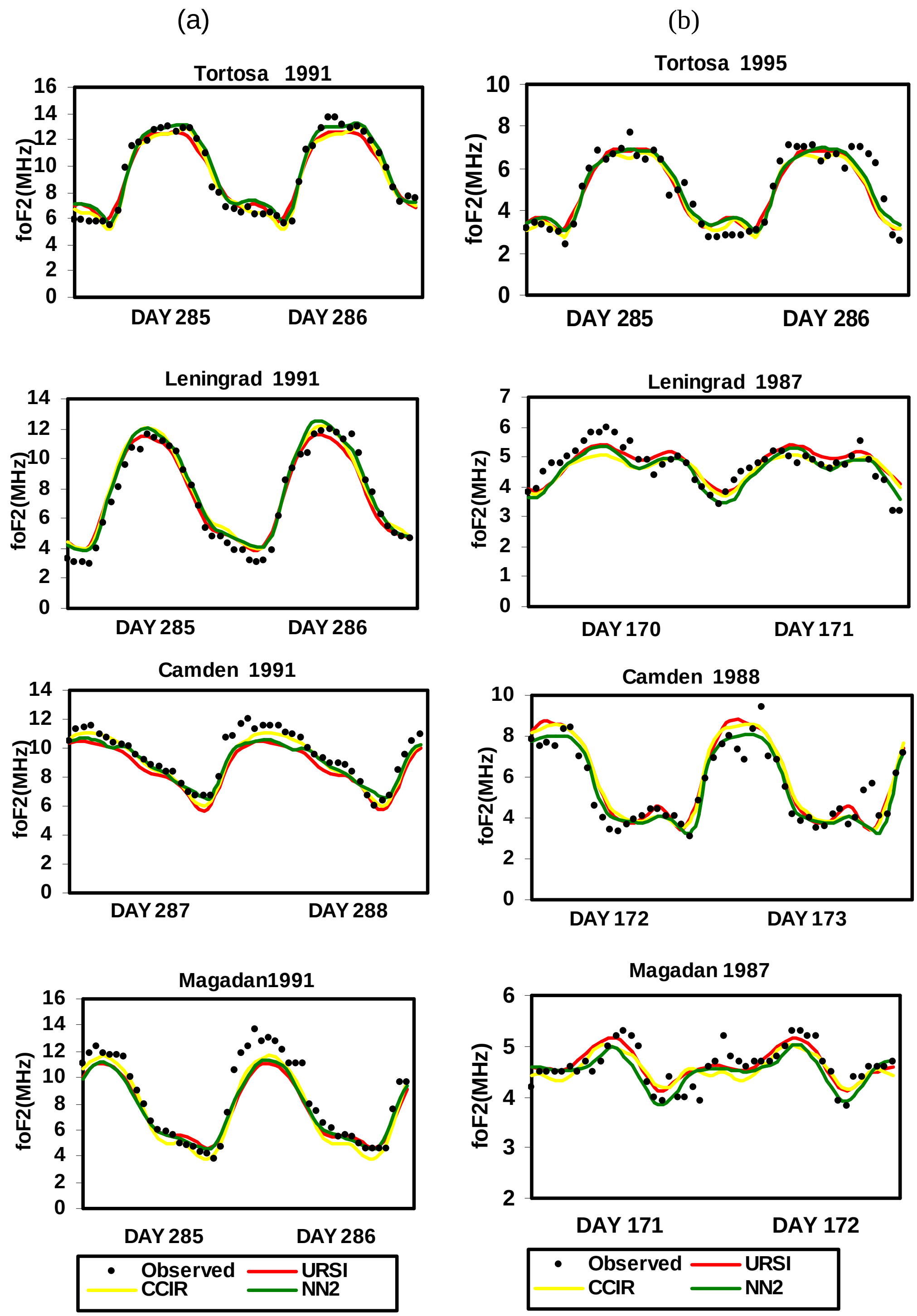

Figure 3-12. Comparisons of the diurnal behaviour of foF2 predicted values by NN2 model with the IRI model (URSI, CCIR) predictions and observed values for 2 consecutive days starting at 00h00UT on the first day of the days as indicated above during (a) solar maximum and (b) solar minimum periods.

3.3.3.2 Temporal diversity verification

In order to test for the predictive ability of NN2 *temporally* beyond the training period, 11 stations were used as verification stations. All the available observed daily hourly values of foF2 from 1987 to 1992 were used for each of the stations in Table 6. The exception is Tortosa where data are not available from 1987 to 1990, and instead data from 1991 to 1995 were used. Four stations (i.e. Tortosa, Camden, Leningrad and Magadan) among these 11 stations were not part of the training stations. Similar RMSE differences, RMSE averages and percentage error differences are as shown in Table 6. Although, the percentage error differences from Table 6 are not as high as those obtained in Tables 5a and 5b (i.e. for years within the training period), the results obtained indicate that predictions of NN2 are not limited to the training period. Figures 3-13 and 3-14 respectively present RMSE and RMSE average values calculated from Table 6.

Table 6. The foF2 RMSE difference (MHz) at some selected verification stations outside the training period as indicated in the table below.

S/N	Station name	LAT °N	LONG °E	RMSE (MHz)			% Error difference between URSI and NN2	% Error difference between CCIR and NN2	Period
				URSI	CCIR	NN2			
1	Point Arguello	34.6	239.4	1.193	1.131	1.111	6.873	1.768	1987-1992
2	Camden	-34.0	150.7	1.178	1.167	1.081	8.234	7.369	1987-1992
3	Uppsala	59.8	17.7	1.037	1.013	0.941	9.257	7.108	1987-1992
4	Hobart	-42.0	147.0	1.069	1.041	0.934	12.629	10.279	1987-1992
5	Leningrad	59.9	30.7	1.250	1.246	1.163	6.960	6.661	1987-1992
6	Magadan	60.0	151.0	1.301	1.294	1.184	8.993	8.501	1987-1992
7	Tortosa	40.0	0.3	1.070	1.040	0.988	7.664	5.000	1991-1995
8	Canberra	-35.3	149.0	1.339	1.316	1.281	4.332	2.660	1987-1992
9	Mundaring	-32.0	116.3	1.148	1.062	1.001	12.805	5.744	1987-1992
10	Boulder	40.0	254.7	1.096	1.061	1.000	8.759	5.749	1987-1992
11	Grahamstown	-33.3	26.5	1.219	1.062	1.023	16.079	3.672	1987-1992
	RMSE average			**1.173**	**1.130**	**1.064**	**9.248%**	**5.839%**	

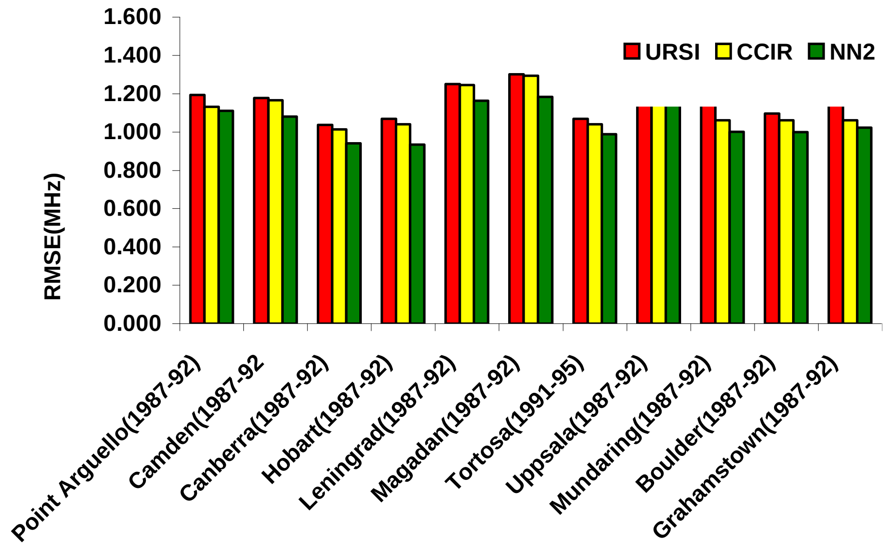

Figure 3-13. Bar graph illustrating the RMSE differences between measured and URSI, CCIR and NN2 predictions for all daily hourly values of foF2 for each station for the period indicated (from Table 6).

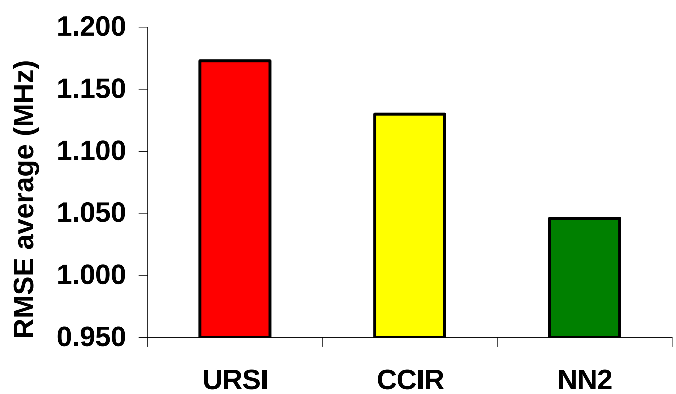

Figure 3-14. Bar graph illustrating the RMSE average calculated for URSI, CCIR and NN2 for all the years indicated (from Table 6).

The relative performance of NN2 over the IRI model (URSI and CCIR) was further verified on the observed data (outside the training period) from ionospheric stations in Table 6 using the relative error method from Houminer et al. (1993) and Richard et al. (2004). The relative errors eURSI, eCCIR and eNN2 for the URSI, CCIR and NN2 predicted values respectively were defined as

$$\mathrm{eURSI} = \frac{\left|\mathrm{foF2}_{\mathrm{obs}} - \mathrm{foF2}_{\mathrm{URSI}}\right|}{\mathrm{foF2}_{\mathrm{obs}}} \qquad 3.16$$

$$\mathrm{eCCIR} = \frac{\left|\mathrm{foF2}_{\mathrm{obs}} - \mathrm{foF2}_{\mathrm{CCIR}}\right|}{\mathrm{foF2}_{\mathrm{obs}}} \qquad 3.17$$

$$\mathrm{eNN2} = \frac{\left|\mathrm{foF2}_{\mathrm{obs}} - \mathrm{foF2}_{\mathrm{NN2}}\right|}{\mathrm{foF2}_{\mathrm{obs}}} \qquad 3.18$$

The NN2 model can be regarded as successful when both (eURSI-eNN2) > 0 and (eCCIR-eNN2) > 0 is true. This test was carried out on all the available data points for each station for the period listed in Table 6. The cases for which (eURSI-eNN2) and (eCCIR-eNN2) are positive and negative is presented in Figure 3-15a. The relative performance of NN2 model over the IRI model is further clarified by considering only the number of cases for which the absolute values of (eURSI-eNN2) and (eCCIR-eNN2) in each case is greater than 0.05. This is done to ensure that those cases for which the performance of the three models differed only marginally are eliminated. This is illustrated in Figure 3-15b. It can be observed that NN2 model is better than the IRI model (URSI and CCIR) on average since the number of cases for which each of (eURSI-eNN2) and (eCCIR-eNN2) is greater than 0 always exceeds the number for which each of (eURSI-eNN2) and (eCCIR-eNN2) is less than 0 (Figure 3-15a). Also in Figure 3-15b are shown the number of cases for which each of (eURSI-eNN2) and (eCCIR-eNN2) is greater than 0.05 exceeds the number of cases for which each is less than - 0.05. The exceptions are for

Magadan and Tortosa stations where the performance of the NN2 model and the IRI (CCIR option) are much the same (Figure 3-15b). A closer inspection of Figures 3-15(a and b) also reveals that the CCIR predictions are better than the URSI predictions.

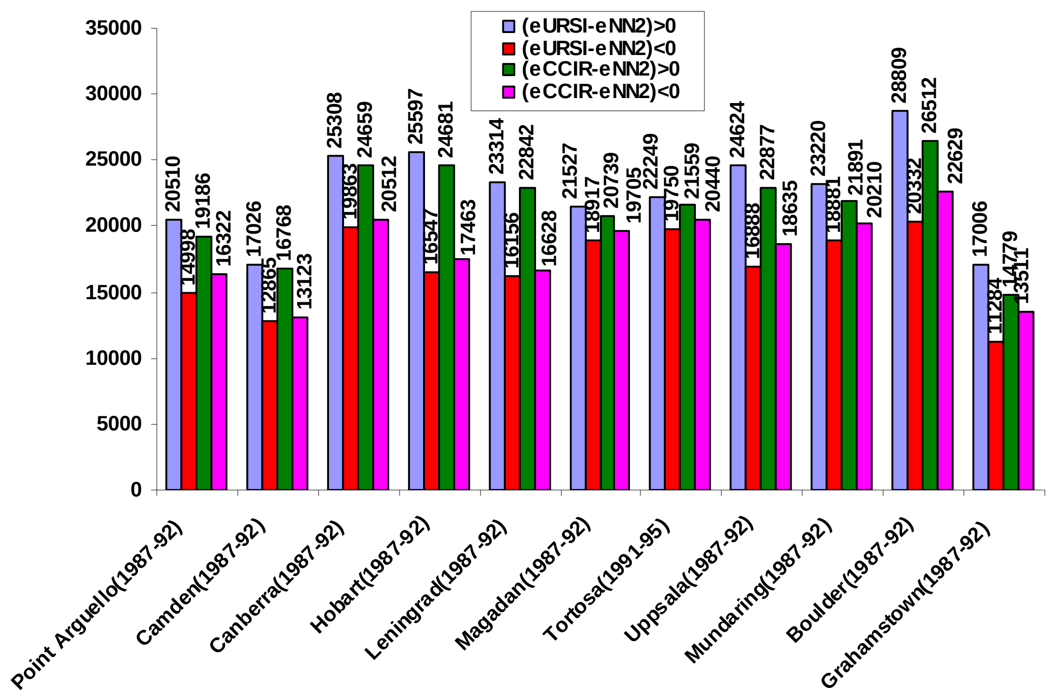

Figure 3-15a. Bar graph illustrating the cases where the NN2 model performs better than the IRI model (URSI light purple, CCIR green) and where the NN2 model performs worse than IRI model (URSI red, CCIR pink) for all the available hourly values of foF2 for each station for the period indicated.

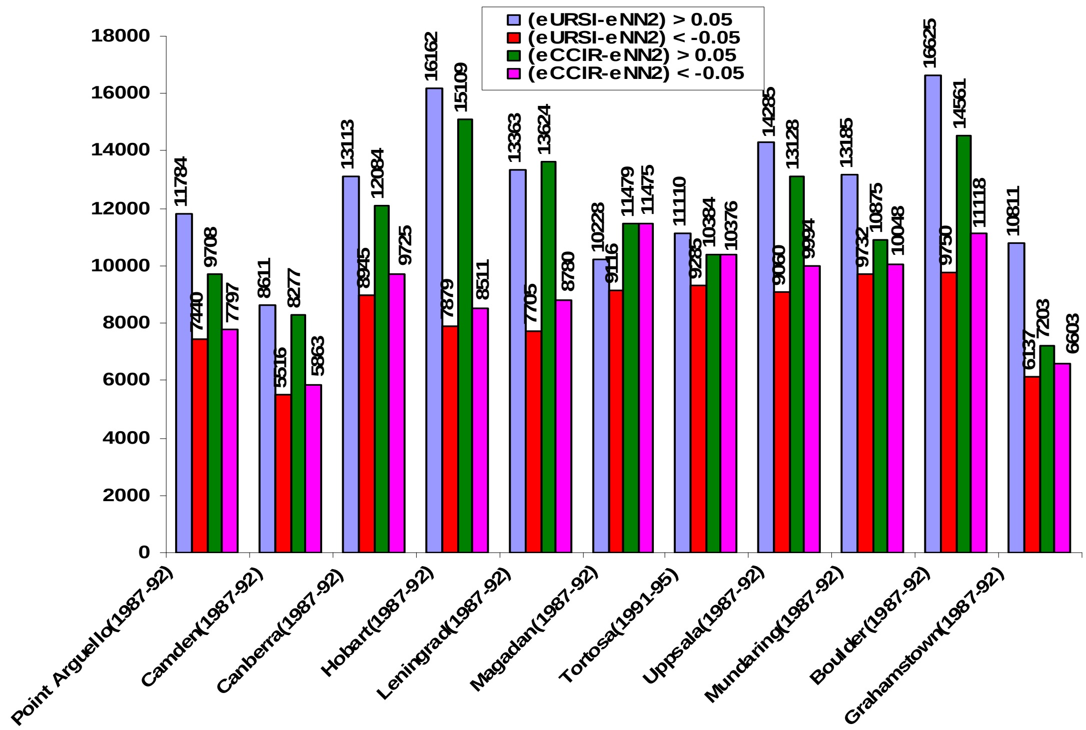

Figure 3-15b. Bar graph illustrating only cases where the difference in the absolute values of (eURSI-eNN2) and (eCCIR-eNN2) in each case is greater than 0.05.

Figures 3-16a, 3-16b and 3-16c respectively show examples of the global distribution of foF2 values predicted by the NN2 model, URSI and CCIR coefficients for October 12, 1991 at 12h00UT. Values of foF2 were obtained using a scale size interval of 10 degrees for both geographic longitude and latitude. Figures 3-17a, 3-17b and 3-17c illustrate a similar global variation of daily hourly values of foF2 for June 21, 1996 at 12h00UT. The contour maps of Figures 3-16 and 3-17 show examples of the global distribution of foF2 for the periods of solar minimum and solar maximum activities respectively. These maps are similar because the differences are not large but serve to show that the NN2 model does predict a similar global distribution of foF2 to those of the other two models (URSI and CCIR). As can be observed from Figures 3.9 and 3.14, the RMSE averages obtained from NN2 and from NN1 (Figure 3.9) are less than those obtained from URSI and CCIR.

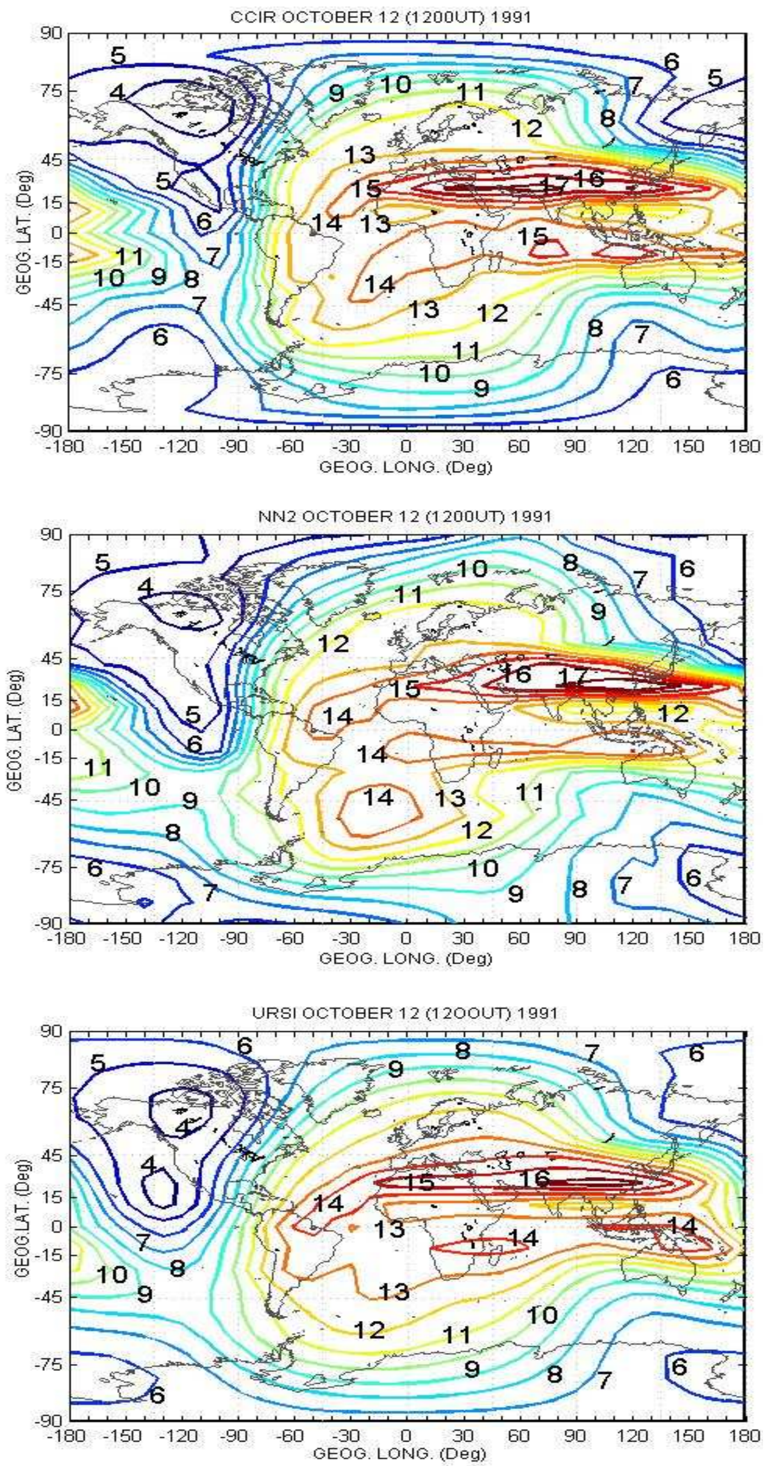

(a)

(b)

(c)

Figure 3-16. Contour map of the global representation of foF2 values for October 12, 1991 at 12h00UT derived from (a) CCIR, (b) NN2 and (c) URSI models.

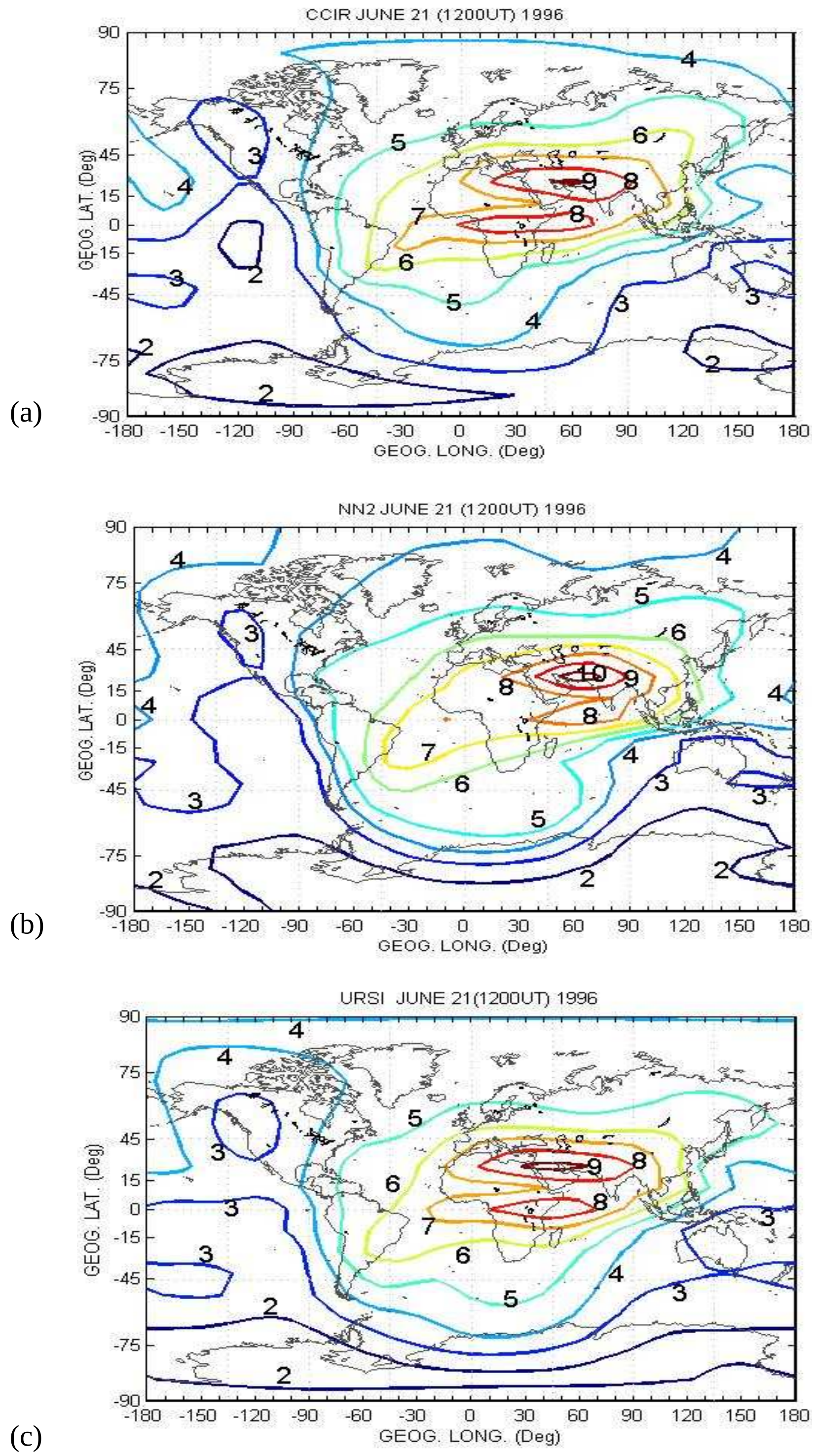

Figure 3-17. Contour map of the global representation of foF2 values for June 21, 1996 at 12h00UT derived from (a) CCIR, (b) NN2 and (c) URSI models.

Also illustrated in Figures 3-18 and 3-19 are the comparisons of the seasonal variations of predicted foF2 values at 12h00UT and 18h00UT by the NN2 model with the IRI model (URSI and CCIR coefficients) and observed values. The comparisons are shown for eight selected stations (Boulder, 40^{o}N, 254.7^{o}E; Point Arquello, 34.6^{o}N, 239.4^{o}E; Canberra, 35.3^{o}S, 149^{o}E; Leningrad, 59.9^{o}N, 30.7^{o}E; Mundaring, 32^{o}S, 116.3^{o}E; Tortosa, 40^{o}N, 0.3^{o}E; Grahamstown, 33.3^{o}S, 26.5^{o}E and Uppsala, 59.8^{o}N, 17.7^{o}E, geographic) around solar minimum period, 1987 and 1995, (Figure 3-18) and solar maximum period, 1991 (Figure 3-19) based on data availability. This comparison shows that the NN2 model predictions follow the expected trend of seasonal behaviour of foF2 for periods beyond the training period from these selected stations. It also provides a better understanding of the performance of this model in comparison with the diurnal variations of Figures 3-11 and 3-12 that are limited to only two consecutive days in a year. It is evident from Figures 3-18 and 3-19 that application of NN2 model is not limited to the training period alone.

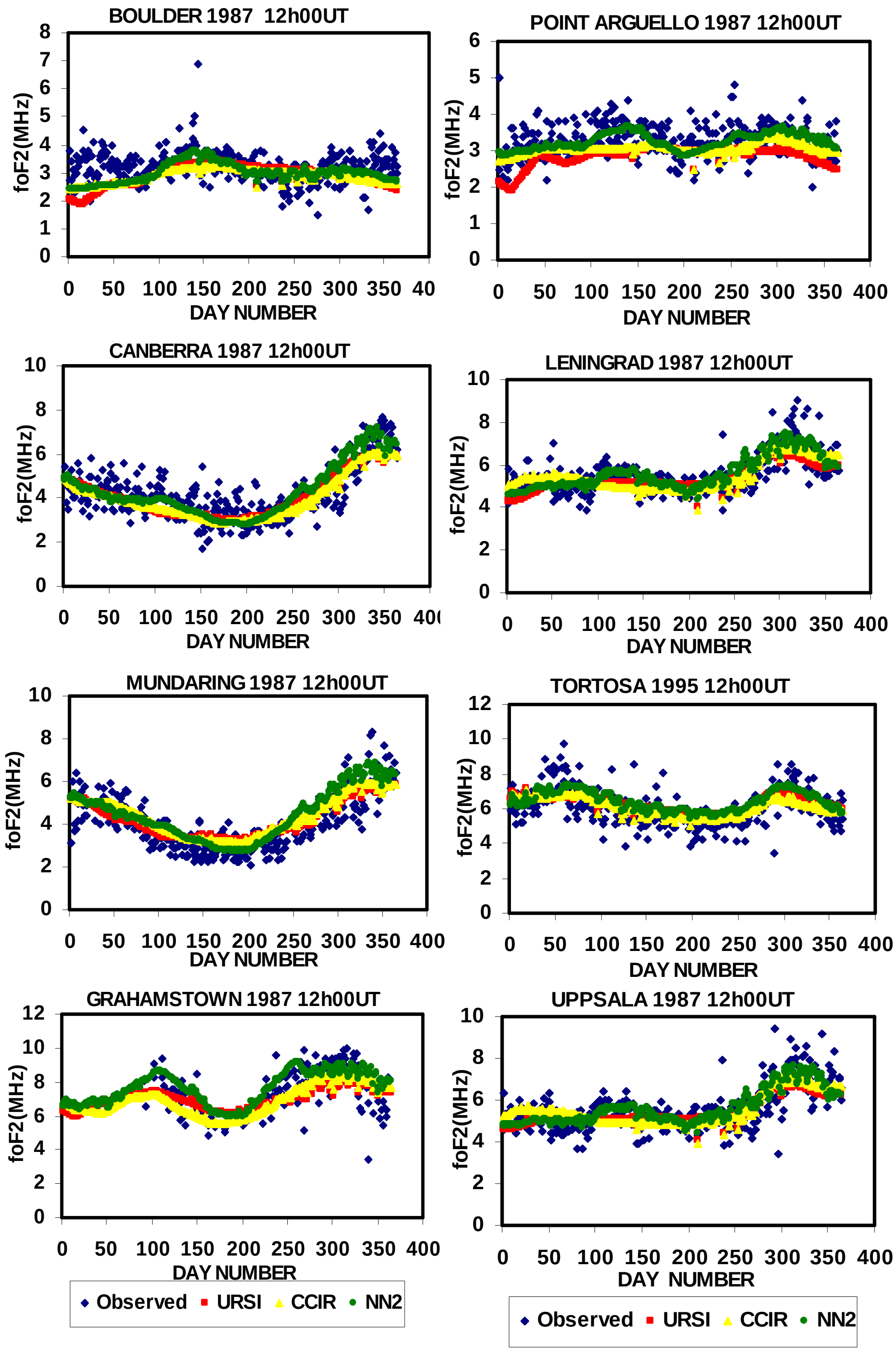

Figure 3-18a. Comparisons of seasonal variations of predicted foF2 values around solar minimum (1987 and 1995) at 12h00UT by NN2 model with predicted values from URSI and CCIR and observed values.

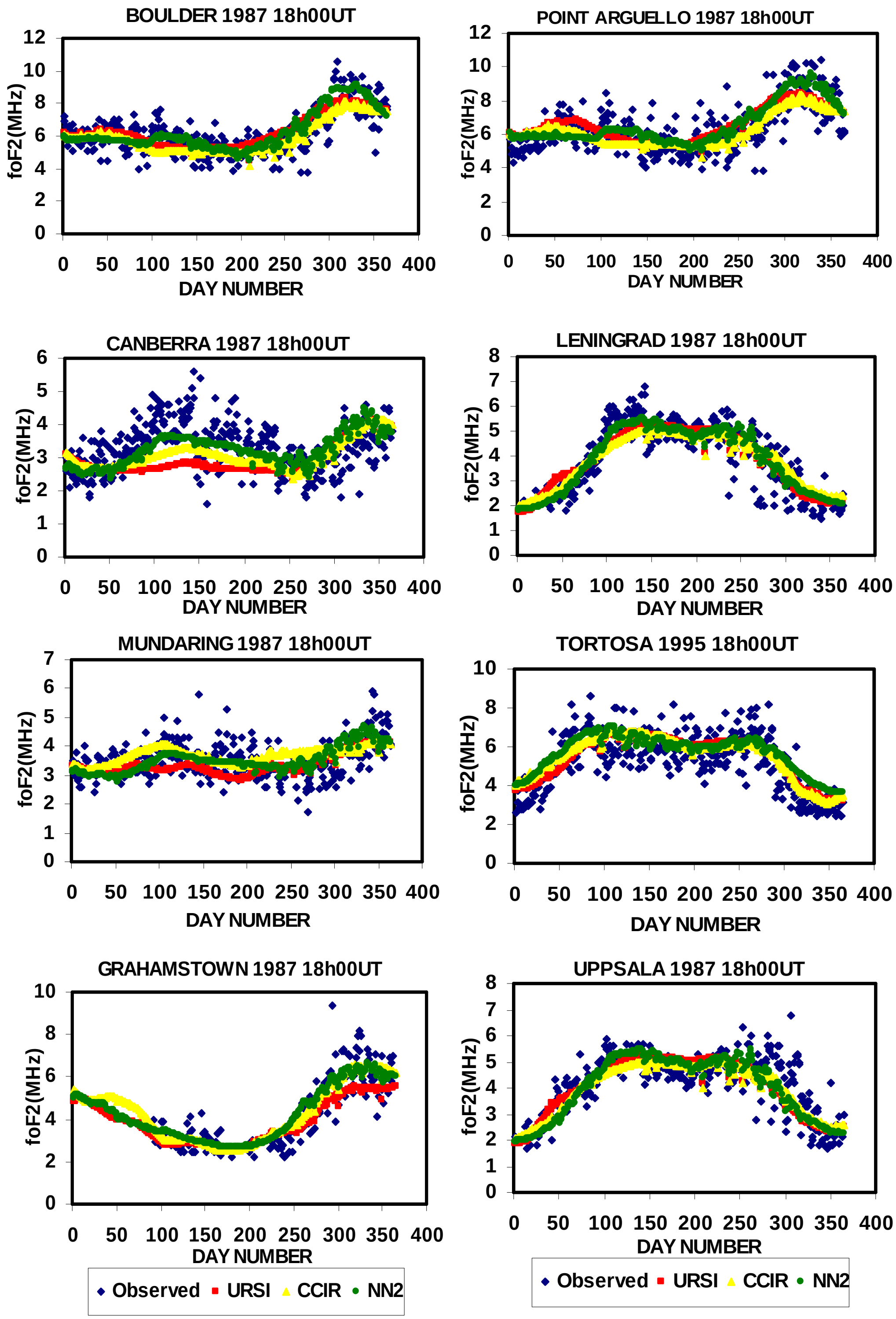

Figure 3-18b: Comparisons of seasonal variations of predicted foF2 values around solar minimum (1987 and 1995) at 18h00UT by NN2 model with predicted values from URSI and CCIR and observed values.

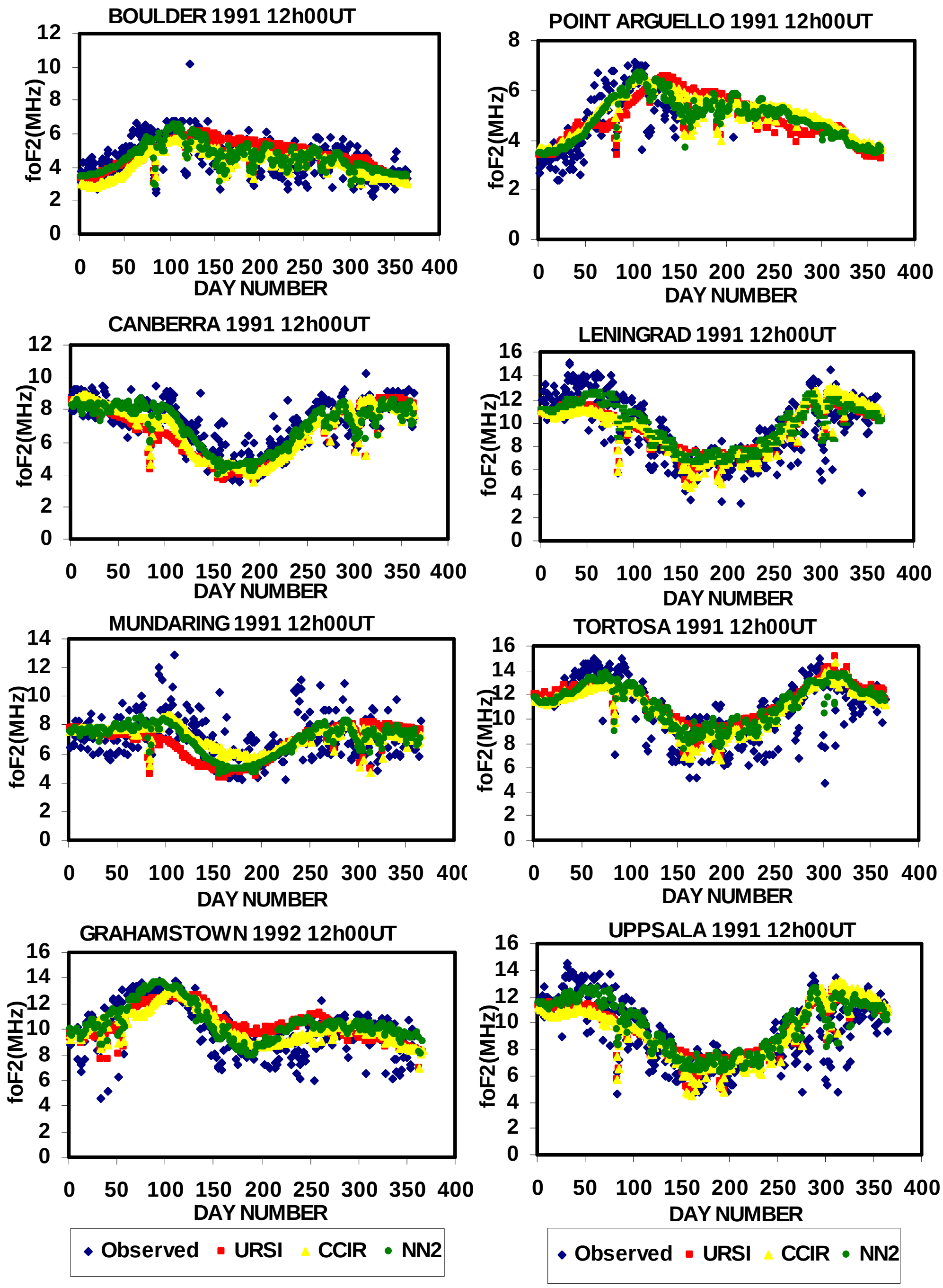

Figure 3-19a: Comparisons of seasonal variations of predicted foF2 values around solar maximum (1991, 1992) at 12h00UT by NN2 model with predicted values from URSI and CCIR and observed values.

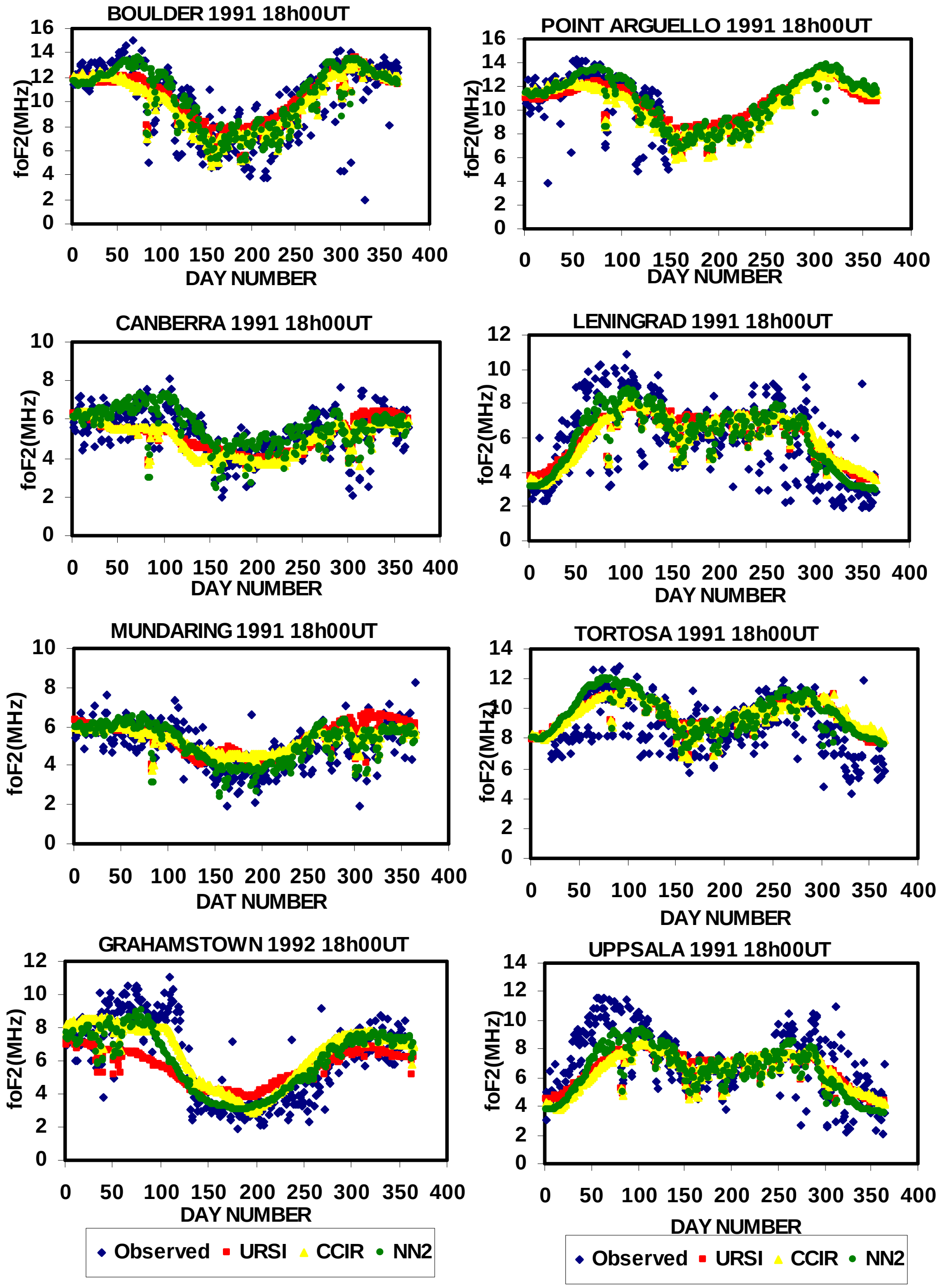

Figure 3-19b: Comparisons of seasonal variations of predicted foF2 values around solar maximum (1991, 1992) at 18h00UT by NN2 model with predicted values from URSI and CCIR and observed values.

3.3.4 Conclusion

These results have shown the potential of NNs for modeling of the ionospheric parameter foF2 on a global scale. Based on the RMSE values obtained, the CCIR model performs better than the URSI model. The NN2 model is an improvement on the CCIR model on average by a margin in the order of 15 – 16%. Also, results obtained from few selected stations (Table 6) outside the training period coupled with the global contour maps of Figures 3-16 and 3-17 are indications that the NN2 is a successfully *spatial-temporal* model that can be used to produce daily hourly values of foF2 at any point across the globe with minimal error. These results further inspired me into investigating the application of NNs to the development of a global model for the propagation factor M(3000)F2, which is another important ionospheric parameter for HF communication purposes. This is discussed in the next section of this chapter.

3.4 M(3000)F2 NN model

3.4.1 Introduction

This section discusses the development of a global empirical model for the propagation factor M(3000)F2 using the same approach as that of the global foF2 empirical model discussed earlier. The M(3000)F2 parameter is related to the maximum usable frequency MUF(3000), which is defined as the highest frequency at which a radio wave can be received over a distance of 3000 km after refraction in the ionosphere (Bradley and Dudeney, 1973). M(3000)F2 is defined as M(3000)F2 = MUF(3000)/foF2). Just like foF2, M(3000)F2 is another ionospheric parameter that is also important for frequency planning for various applications in HF radio communications and ionospheric models. For instance, the height of the F2 peak (hmF2) can be obtained from its close correlation with the propagation factor M(3000)F2 with the empirical formula

$$\mathrm{hmF2} = \frac{1490}{\left[\mathrm{M}(3000)\mathrm{F2} + \mathrm{CF}\right]} - 176$$

where CF is a correction factor that accounts for the effects of the E-layer. CF is a function of the solar sunspot number R_{12}, magnetic dip angle, and the peak plasma frequencies of the F2 and E layers (Bilitza et al., 1979). The M(3000)F2 value is routinely scaled from ionograms, and numerical maps of these values have been developed by the CCIR using a Fourier series. As has been pointed out (Bilitza 2002), unlike foF2 models, there has not been any significant progress in M(3000)F2 modeling since early models due to the overall satisfactory performance of the M(3000)F2-based hmF2 models. Recently, observations have shown that although the overall diurnal variation of M(3000)F2 is well represented by the CCIR M(30000)F2 model, the resolution achieved at some equatorial latitude stations (e.g.

Ouagadougou and Burkina Faso) is not enough to reproduce small-scale temporal and spatial features like the sharp drop in M(3000)F2 after sunset that corresponds to the post-sunset peak in hmF2 (Adeniyi et al., 2003; Obrou et al., 2003). This may be partly due to the limited number of terms (i.e. geographic latitude and longitude Universal Time, modified dip latitude and 12-month running mean of monthly sunspot number) used in the development of the CCIR M(3000)F2 model. As a result, the present model is based on the application of NNs which, together with the other relevant terms that are known to cause variations in F2 peak electron density, provide a predictive tool for the non-linear behaviour of the M(3000)F2 parameter.

As in the case with foF2, the application of NNs does not require evenly distributed data points and there is no need to generate artificial data for missing points. Unlike the other ionospheric parameters, NNs have not been widely employed for M(3000)F2 predictions. Xenos (2002) has successfully employed NNs for single station modeling and regional mapping of M(3000)F2 in the European sector.

3.4.2 Database

As in the case of the foF2 model, the data used for training the M(3000)F2 NNs are hourly values of the propagation factor M(3000)F2, depending on the availability, from ionosonde stations across the globe for the period 1964 – 1986 which also included all periods of calm and disturbed magnetic activities. The database is also spread across the latitudes (low, mid and high latitudes). The same approach for the selection of training stations in the development of the foF2 model was also employed, such that any station with at least seven years of data within a solar cycle was considered for training. The ionospheric stations and their positions used for training and verification are presented in Table 7. Their geographic locations are illustrated with a geographic map shown in Figure 3-20a.

Table 7. Ionosonde stations used in the training and verification of M(3000)F2 NN models.

	Station Name	**Latitude °N**	**Longitude °E**	**Training stations**	**Verification stations**
1	Resolute Bay	74.7	265.1	A	
2	Kiruna	67.8	20.4	A	
3	Lycksele	64.6	18.7	A	
4	Magadan	60.0	151.0	A	
5	Uppsala	59.8	17.6	A	
6	Sverdlovsk	56.4	58.6		B
7	Moscow	55.5	37.3		B
8	Kaliningrad	54.7	20.6	A	
9	Juliusruh/Rugen	54.6	13.4	A	
10	Irkutsk	52.4	104.0		B
11	Slough	51.5	359.4	A	
12	Dourbes	50.1	4.6	A	
13	Winnipeg	49.8	256.6	A	
14	Lannion	48.5	356.7	A	
15	St Johns	47.6	307.3	A	
16	Poitiers	46.6	0.4	A	
17	Ottawa	45.4	284.1	A	
18	Wakkanai	45.4	141.7	A	
19	Tortosa	40.4	0.3	A	
20	Boulder	40.0	254.7		B
21	Akita	39.7	140.1	A	
22	Wallops Is	37.9	284.5		B
23	Kokubunji	35.7	139.5	A	
24	Point Arguello	34.6	239.4	A	
25	White Sands	32.3	253.5	A	
26	Yamagawa	31.2	130.6	A	
27	Okinawa	26.3	127.8	A	
28	Maui	20.8	203.5	A	
29	Dakar	14.8	341.6	A	
30	Vanimo	-2.7	141.3	A	
31	Huancayo	-12.0	284.7		B
32	Tahiti	-17.7	210.7	A	
33	La Reunion	-21.1	55.9	A	
34	Raratonga	-21.2	200.2	A	
35	Brisbane	-27.5	152.9	A	
36	Norfolk Is	-29.0	169.0	A	
37	Mundaring	-32.0	116.3	A	

Table 7 continues

	Station Name	Latitude ^oN	Longitude^oE	Training stations	Verification stations
38	Grahamstown	-33.3	26.5		B
39	Salisbury	-34.7	138.6	A	
40	Canberra	-35.3	149.0	A	
41	Concepcion	-36.6	287.0	A	
42	Hobart	-42.9	147.2	A	
43	Kerquelen	-49.4	70.3	A	
44	Port Stanley	-51.7	302.2	A	
45	Campbell Is	-52.5	169.2		B
46	Macquarie Is	-54.5	159.0	A	
47	Argentine Is	-65.2	295.7		B
48	Terre Adelie	-66.7	140.0	A	
49	Mawson	-67.6	62.9	A	
50	Halley Bay	-75.5	333.4	A	
51	Scott Base	-77.9	166.8	A	

3.4.3 The inputs

The M(3000)F2 value has a similar dependence as the measurable geophysical parameter, foF2. Diurnal and seasonal variations are represented by the quadrature components of HR and DN as defined in equations 3.1 and 3.5 respectively. Similarly, solar activity and magnetic activity are respectively represented by R2 (2-month running mean value of daily SSN) and A16 (2-day running mean value of the 3-hour planetary magnetic index, a_p). Other input parameters: geographic latitude θ, solar zenith angle CHI, angle of meridian relative to subsolar point M, earth's magnetic field inclination (I) and declination (D) are as represented in the foF2 NN model.

3.4.4 Training the M(3000)F2 NN

The inputs and outputs to the M(3000)F2 NNs are shown in Figure 3-20b. As in the case of the foF2 NN, an initial attempt on the predictability of M(3000)F2 using NN techniques was carried out. Hourly values of M(3000)F2 from ionosonde stations (stations with letter A in Table 7) across the globe were used to train an initial M(3000)F2 NN (referred to as NNMA in the text). These stations are marked with blue and black circles in Figure 3-20a. The letter B in Table 7 (stations represented with red circles in Figure 3-20a) refers to the stations used to verify the ability of the NNMA model to predict M(3000)F2 *spatially*. These stations were not included in the training of the NNMA model. The idea behind this initial attempt was to justify the application of NN techniques for M(3000)F2 predictions on a global scale. After this initial attempt, a second NN (referred to as NNM later in the text) was trained with data from all the stations in Table 7. In addition to the NNMA verification stations (i.e. stations represented with red circles in Figure 3-20a), data from stations with blue circles were also used for verification of the performance of the second NN (i.e. NNM). A number of NNs with different architectures were trained in each case in order to determine the optimum NN that can produce predictions of M(3000)F2. These network architectures include (a) one hidden layer each having 30, 40 and 50 neurons, (b) two hidden layers each having 15/15, 20/20, 20/15, 25/15, 25/25, 30/25, neurons, and (c) three hidden layers each having 10/10/15, 20/20/15, 20/20/15, 20/20/20, 15/15/15, 20/15/15, 30/30/25 neurons in the middle layers respectively. The NN configuration with the best performance for the prediction of M(3000)F2 in each case was found to be the one with two hidden layers having 20/20 neurons respectively. Best performance is based on the RMSE difference between the target and predicted values obtained when the results from all configurations were compared. Also, from experience, based on the large volume of data points from all the stations, which requires a lot of time to train a NN, only ten percent (10%) of the total hourly M(3000)F2 values randomly chosen from all the available stations were used to train NNMA and NNM. The 10% data set was again randomly divided into training and testing data sets in the ratio 70% and 30% respectively. While the 70% training data set was used in the training of the network, the remaining 30% testing data set was used in the training process to check that the NN was not being over-trained. This enables the NN to generalize well when presented with input patterns that were not used for the training. The difference between NNMA model and NNM model is in the number of training vectors.

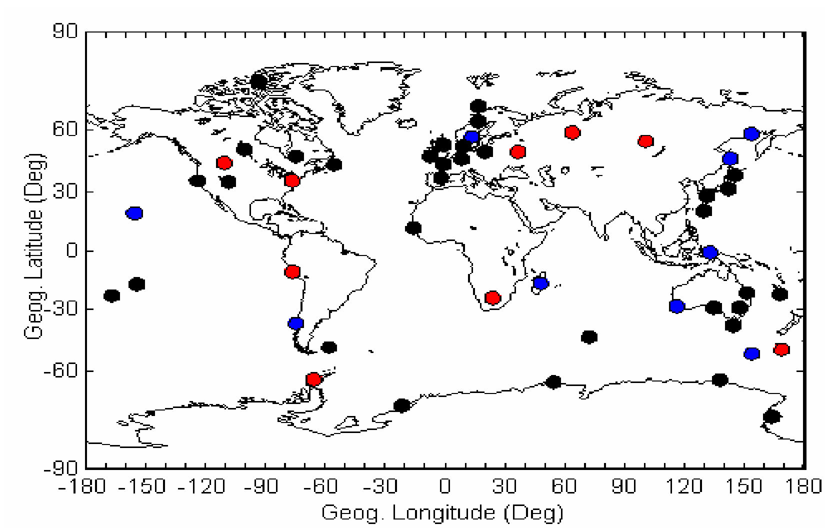

Training stations for NNMA (initial M(3000)F2 model attempt)

Verification stations for NNMA (initial M(3000)F2 model attempt)

Training stations for NNM (final M(3000)F2 model attempt)

Verification stations for NNM (final M(3000)F2 model attempt)

Figure 3-20a. Global map of coordinates of training and verification stations for M(3000)F2 NNs.

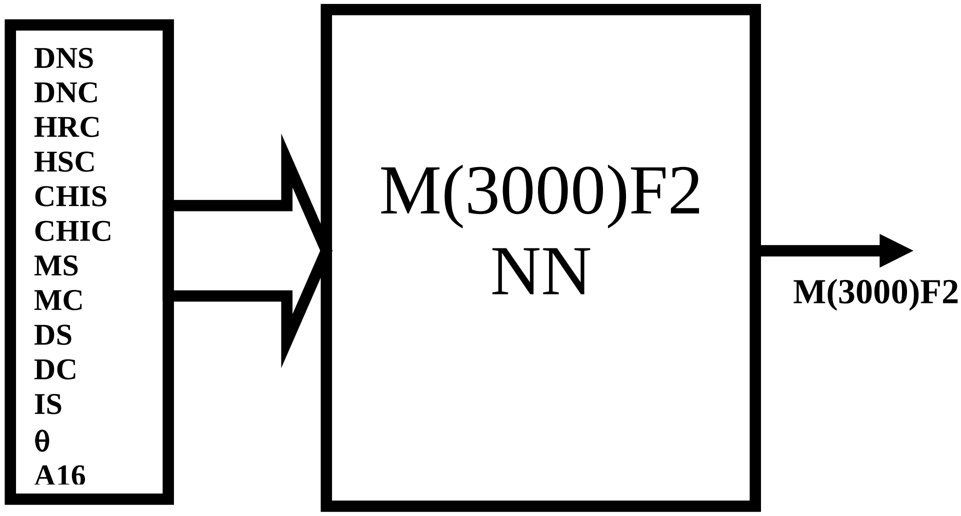

Figure 3-20b: A block diagram of the inputs and output to M(3000)F2 NNs.

3.4.5 Results and discussion

The performance of the NNMA model was verified using data from 9 ionospheric stations (stations with letter B in Table 7) for the period indicated as shown in Table 8. These stations (not included in the training of the NNMA model) were chosen for their geographic remoteness from the training stations (stations with letter A in Table 7) to verify the ability of the NNMA model to predict M(3000)F2 spatially. The performance was carried out using RMSE equation 3.1. All the available daily hourly values of M(3000)F2 for the period indicated for each of the verification stations in Table 8 were used to compute error differences between measured and predicted values by the NNMA model and the IRI model (using the CCIR M(3000)F2 model). As can be observed from Table 8, a comparison of error differences obtained for the IRI and NNMA justify the potential of NN techniques for M(3000)F2 predictions on a global scale, since in all cases the NNMA model RMSE is smaller than that of the IRI model. Evidence of this is clearly shown in Figure 3-21 where the error bars from NNMA model predictions are smaller than that of the IRI model. Figures 3-22 and 3-23 illustrate comparisons of the seasonal variation of the predicted values of M(3000)F2 by the NNMA model with the IRI model predictions and observed values. On the average both models fit the seasonal variation of M(3000)F2. And not only do the NNMA results compare favourably with the IRI model, but the NNMA predictions show a slightly better fit with the observed values than the IRI model for Wallops Is 1976, 1980 at 12h00UT and 00h00UT (Figure 3-22b and 3-23b), Huancayo 1980 at 12h00UT and Grahamstown 1980 at 00h00UT (Figure 3-23b).

Table 8. RMS prediction errors (MHz) in M(3000)F2 at selected verification stations by NNMA and IRI models for the period indicated.

S/N	Station name	LAT °N	LONG °E	RMSE (MHz)		% Error difference between IRI and NNMA	Period
				IRI	NNMA		
1	Sverdlovsk	56.4	58.6	0.152	0.141	7.237	1964 - 1969
2	Moscow	55.5	37.3	0.168	0.156	7.142	1976 - 1981
3	Irkutsk	52.5	104.0	0.152	0.144	5.263	1964 - 1969
4	Boulder	40.0	254.7	0.174	0.171	1.724	1976 - 1981
5	Wallops Is	37.9	284.5	0.162	0.146	9.877	1976 - 1981
6	Huancayo	-12.0	284.7	0.190	0.179	5.789	1976 - 1981
7	Grahamstown	-33.3	26.5	0.267	0.253	5.243	1976 - 1981
8	Campbell Is	-52.5	169.2	0.189	0.181	4.233	1976 - 1981
9	Agentine Is	-65.2	295.7	0.225	0.214	4.889	1976 - 1981

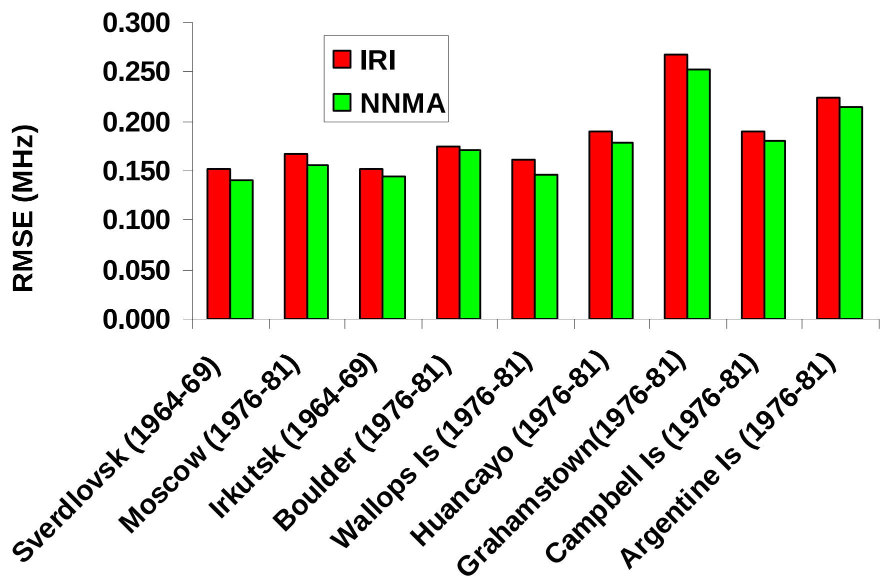

Figure 3-21. Bar graph illustrating the RMSE differences between measured and predictions by NNMA model and IRI model for all the daily hourly values of M(3000)F2 for each station for the period indicated (from Table 8).

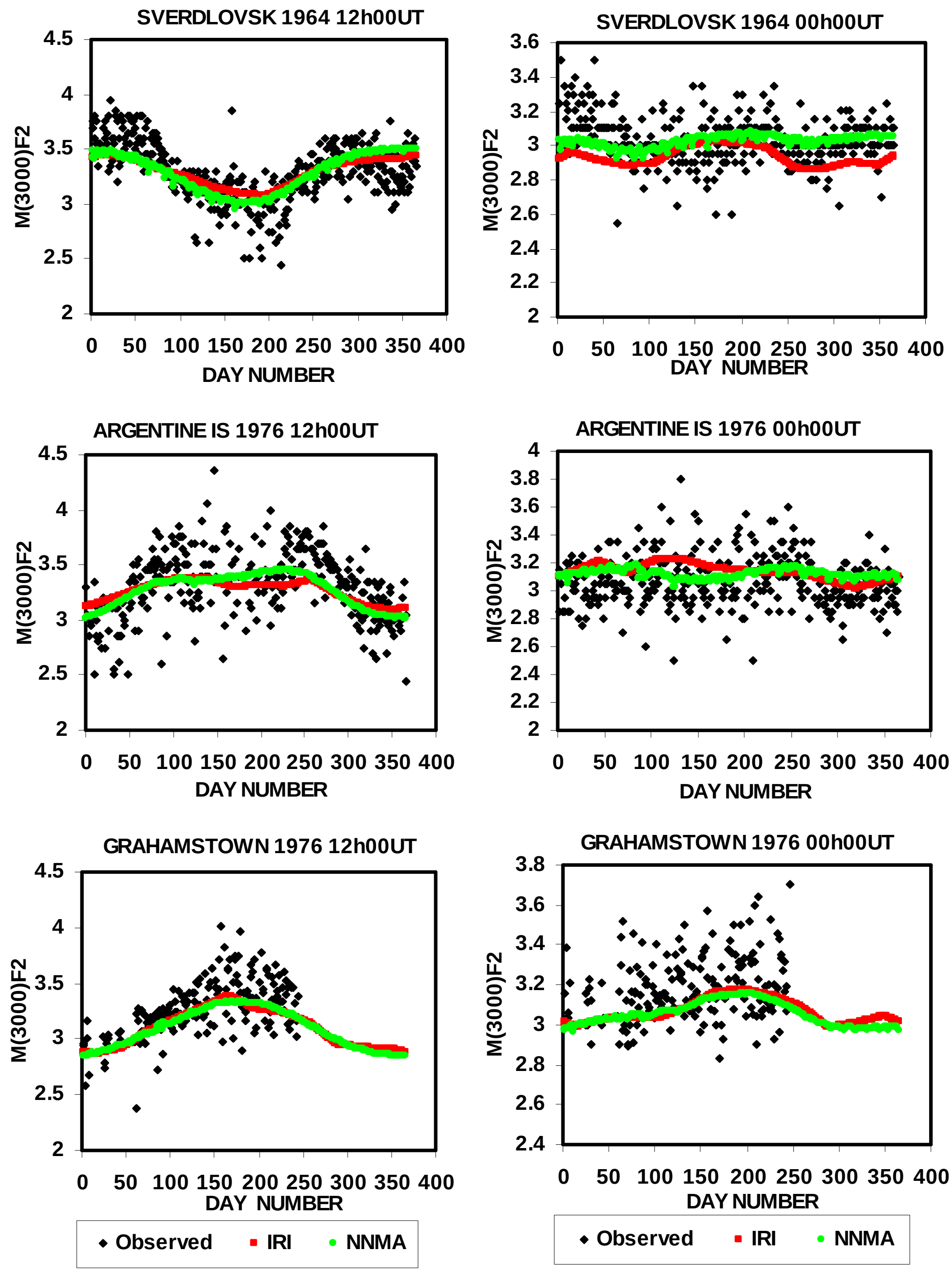

Figure 3-22a Comparisons of the seasonal variation of measured M(3000)F2 (Observed) with NNMA model and IRI model predictions at 12h00UT and 00h00UT for some selected stations during years of low solar activity.

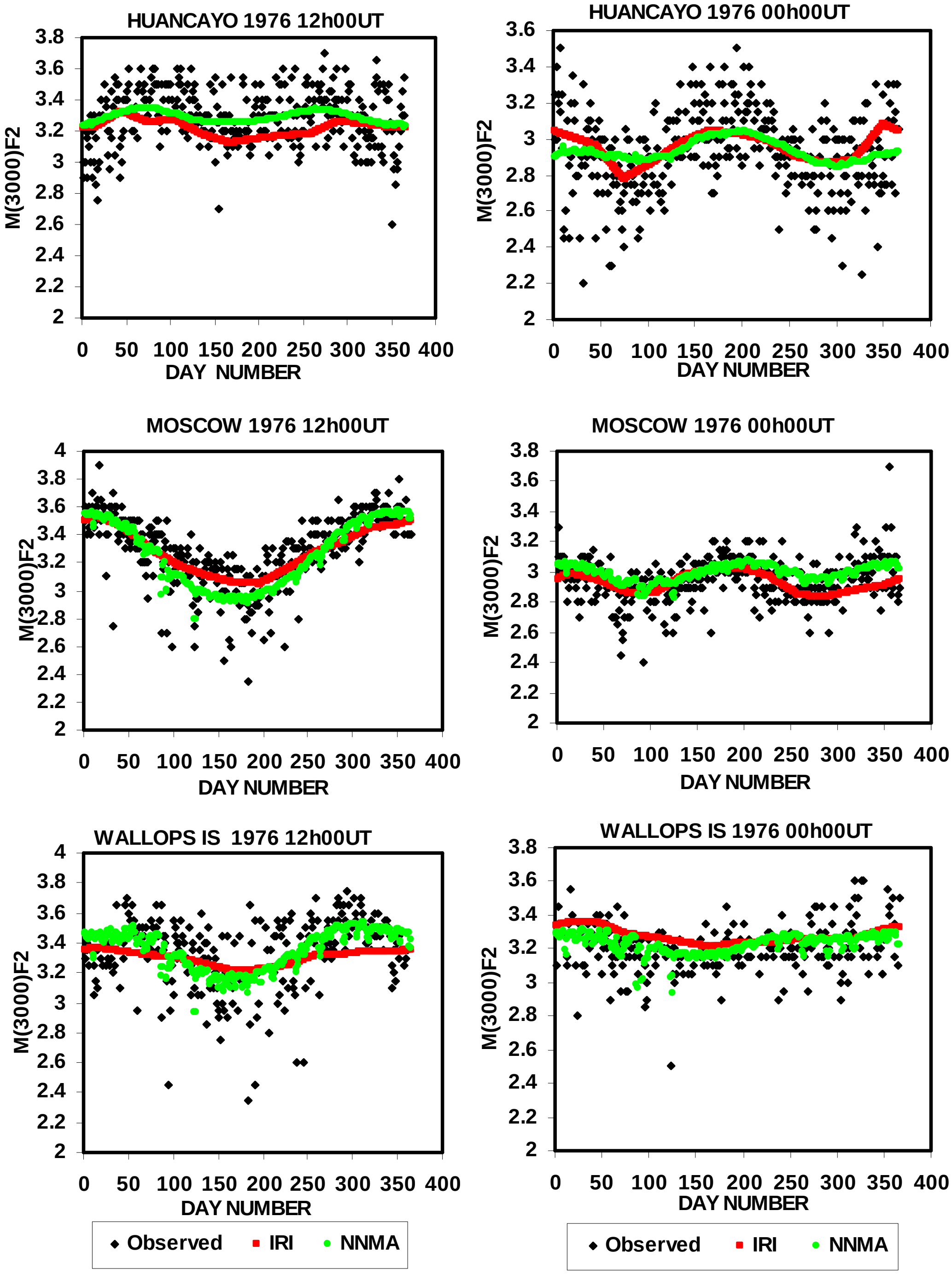

Figure 3-22b. Comparisons of the seasonal variation of measured M(3000)F2 (Observed) with NNMA model and IRI model predictions at 12h00UT and 00h00UT for som3 selected stations for year 1976 (year of low solar activity).

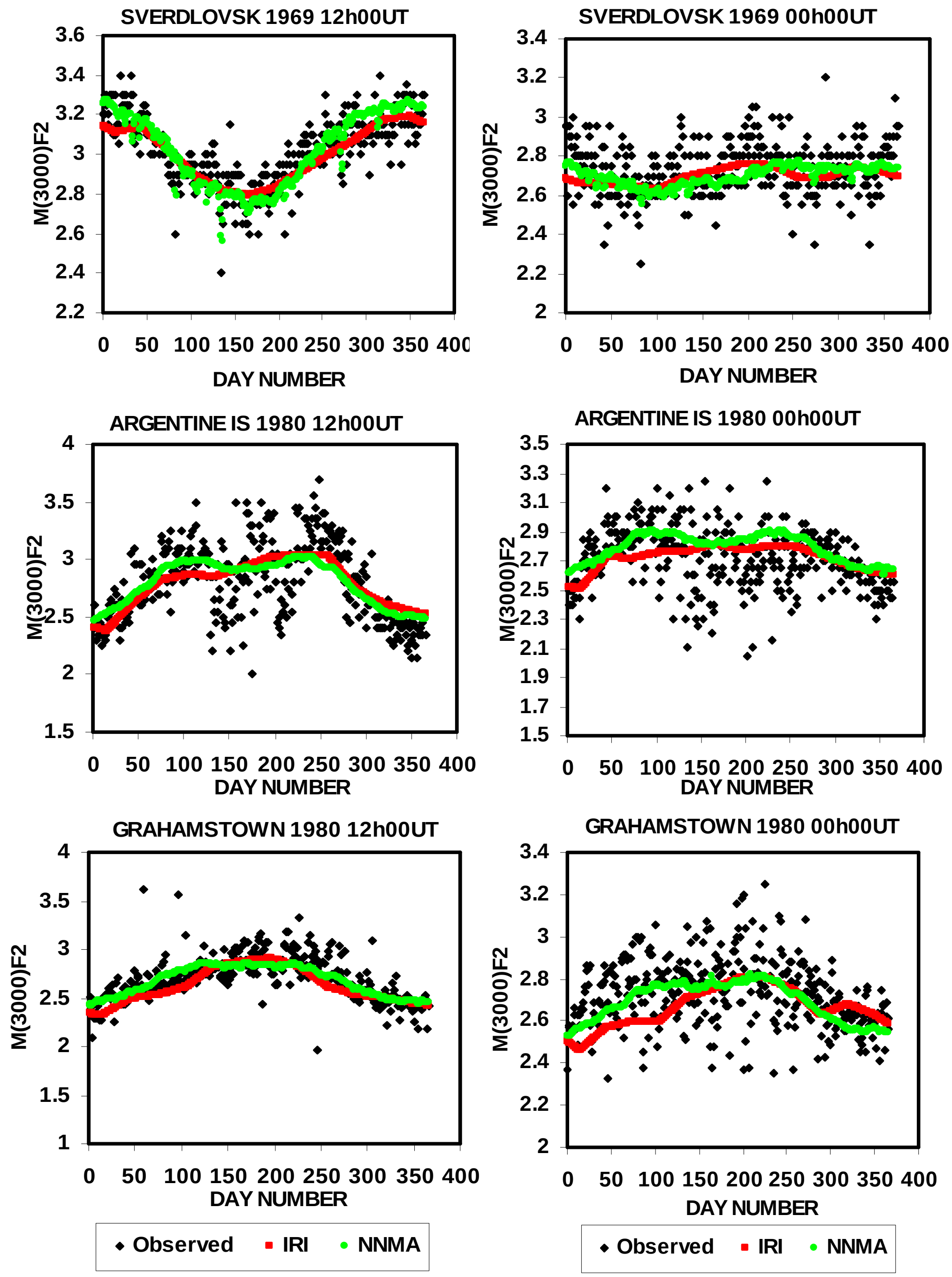

Figure 3-23a. Comparisons of the seasonal variation of measured M(3000)F2 (Observed) with NNMA model and the IRI model predictions at 12h00UT and 00h00UT for some selected stations during years of high solar activity.

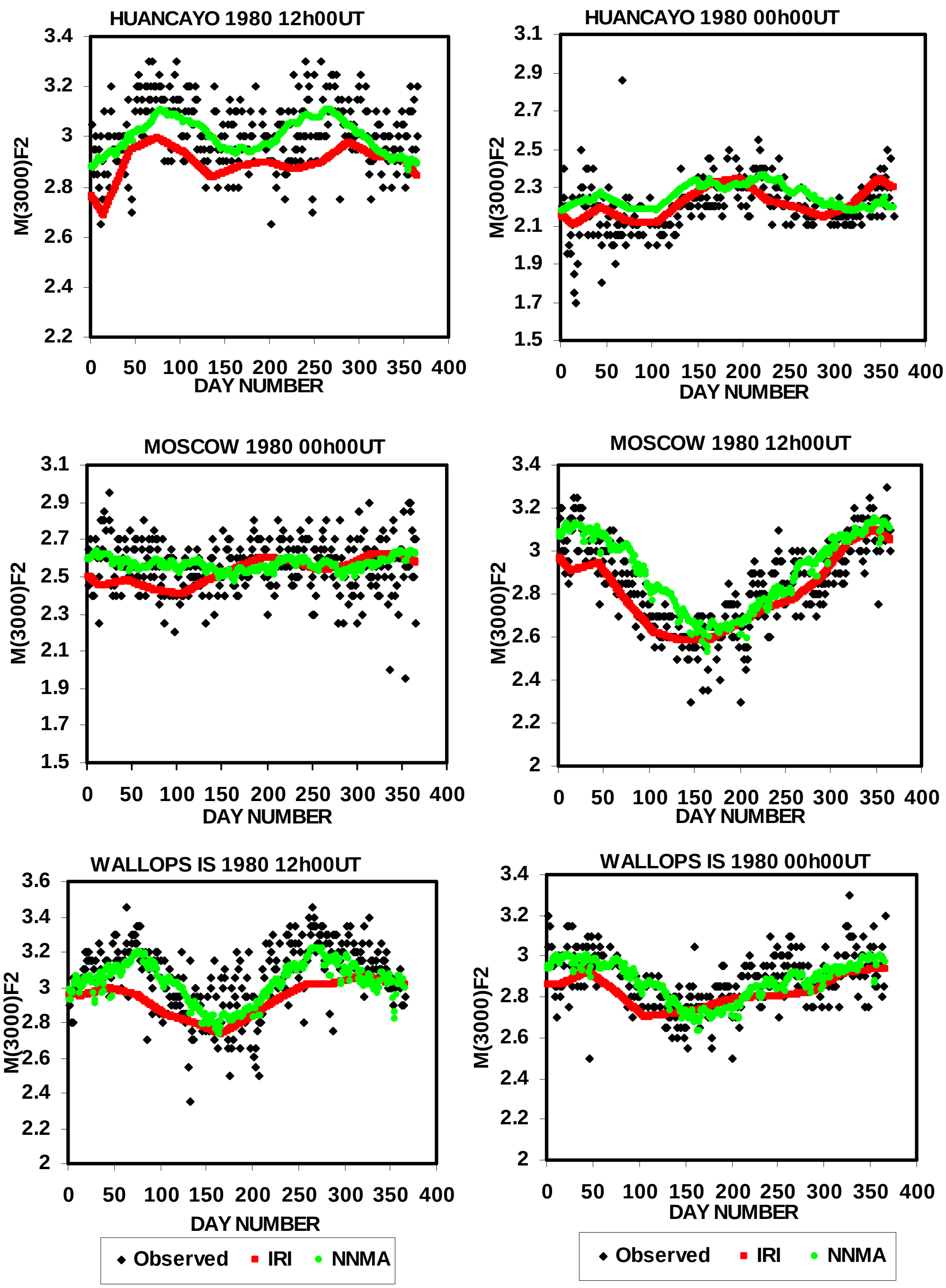

Figure 3-23b. Comparisons of the seasonal variation of measured M(3000)F2 (Observed) with NNMA model and the IRI model predictions at 12h00UT and 00h00UT for some selected stations for year 1980 (year of high solar activity).

The performance of the NN (NNM) model (i.e. final M(3000)F2 NN) that was trained with M(3000)F2 values from all the stations in Table 7 was determined in three different ways using equations 3.12 and 3.13 of RMSE and RMSE average respectively. Firstly, M(3000)F2 values predicted by the NNM model were compared with the IRI model predictions and measured values from a few selected stations (Table 9) within the training period. Secondly, measured data from a few selected stations (Table 10) for some years outside the training period were used to compute error differences for NNM and the IRI models. This evaluates the performance of the NNM model temporally beyond the training period. And thirdly, the predictive ability of NNM was verified on a few selected high latitude stations and compared with the IRI predictions (this is discussed in chapter four). Again, a test on the relative performance of NNM model over the IRI model was carried out. The choice of these verification stations and the corresponding years is based on data availability, as it is not possible to get data for the same years for all stations. This is due to the fact that some stations were inactive for some periods due to one reason or the other.

In Tables 9 and 10 the RMSE differences between the measured M(3000)F2 values and the predicted values by NNM model and the IRI model were obtained by taking the averages of the root mean square errors of all M(3000)F2 data points present for the period indicated for each station. Also shown in Table 9 are the RMSE averages (0.171 and 0.189) for NNM and the IRI models respectively. Figures 3-24 and 3-25 illustrate the RMSE differences and RMSE averages calculated for NNM and the IRI models. A closer inspection of the percentage error differences in Table 9 shows that the NNM model is an improvement on the IRI model on average by a margin of the order of 5 – 13 % with an overall average of 9.7%. Evidence of this is also shown in Figures 3-24 and 3-25 where error bars for the NNM model predictions are smaller than that for the IRI model.

Table 9. RMS prediction errors (MHz) in M(3000)F2 at selected verification stations by NNM and IRI models within the training period of the NNM model.

S/N	Station name	LAT °N	LONG °E	RMSE (MHz)		% Error difference between IRI and NNM	Period
				IRI	**NNM**		
1	Sverdlovsk	56.4	58.6	0.152	0.138	9.211	1964 - 1969
2	Moscow	55.5	37.3	0.167	0.153	8.383	1976 - 1981
3	Irkutsk	52.5	104.0	0.152	0.136	10.526	1964 - 1969
4	Wakkanai	45.4	141.7	0.166	0.158	4.819	1976 - 1981
5	Boulder	40.0	254.7	0.174	0.159	8.621	1976 - 1981
6	Wallops Is	37.9	284.5	0.162	0.148	8.642	1976 - 1981
7	Maui	20.8	203.5	0.216	0.189	12.500	1976 - 1981
8	Huancayo	-12.0	284.7	0.190	0.176	7.368	1976 - 1981
9	Grahamstown	-33.3	26.5	0.267	0.230	13.858	1976 - 1981
10	Concepcion	-36.6	287.0	0.211	0.197	6.635	1964 - 1969
11	Campbell Is	-52.5	169.2	0.186	0.167	10.215	1976 - 1981
12	Agentine Is	-65.2	295.7	0.225	0.198	12.000	1976 - 1981
	RMSE average			**0.189**	**0.171**	**9.656**	

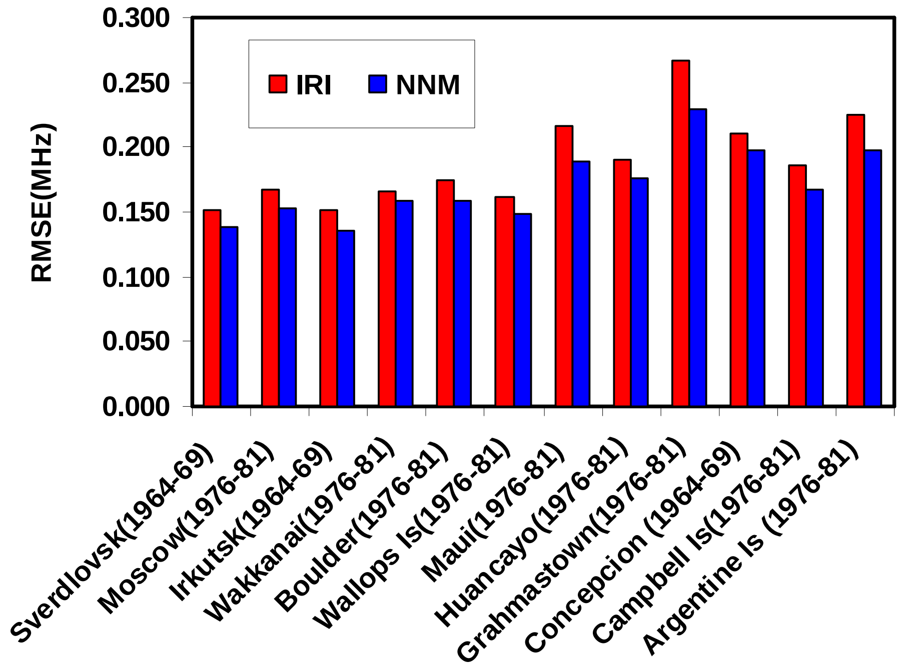

Figure 3-24. Bar graph illustration of RMSE differences between measured M(3000)F2 and predictions by the NNM model and the IRI model for all daily hourly values of M(3000)F2 for each station over the period indicated.

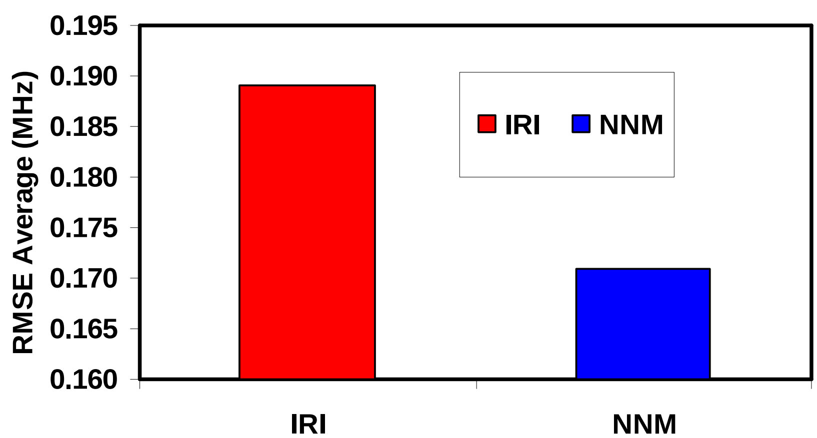

Figure 3-25. Comparisons of RMSE average between NNM model and the IRI model using bar graph illustration (from Table 9)

Figures 3-26 and 3-27 show examples of the diurnal variation of M(3000)F2 predicted by the NNM model compared with the IRI model predictions and observed values starting at 00h00UT on the first of the days of the year indicated for each station. Results are shown for low solar activity (Figures 3-26a and b) and high solar activity (Figures 3-27a and b) periods. Due to missing data points, it was not easy to get complete data on the days that coincide with solstices and equinoxes for some stations. As a result, efforts were made to look for days where data are available as close as possible to the solstice and equinox days. A closer inspection of Figures 3-26 and 3-27 show that predicted values of M(3000)F2 by the two models closely follow the diurnal structure seen in the measurements. There are cases where the NNM model performs slightly better than the IRI model predictions and vice versa. For instance in Figure 3-26a the IRI model underestimates M(3000)F2 for Wakkanai (day 83 and 84) and Boulder (day 84 and 85). This can also be observed in Figure 3-27a for Grahamstown (day 82 and 83, 267 and 268) and Boulder (day 82 and 83). On the other hand, the NNM model overestimates M(3000)F2 around 16h00-23h00UT for Irkutsk (day 82 and 83) (Figure 3-26b) and also for Huancayo (day 86 and 87) (Figure 3-27a).

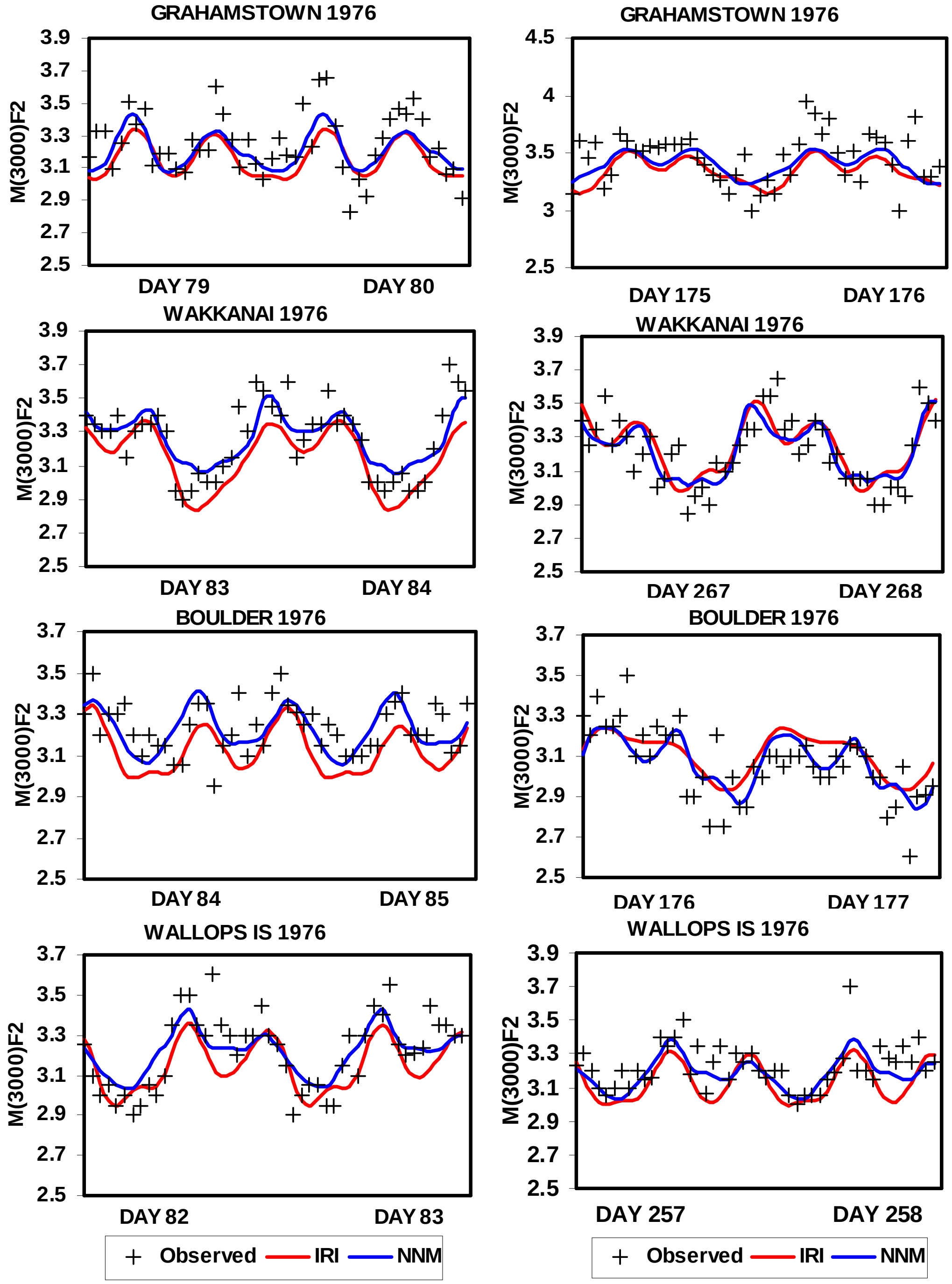

Figure 3-26a. Comparisons of the diurnal variation of M(3000)F2 predicted values by the NNM model with the IRI model predictions and observed values for 2 days starting at 00h00UT on the first day of the days indicated for a few selected stations for year 1976 (year of low solar activity).

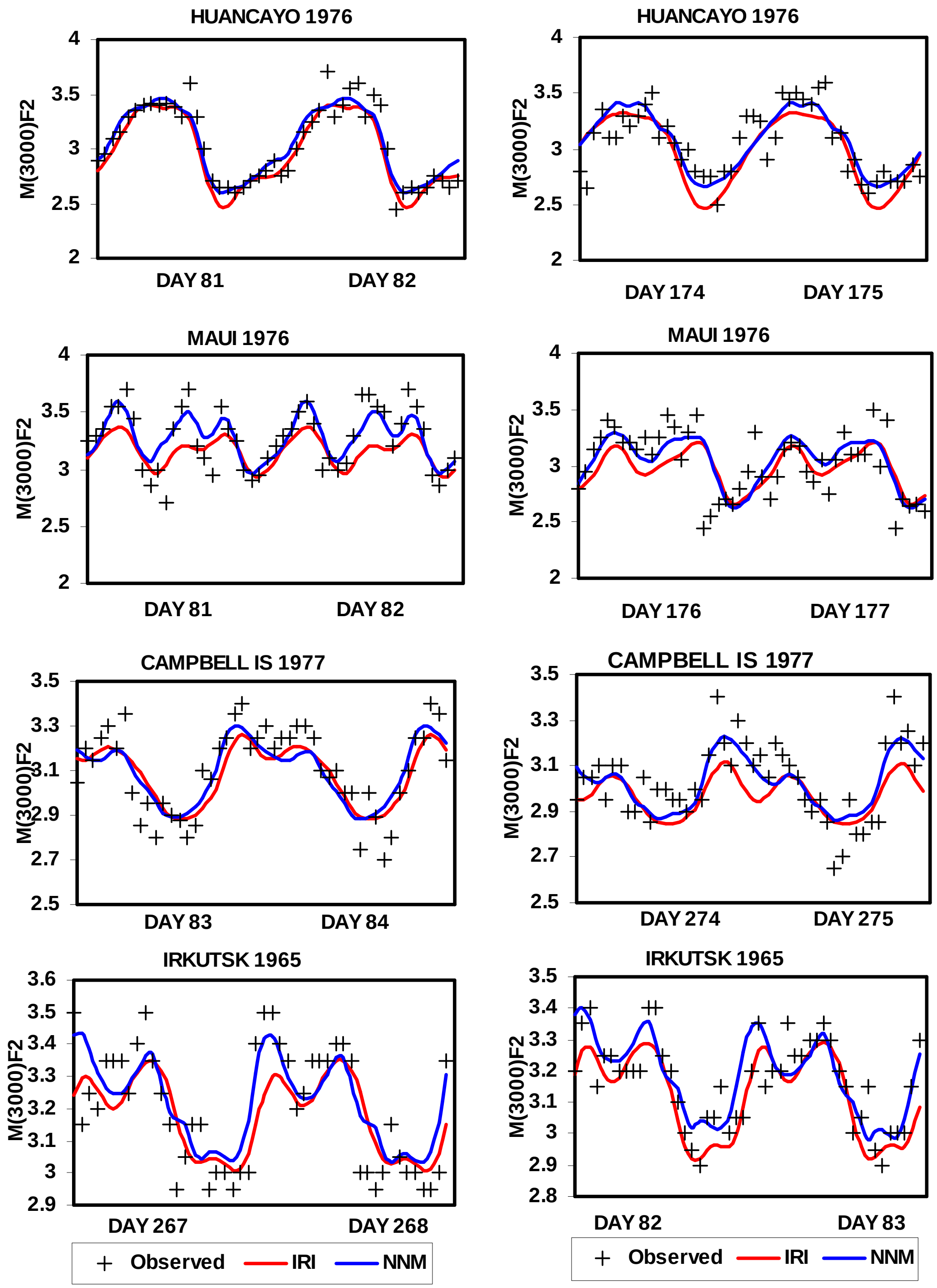

Figure 3-26b. Comparisons of the diurnal variation of M(3000)F2 predicted values by the NNM model with the IRI model predictions and observed values for 2 days starting at 00h00UT on the first day of the days indicated for a few selected stations during low solar activity.

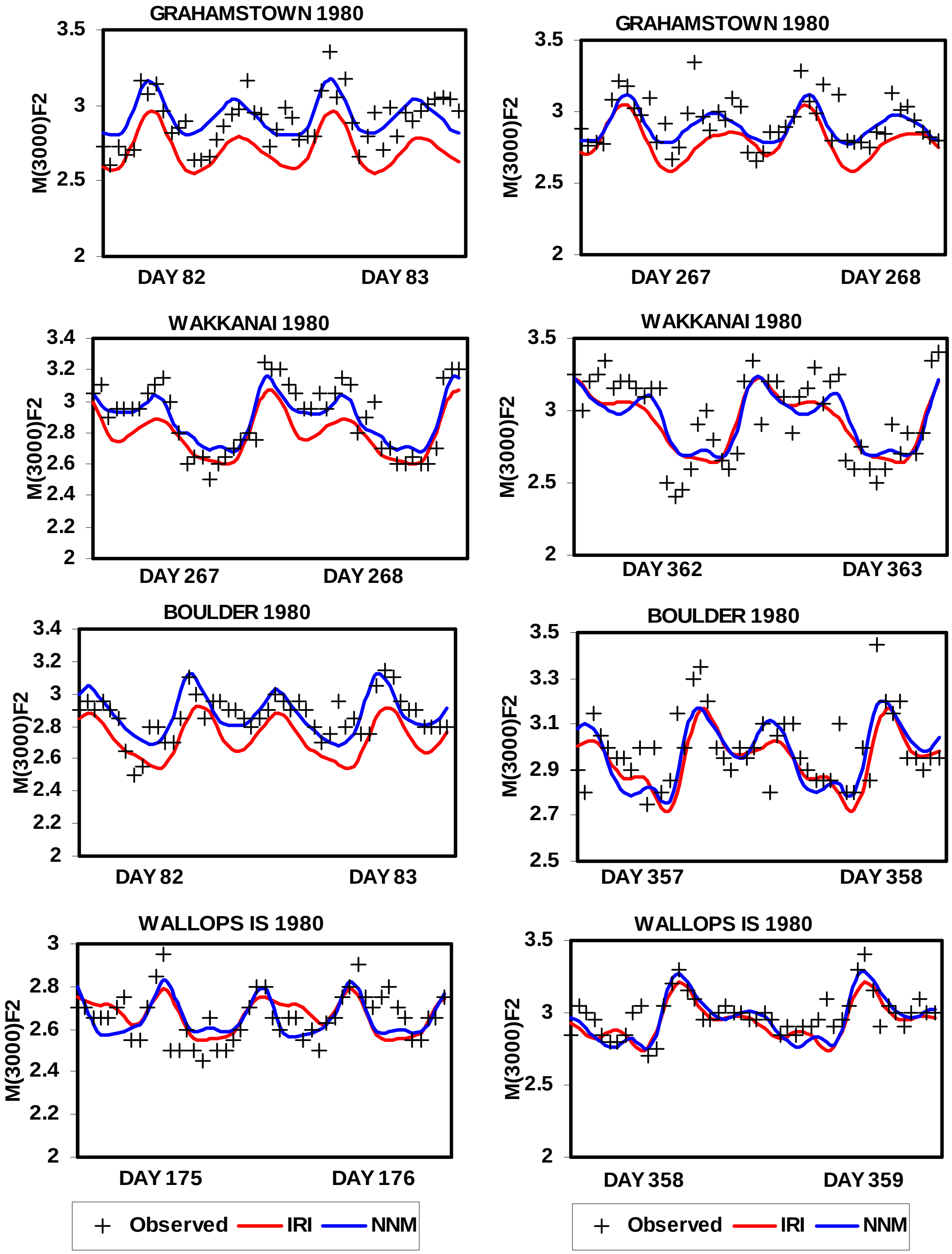

Figure 3-27a. Comparisons of the diurnal variation of M(3000)F2 predicted values by the NNM model with the IRI model predictions and observed values for 2 days starting at 00h00UT on the first day of the days indicated for a few selected stations for year 1980 (year of high solar activity).

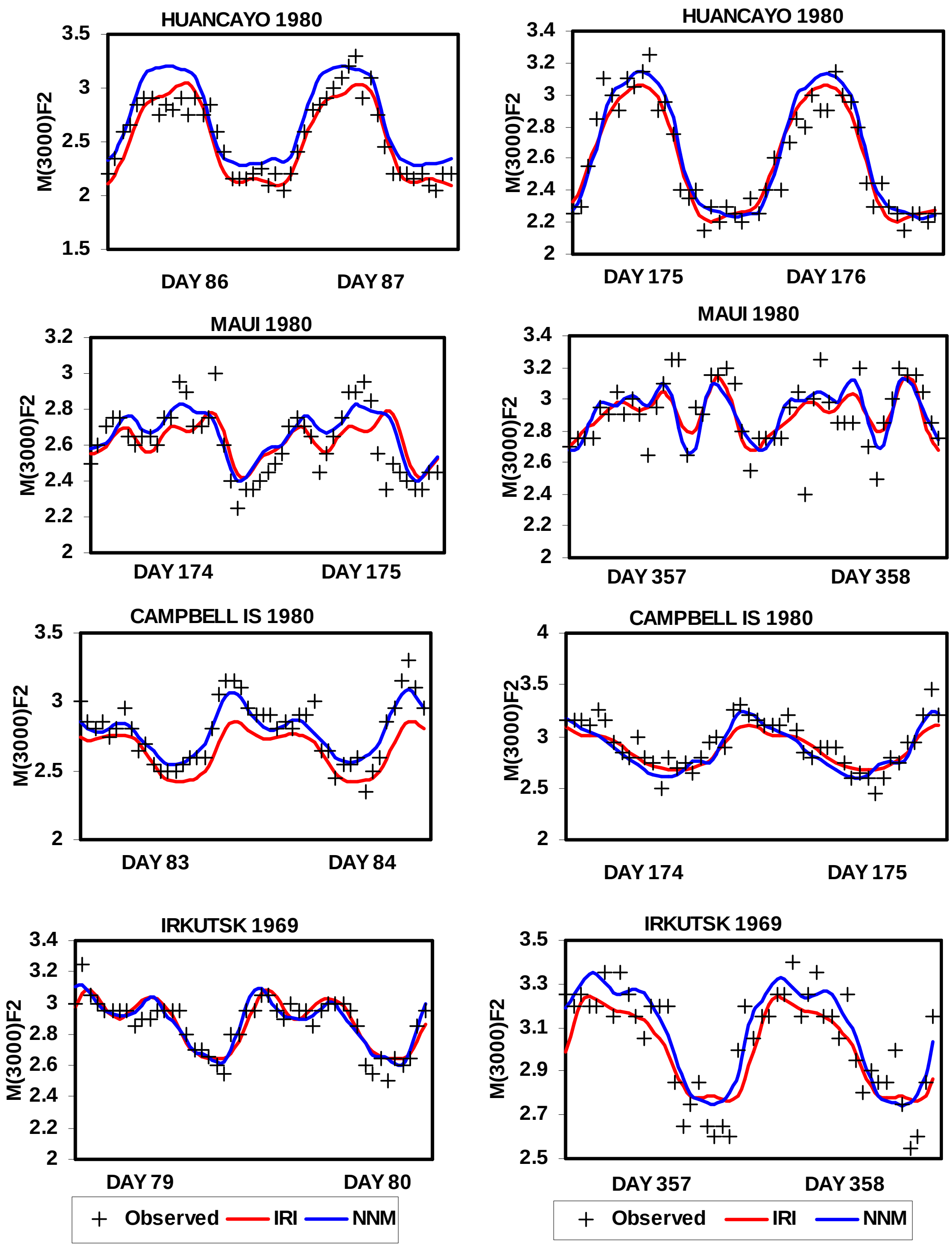

Figure 3-27b. Comparisons of the diurnal variation of M(3000)F2 predicted values by the NNM model with the IRI model predictions and observed values for 2 days starting at 00h00UT on the first day of the days indicated for a few selected stations during high solar activity.

In order to estimate the performance of the NNM model over a period of time longer than the two days shown in Figures 3-26 and 3-27, seasonal variations have been considered for a few selected stations during low (1976) and high (1980) solar activity periods respectively. From this it is possible to see how well the NNM model predictions follow the seasonal structure of M(3000)F2 measurements. Figures 3-28(a-d) (for low solar activity) and 3-29(a-d) (for high solar activity) illustrate comparisons of the seasonal variations of the NNM model predicted M(3000)F2 values model with the IRI model predictions and observed values. The comparisons are shown for 12h00UT and 18h00UT for each of the years indicated for each station. As can be observed, the figures clearly show that both models predict the seasonal trend of M(3000)F2. There are a few cases where on average the NNM model predictions are much closer to the observed values than that of the IRI model predictions. These are the cases of Maui 1976 at 12h00UT (Figure 3-28a), Wakkanai and Huancayo 1976 at 18h00UT (Figure 3-28d), Boulder and Maui 1980 at 12h00UT (Figure 3-29a), Huancayo and Wallops Is 1980 at 12h00UT (Figure 3-29b) and Wakkanai and Wallops Is 1980 at 18h00UT (Figure 3-29d). Again, although the two models' predictions closely follow the seasonal structure of the measurements, they both underestimate M(3000)F2 for stations like Huancayo and Wallops Is 1976 at 12h00UT (Figure 3-28b) and Wallops Is 1980 at 12h00UT.

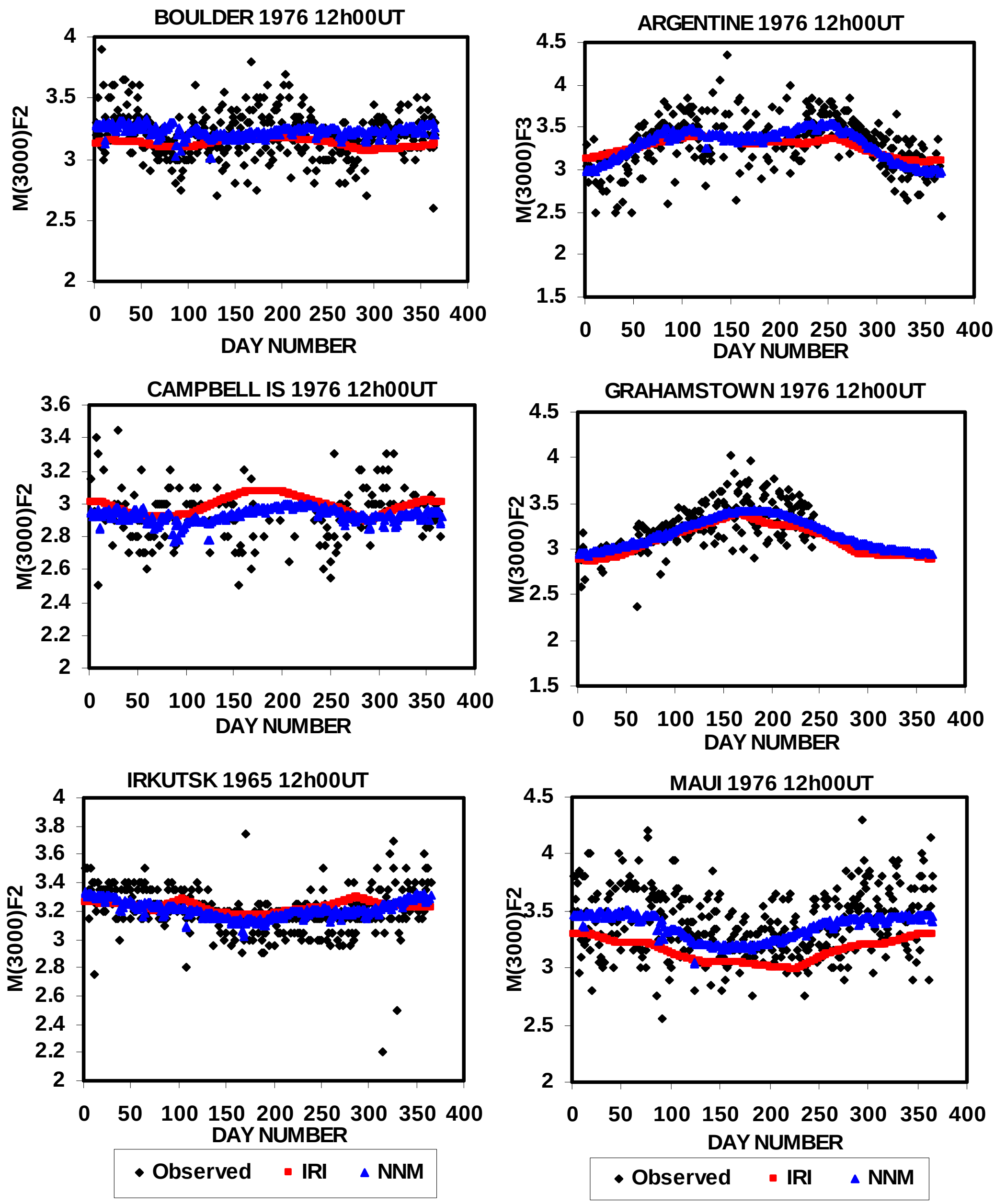

Figure 3-28a. Comparisons of the seasonal variation of measured M(3000)F2 (Observed) with the NNM model and the IRI model predictions during a year of low solar activity for Boulder, Argentine, Campbell Is, Grahamstown, Irkutsk and Maui at 12h00UT.

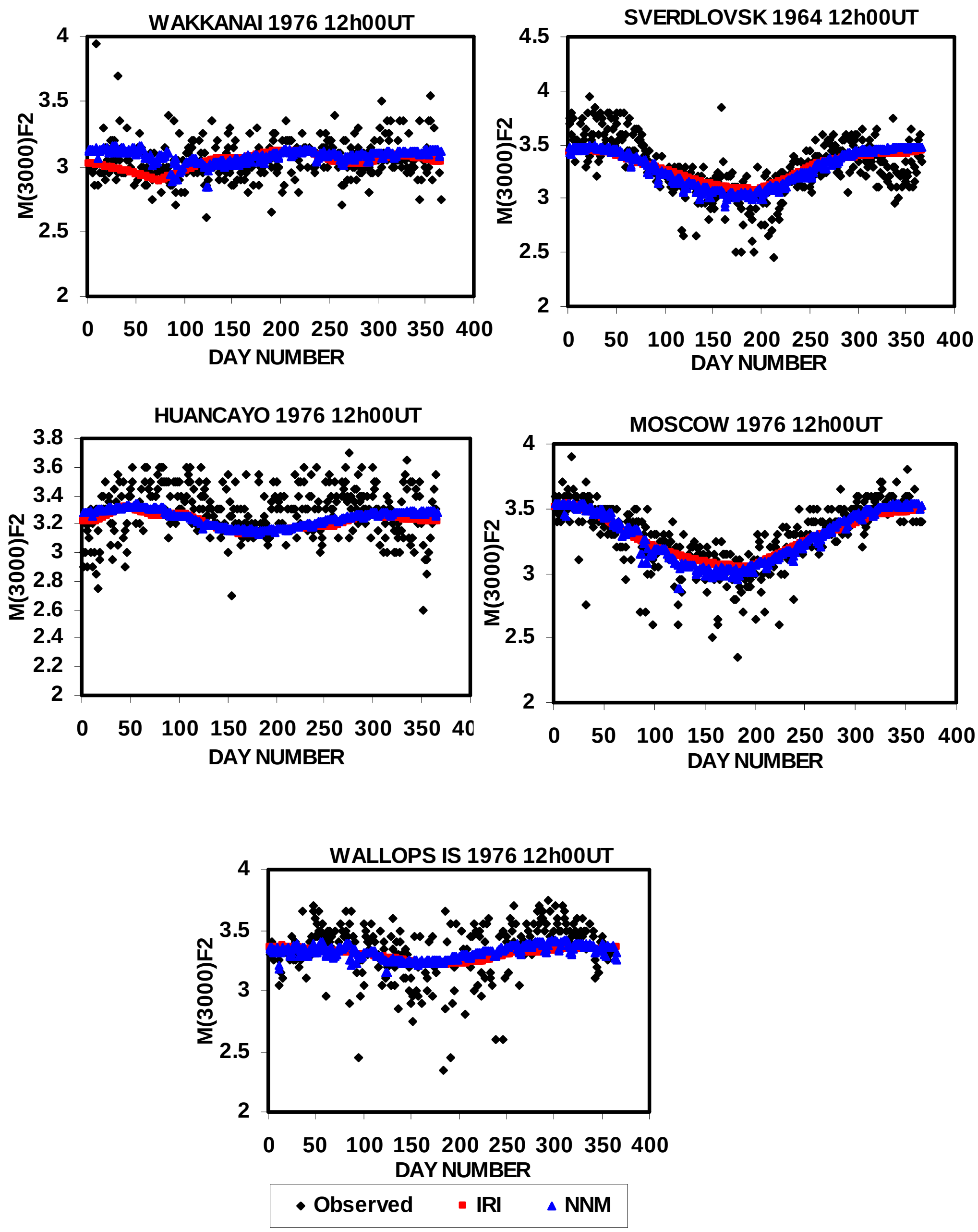

Figure 3-28b. Comparisons of the seasonal variation of measured M(3000)F2 (Observed) with the NNM model and the IRI model predictions during a year of low solar activity for Wakkanai, Sverdlovsk, Huancayo, Moscow and Wallops Is stations at 12h00UT.

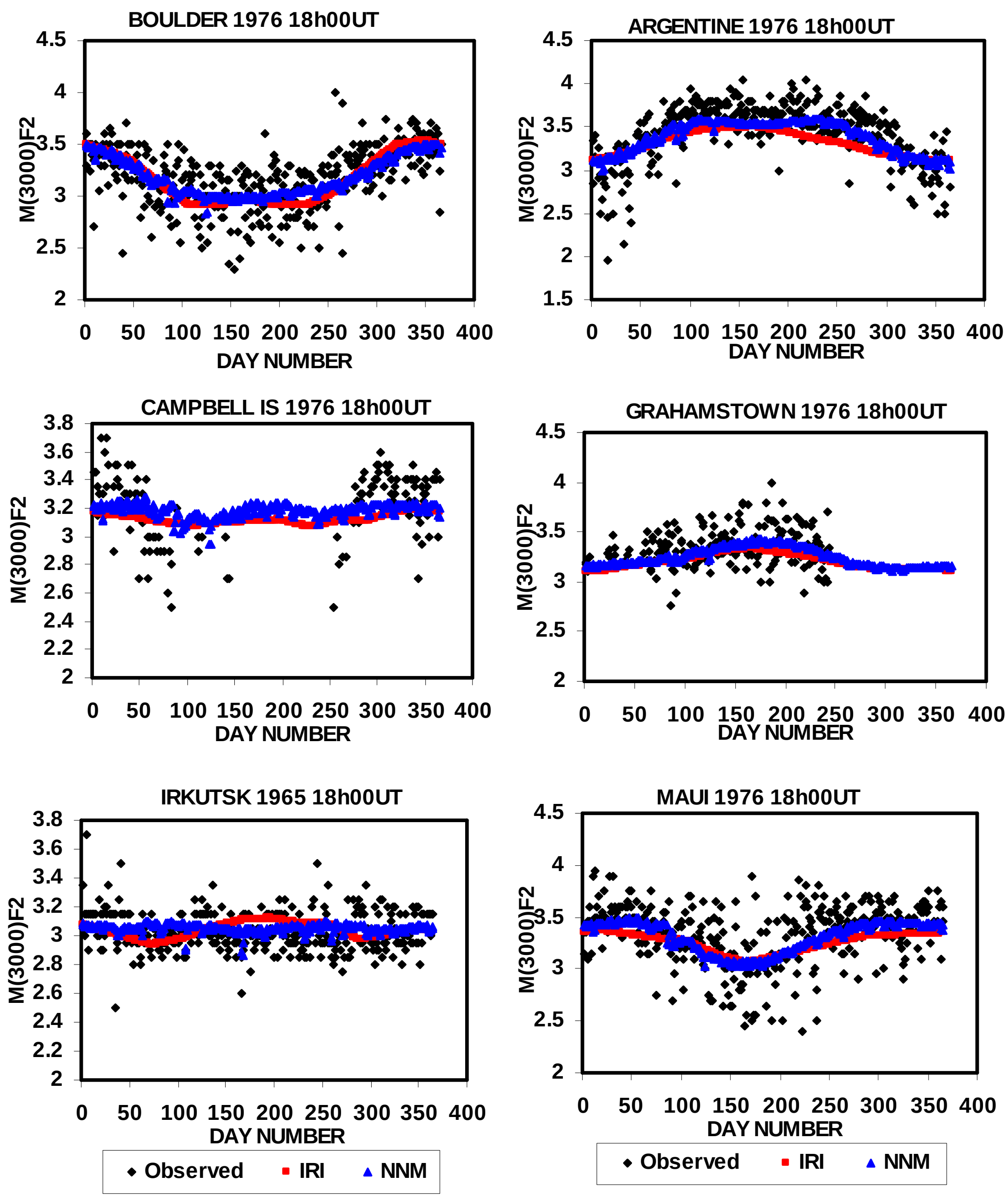

Figure 3-28c. Comparisons of the seasonal variation of measured M(3000)F2 (Observed) with NNM model and the IRI model predictions during a year of low solar activity for Boulder, Argentine, Campbell Is, Grahamstown, Irkutsk and Maui at 18h00UT.

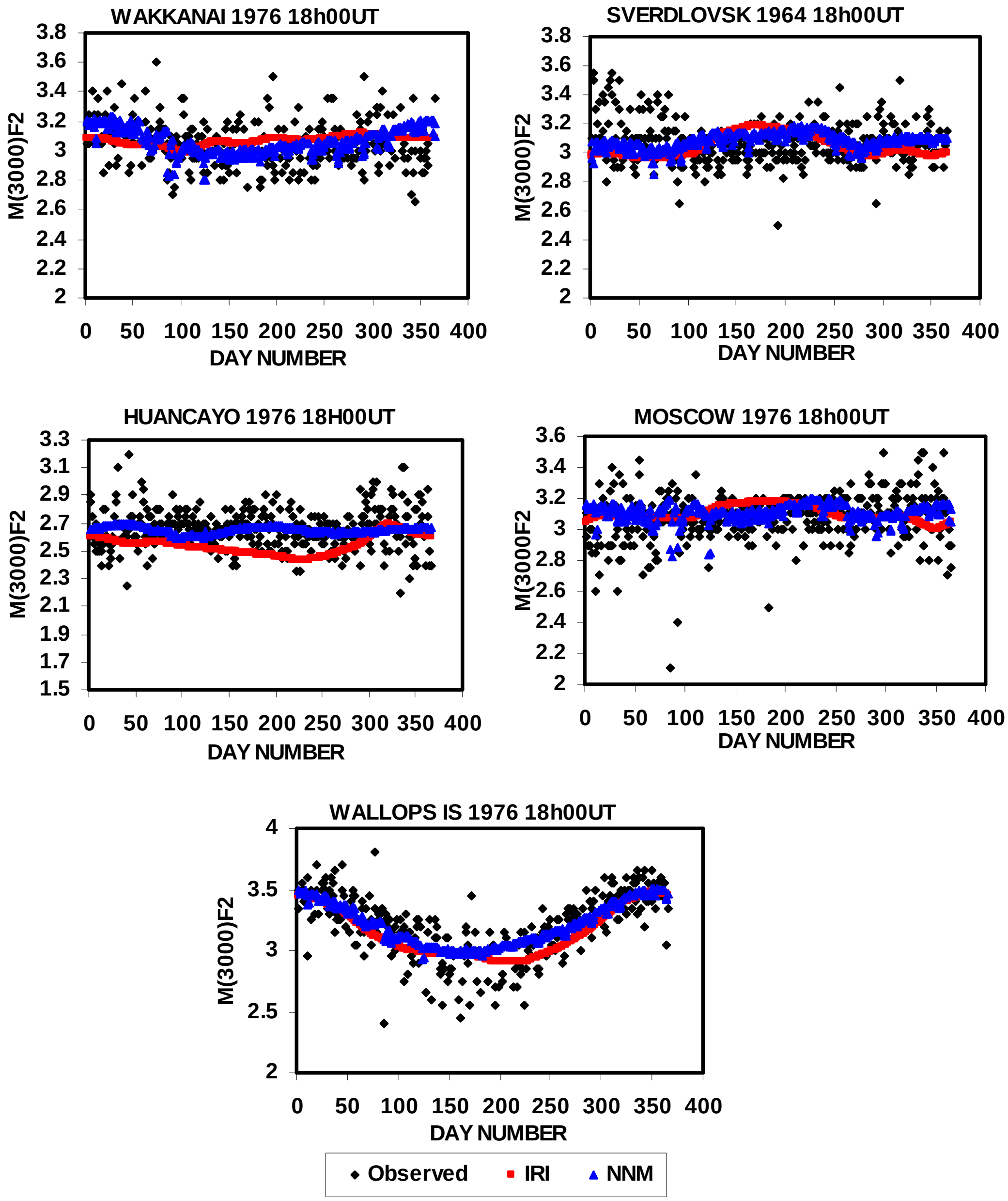

Figure 3-28d. Comparisons of the seasonal variation of measured M(3000)F2 (Observed) with the NNM model and the IRI model predictions during a year of low solar activity for Wakkanai, Sverdlovsk, Huancayo, Moscow and Wallops Is stations at 18h00UT.

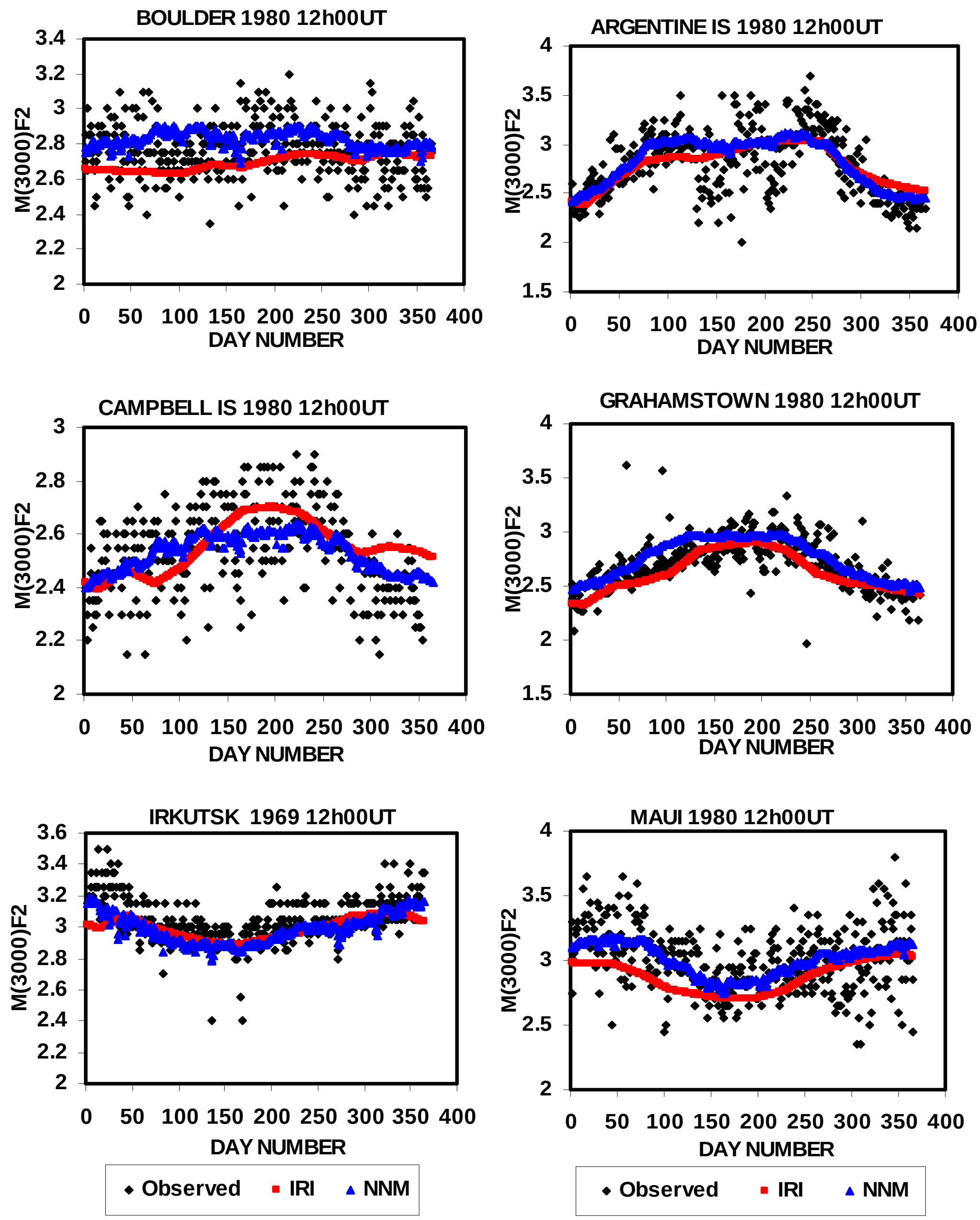

Figure 3-29a. Comparisons of the seasonal variation of measured M(3000)F2 (Observed) with the NNM model and the IRI model predictions during a year of high solar activity for Boulder, Argentine, Campbell Is, Grahamstown, Irkutsk and Maui Irkutsk at 12h00UT.

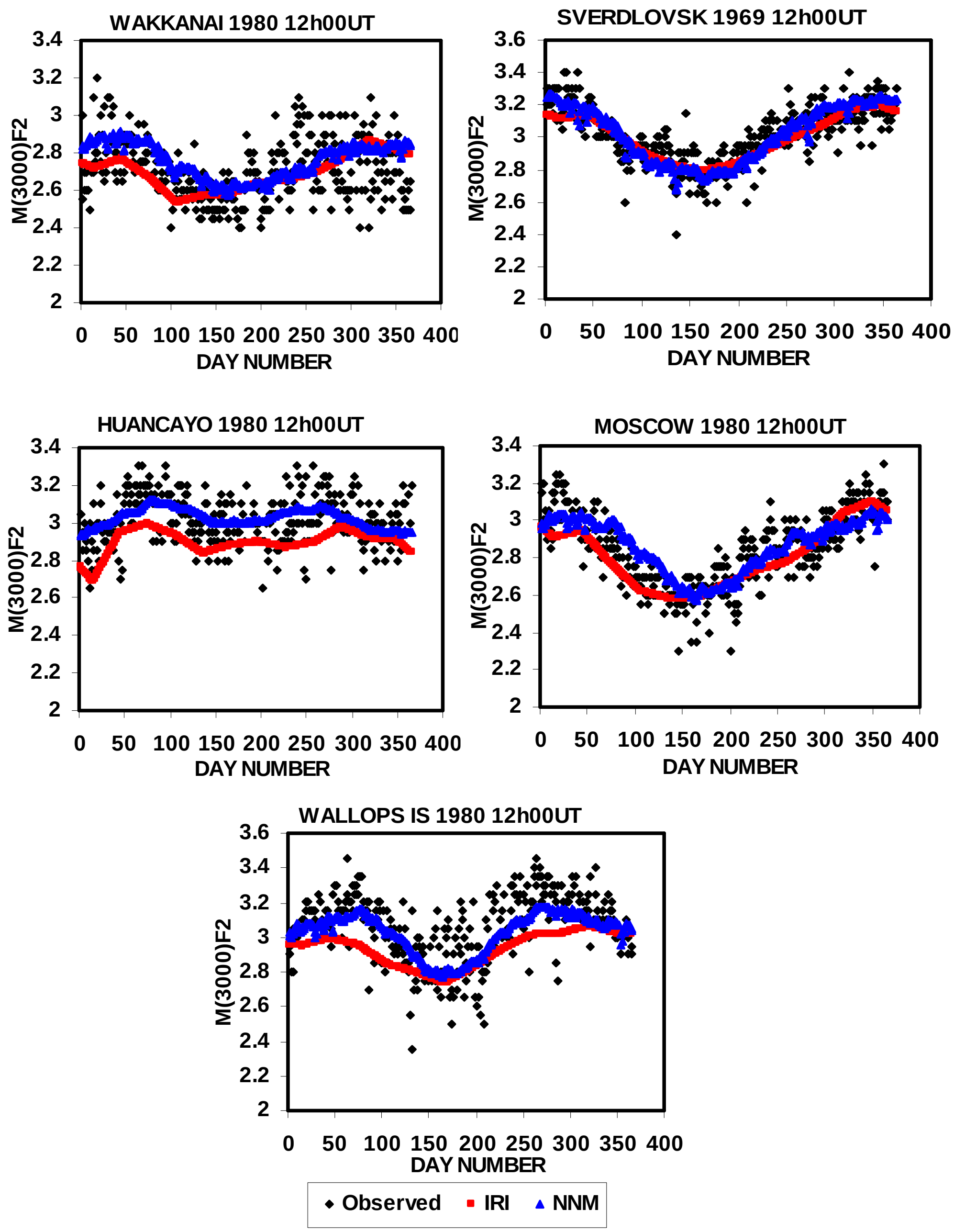

Figure 3-29b. Comparisons of the seasonal variation of measured M(3000)F2 (Observed) with the NNM model and the IRI model predictions during a year of high solar activity for Wakkanai, Sverdlovsk, Huancayo, Moscow and Wallops Is stations at 12h00UT.

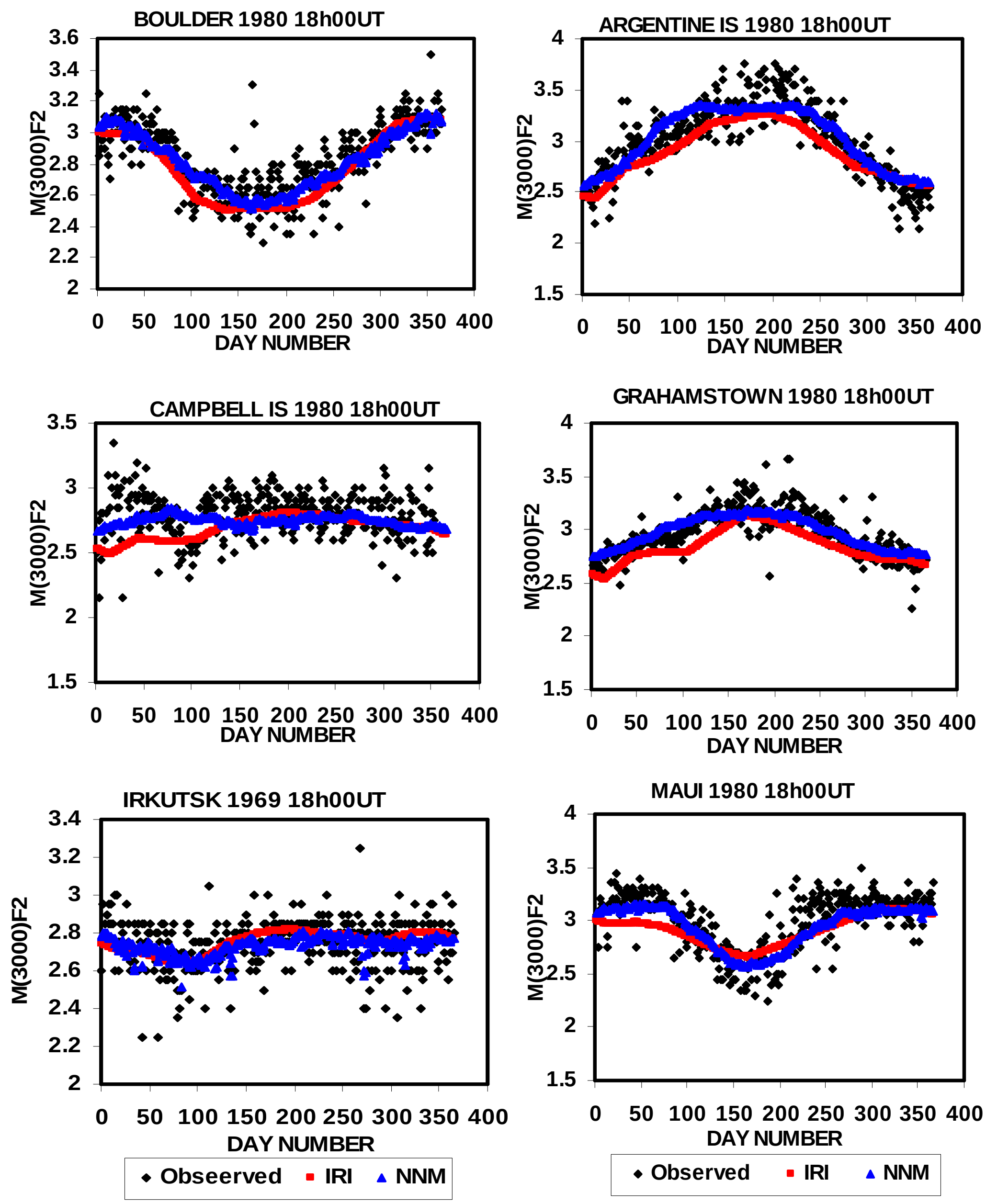

Figure 3-29c. Comparisons of the seasonal variation of measured M(3000)F2 (Observed) with the NNM model and the IRI model predictions during a year of high solar activity for Boulder, Argentine, Campbell Is, Grahamstown, Irkutsk and Maui Irkutsk at 18h00UT.

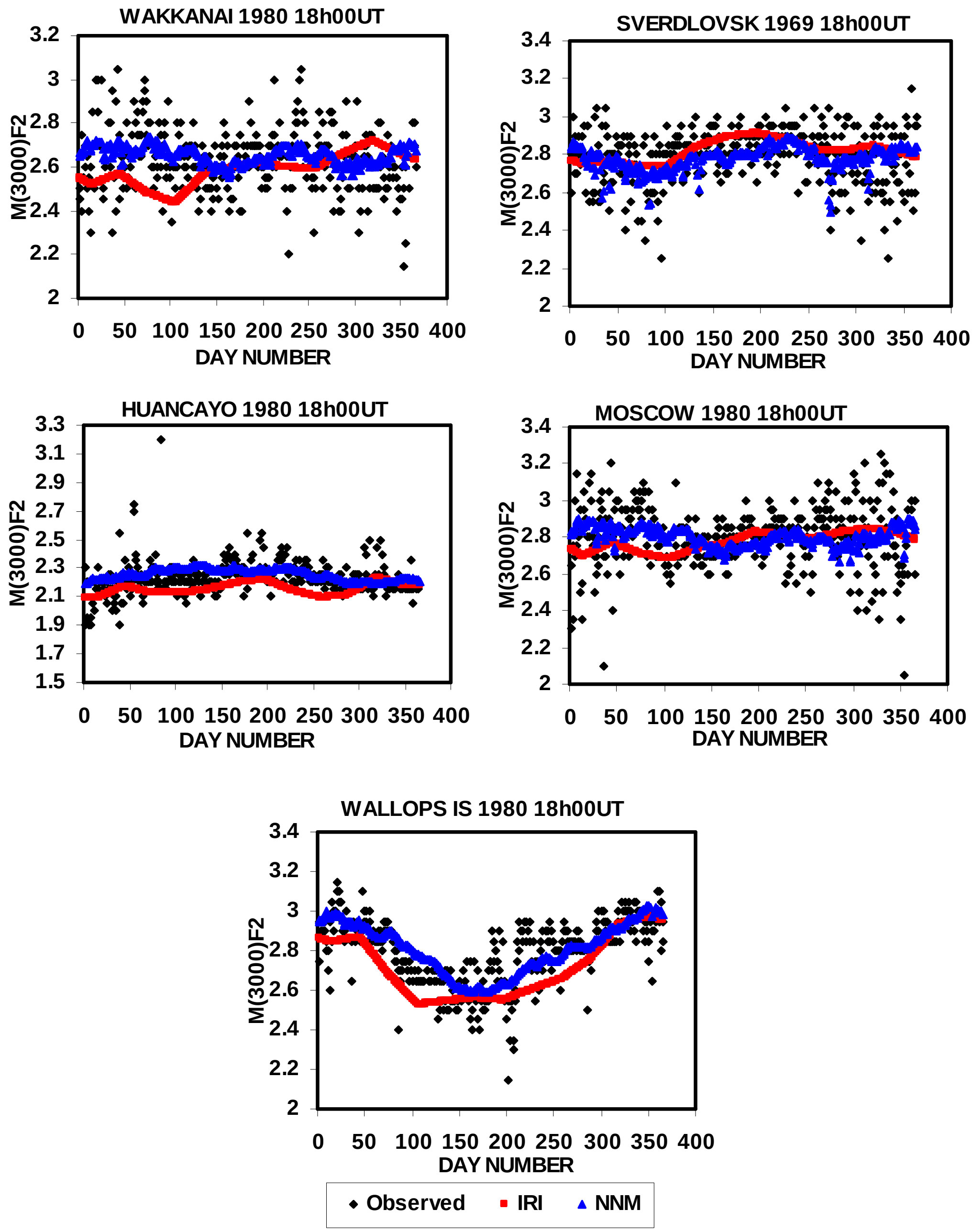

Figure 3-29d. Comparisons of the seasonal variation of measured M(3000)F2 (Observed) with the NNM model and the IRI model predictions during a year of high solar activity for Wakkanai, Sverdlovsk, Huancayo, Moscow and Wallops Is stations at 18h00UT.

The predictive ability of the NNM model temporally beyond the training period has also been verified with measured M(3000)F2 data from 11 ionospheric stations (Tables 10a and 10b). Among these 11 stations, data from one of them (Jicamarca 11.95 ^{o}S, 284.14 ^{o}E) was not included in the training vectors because of a lack of sufficient data within the training period (1964 to 1986). A test like this is necessary since the model is intended for long-term predictions. As mentioned earlier the choice of these stations is based on the availability of data since it is difficult to get data from the same year for all stations. Because of this, different years for which data were available have been used for each station. Efforts have been made to get data around solar minimum activity (1987 and 1988) and around solar maximum activity (1991, 1992, 1999, 2001 and 2002) as the case may be for each of the verification stations.

Tables 10a and 10b show the error differences between measured and predicted values of M(3000)F2 by the NNM model and the IRI model for low and high solar activity periods respectively. The results obtained show that the NNM model can be successfully used for long-term predictions. There are a few stations (Wallops, Jicamarca and Argentine Is (Table 10a) and Uppsala, Vanimo, La Reunion and Mundaring (Table 10b)) where on average the error margin between the two models is very small when considering percentage errors. On the other hand, the NNM model is an improvement on the IRI model on average by a margin of the order of 10 – 20%. This can be clearly observed in Figures 3-30 and 3-31 where bar graphs have been used to illustrate the error differences.

Table 10a. RMS prediction errors (MHz) in M(3000)F2 at selected verification stations by the NNM model and the IRI model around high solar activity outside the training period of the NNM model.

S/N	Station name	LAT °N	LONG °E	RMSE (MHz)		% Error difference between IRI and NNM	Period
				IRI	NNM		
1	Magadan	60.0	151.0	0.195	0.181	7.179	1991
2	Uppsala	59.8	17.6	0.176	0.165	6.250	1999
3	Moscow	55.5	37.3	0.255	0.230	9.804	1992
4	Boulder	40.0	254.7	0.196	0.154	21.429	2001
5	Boulder	40.0	254.7	0.173	0.150	13.295	1991
6	Wallops Is	37.9	284.5	0.245	0.241	1.633	1991
7	Jicamara	-11.9	283.1	0.207	0.200	3.382	2002
8	Mundaring	-32.0	116.3	0.173	0.164	5.202	1991
9	Grahamstown	-33.3	26.5	0.241	0.192	20.332	2001
10	Grahamstown	-33.3	26.5	0.215	0.175	18.605	1992
11	Macquarie	-54.5	159.0	0.174	0.158	9.195	1992
12	Agentine Is	-65.2	295.7	0.315	0.310	1.587	1992
	RMSE average			**0.214**	**0.193**	**9.552**	

Table 10b RMS prediction errors (MHz) in M(3000)F2 at selected verification stations by the NNM model and the IRI model around low solar activity outside the training period of the NNM model.

S/N	Station name	LAT °N	LONG °E	RMSE (MHz)		% Error difference between IRI and NNM	Period
				IRI	NNM		
1	Magadan	60.0	151.0	0.211	0.167	20.853	1987
2	Uppsala	59.8	17.6	0.191	0.185	3.141	1997
3	Moscow	55.5	37.3	0.158	0.145	8.228	1987
4	Boulder	40.0	254.7	0.188	0.163	13.298	1987
5	Wallops Is	37.9	284.5	0.186	0.176	5.376	1987
6	Vanimo	-2.7	141.3	0.220	0.218	0.909	1987
7	La Reunion	-21.1	55.9	0.183	0.177	3.279	1987
8	Mundaring	-32.0	116.3	0.175	0.174	0.571	1987
9	Grahamstown	-33.3	26.5	0.270	0.237	12.222	1988
10	Macquarie	-54.5	159.0	0.176	0.165	6.250	1987
11	Agentine Is	-65.2	295.7	0.244	0.226	7.377	1987
	RMSE average			**0.200**	**0.185**	**7.675**	

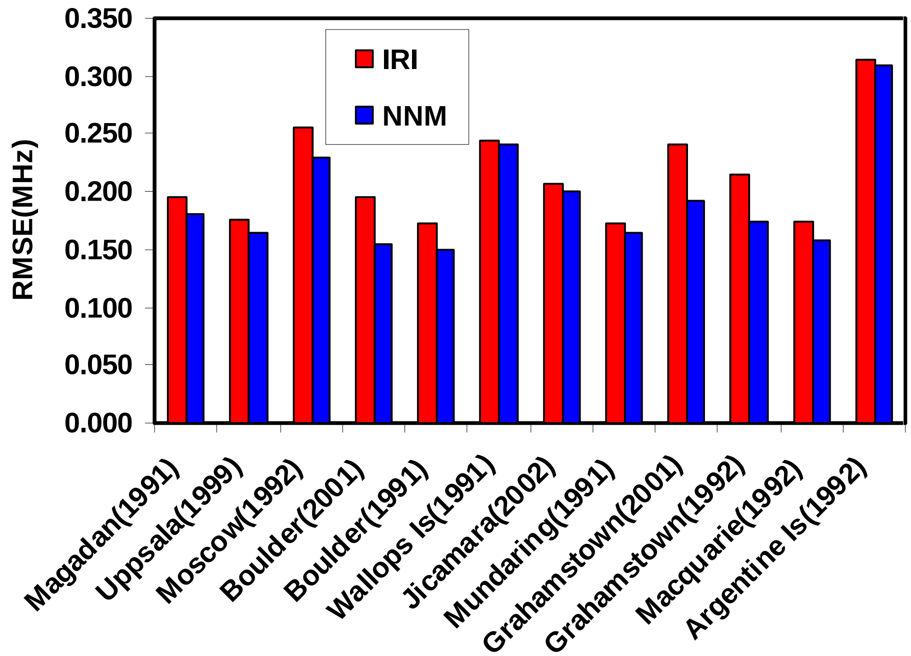

Figure 3-30a. Bar graph illustration of RMSE differences between measured M(3000)F2 and predictions by NNM model and the IRI model for all daily hourly values of M(3000)F2 for each station for the year indicated around high solar activity.

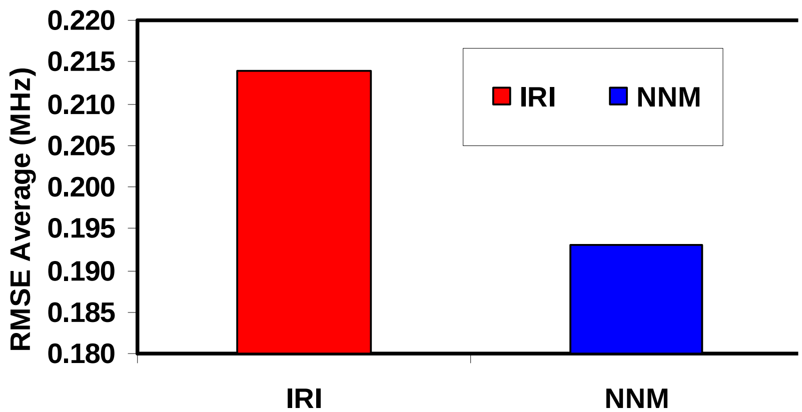

Figure 3-30b. Comparisons of RMSE average between NNM model and the IRI model using bar graph illustration (from Table 10a).

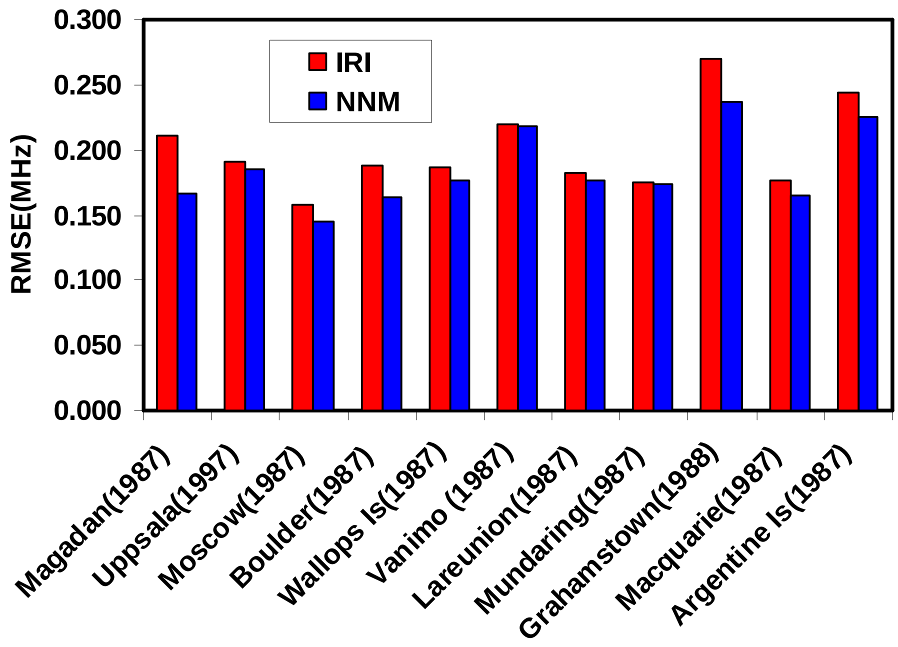

Figure 3-31a. Bar graph illustration of RMSE differences between measured M(3000)F2 and predictions by NNM model and the IRI model for all daily hourly values of M(3000)F2 for each station for the year indicated around low solar activity.

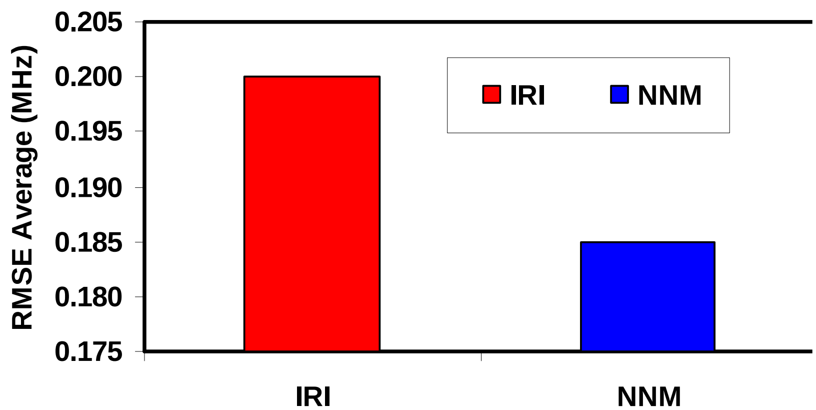

Figure 3-31b. Comparisons of RMSE average between NNM model and the IRI model using bar graph illustration (from Table 10b).

Again, as in the case of the foF2 NN2 model, the relative performance of the NNM model over the IRI model was further verified on the observed data (outside the training period) from the ionospheric stations listed in Tables 10a and 10b during high and low solar activity respectively using the relative error equations

$$eIRI = \frac{\left|M(3000)F2_{obs} - M(3000)F2_{IRI}\right|}{M(3000)F2_{obs}} \qquad 3.19$$

$$eNNM = \frac{\left|M(3000)F2_{obs} - M(3000)F2_{NNM}\right|}{M(3000)F2_{obs}} \qquad 3.20$$

The relative errors, eIRI and eNNM, in the IRI and NNM predicted values were calculated. The cases for which (eIRI-eNNM) is positive and negative are presented in Figures 3-32a and 3-32c for high and low solar activity respectively. A positive value (i.e. eIRI-eNNM > 0) indicates that the NNM model is better than the IRI model, while a negative value indicates the reverse case. From Figures 3-32a and 3-32c, with the exception of Argentine Is (1992), the number of cases for which (eIRI-eNNM) > 0 is always greater than the number of cases for which (eIRI-eNNM) < 0. In order to eliminate those cases for which the performance of the two models differed only marginally, Figures 3-32b and 3-32d have been used to illustrate the relative performance of the NNM model over the IRI model for those cases for which the absolute value of (eIRI-eNNM) exceeds 0.05. It is evident, particularly during high solar activity (Figure 3-32b), that the performance of the NNM model is relatively better when compared with that of the IRI model. During low solar activity (Figure 3-32d), the performance of the NNM model is still relatively better but the number of cases may be too small to be statistically significant except for Magadan, Boulder and Argentine Is with a clear margin. The overall performance indicates the significance of the neural network technique for global predictions of M(3000)F2.

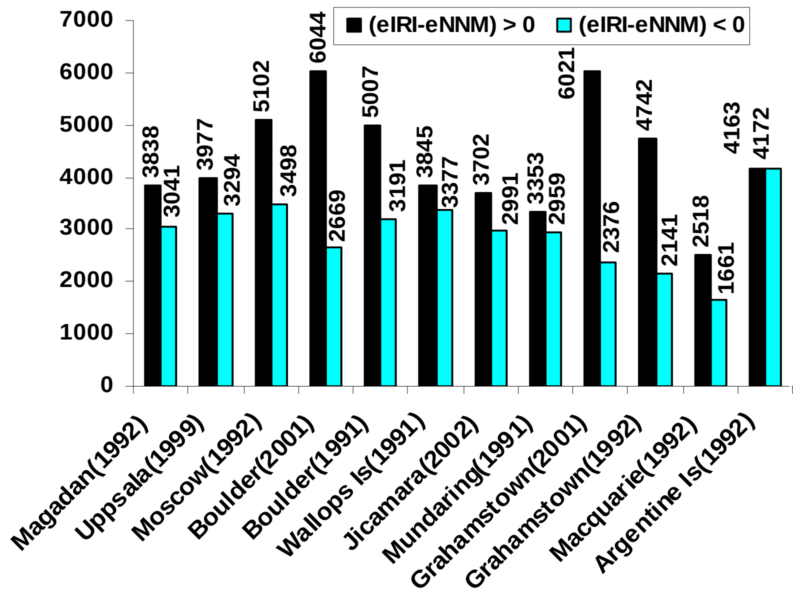

Figure 3-32a. Bar graph illustration for the cases where the NNM model performs better than the IRI model (black) and where the NNM model performs worse than the IRI model (blue) for all the available hourly values of M(3000)F2 around solar maximum for each station for the year indicated.

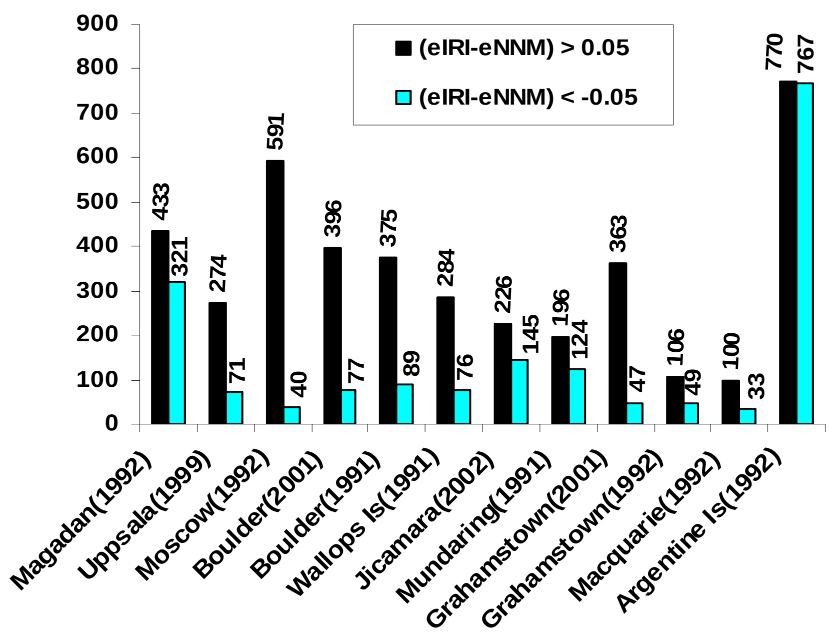

Figure 3-32b. Bar graph illustration for only those cases where the difference in the relative errors eIRI and eNNM is greater than 0.05 during high solar activity.

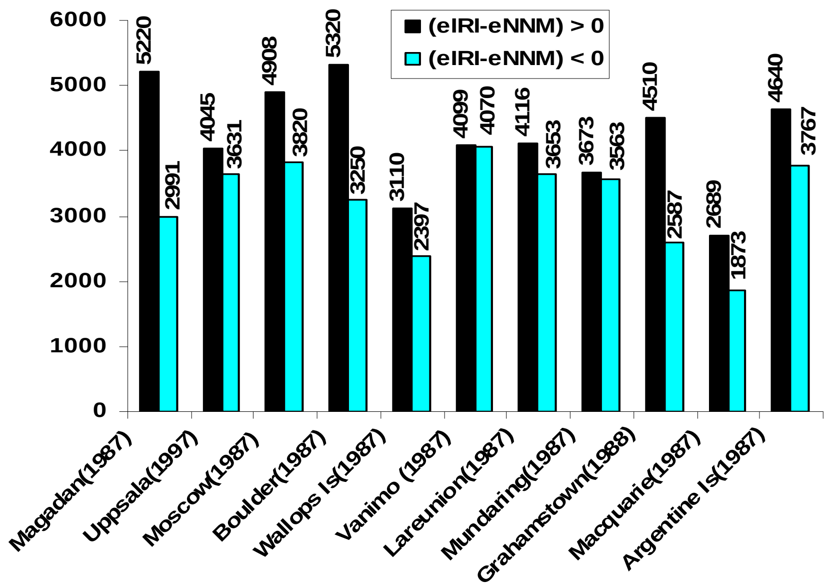

Figure 3-32c. Bar graph illustration for the cases where the NNM model performs better than the IRI model (black) and where the NNM model performs worse than the IRI model (blue) for all the available hourly values of M(3000)F2 around solar minimum for each station for the year indicated.

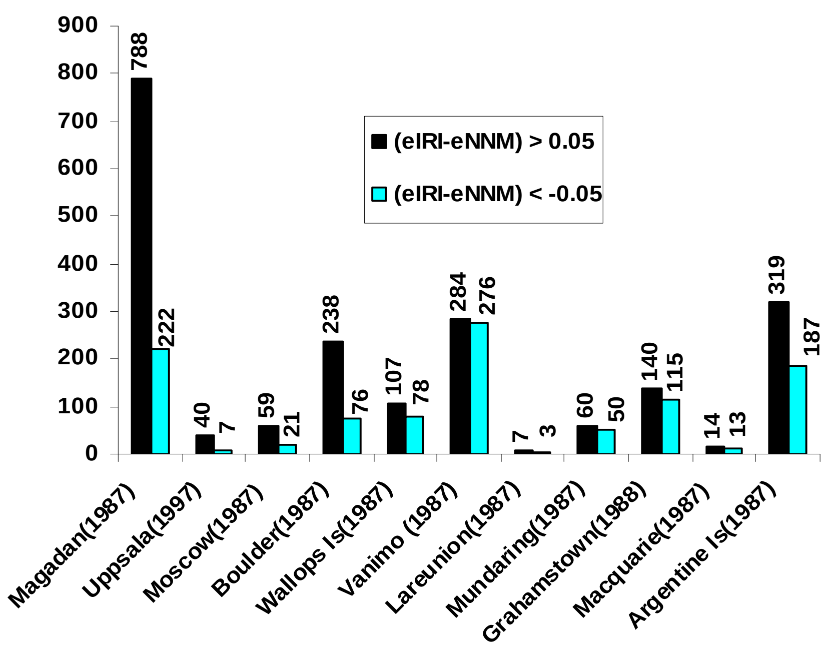

Figure 3-32d. Bar graph illustration for only those cases where the difference in the relative errors eIRI and eNNM is greater than 0.05 during low solar activity.

Figures 3-33a-c and 3-34a-c show examples of comparisons between the NNM model and the IRI model M(3000)F2 predictions and observed values for a few selected verification stations from outside the training period. A close observation of these graphs shows that the two models successfully predict the general diurnal structure of M(3000)F2 behaviour. Again, this is an indication that the NNM model predictive ability is not limited to the training period, and therefore, is capable of long-term predictions on a global scale. As in the case of the NN2 model for foF2, such differences that do exist are short term variations in M(3000)F2 for which neither the NNM nor the IRI models are designed to predict.

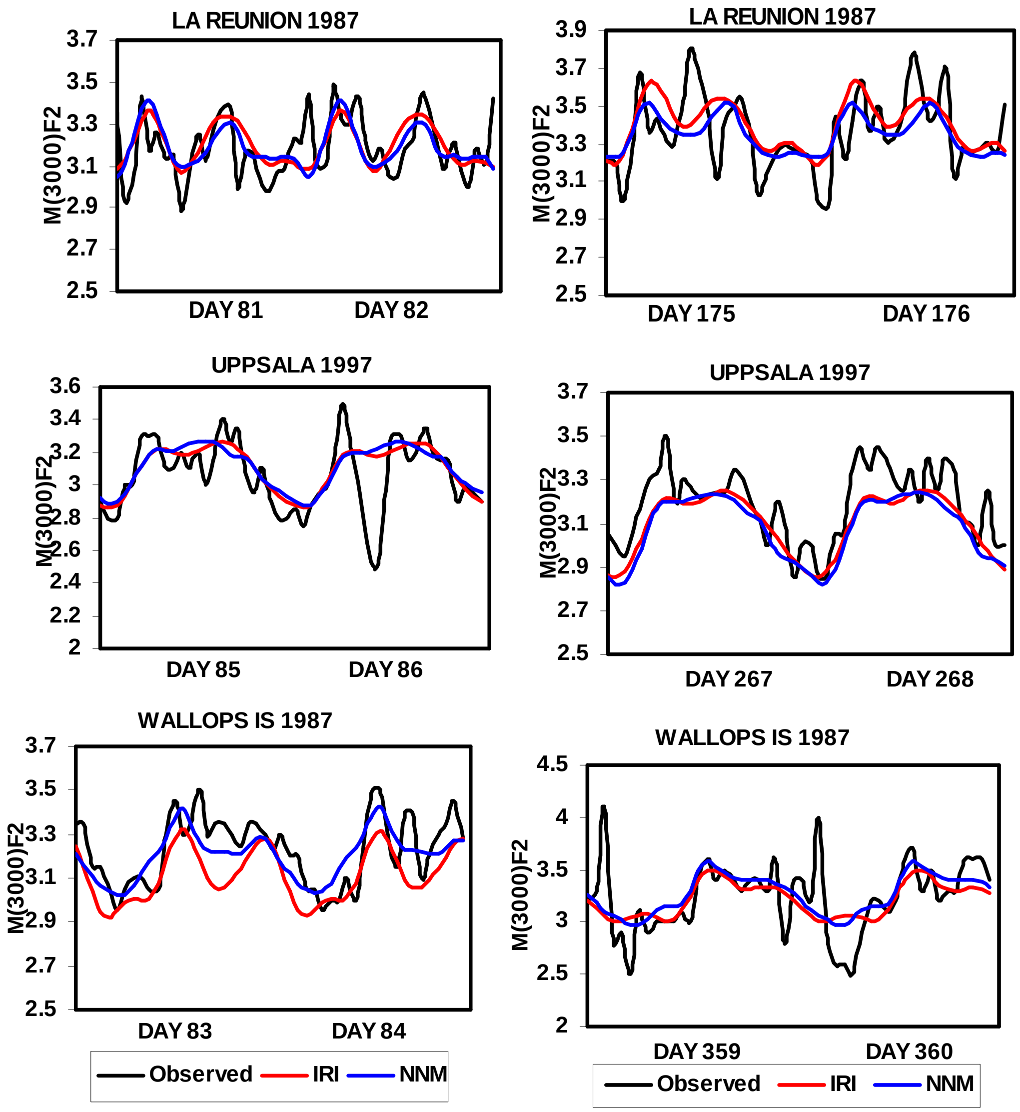

Figure 3-33a. Comparisons of the diurnal variation of M(3000)F2 predicted values by the NNM model and the IRI model with observed values for 2 days starting at 00h00UT on the first day of the days indicated for a few selected stations around low solar activity.

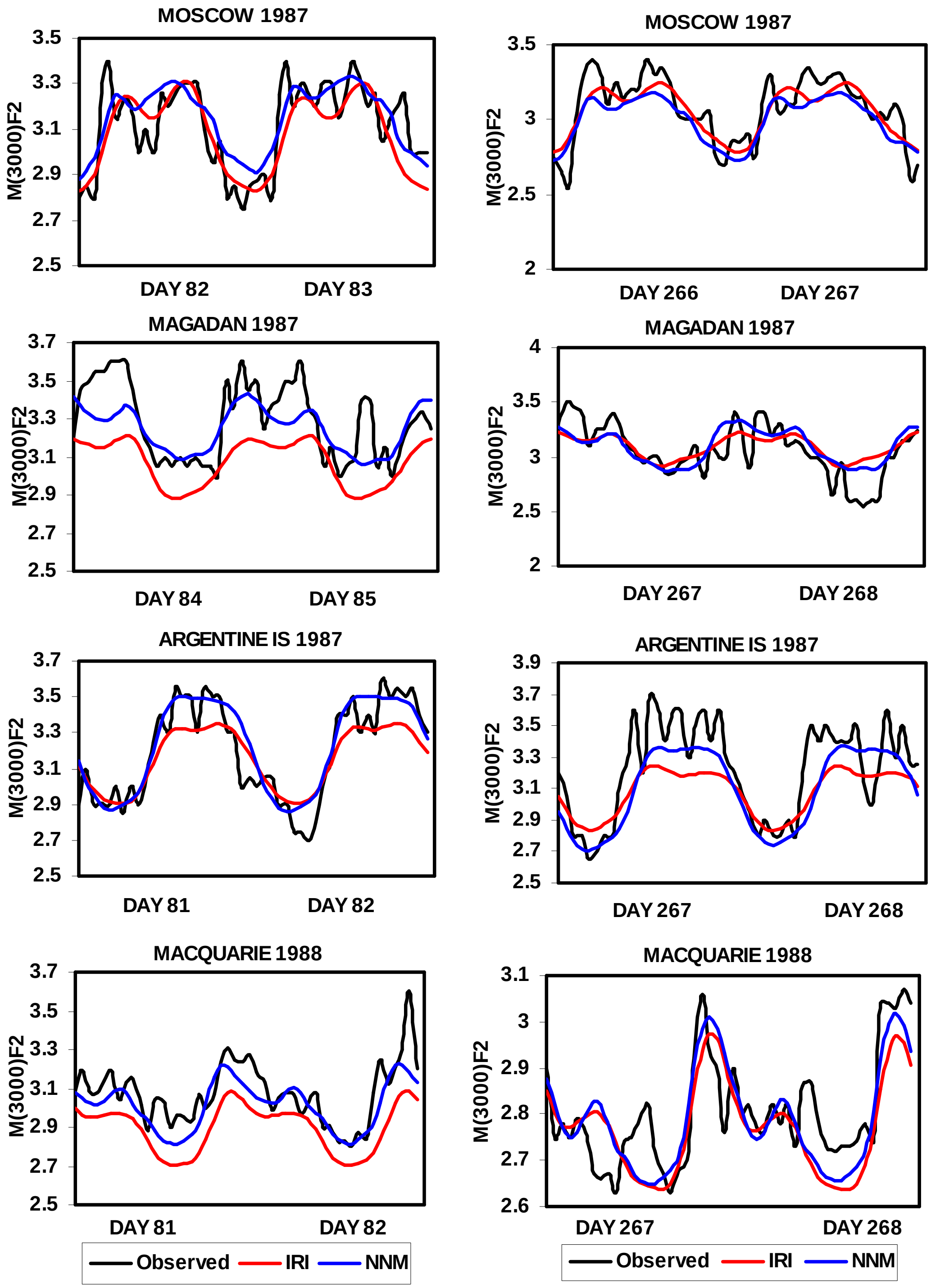

Figure 3-33b. Comparisons of the diurnal variation of M(3000)F2 predicted values by the NNM model and the IRI model with observed values for 2 days starting at 00h00UT on the first day of the days indicated for a few selected stations around low solar activity.

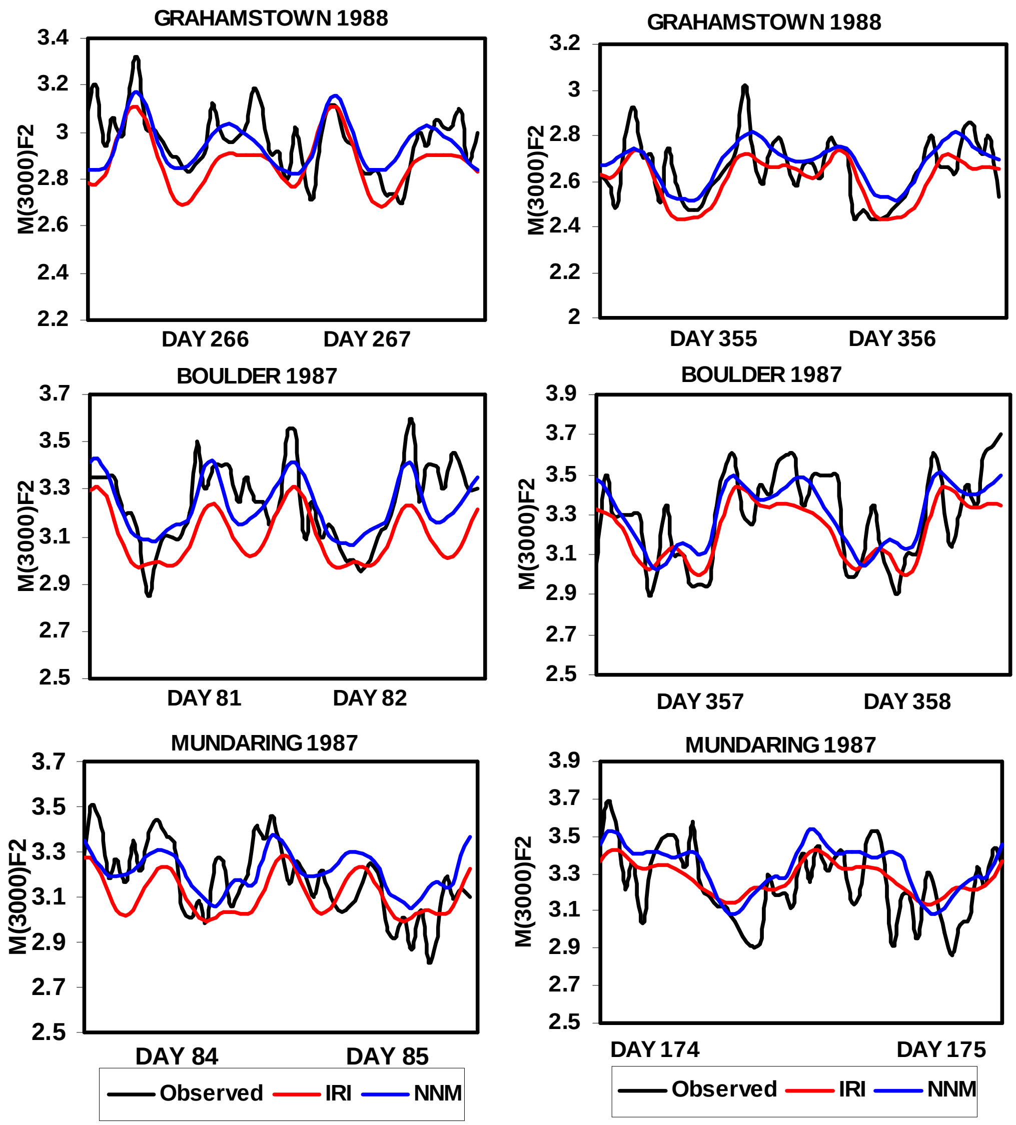

Figure 3-33c. Comparisons of the diurnal variation of M(3000)F2 predicted values by the NNM model and the IRI model with observed values for 2 days starting at 00h00UT on the first day of the days indicated for a few selected stations around low solar activity.

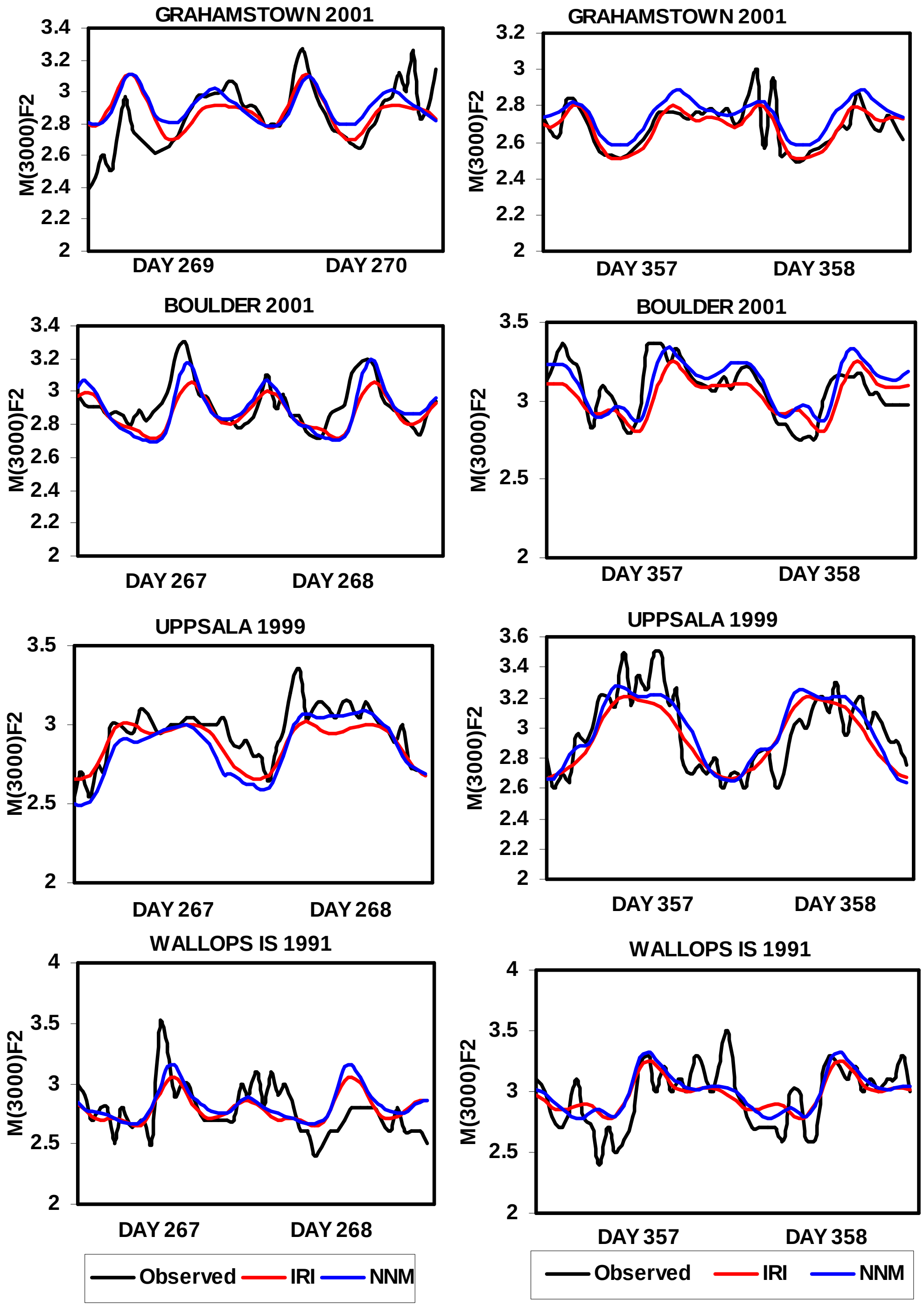

Figure 3-34a. Comparisons of the diurnal variation of M(3000)F2 predicted values by the NNM model and the IRI model with observed values for 2 days starting at 00h00UT on the first day of the days indicated for a few selected stations around high solar activity.

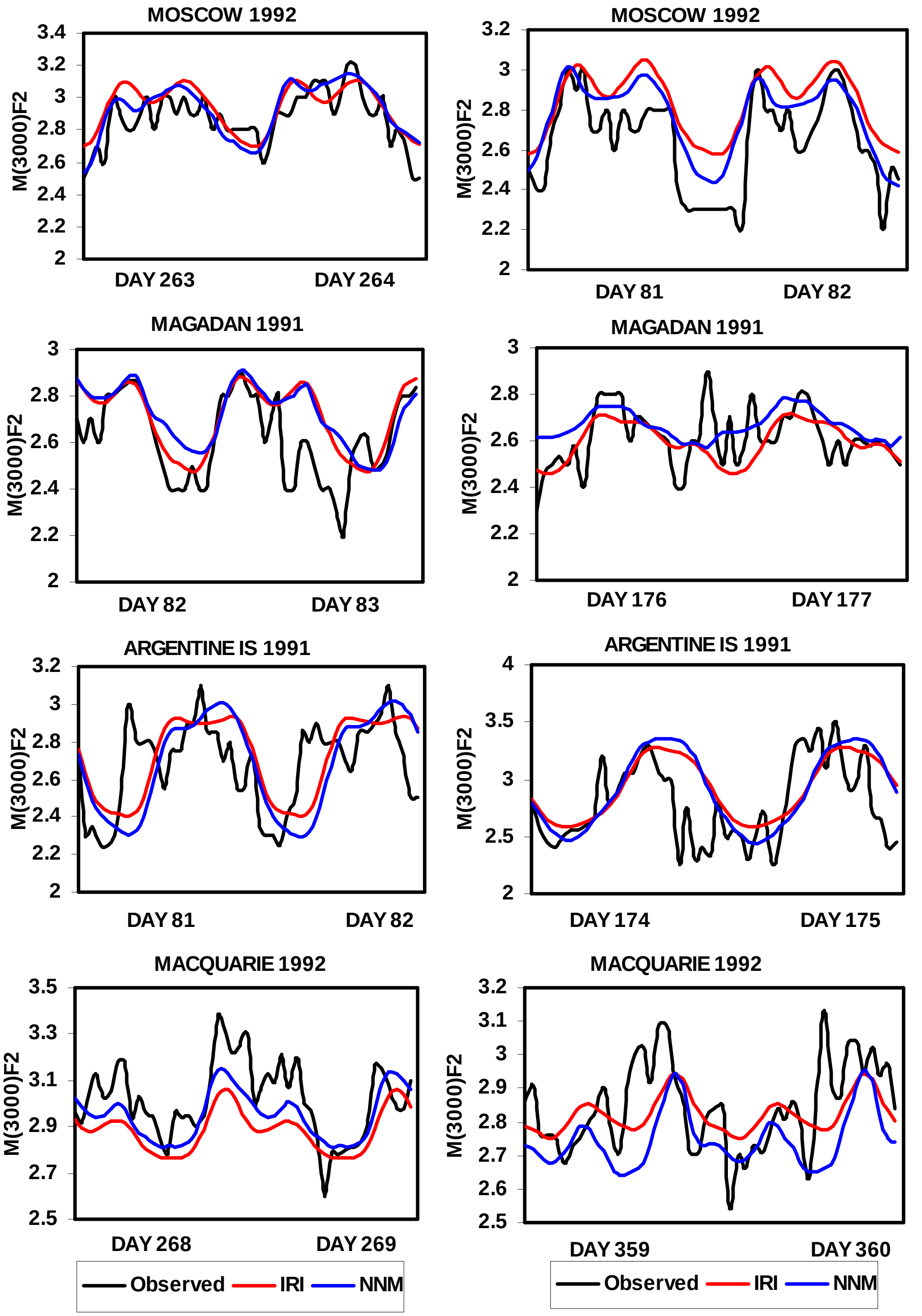

Figure 3-34b. Comparisons of the diurnal variation of M(3000)F2 predicted values by the NNM model and the IRI model with observed values for 2 days starting at 00h00UT on the first day of the days indicated for a few selected stations around high solar activity.

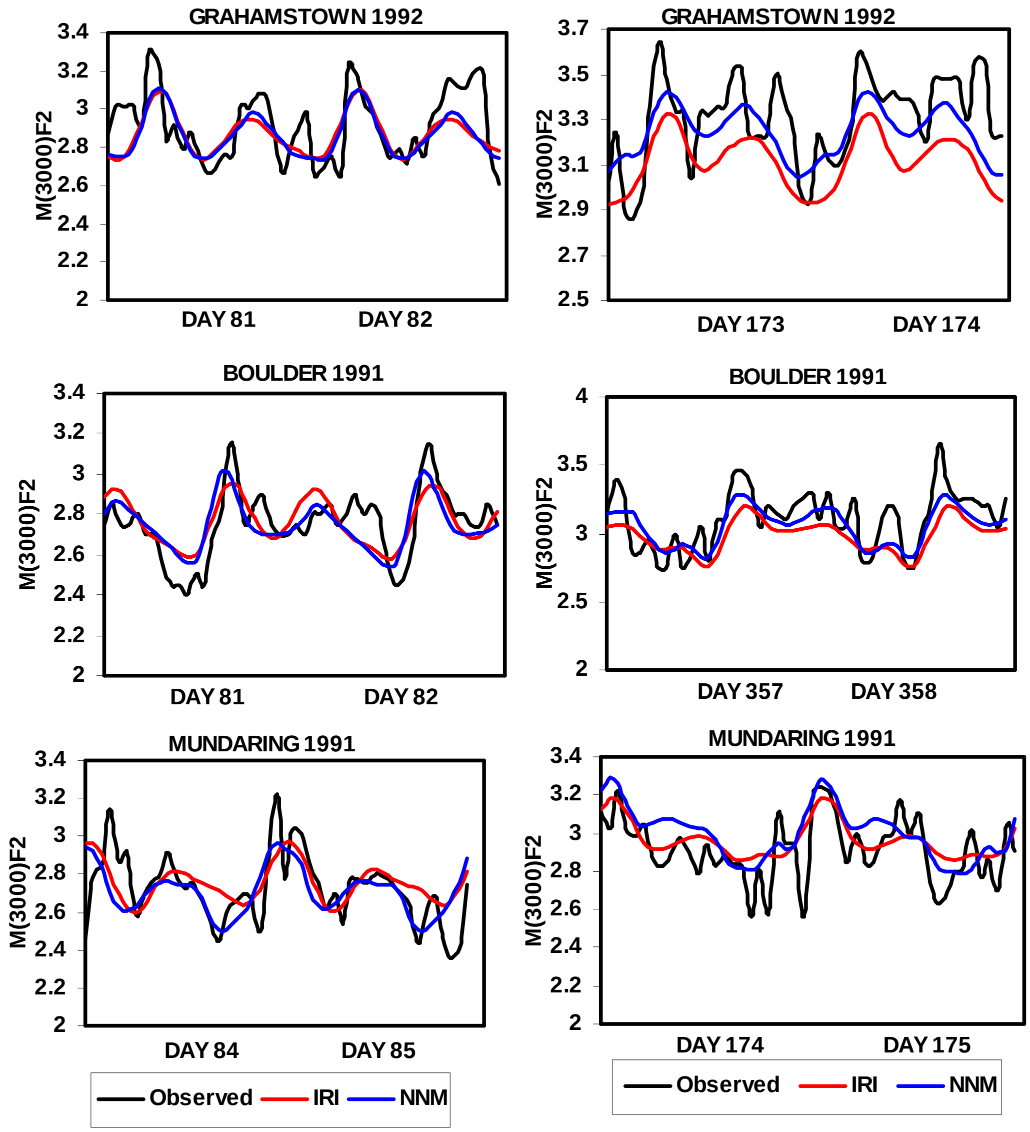

Figure 3-34c. Comparisons of the diurnal variation of M(3000)F2 predicted values by the NNM model and the IRI model with observed values for 2 days starting at 00h00UT on the first day of the days indicated for a few selected stations around high solar activity.

A comparison of the seasonal variation of M(3000)F2 NNM model predictions at 12h00UT and 18h00UT with the IRI model predictions and observed values around periods of low and high solar activity are shown in Figures 3-35 (a and b) and 3-36 (a and b) respectively. These figures further exemplify the predictive ability of the NNM model for long-term prediction purposes, since the years for which the model was tested do not fall within the training period. It can be observed that the predictions from the two models closely follow the seasonal behaviour of M(3000)F2 for these selected stations. There are a few cases, for instance Argentine Is 1987 at 18h00UT (Figure 3-35b), Argentine Is 1992 at 12h00UT, Boulder 2001 at 12h00UT, Grahamstown 1992 at 18h00UT (Figure 3-36b), where the models underestimate M(3000)F2 values and Moscow 1992 at 12h00UT (Figure 3-36a) where the models overestimate.

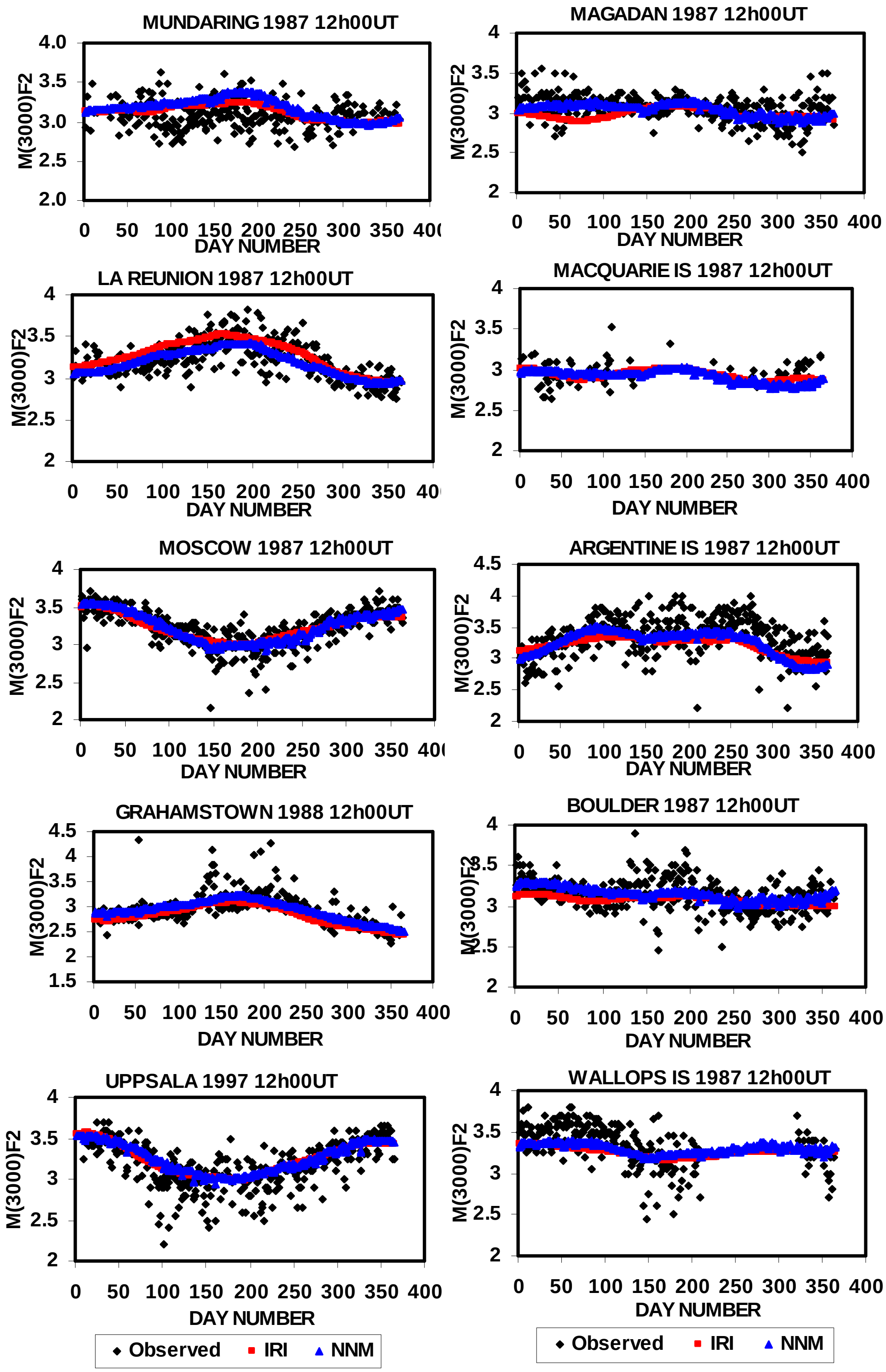

Figure 3-35a. Comparisons of the seasonal variation of measured M(3000)F2 (Observed) with the NNM model and the IRI model predictions during low solar activity at selected stations for 12h00UT.

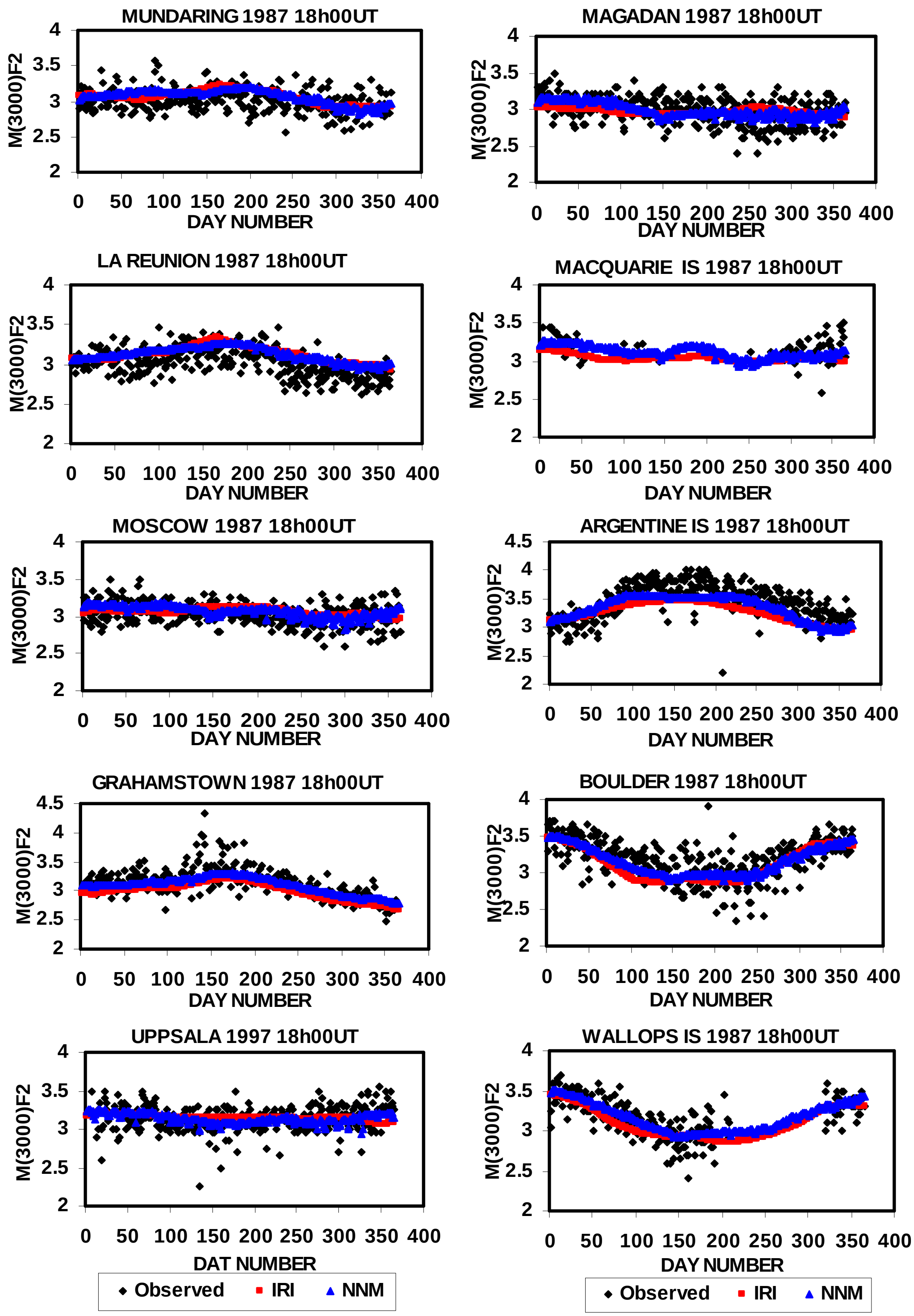

Figure 3-35b. Comparisons of the seasonal variation of measured M(3000)F2 (Observed) with the NNM model and the IRI model predictions during low solar activity at selected stations for 18h00UT.

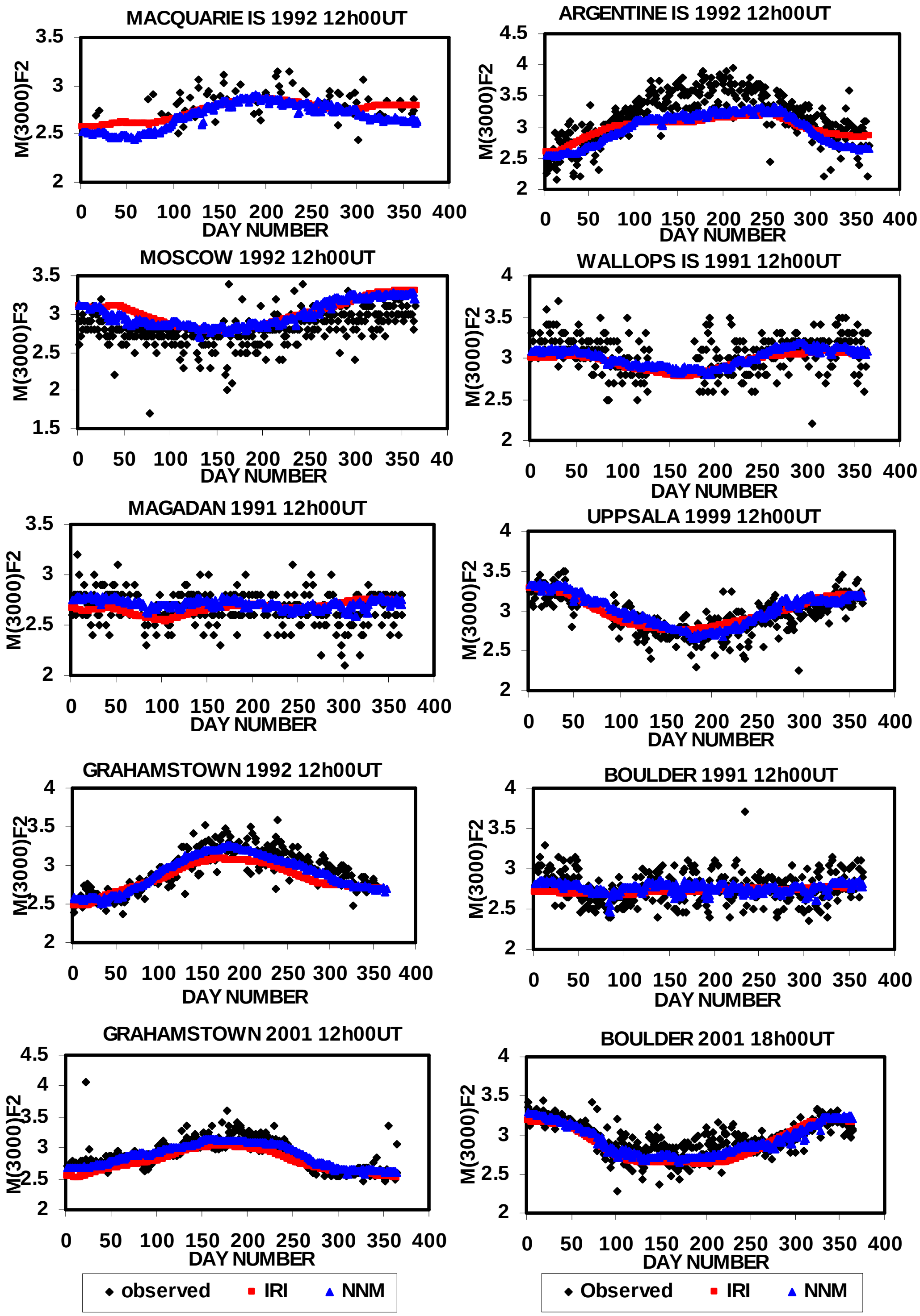

Figure 3-36a. Comparisons of the seasonal variation of measured M(3000)F2 (Observed) with the NNM model and the IRI model predictions during high solar activity at selected stations for 12h00UT.

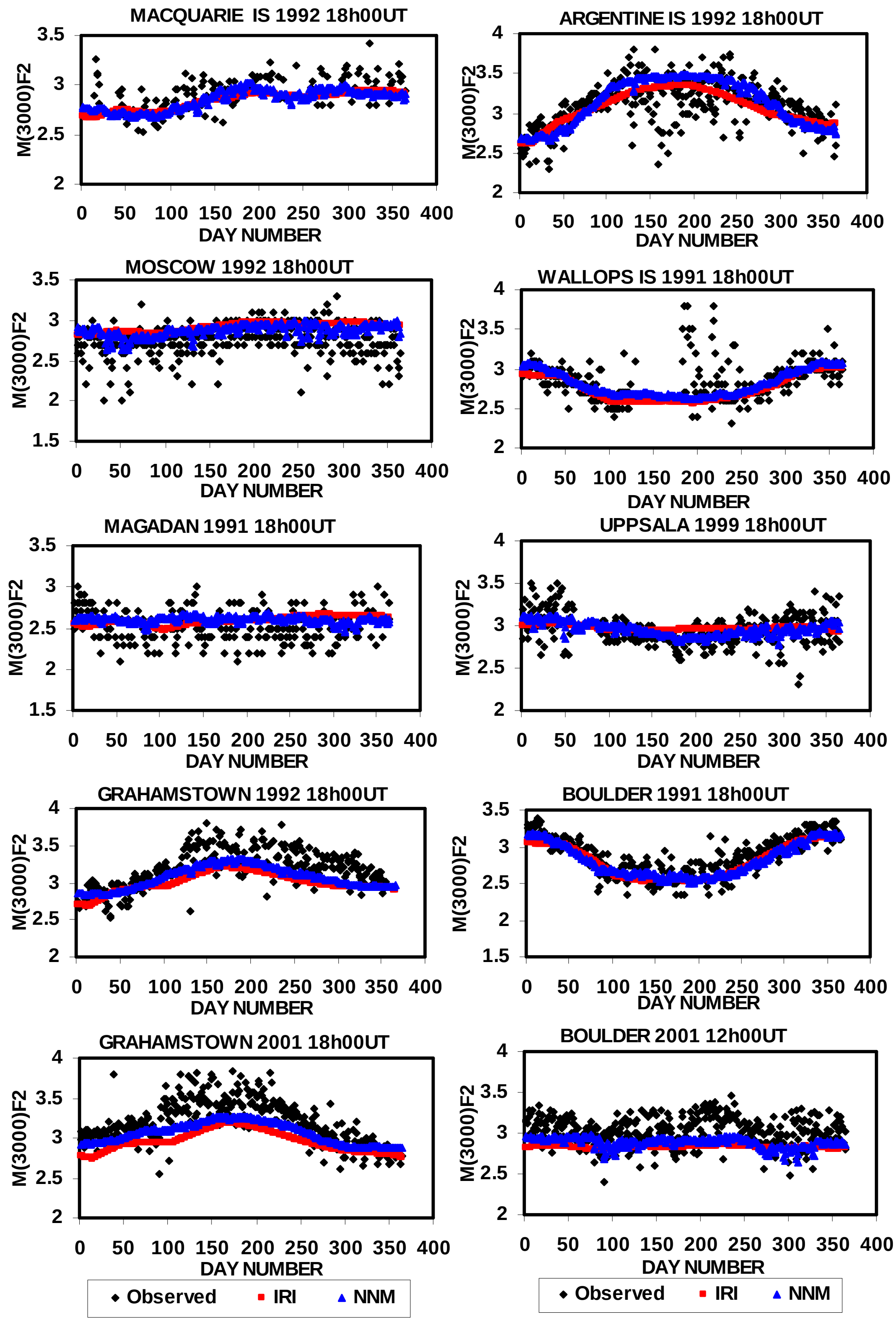

Figure 3-36b. Comparisons of the seasonal variation of measured M(3000)F2 (Observed) with the NNM model and the IRI model predictions during high solar activity at selected stations for 18h00UT.

3.4.6 Conclusion

Comparisons of the results obtained from this section with the IRI model predictions and the observed values of M(3000)F2 also reveal that NNM is a successful s*patial-temporal* model that can be used to predict M(3000)F2 on a global scale with minimal error. It is evident that the NN has been able to predict the normal trend of M(3000)F2 and that the NNM model can be equally used for long-term predictions. The next two sections are based on the applications of NNs for global short-term and real time forecasting of foF2.

3.5 Short-term foF2 NN

3.5.1 Introduction

This section details the development of a global empirical model for short-term forecasting of the daily hourly values of the ionospheric F2 region critical frequency (foF2) at any target geographical location up to five hours in advance. Various groups have carried out studies on the use of neural networks (NNs) to investigate the short-term variation of this ionospheric parameter. For example, several models such as one hour ahead prediction of foF2 (Altinay et. al., 1997; Cander and Lamming, 1997; Kumluca et. al., 1999; Wintoft and Cander, 1999) and *temporal* and *spatial* forecasting of foF2 values up to 24 hours in advance (Wintoft and Cander, 2000; Tulunay et. al., 2000; Wintoft, 2000) have been developed using the NN techniques. These successful applications of NNs to single station forecasting of foF2, together with my own successful application of NNs to global modeling of foF2 and M(3000)F2 ionospheric parameters (discussed in the previous sections of this chapter), have inspired me to further apply the NN techniques to global short-term predictions of foF2. The role of forecasting foF2 one hour ahead in communication and guidance applications has been shown to be of great importance (Altinay et. al., 1997; Kumluca et. al., 1999). McKinnell and Poole (2000), Wintoft and Cander (2000) and Kumluca et. al. (1999) have demonstrated that foF2 is best predicted by using past observations of foF2 itself. My approach is unlike single station models in that the model presented here can be employed to forecast foF2 up to five hours ahead at any geographic point on the globe knowing geographic coordinates, magnetic declination and inclination, and recent past observations of foF2 at that geographic point. In other words, it is a short term, global spatio-temporal model.

3.5.2 Database

As in the case of the previous models (foF2 and M(3000)F2 models) discussed earlier, the data used for training the NNs to forecast foF2 values five hours in advance are the hourly values of the F2 region critical frequency, depending on the availability, from the worldwide ionospheric stations spanning the period 1964 to 1986. The problem of missing data points is more critical here since the model requires past observations of foF2 itself. Because of this, I could not use as many stations as I used in the development of the foF2 model. As a result, I have used data from 50 ionosonde stations where sufficient data were available for training and verification of the performance of the NNs. These stations are listed in Table 11. Letters A and B in Table 11 represent the training and verification stations respectively. Figure 3-37 is a map illustrating the geographical locations of the training and verification stations.

Table 11. Ionosonde stations used for training and verification of the short-term foF2 NNs.

S/N	**Station Name**	**Latitude ^oN**	**Longitude ^oE**	**Training stations**	**Verification stations**
1	Lycksele	64.6	18.7	A	
2	Narssarssuaq	61.2	314.6	A	
3	Uppsala	59.8	17.6	A	
4	Tomsk	56.5	84.9		B
5	Moscow	55.5	37.3	A	
6	Kaliningrad	54.7	20.6	A	
7	Juliusruh/Rugen	54.6	13.4	A	
8	Goose Bay	53.3	299.2	A	
9	Irkutsk	52.4	104.0	A	
10	Dourbes	50.1	4.6	A	
11	Winnipeg	49.8	256.6	A	
12	Freiburg	48.1	7.6	A	
13	St Johns	47.6	307.3	A	
14	Ottawa	45.4	284.1	A	
15	Wakkanai	45.4	141.7	A	
16	Rome	41.8	12.5	A	
17	Boulder	40.0	254.7		B
18	Akita	39.7	140.1	A	
19	Ashkhabad	37.9	58.3		B
20	Kokubunji	35.7	139.5	A	
21	Point Arguello	34.6	239.4	A	
22	Yamagawa	31.2	130.6		B
23	Grand Bahama	26.6	281.8	A	
24	Okinawa	26.3	127.8	A	
25	Dakar	14.8	341.6	A	
26	Djibouti	11.5	42.8	A	
27	Bogota	4.5	285.8	A	
28	Singapore	1.3	103.8	A	
29	Vanimo	-2.7	141.3		B
30	Huancayo	-12.0	284.7		B
31	Tahiti	-17.7	210.7	A	
32	La Reunion	-21.1	55.9	A	
33	Raratonga	-21.2	200.2	A	
34	Brisbane	-27.5	152.9	A	
35	Norfolk Is	-29.0	169.0	A	
36	Mundaring	-32.0	116.3	A	
37	Grahamstown	-33.3	26.5		B
38	Salisbury	-34.7	138.6	A	
39	Concepcion	-36.6	287.0	A	
40	Hobart	-42.9	147.2		B

Table 11. Continues

S/N	Station Name	Latitude °N	Longitude °E	Training stations	Verification stations
41	Christchurch	-43.3	172.8	A	
42	Kerquelen	-49.4	70.3	A	
43	Port Stanley	51.7	302.2		B
44	Campbell Is	-52.5	169.2	A	
45	South Georgia	-54.3	323.5	A	
46	Macquarie Is	-54.5	159.0	A	
47	Argentine Is	-65.2	295.7		B
48	Casey Base	-66.3	110.5	A	
49	Halley Bay	-75.5	333.4	A	
50	Scott Base	-77.9	166.8	A	

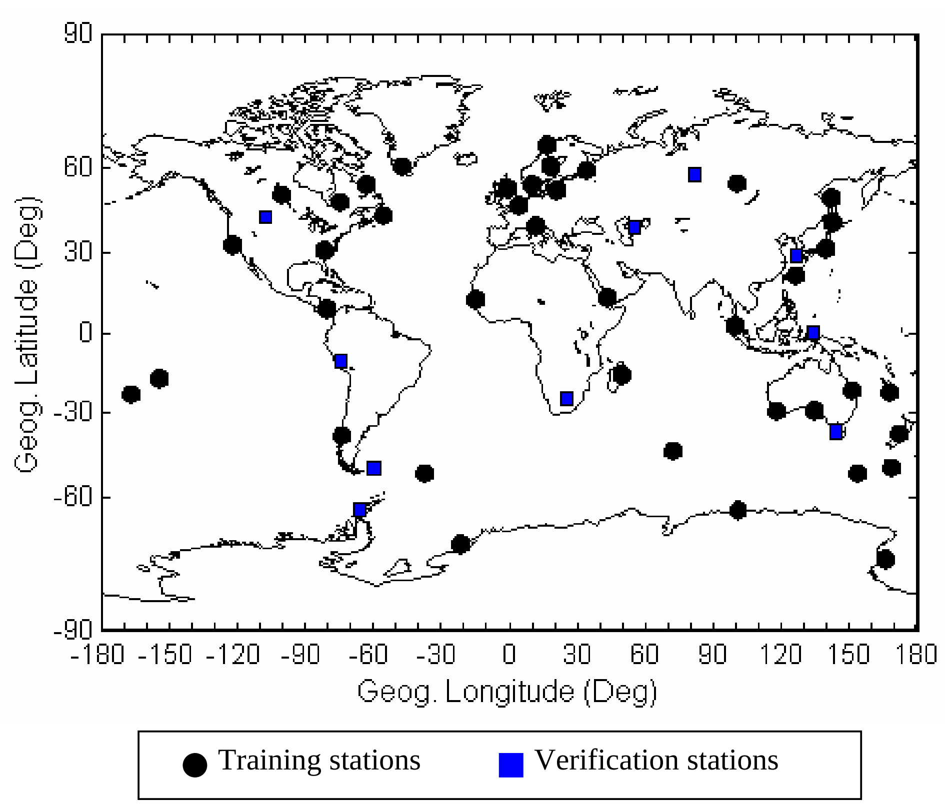

Figure 3-37. Map of geographical coordinates of training and verification stations for the short-term foF2 NN (initial attempt NNSA).

3.5.3 The inputs

For the purpose of this short-term empirical foF2 model there are two separate sets of input parameters to the NN. The first set is made up of the same set of inputs that were used for the foF2 and M(3000)F2 models discussed earlier in this chapter (section 3.2.3), since foF2 is still the output. These inputs are the Universal Time (UT), day number of the year (DN), a 2-month running mean of the daily sunspot number (R2), a 2-day running mean of the 3-hour planetary magnetic a_p index (A16), solar zenith angle (CHI), geographic latitude (θ), angle of magnetic inclination (I), angle of magnetic declination (D) and angle of the meridian relative to subsolar point (M). The second set of input parameters to the NN is related to the target location itself. These are the 4 recent past observations of foF2 values: F_{-3}, F_{-2}, F_{-1} and F_0, from the target stations which are listed in Table 11(A). F_0 corresponds to the foF2 value at the hour represented by the UT input. It should be made clear at this point that there is no restriction to the number of recent past observations of foF2 that could be used when training a NN, but in order not to make the inputs cumbersome, I have decided to use only the 4 recent past observations. Following McKinnell and Poole (2000), there is not much improvement to be gained by increasing this number beyond 4.

3.5.4 NN outputs

Since the primary objective is to develop a NN based model to forecast foF2 values up to five hours ahead at any geographic location globally, the outputs of the NN are F_{+1}, F_{+2}, F_{+3}, F_{+4} and F_{+5} representing the values of foF2 up to five hours ahead of F_0, foF2 at the hour UT. However, studies have shown that there is no restriction on the number of outputs when designing a NN of this type. This is evidenced by researchers who have developed NNs to forecast foF2 for a different number of hours in advance (Altinay et. al., 1997; Cander and Lamming, 1997; Kumluca et. al., 1999; Wintoft and Cander, 2000; Tulunay et. al., 2000, Wintoft, 2000; McKinnell and Poole, 2000; Tulunay et. al., 2000 to mention a few). The input and output parameters to the NN are as illustrated in the block diagram of figure 3-38.

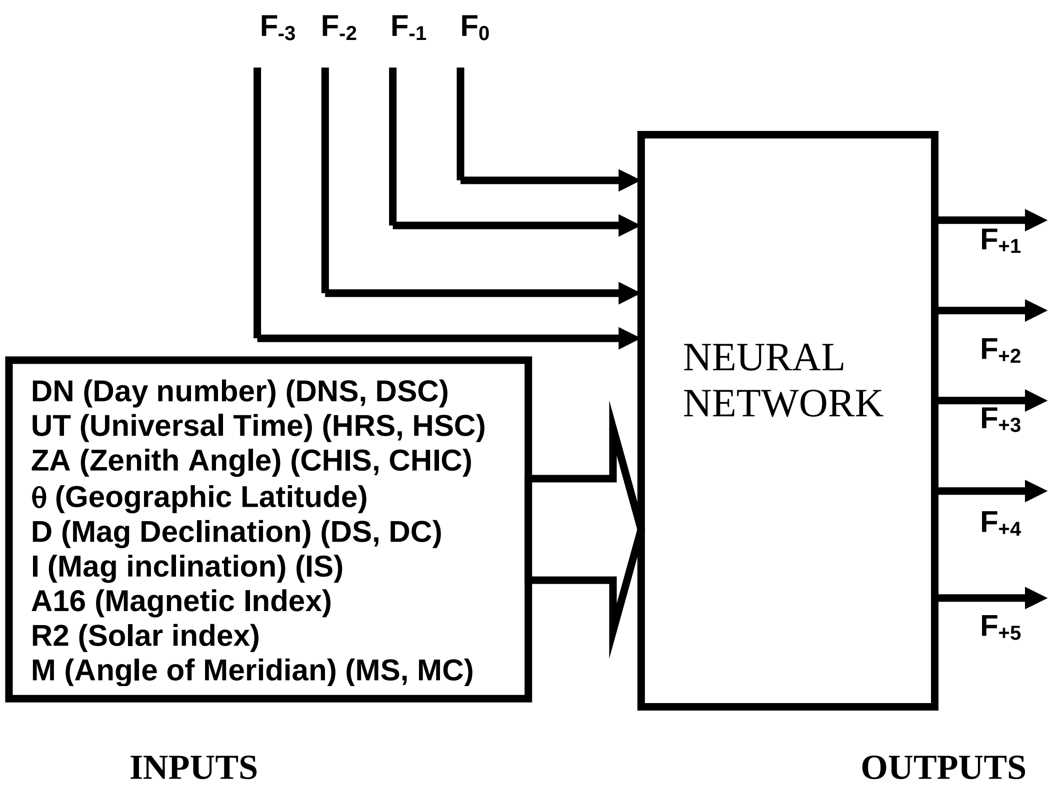

Figure 3-38. A block diagram of the inputs and outputs to the short-term foF2 NNs.

3.5.5 Neural network architecture

A standard fully connected feed-forward network with backpropagation is also employed for the short-term forecasting of foF2. The block diagram of the network architecture illustrating the inputs and outputs is as shown in Figure 3-38. The number of input and output units is determined by what is considered in sections 3.5.3 and 3.5.4 respectively. The NN has 18 input nodes with 5 output nodes as shown in figure 3-38. Since both the numbers of inputs and outputs to the NN in this case are different from the previous NNs (foF2 and M(3000)F2), it is required to determine the optimum NN architecture that will produce the minimum error for the forecasting of foF2 up to five hours in advance. To do this, I trained several different NNs with different architectures. Among the various NN architectures, the best configuration for this purpose based on the minimization of the RMSE difference between the target and the predicted values was found to be the one with three hidden layers with 20, 20 and 20 nodes respectively.

3.5.6 Training, testing and verification of the short-term foF2 NN

As in the case of the previous NN models, a preliminary investigation was carried out to determine how well a NN trained with the inputs described above could be employed for *temporal* and *spatial* short-term forecasting of foF2 on a global scale. To do this I trained an initial network (NNSA) with data from 40 ionosonde stations (stations represented by letter A in Table 11 and black circles in Figure 3-37). The performance of the NNSA model was verified with data from 10 stations (stations represented by letter B in blue squares Table 11 and blue squares in Figure 3-37) that were not included in the training of the NNSA network. After this preliminary attempt, which produced promising results, a second NN (NNSB) (the final short-term foF2 model), was trained with data from all the stations in Table 11 (a total of 50 stations). The difference between the two NNs is, therefore, in the number of training vectors. In addition to those stations used to verify the performance of the NNSA model, data from 7 other stations (see Table 12) were also used to verify the predictive ability of the NNSB model *temporally* and *spatially*. The choice of these stations is based on the availability of data. The first three stations in Table 12 (green squares in Figure 3-39) were included in the training process (already included in Table 11), while the other four stations (red squares in Figure 3-39) were not included in the training process because of a lack of sufficient data points within the training period (i.e. 1964 to 1986) for the purpose of short-term predictions. Again, because of the large volume of the data involved, which requires a lot of time for training a NN, only 10% of the total data randomly selected from all the available stations was used to train the NNs. The 10% was further randomly divided into training and testing data sets in the ratio 70% and 30% respectively. The training data set was used to train the network and the testing data set was used in the training process to check the generalization of the network. As mentioned earlier, the training and testing data sets are chosen from the year 1964 to 1986, which cover solar cycles 20 and 21. During training, the NN is presented with values of the 18 inputs corresponding to five output values F_{+1}, F_{+2}, F_{+3}, F_{+4} and F_{+5}. As the training is continued, the difference between the observed and predicted F_{+1}, F_{+2}, F_{+3}, F_{+4} and F_{+5} values is computed and the weights of the NN adjusted so as to minimize the difference. Training ceases when no further improvement in the difference is found. At this stage the NN can be used for the purpose for which it was trained.

Table 12. Additional stations used for verification of the final short-term foF2 NN model (NNSB)

S/N	Station name	Latitude °N	Longitude °E
1	Uppsala	59.8	17.6
2	Point Arguello	34.6	239.4
3	Mundaring	-32.0	116.3
4	Tortosa	40.0	0.3
5	Magadan	60.0	151.0
6	Canberra	-35.3	149.0
7	Maui	20.8	203.5

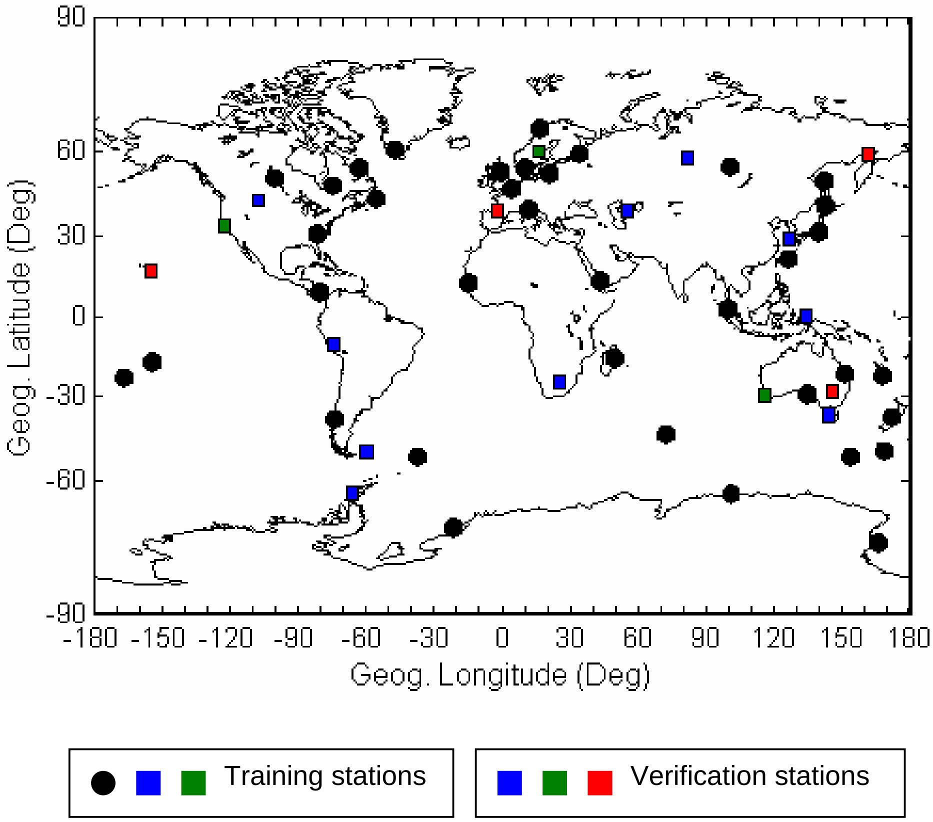

Figure 3-39. Map of geographical coordinates of training and verification stations used for the final short-term foF2 NN (NNSB).

3.5.7 Results and Discussion

After training the initial NN (NNSA) as described in section 3.5.6 above, observed data from ten ionospheric stations (Table 13, not included in the training of NNSA) were used to verify the performance of the NNSA using the RMSE equation 3.12 (section 3.2.6). This dataset is independent of the randomly chosen test set mentioned in section 3.5.6. This verification was necessary to test the hypothesis that a NN trained with the inputs described in section 3.5.4 could successfully model both *spatial* and *temporal* variations of the ionospheric parameter foF2 globally up to 5 hours in advance. These years (i.e. 1976 to 1986) were considered because most stations, with the exception of Ashkhabad (1964 to 1969) have sufficient data points for this period to allow inclusion in the training set. Again, the data covers all periods of calm and disturbed magnetic activity. In Table 13 the error differences between the observed and the NNSA predicted values were evaluated by taking the averages of the root mean square errors of all foF2 data points present during the period indicated for each station. Figures 3-40 (a to f) show examples of daily variations of observed and forecasted foF2 values up to 5 hours ahead for 3 consecutive days starting at 00h00UT on the first of the days for six ionospheric stations (Tomsk, 56.5 ^{o}N, 84.9 ^{o}E; Boulder, 40.0 ^{o}N, 254.7 ^{o}E; Vanimo, 2.7 ^{o}S, 141.3 ^{o}E, Argentine Is, -65.2 ^{o}N, 295.7 ^{o}E, Hobart, -42.9 ^{o}N, 147.2 ^{o}E, and Grahamstown, 33.3 ^{o}S, 26.5 ^{o}E). From the graphs of Figures 3-40(a to f), which show almost the same type of variation in time, and the RMS errors shown in Table 13, I was able to deduce that a NN trained with these aforementioned input parameters can be employed to forecast foF2 up to 5 hours ahead spatially.

One can observe in Figure 3-40 the expected deterioration in the predictive ability of the NN as the forecast increases from 1 to 5 hours. This is confirmed by the increase in RMSE with increasing forecast period in Table 13. A summary of training and verification stations for NNSB model is shown in Table 14

Table 13. RMS Prediction Errors (MHz) up to five hours ahead forecast of foF2 by NNSA model (initial short-term foF2 model) for ten selected verification stations (that were not included in the training) during the period indicated for each station.

Station	Lat ^{o}N	Long ^{o}E	RMSE (MHz)					Period
			1 hour	2 hour	3 hour	4 hour	5 hour	
Tomsk	56.50	84.90	0.445	0.543	0.610	0.665	0.726	1976-86
Boulder	40.00	254.70	0.482	0.604	0.679	0.722	0.756	1976-86
Ashkhabad	37.90	58.30	0.564	0.675	0.803	0.876	0.935	1964-69
Yamagawa	31.20	130.60	0.756	0.982	1.046	1.081	1.105	1976-86
Vanimo	-2.70	141.30	0.977	1.22	1.275	1.332	1.303	1976-86
Huancayo	-12.00	284.70	0.526	0.612	0.725	0. 895	0.964	1976-86
Grahamstown	-33.30	26.50	0.535	0.731	0.815	0.861	0.882	1976-86
Hobart	-42.90	147.20	0.473	0.558	0.614	0.664	0.710	1976-86
Port Stanley	-51.70	302.20	0.881	1.174	1.356	1.495	1.531	1976-86
Argentine Is	-65.20	295.70	0.639	0.890	1.111	1.256	1.347	1976-86

Table 14. A summary of training and verification of the NNSA (initial short-term foF2) model.

NNSA Spatial verification				
Training stations	Training data period	Verification stations	Verification data period	Results
Table 11 (letter A)	1964 -1986	Table 11 (letter B)	1964 -1986	Table 13

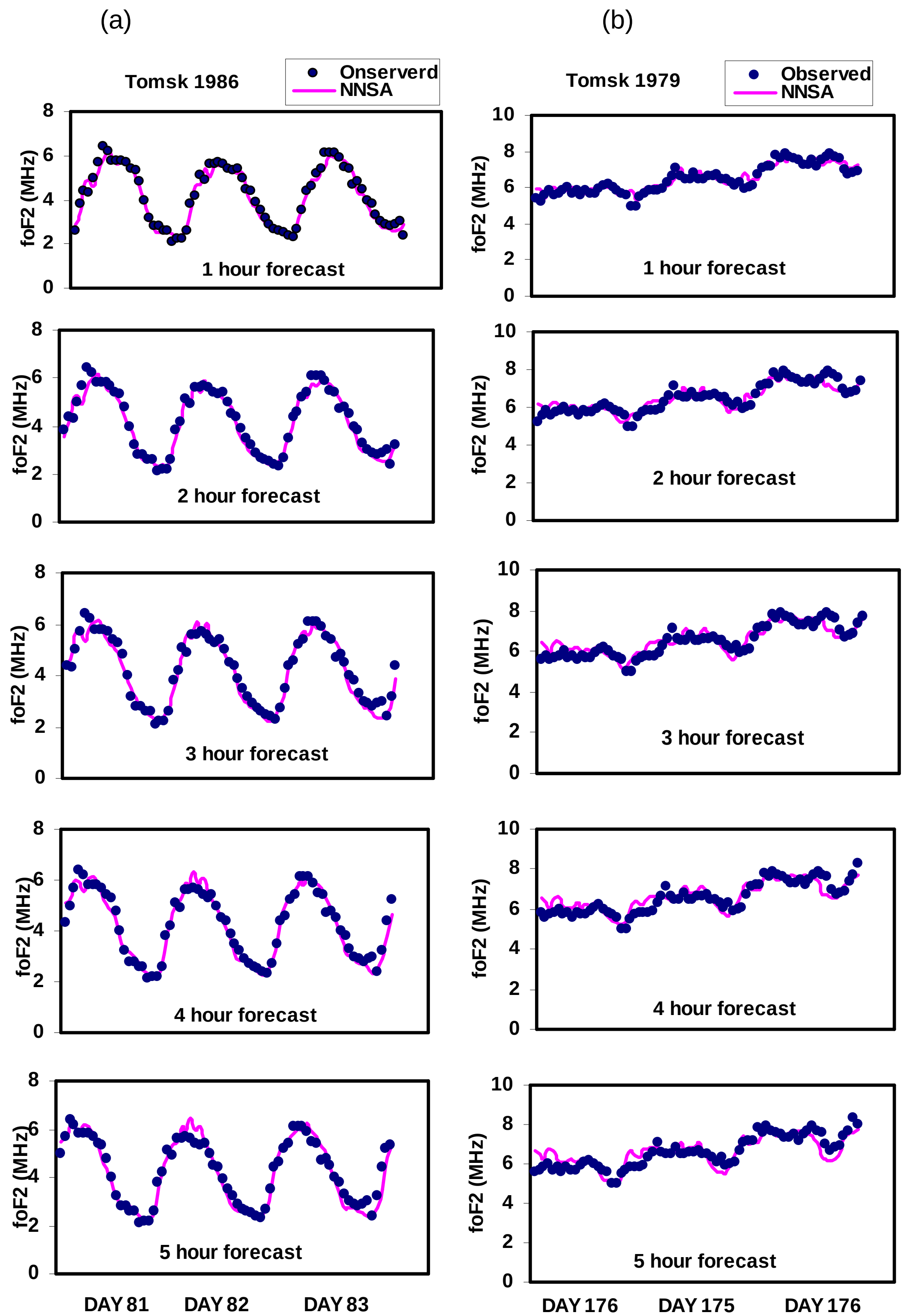

Figure 3-40a. Examples of comparisons between observed and NNSA model predicted-values of foF2 (5 hours ahead) for 3 consecutive days for Tomsk during (a) low solar activity, 1986 and (b) high solar activity, 1979.

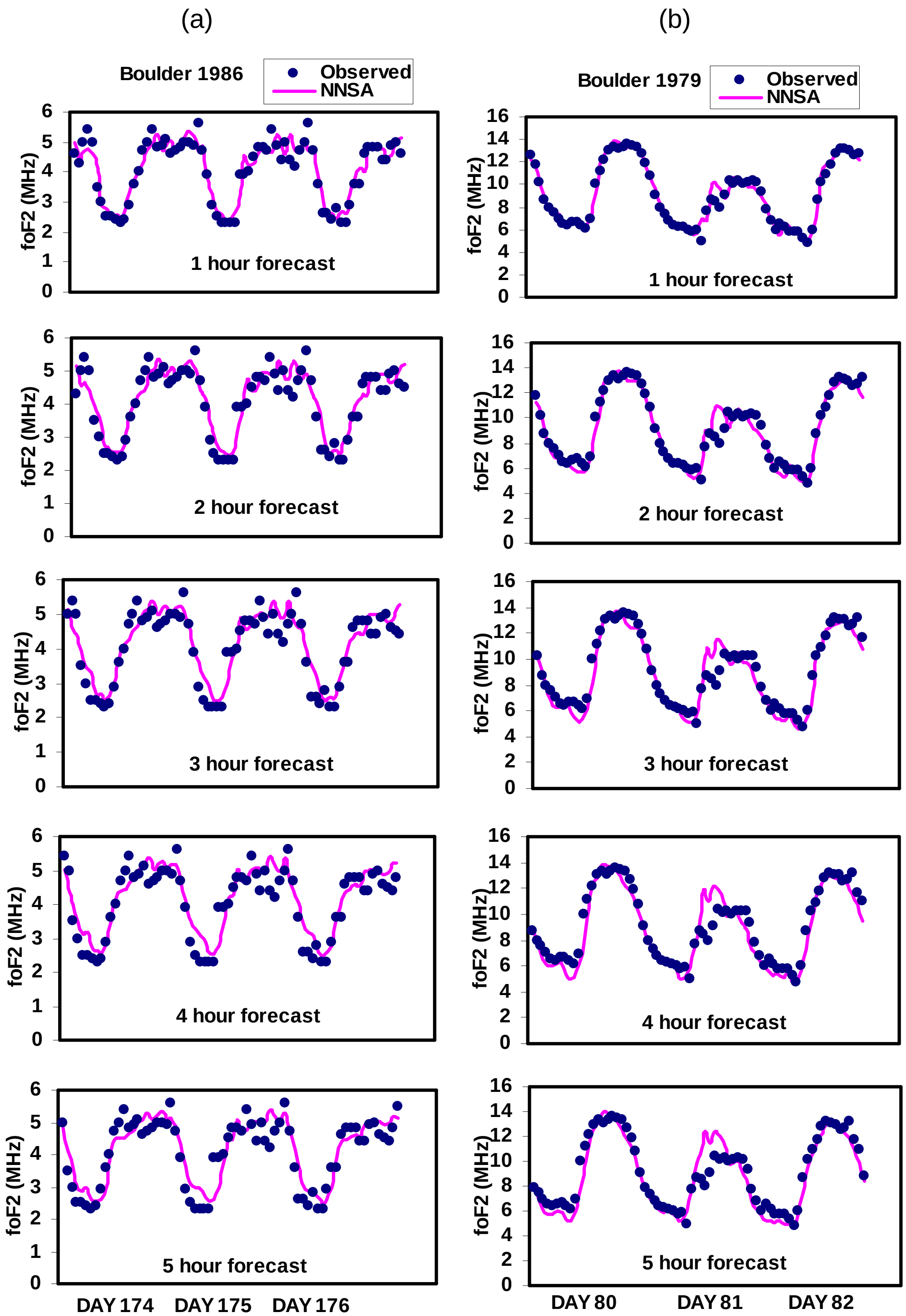

Figure 3-40b. Examples of comparisons between observed and NNSA model predicted-values of foF2 (5 hours ahead) for 3 consecutive days for Boulder during (a) low solar activity, 1986 and (b) high solar activity, 1979.

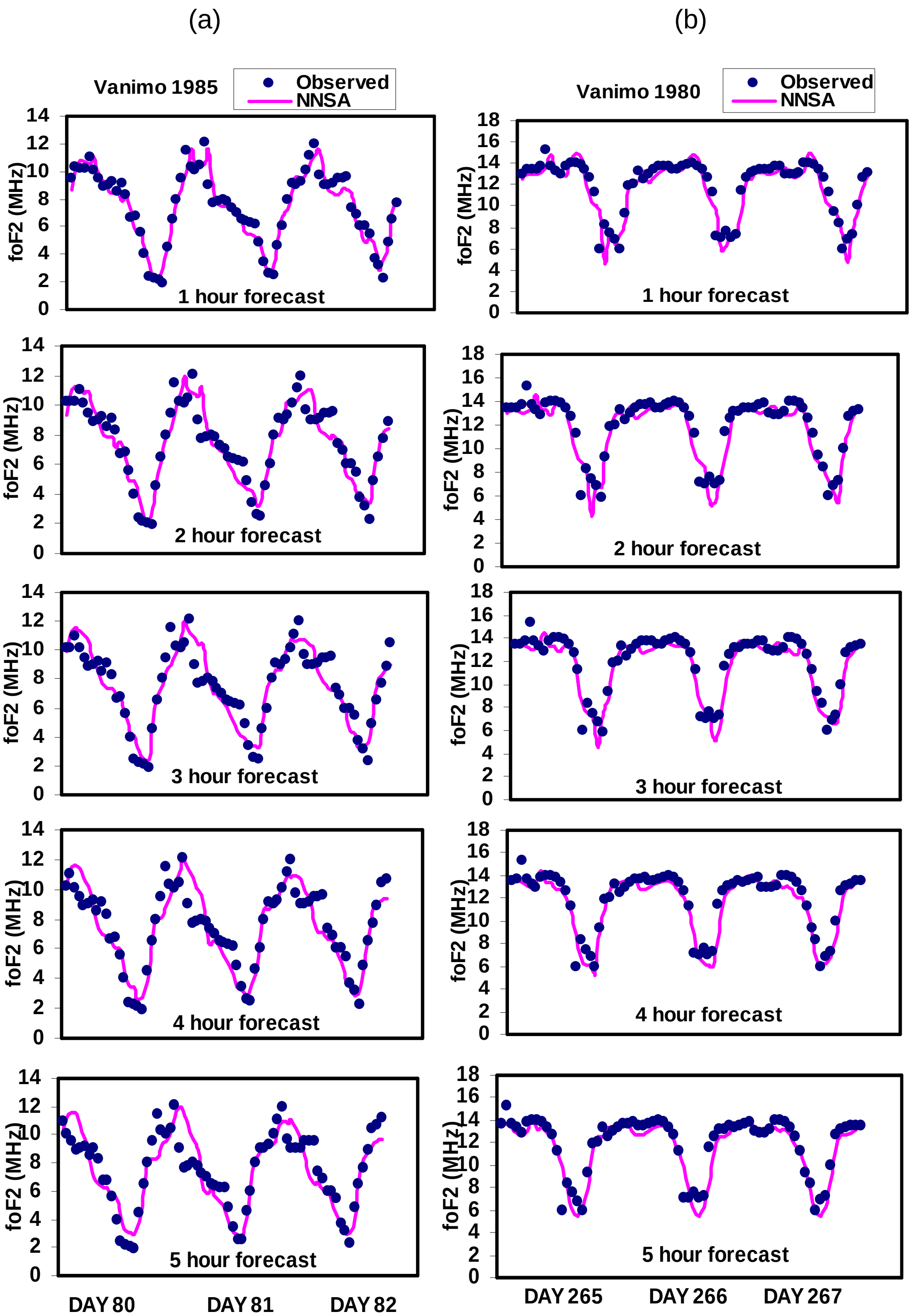

Figure 3-40c. Examples of comparisons between observed and NNSA model predicted-values of foF2 (5 hours ahead) for 3 consecutive days for Vanimo during (a) low solar activity, 1985 and (b) high solar activity, 1980.

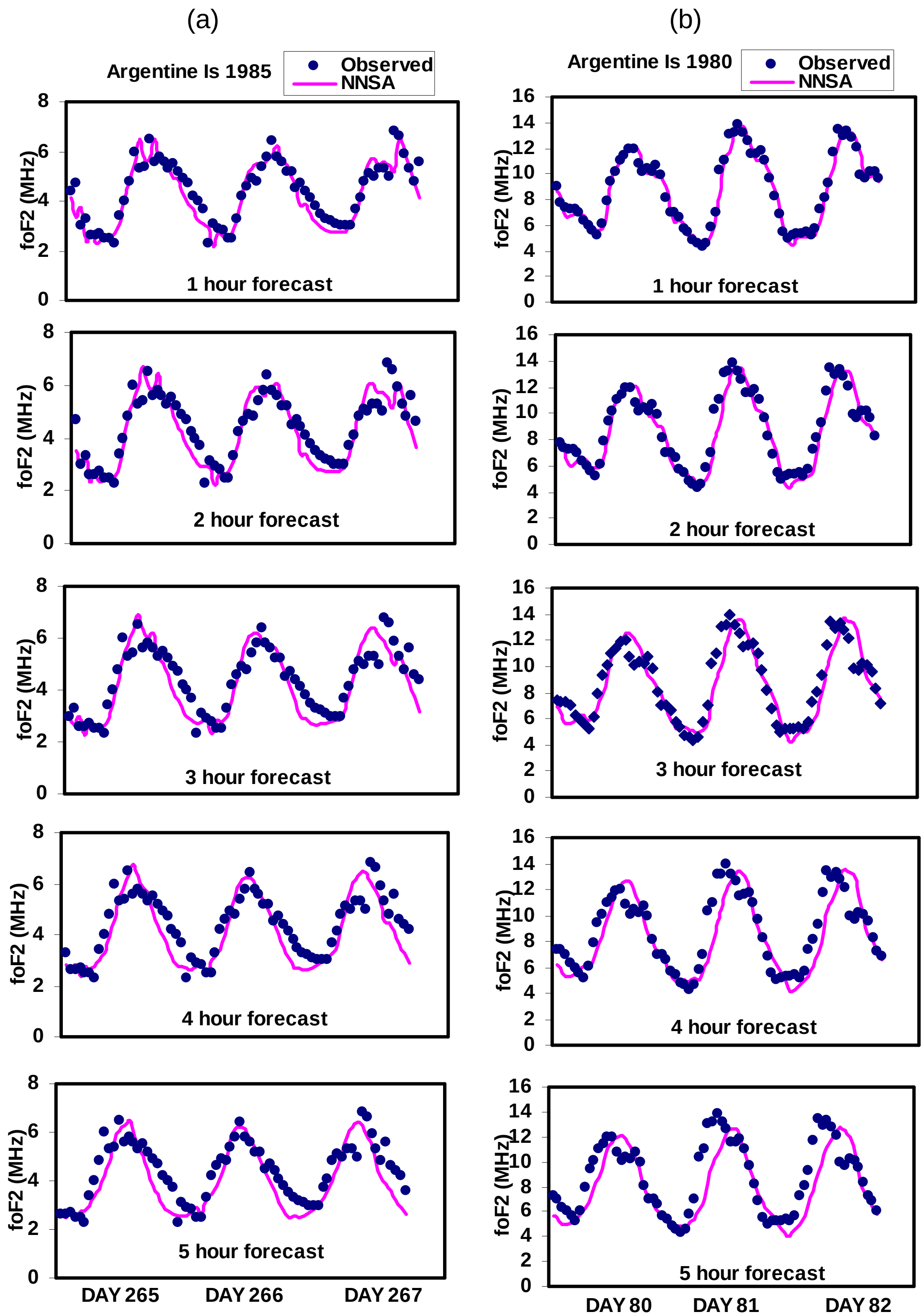

Figure 3-40d. Examples of comparisons between observed and NNSA model predicted-values of foF2 (5 hours ahead) for 3 consecutive days for Argentine Is during (a) low solar activity, 1985 and (b) high solar activity, 1980.

(a) (b)

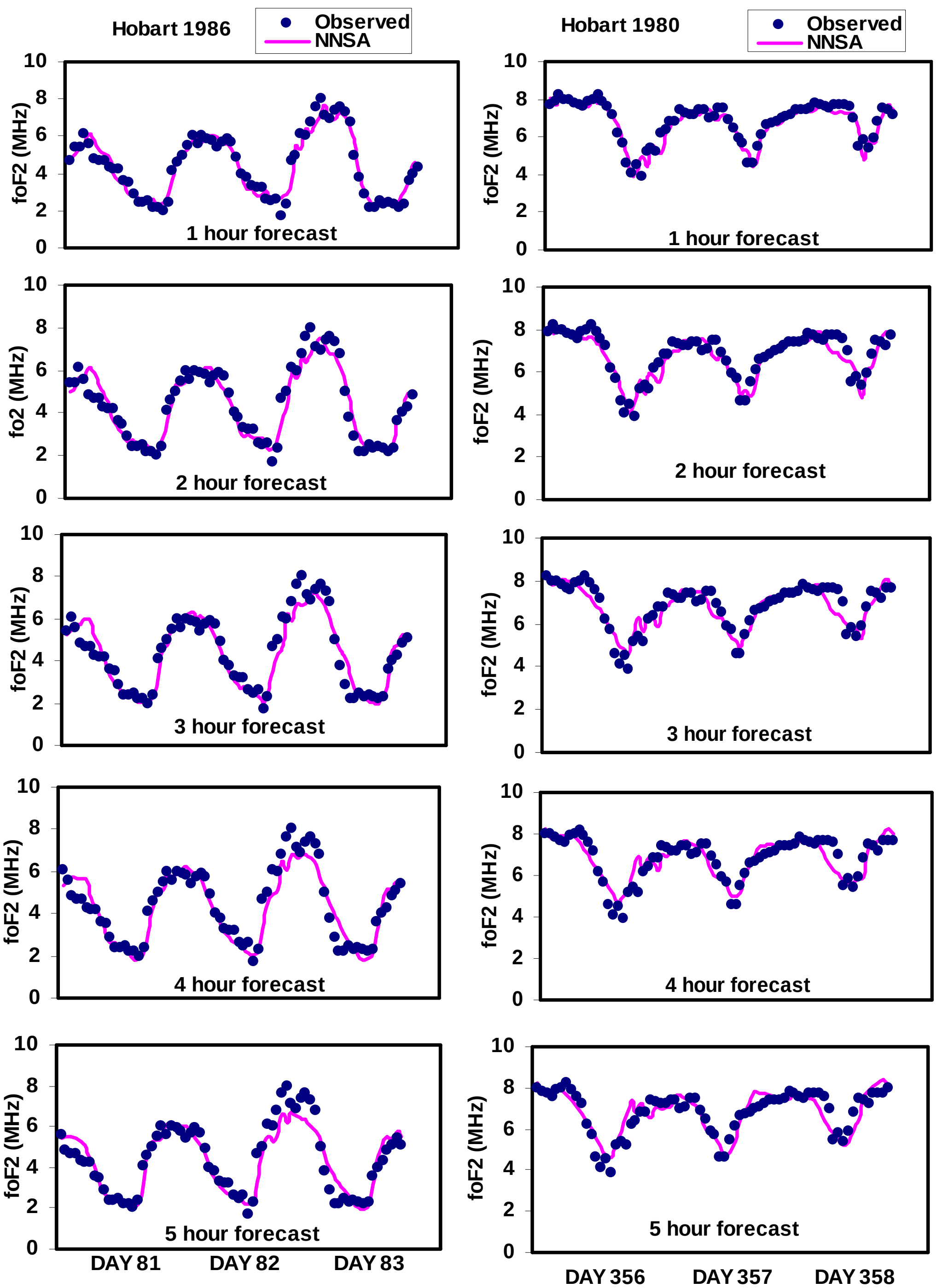

Figure 3-40e. Examples of comparisons between observed and NNSA model predicted-values of foF2 (5 hours ahead) for 3 consecutive days for Hobart during (a) low solar activity, 1986 and (b) high solar activity, 1980.

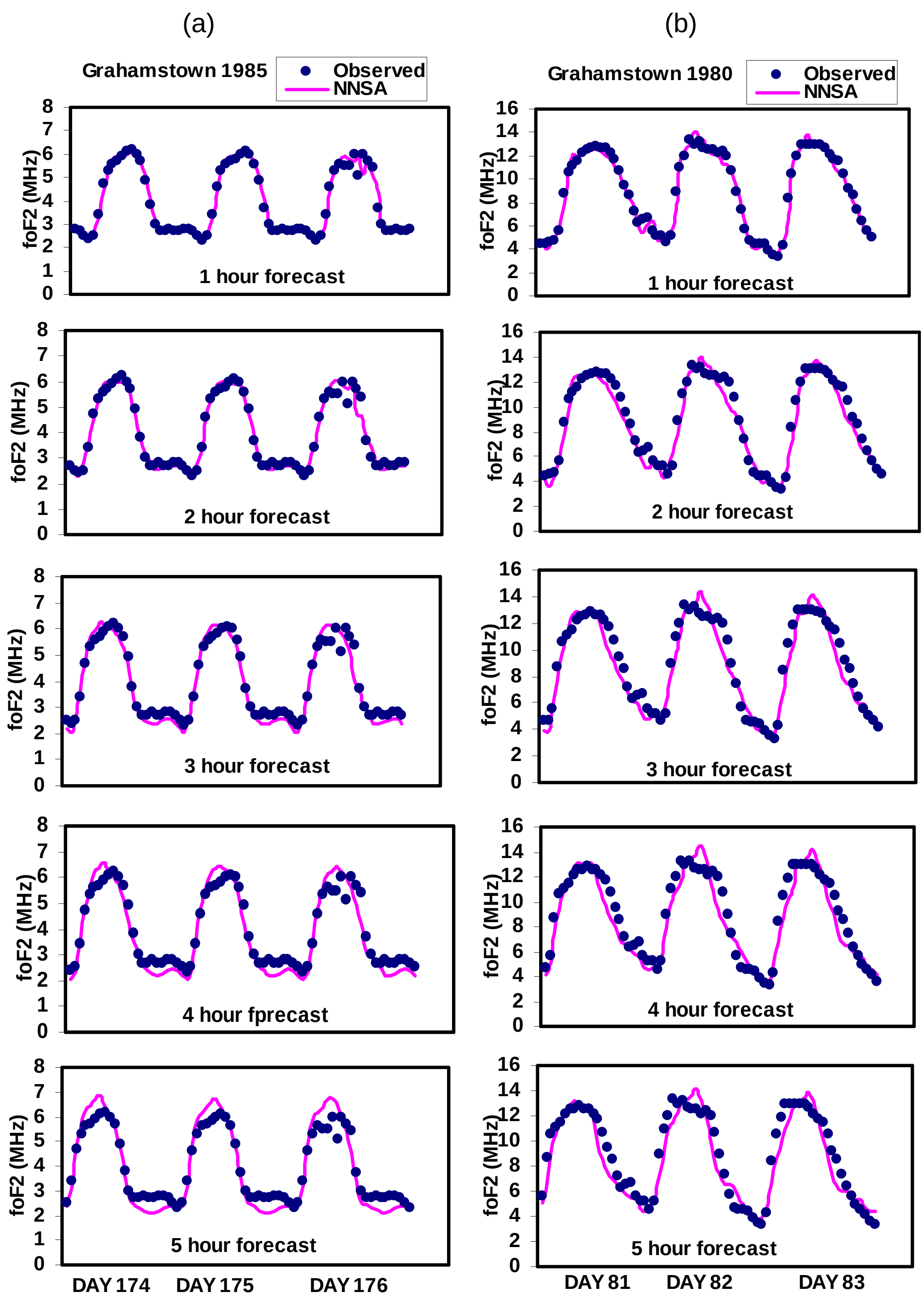

Figure 3-40f. Examples of comparisons between observed and NNSA model predicted-values of foF2 (5 hours ahead) for 3 consecutive days for Grahamstown during (a) low solar activity, 1985 and (b) high solar activity, 1980.

Having confirmed that the NNSA model (initial short-term foF2 model) is capable of modeling *spatial* variations of foF2, I verified the predictive ability of the second network (i.e. final short-term foF2 model, NNSB that was trained with data from all the stations in Table 11) both *temporally* and *spatially* beyond the training period. This was carried out in two stages. Firstly, I used all the available observed daily hourly values of foF2 from 1987 to 1992 from nine selected stations and from 1991 to 1995 for Tortosa (Table 15). The choice of these stations was based on the availability of sufficient data points during this period. Among these ten stations, four of them (Tortosa, 40.00 ^{o}N, 0.30 ^{o}E, Canberra, 35.30 ^{o}E, 149.00 ^{o}E, Magadan, 60.00 ^{o}N, 151.00 ^{o}E and Maui, 20.80 ^{o}N, 203.50 ^{o}E) were not included in the training of the NNSB model. Secondly, the performance of the NNSB model was verified by using only observed data around low and high solar activity periods from some stations (Tables 16 and 17). Therefore, the performance of the NNSB model during these two levels of solar activity can be tested. Because it is difficult to get sufficient data points from the same year for all the stations, I have used different years where data are reasonably available. Results of the RMSE differences between the NNSB model forecasted values and the observed values reveal that the model can successfully model both *spatial* and *temporal* short-term variations of foF2 (Table 15). The errors of the forecasted foF2 are small compared with the value of foF2. A closer inspection of the RMS errors in Table 15 shows an improvement over the errors of Table 6 (section 3.3.3.2) obtained by using URSI, CCIR and NN2 models for long-term predictions of foF2 during the same period. This indicates that predictions of foF2 values are much improved by including past observations of foF2 itself.

Table 15. RMS Prediction Errors (MHz) up to five hours ahead forecast of foF2 by NNSB model (final short-term foF2 model) at selected verification stations beyond training period.

Station	Lat	Long	RMSE (MHz)					Period
	^{o}N	^{o}E	1 hour	2 hour	3 hour	4 hour	5 hour	
Magadan	60.0	151.0	0.574	0.745	0.852	0.924	0.978	1987-92
Leningrad	59.9	30.7	0.598	0.762	0.868	0.935	0.981	1987-92
Uppsala	59.8	17.7	0.584	0.809	0.965	1.051	1.110	1987-92
Boulder	40.0	254.7	0.492	0.642	0.738	0.803	0.856	1987-92
Tortosa	40.0	0.3	0.624	0.774	0.842	0.881	0.922	1991-95
Point Arguello	34.6	239.4	0.606	0.757	0.836	0.844	0.899	1987-92
Mundaring	-32.0	116.3	0.582	0.704	0.767	0.810	0.848	1987-92
Grahamstown	-33.3	26.5	0.460	0.619	0.695	0.728	0.777	1987-92
Hobart	-42.9	147.2	0.460	0.583	0.662	0.723	0.774	1987-92
Canberra	-53.3	149.0	0.463	0.595	0.680	0.740	0.796	1987-92

Table 16. RMS Prediction Errors (MHz) up to five hours ahead forecast of foF2 by NNSB model (final short-term foF2 model) at selected verification stations beyond training period around high solar activity.

Station	Lat	Long	RMSE (MHz)					Period
	^{o}N	^{o}E	1 hour	2 hour	3 hour	4 hour	5 hour	
Tomsk	56.6	84.9	0.447	0.538	0.624	0.705	0.783	2001
Boulder	40.0	254.7	0.421	0.621	0.730	0.811	0.860	2001
Maui	20.8	203.5	0.932	1.396	1.654	1.810	1.960	1992
Vanimo	-2.7	141.3	1.179	1.463	1.567	1.635	1.677	1991
Grahamstown	-33.3	26.5	0.550	0.751	0.852	0.919	1.003	2001
Hobart	-42.9	147.2	0.465	0.569	0.642	0.705	0.758	1999
Port Stanley	-51.7	302.2	0.736	0.927	1.031	1.091	1.166	2001
Argentine is	-65.2	295.7	0.668	0.828	0.936	1.016	1.069	1992

Table 17. RMS Prediction Errors (MHz) up to five hours ahead forecast of foF2 by NNSB model (final short-term foF2 model) at selected verification stations beyond training period around low solar activity.

Station	Lat ^{o}N	Long ^{o}E	RMSE (MHz) 1 hour	2 hour	3 hour	4 hour	5 hour	Period
Tomsk	56.6	84.9	0.441	0.530	0.584	0.624	0.660	1995
Boulder	40.0	254.7	0.402	0.501	0.534	0.564	0.598	1994
Grahamstown	-33.3	26.5	0.420	0.539	0.600	0.624	0.660	1994
Ashkhabad	-37.9	58.3	0.647	0.752	0.803	0.830	0.865	1995
Port Stanley	-51.7	302.2	0.637	0.774	0.853	0.886	0.894	1994
Argentine is	-65.2	295.7	0.540	0.681	0.768	0.821	0.836	1994

A comparison of the RMSE differences in Tables 15 and 16 shows that the error appears to be larger during the high solar activity period than during the low solar activity period. This could be due to the fact that the ionosphere is relatively less disturbed during low solar activity than during high solar activity. The RMS errors shown in Tables 15, 16 and 17, which increase with increasing delay time, give the expected result that the NN will forecast 1 hour ahead with better accuracy than 5 hours ahead. Typical examples of stations where errors of between 1.0 and ~2.0 MHz were obtained for specific years (Table 16) are Maui (1992), Vanimo (1991), Grahamstown (2001), Port Stanley (2001) and Argentine Is (1992). This might be as a result of the wide range in behaviour of the polar and equatorial regions to which these stations belong, due to complex electrodynamic interactions involving the neutral wind, the Earth's magnetic field and electric fields produced by dynamo action in the F region. However, despite the fact that the errors are relatively large for these stations, the RMS errors of the forecasted foF2 are small compared with the value of foF2 itself. This can be clearly observed in Figures 3-41(a to e) where graphs of forecasted foF2 values have almost the same variation in time with that of the observed values. Results also revealed that the NN responds to an increase or decrease in solar or magnetic activity. Evidence of this can be observed in Figures 3-40b, 3-40e and 3-41a. Similar summary of the training and verification procedures for the NNSB model is shown in Table 18.

Table 18. Summary of training and verification of the NNSB (final short-term foF2) model.

NNSB model Spatial and Temporal verification				
Training stations	Training data period	Verification stations	Verification data period	Results
Table 11 (A +B)	1964 -1986	Table 11 (letter B) Table 12	1987-1992 1991-1995	Table 14
			Around high solar activity (1991, 1992, 1999, 2001)	Table 15
			Around low solar activity (1994, 1995)	Table 16

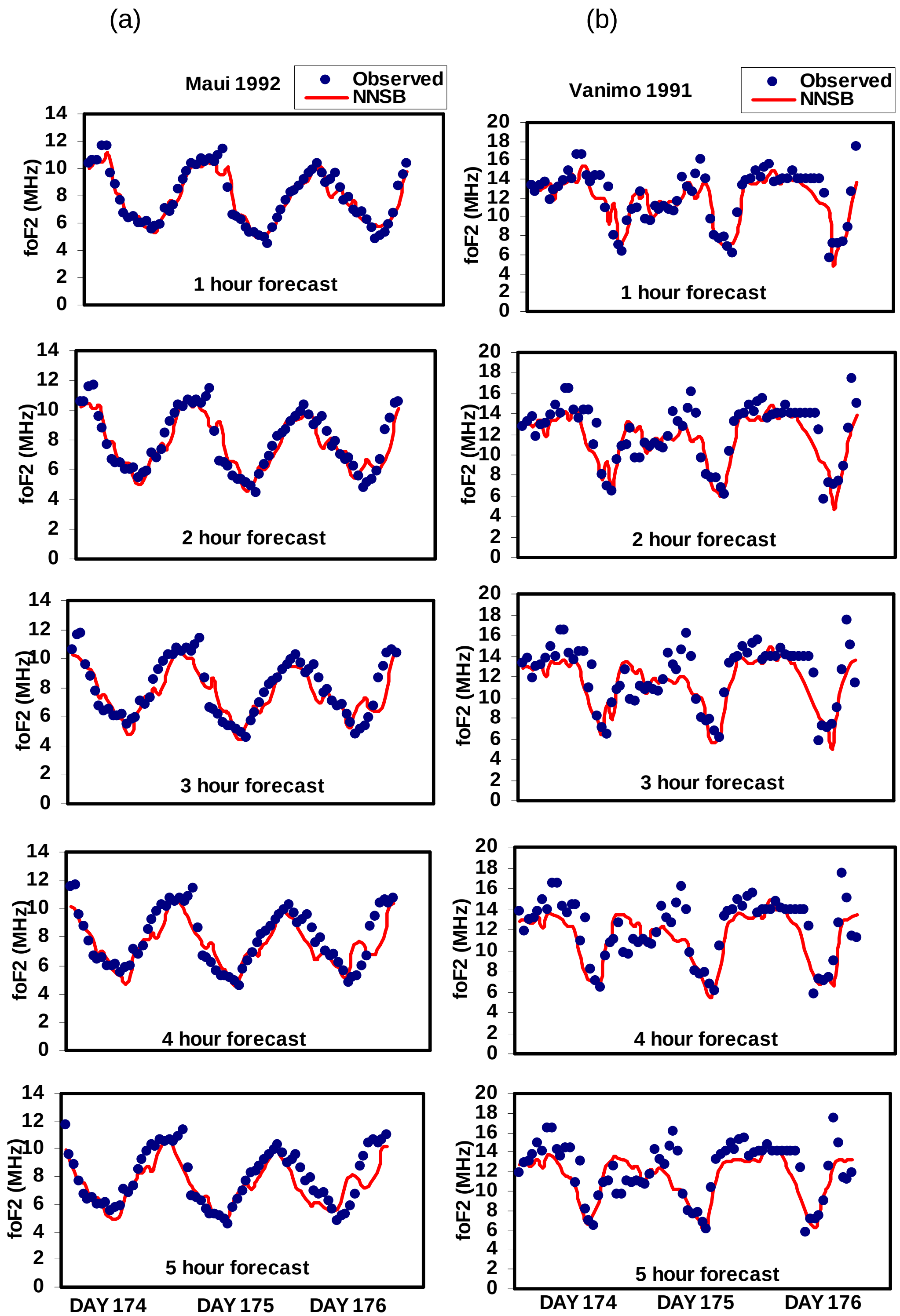

Figure 3-41a. Examples of comparisons between observed and NNSB model predicted-values of foF2 (5 hours ahead) for 3 consecutive days during high solar activity for (a) Maui 1992 and (b) Vanimo 1991.

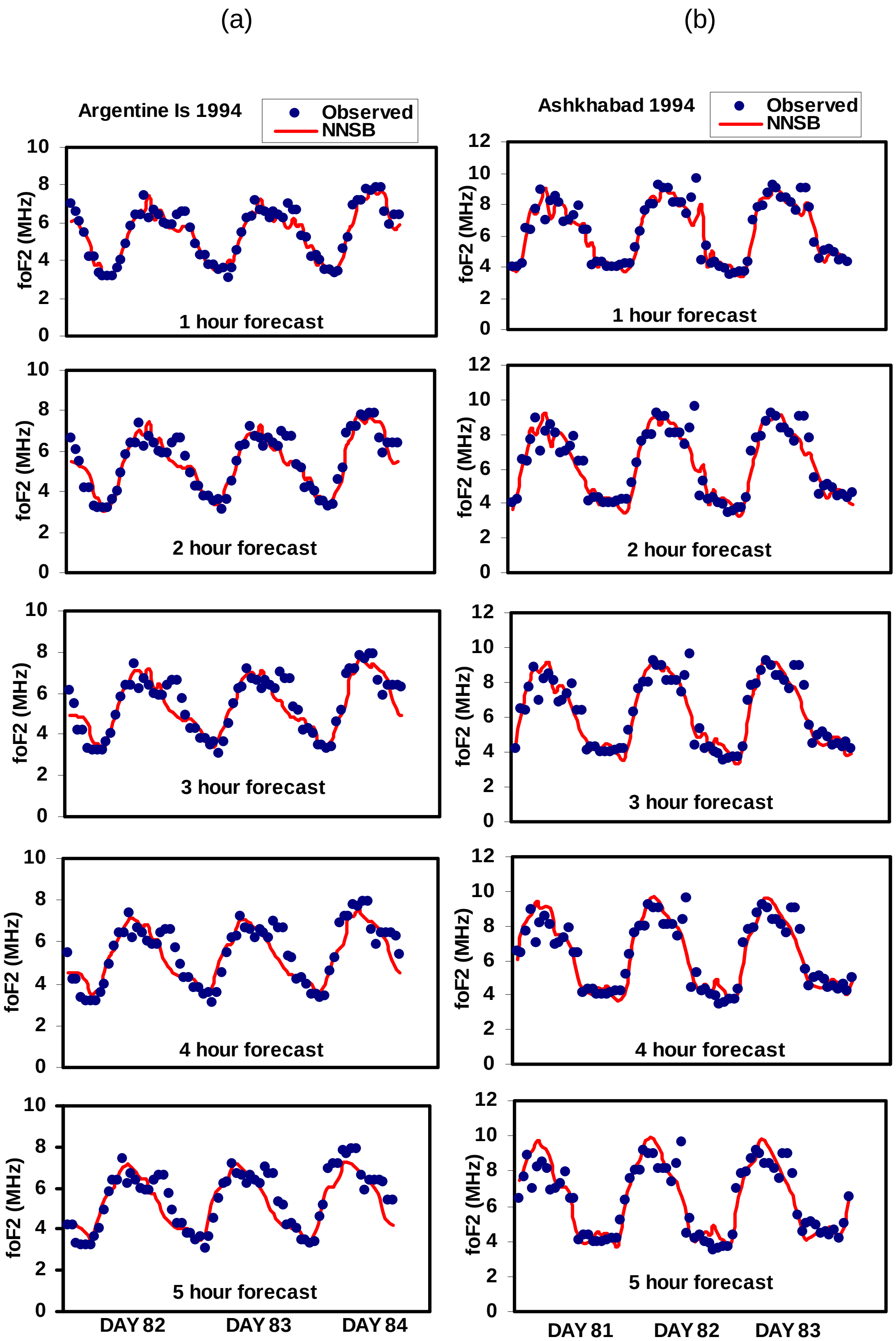

Figure 3-41b. Examples of comparisons between observed and NNSB model predicted-values of foF2 (5 hours ahead) for 3 consecutive days during low solar activity, 1994 for (a) Argentine Is and (b) Ashkhabad.

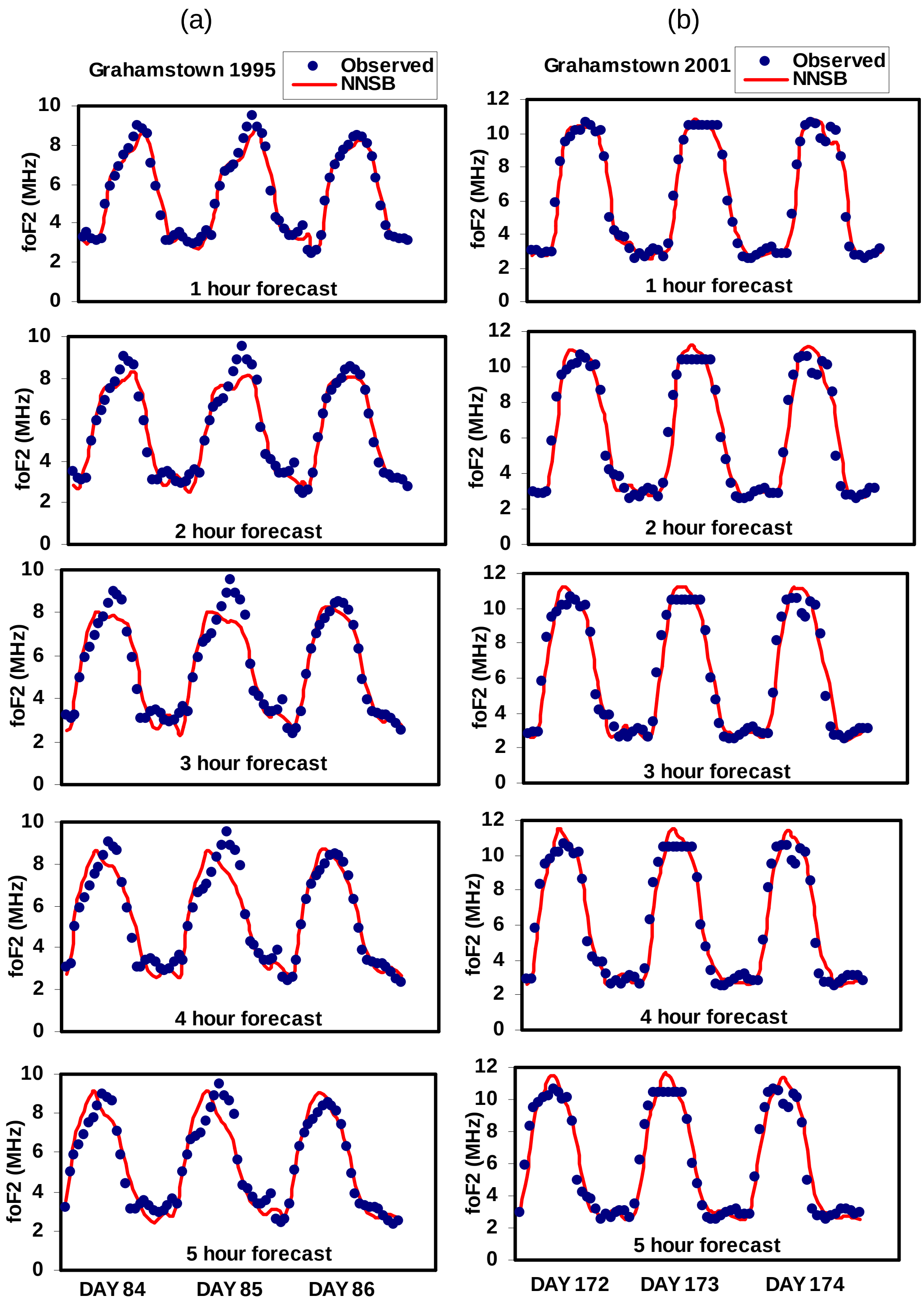

Figure 3-41c. Examples of comparisons between observed and NNSB model predicted-values of foF2 (5 hours ahead) for 3 consecutive days for Grahamstown during (a) low solar activity, 1995 and (b) high solar activity, 2001.

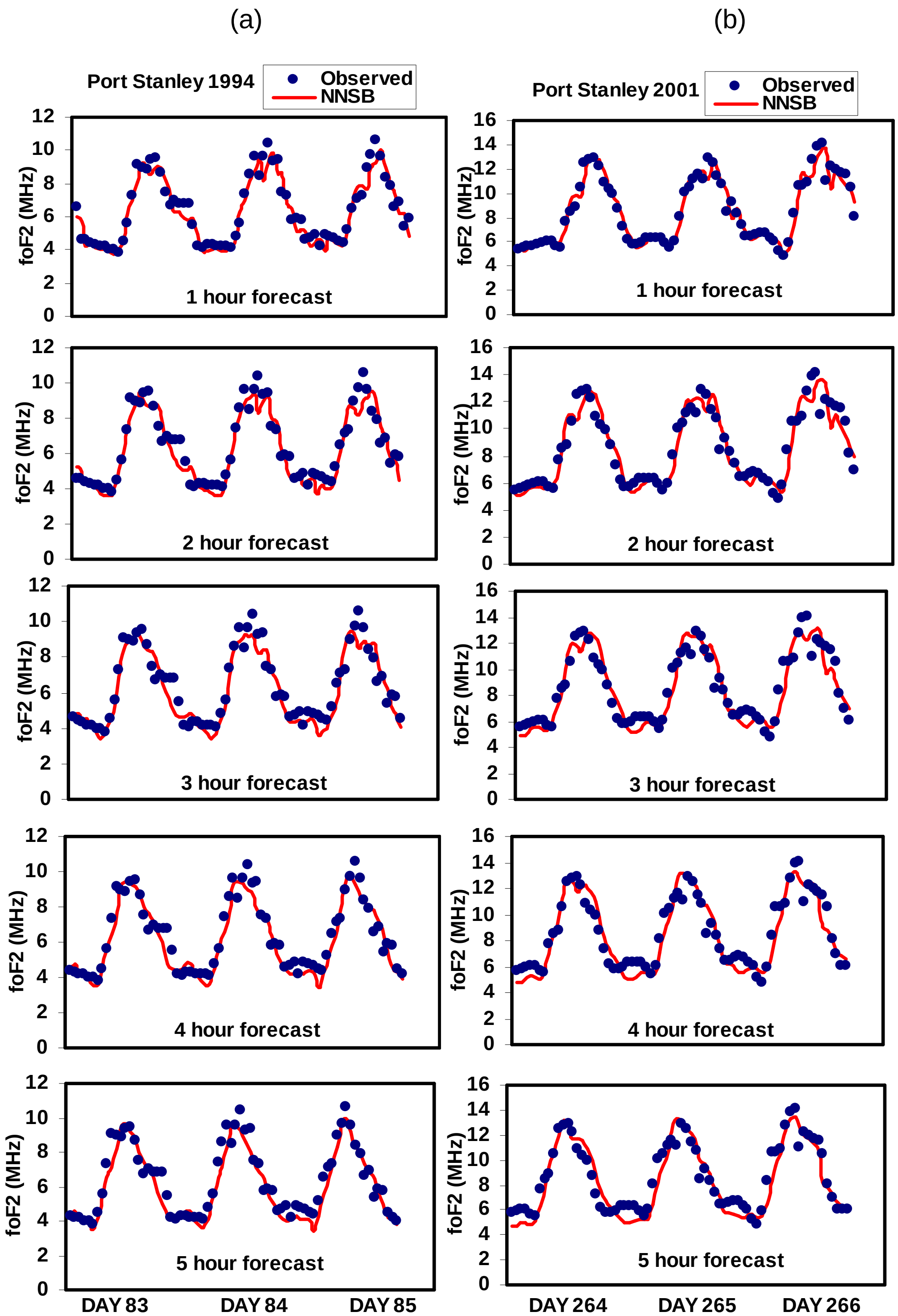

Figure 3-41d. Examples of comparisons between observed and NNSB model predicted-values of foF2 (5 hours ahead) for 3 consecutive days for Port Stanley during (a) low solar activity, 1994 and (b) high solar activity, 2001.

(a) (b)

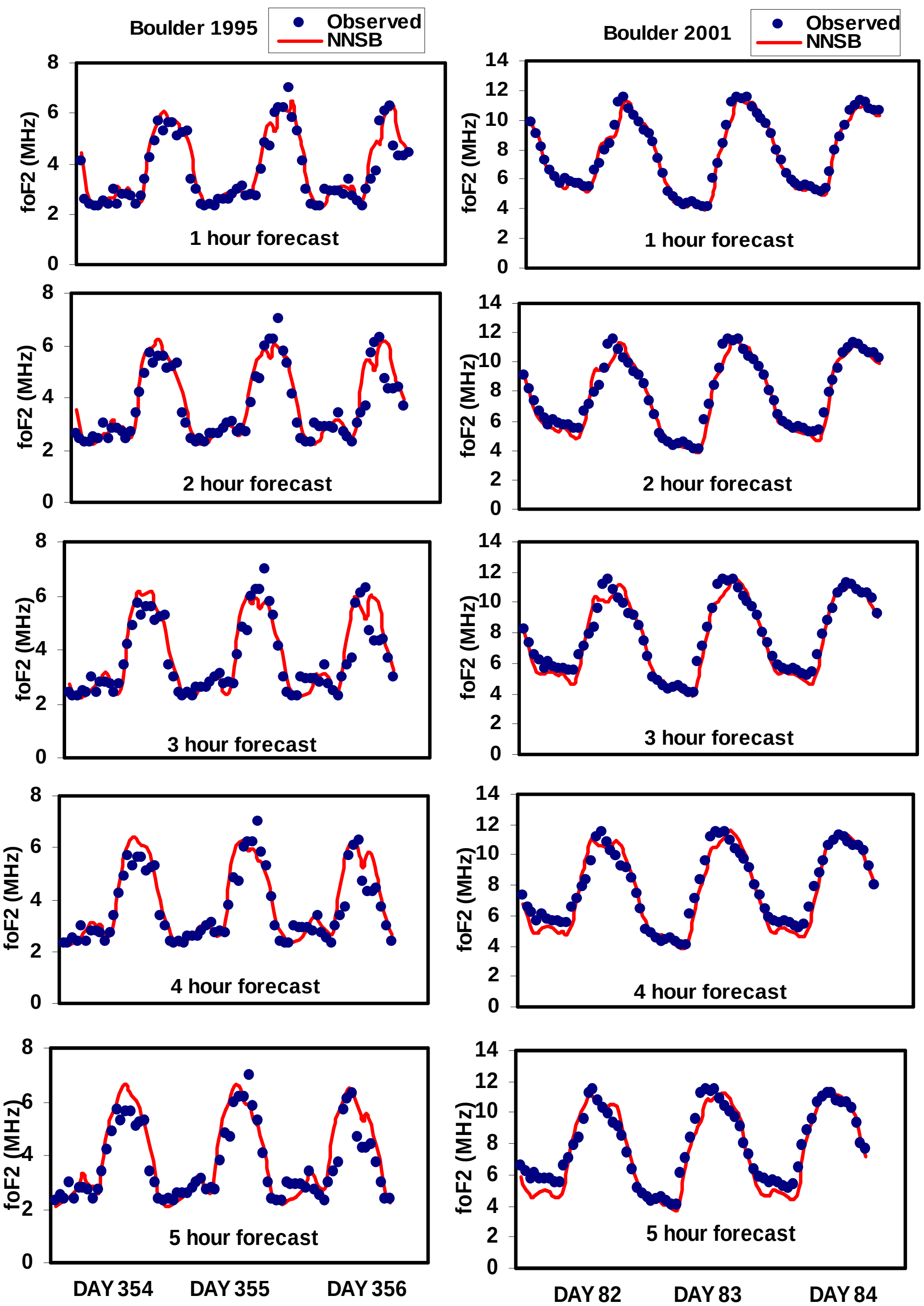

Figure 3-41e. Examples of comparisons between observed and NNSB model predicted-values of foF2 (5 hours ahead) for 3 consecutive days for Boulder during (a) low solar activity, 1995 and (b) high solar activity, 2001.

3.5.8 Conclusion

The results presented in this section successfully demonstrate the potential of a NN based empirical model for *spatial* and *temporal* forecasting of the ionospheric parameter foF2, up to 5 hours ahead on a global scale. The error analysis shown in Tables 13, 15, 16 and 17 reveals that the forecasting can perform well within reasonable error limits. The results also show that short-term predictions of foF2 are much improved by including past observations of foF2 itself, in addition to those *temporal* and *spatial* input variables discussed in section 3.5.3, and that the NNSB model can successfully be applied to the task of global forecasting. One limitation of this model is that it cannot be applied to a geographic location where observed data are not available, most especially the ocean areas. That is, the model is limited to those areas where we have ionosonde stations with available data points. In view of this shortcoming, I therefore developed a near-real time NN based model, which does not require past observations of foF2 from the target location, but rather from only four ionosonde stations that are known to have data in real time. This is the subject of the next section.

3.6 Near-real time foF2 NN model

3.6.1 Introduction

The previous section discussed the development of a global empirical model for short-term forecasting of the daily hourly values of the ionospheric F2 region critical frequency (foF2) at any target geographical location up to five hours in advance. As pointed out earlier in section 3.5.8, the limitation of the short-term foF2 model is that it cannot be applied to a geographic location where measured data are not readily available. As a result, and considering the fact that ionospheric data is not available for the vast areas occupied by the oceans, instead of using recent past observations of foF2 from a target geographic location to forecast for the next five hours ahead of that location, I have considered recent past observations of foF2 from only four selected ionosonde stations across the globe to develop a near-real time foF2 model. The choice of these four stations is based on the fact that they are reliably known to have data in real time (based on records from the Digital Ionogram Database, DIDBase). These stations are Boulder (40 ^{o}N, 254.7 ^{o}E), Grahamstown (33.3 ^{o}S, 26.5 ^{o}E), Dourbes (50.1 ^{o}N, 4.6 ^{o}E) and Port Stanley (51.7 ^{o}S, 302.2 ^{o}E), and their geographic locations are represented as yellow squares in Figure 3-42. Details of the development of this model (that is, inputs to, and output of the NN, NN configuration, results and discussion) are discussed in the following sections.

3.6.2 NN inputs and output

As in the case of the short-term foF2 model, the inputs to the near-real time foF2 model are also of two categories. The first category consists of the same input set already discussed earlier in section 3.2.3 of this chapter (see Figure 3-2 for these input parameters). The second set of inputs is closely related to the second set of inputs to the previous NN model (i.e. the short-term foF2 NN), in the sense that they are also related to the foF2 itself. The difference is that instead of using recent past observations of foF2 from the target location, I have used 3 recent past observations of foF2 from only four ionospheric stations (Boulder (40.0 ^{o}N, 254.7 ^{o}E), Grahamstown (33.3 ^{o}S, 26.5 ^{o}E), Dourbes (50.1 ^{o}N, 4.6 ^{o}E) and Port Stanley (51.7 ^{o}S, 302.2 ^{o}E). Studies carried out by researchers (Appleton, 1950; Kane, 1992; Bradley, 1993; Williscroft and Poole, 1996; Kouris et al., 1998; Zakharov and Tyrnov, 1999; Chen et al., 2000; Forbes et al., 2000; Richards, 2001; Rishbeth and Mendillo, 2001; Sethi et al., 2002; Liu et al., 2003) have shown the existence of strong relationships between foF2 and solar activity. Also, Rao and Rao (1969), Smith and King (1981), and Triskova and Chum (1996) have carried out studies on the uniqueness of the connection between foF2 and solar activity during the growth and decay phase of the solar cycle. Evidence of this relationship between foF2 and solar variations over a period of one day (diurnal), one year (seasonal) and the 11-year solar cycle has also been demonstrated in section 1.2.1 by the applications of Fourier transform techniques to variations of foF2 measured-values at the Grahamstown station over a period of 27 years. In view of these findings, it is reasonable to assume that foF2 from certain fixed ionosonde stations will correlate well with foF2 at any other geographic location on the globe. These foF2 related inputs are the 3 recent past observations of foF2 values: F_{-2}, F_{-1} and F_0, from each of the four selected stations. These are F_{-2p}, F_{-1p}, F_{0p}, F_{-2g}, F_{-1g}, F_{0g}, F_{-2b}, F_{-1b}, F_{0b}, F_{-2d}, F_{-1d} and F_{0d}. The letters p, g, b and d represent observations from Port Stanley, Grahamstown, Boulder and Dourbes stations respectively. In addition to the first set of inputs, this makes a total of 26 input parameters to the NN. See the block diagram of the NN architecture in Figure 3-43 for a detailed illustration. It should be made clear at this point that apart from the observed values of foF2 from the chosen four stations that were used as inputs to the NN, the NN knows nothing about their geographical information. The choice of the 3 recent observations is based on the fact that these values will have the same magnetic effect considering the 3-hourly planetary magnetic index, ap. The NN target output is the observed foF2 value from every other station used for training the NN corresponding to the most recent foF2 (i.e. F_{0p}, F_{0g}, F_{0b} and F_{0d}) from the four selected stations.

3.6.3 Database

The data used for training the NN to predict near-real time foF2 values are the hourly values of the F2 region critical frequency depending on the availability, from 26 (Table 19) worldwide ionospheric stations spanning the period 1976 to 1986. These stations are represented as black circles and blue squares in Figure 3-42. For clarification, the stations represented with blue squares were later used for verification of the NN temporally beyond training period. Figure 3-42 shows the geographical distribution of the training and verification stations. The choice of this solar cycle period is based on the fact that one of the four selected stations (i.e. Grahamstown), where the recent past observations of foF2 were obtained, started operation in 1973, and that the availability of foF2 values from these selected stations would determine the number of years for which data will be used to train the

NN. Records from the archive (Space Physics Interactive Data Resource, SPIDR) have also shown that most stations appear to have sufficient data points within the period of 1976 to 1986 than any other solar cycle. As a result, I decided to consider this period where I could easily obtain sufficient data points both from these four selected stations and other stations whose geographic coordinates as well as foF2 values are required for training the NN. Data from 15 stations (Table 20) (stations represented by red and blue squares in Figure 3-42) have been used to verify the predictive ability of the near-real time foF2 model both *temporally* and *spatially.* The letter P in Table 20 refers to stations that were included during the training of the NN (i.e. blue squares in Figure 3-42), while letter Q (i.e. red squares in Figure 3-42) refers to stations that were not included in the training process.

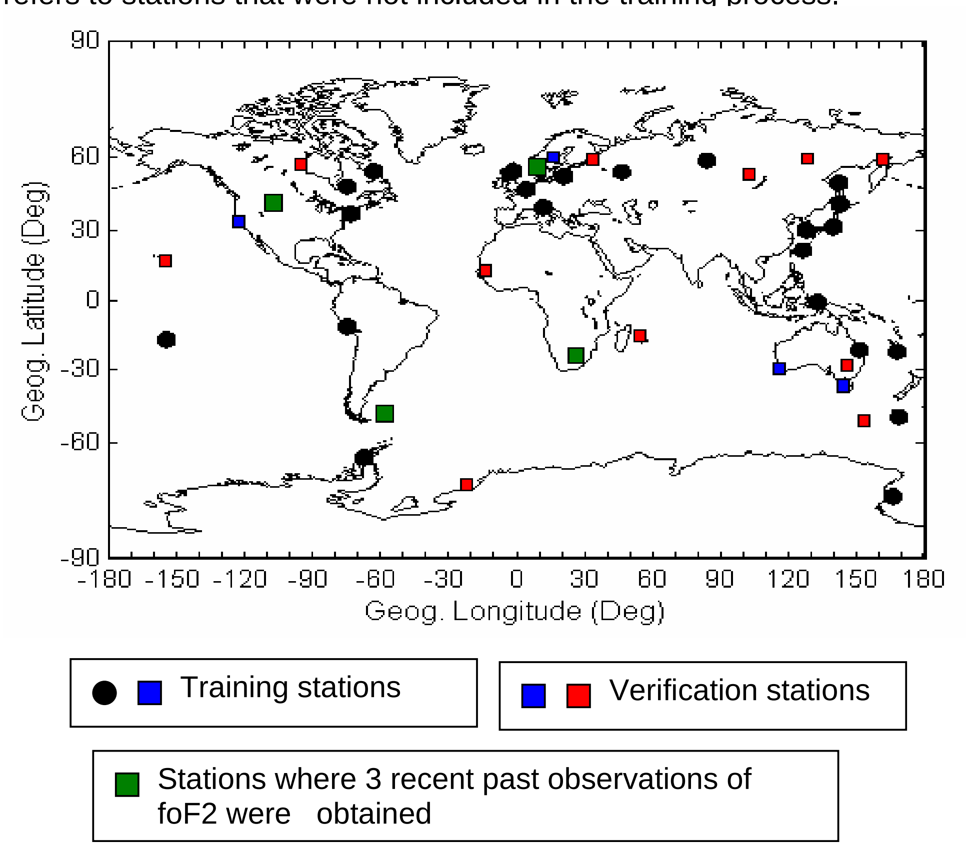

Figure 3-42. Map of global distribution of training and verification stations of the near-real time foF2 NN.

Table 19. Ionosonde stations used for training the near-real time foF2 NN

S/N	Station Name	Latitude ^oN	Longitude ^oE
1	Lycksele	64.6	18.7
2	Uppsala	59.8	17.6
3	Tomsk	56.5	84.9
4	Moscow	55.5	37.3
5	Kaliningrad	54.7	20.6
6	Goose Bay	53.3	299.2
7	Slough	51.5	359.4
8	Pointiers	46.6	0.3
9	Wakkanai	45.4	141.7
10	Rome	41.8	12.5
11	Akita	39.7	140.1
12	Wallops Is	37.9	284.5
13	Kokubunji	35.7	139.5
14	Point Arguello	34.6	239.4
15	Yamagawa	31.2	130.6
16	Okinawa	26.3	127.8
17	Vanimo	-2.7	141.3
18	Huancayo	-12.0	284.7
19	Tahiti	-17.7	210.7
20	Brisbane	-27.5	152.9
21	Norfolk Is	-29.0	169.0
22	Mundaring	-32.0	116.3
23	Hobart	-42.9	147.2
24	Campbell Is	-52.5	169.2
25	Argentine Is	-65.2	295.7
26	Scott Base	-77.9	166.8

Table 20. Selected verification stations for near-real time foF2 NN.

S/N	Station Name	Latitude ^oN	Longitude ^oE	Included in training (blue squares)	Not included in training (red squares)
1	Yakutsk	62.0	129.6		Q
2	Magadan	60.0	151.0		Q
3	Leningrad	59.9	30.7		Q
4	Uppsala	59.8	17.6	P	
5	Churchill	58.8	265.8		Q
6	Irkutsk	52.5	104.0		Q
7	Point Arguello	34.6	239.4	P	
8	La Reunion	21.1	55.9		Q
9	Maui	20.8	203.5		Q
10	Dakar	14.8	341.6		Q
11	Mundaring	-32.0	116.3	P	
12	Canberra	-35.3	149.0		Q
13	Hobart	-42.9	147.2	P	
14	Macquarie Is	-54.5	159.0		Q
15	Halley Bay	-75.5	333.4		Q

3.6.4 NN architecture

The standard fully connected feed-forward NN with backpropagation was also employed in this section. The inputs and outputs of the NN are illustrated by the block diagram of the NN architecture in Figure 3-43. These output and input parameters are determined by what was considered in section 3.6.2. The NN has 26 input nodes with one output node (Figure 3-43). A number of different NNs with different architectures were trained to determine the optimal NN that will produce the minimum error difference between the observed and predicted values of foF2. The best NN configuration in this case was found to be the one with three hidden layers containing 30, 20 and 15 neurons respectively.

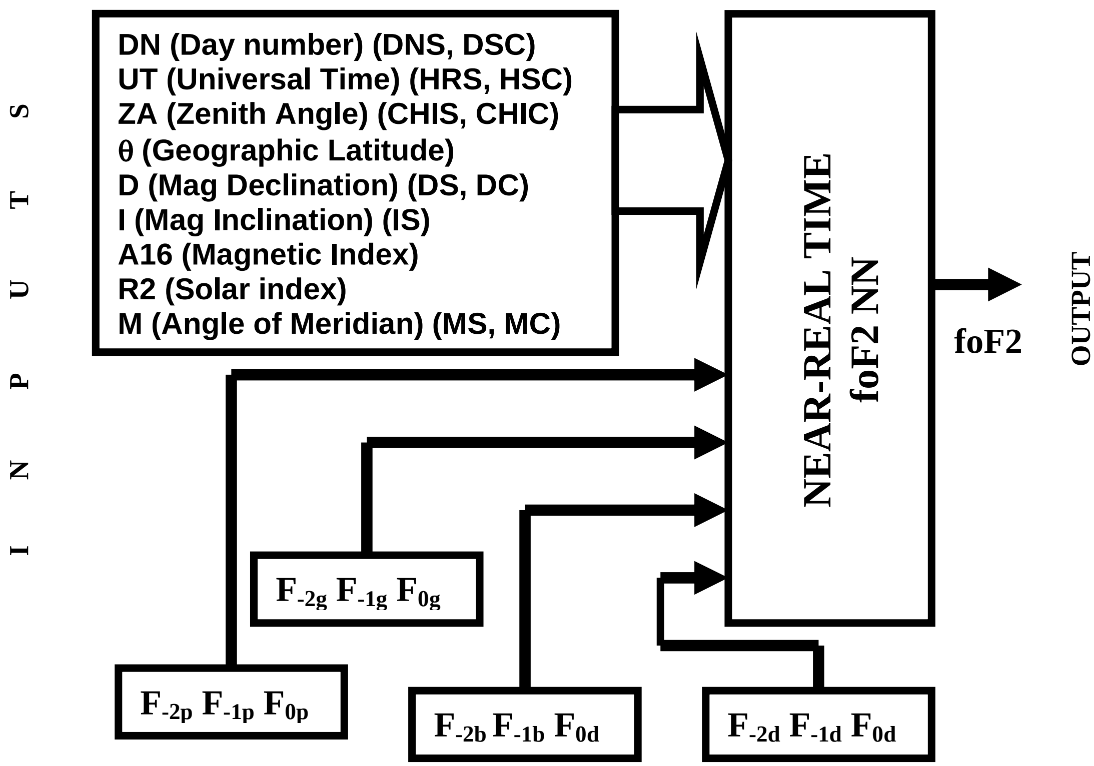

Figure 3-43. A block diagram of the near-real time foF2 NN architecture.

3.6.5 Training, testing and verification sets

Three independent data sets were used for the training (training set), testing (testing set) and verification (verification set) of the NN (Haykin, 1994). Both the training and the testing data sets were randomly selected in the ratio 70% and 30% respectively from all data covering the 26 ionospheric stations in Table 19. The first set of the input parameters in Figure 3-43 contains the geophysical information related to each of these 26 stations. The second input set, which is related to foF2 itself, was extracted from the four selected stations (i.e. Port Stanley, Grahamstown, Boulder and Dourbes). During training the NN is presented with values of the 26 inputs, which produces one output value foF2. As the training is continued, the output is compared with its target value corresponding to these inputs. During this process, a backpropagation algorithm is employed to adjust the weights in such a way as to minimize the error difference between the target and the predicted value of foF2. As mentioned earlier, several different NNs were trained with a different number of hidden layers and nodes. The testing data set was used during training to determine the optimal NN so that the NN was not over-trained. The training of the NN is terminated when the test error values versus the number of training epochs pass through a predetermined amount (Kumluca et al., 1999; Poole and McKinnell, 2000). At this point the NN is said to have achieved generalization, such that it produces a good performance when presented with a new set of input patterns that were not included in the training of the NN (i.e. the testing set). Finally, the verification data set (from the ionospheric stations in Table 20) was used to verify how well the optimal NN could work for a new set of data to predict foF2 both *temporally* and *spatially*. The geographic locations of the verification stations are as illustrated in Figure 3-42.

3.6.6 Results and Discussion

After the training, measured data from 15 ionospheric stations (Table 20) were used to verify the performance of the NN. Verification was carried out in two different ways. Firstly, I used measured data, based on availability from 7 selected stations (Table 21) that were not included in the training to verify the ability of the near-real time foF2 NN model (foF2 NRTNN) to predict spatial variations of foF2 within the training period. I have used different years for each of these stations because it is difficult to get data from the same years. Also an effort was made to make use of stations from all regions of the latitudes (i.e. low, mid and high latitudes). Secondly, data from 8 selected stations (Table 22) were also used to verify the performance of the foF2 NRTNN temporally beyond the training period. Since the NN requires 3 recent past observations of foF2 as inputs from the same period for each of the Port Stanley, Grahamstown, Boulder and Dourbes stations, I had to find a period during which data is available from these four stations simultaneously. This period happened to be from 1987 to 1989, which eventually determined the verification stations.

Tables 21 and 22 show the error differences between the observed and predicted values of foF2 from selected verification stations by taking the averages of the root mean square errors of all foF2 data points present during the period indicated for each station. The errors were evaluated by the application of the RMSE equation 3.12 in section 3.2.6. Figure 3-44 shows samples of daily variations of observed and forecasted foF2 values for six stations. Also shown in Figures 3-45(a and b) are samples of seasonal variations of observed and forecasted foF2 values for selected stations. Similar samples of comparisons between observed and forecasted foF2 values illustrating diurnal and seasonal variations are as shown in Figures 3-46 and

3-47(a and b) respectively. As can be observed from Figures 3-44, 3-45, 3-46 and 3-47 the predicted and forecasted values for these stations have the same type of variation in time. The results from the error Tables 21 and 22, and graphs of diurnal and seasonal behaviour in Figures 3-44, 3-45, 3-46 and 3-47 indicate that NNs could be employed for near-real time foF2 forecasting within reasonable error limits. I have only compared my results with the observed values because I was unable, at this time, to obtain data from any other near-real time global model.

I am reasonably confident that this model will predict foF2 in near-real time with about 1MHz RMS error anywhere on the globe, provided the data is available at the four control stations identified in section 3.6.1.

Table 21. RMS Prediction Errors (MHz) of near-real time foF2 model (foF2 NRTNN model) for 7 selected verification stations (that were not included in the training) during the period indicated for each station. Periods of the verification are within training period (1976-1986)

S/N	Station Name	Latitude °N	Longitude °E	RMSE (MHz)	Period
1	Yakutsk	62.0	129.6	1.171	1978-1979
2	Churchill	58.8	265.8	1.298	1978-1979
3	Irkutsk	52.5	104.0	0.931	1978-1979
4	La Reunion	21.1	55.9	0.979	1982-1983
5	Maui	20.8	203.5	1.263	1977-1978
6	Macquarie Is	-54.5	159.0	0.667	1984-1985
7	Halley Bay	-75.5	333.4	1.120	1978-1979

Table 22. RMS Prediction Errors (MHz) of near-real time foF2 model (foF2 NRTNN model) for 8 selected verification stations during the period indicated for each station. Period of verification (1987-1989) is beyond the training period (1976-1986). Four of these stations (i.e. Magadan, Leningrad, Dakar and Canberra) were not part of the training stations.

S/N	Station Name	Latitude °N	Longitude °E	RMSE (MHz)	Period
1	Magadan	60.0	151.0	1.028	1987-1989
2	Leningrad	59.9	30.7	0.856	1987-1989
3	Uppsala	59.8	17.6	1.049	1987-1989
4	Point Arguello	34.6	239.4	0.784	1987-1989
5	Dakar	14.8	341.6	1.214	1987
6	Mundaring	-32.0	116.3	0.945	1987-1989
7	Canberra	-35.3	149.0	0.940	1987-1989
8	Hobart	-42.9	147.2	0.829	1987-1989

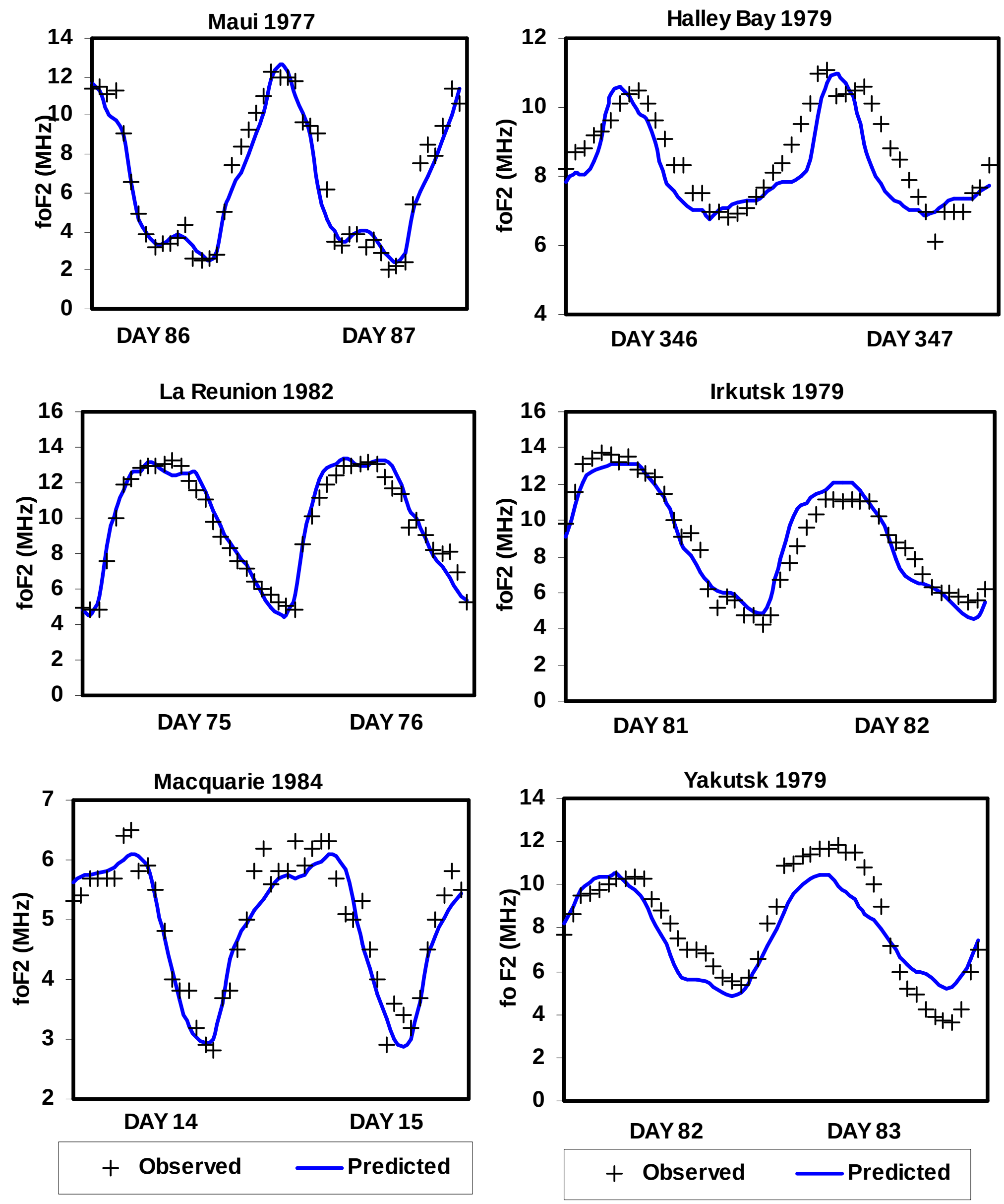

Figure 3-44. Samples of comparisons of daily variations of observed and NRTNN near-real time foF2 model predicted-values (within training period) for 2 consecutive days starting at 00h00UT on the first of the days indicated for each station.

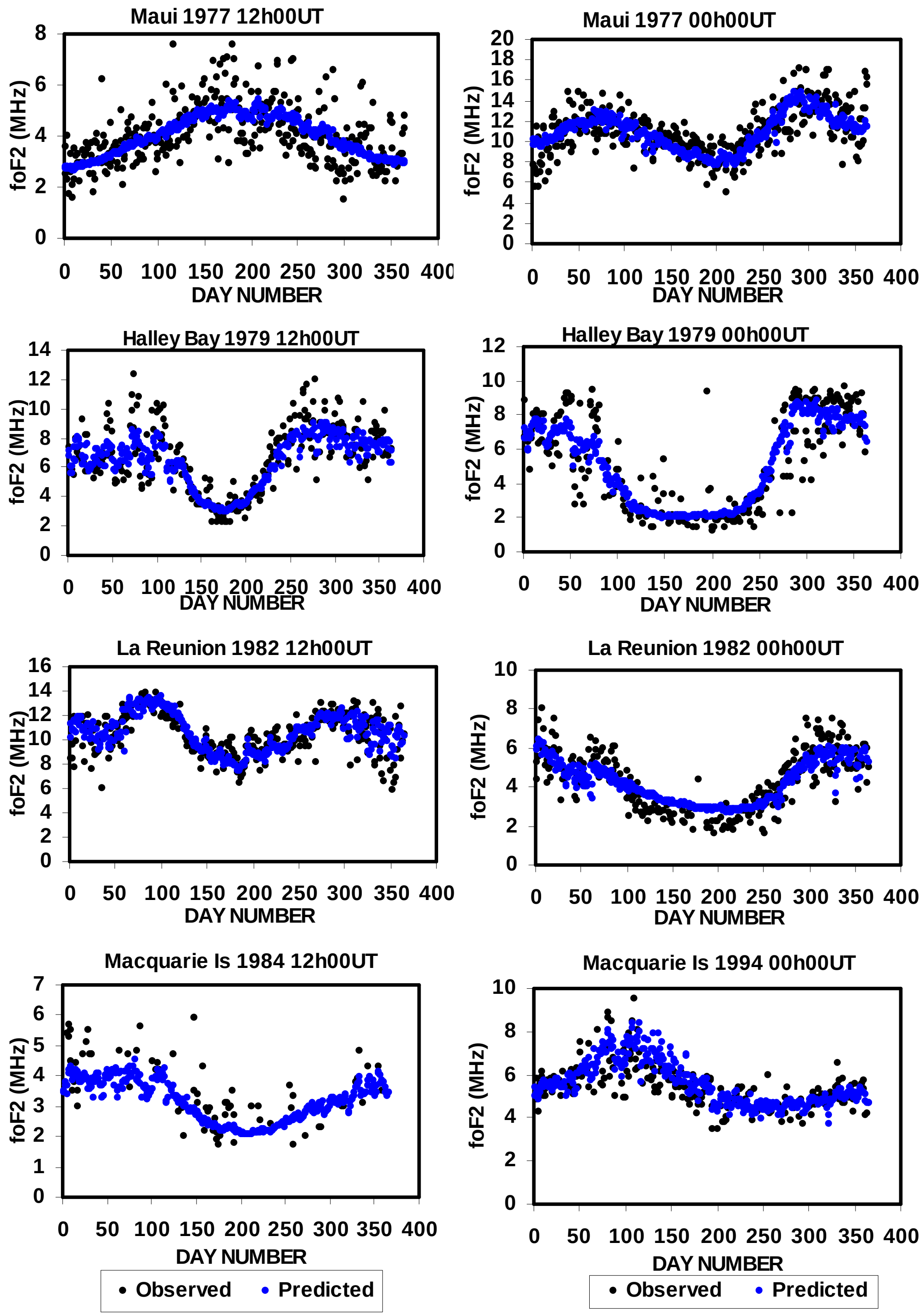

Figure 3-45a. Samples of comparisons of the seasonal variation between measured (observed) and NRTNN near-real time foF2 model predicted values at 00h00UT and 12h00UT for selected verification stations (during training period) for the year indicated.

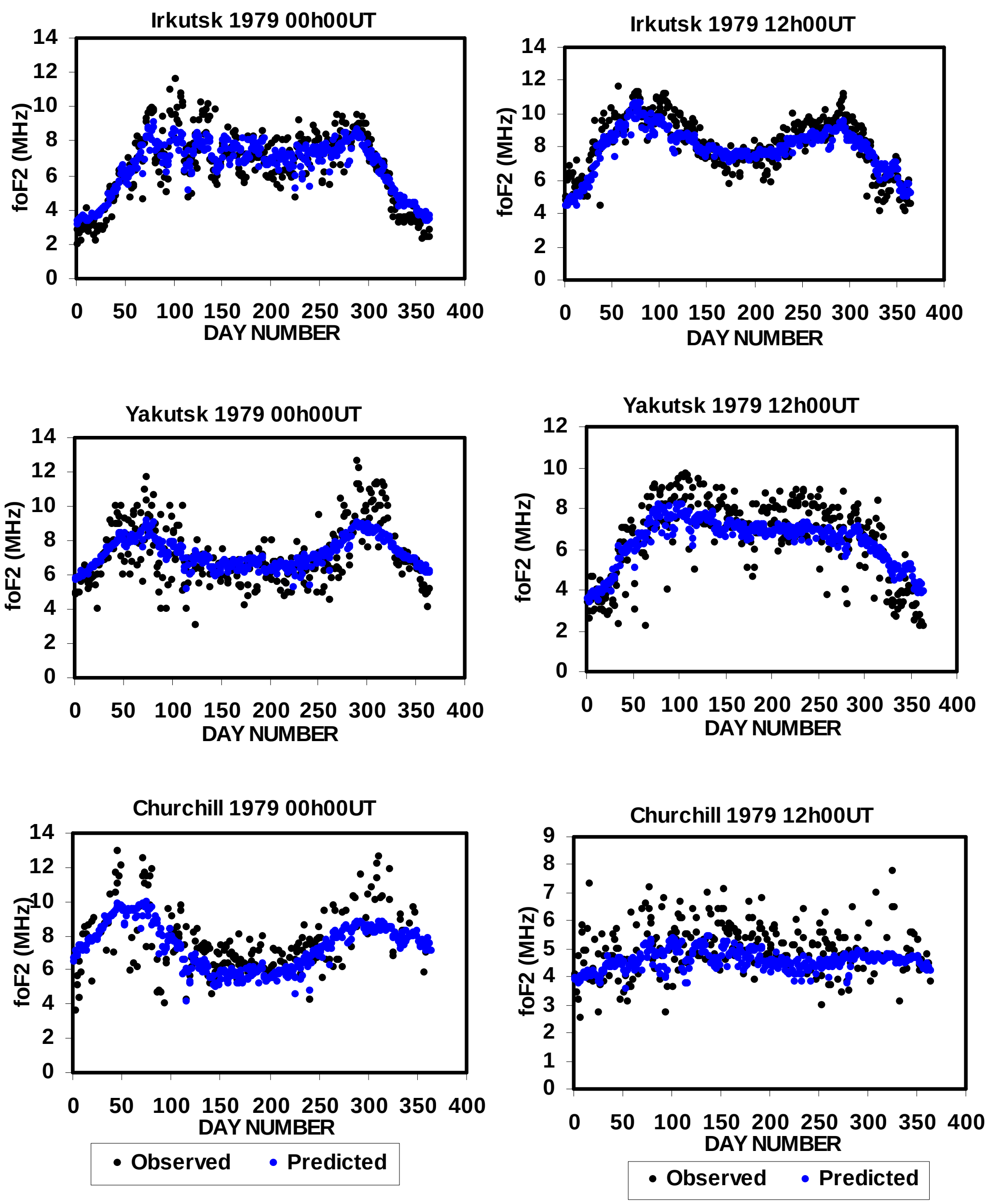

Figure 3-45b. Samples of comparisons of the seasonal variation between measured (observed) and NRTNN near-real time foF2 model predicted values at 00h00UT and 12h00UT for selected verification stations (during training period) for the year indicated.

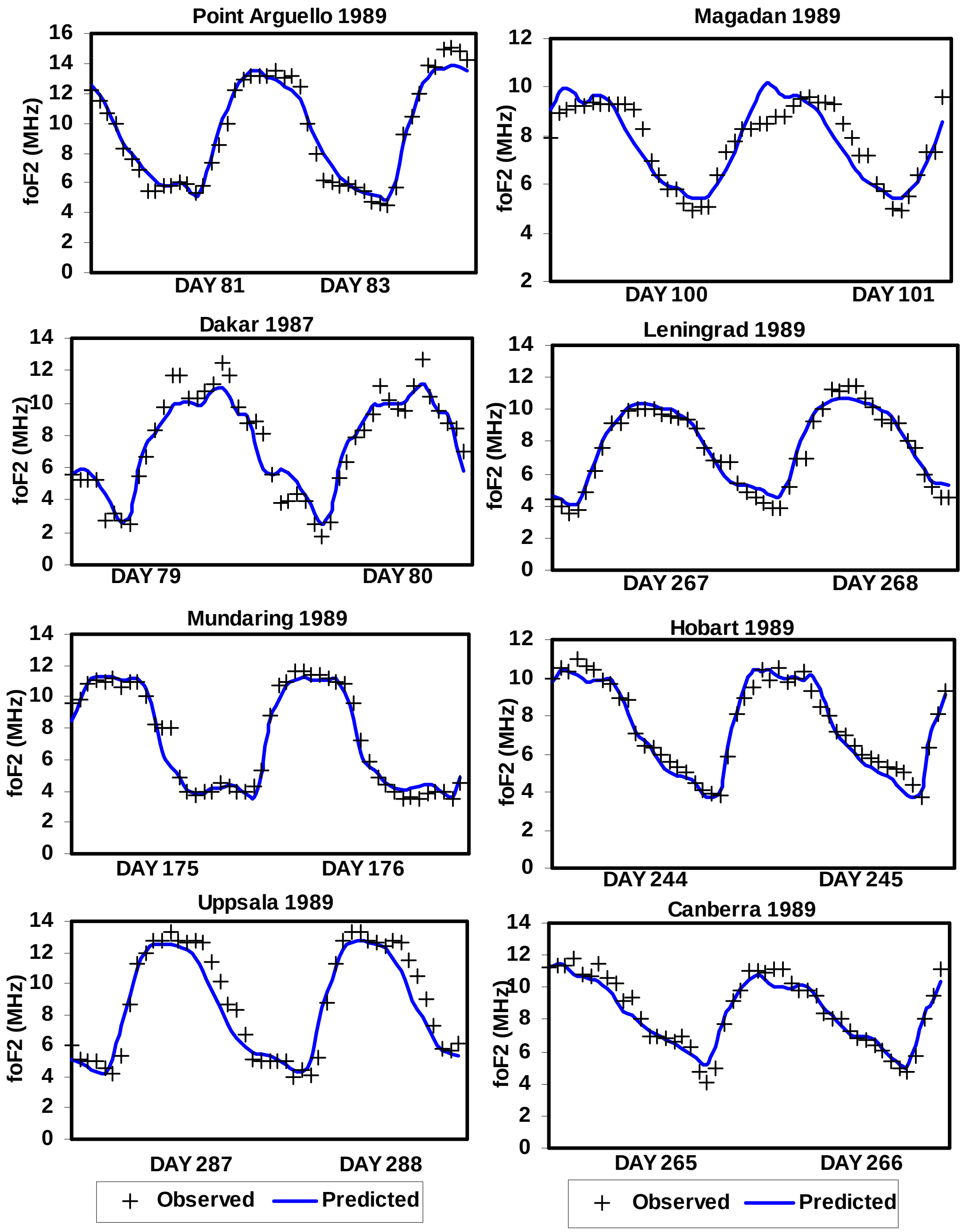

Figure 3-46. Samples of comparisons of daily variations of observed and NRTNN near-real time foF2 model predicted-values (outside training period) for 2 consecutive days starting at 00h00UT on the first of the days indicated for each station.

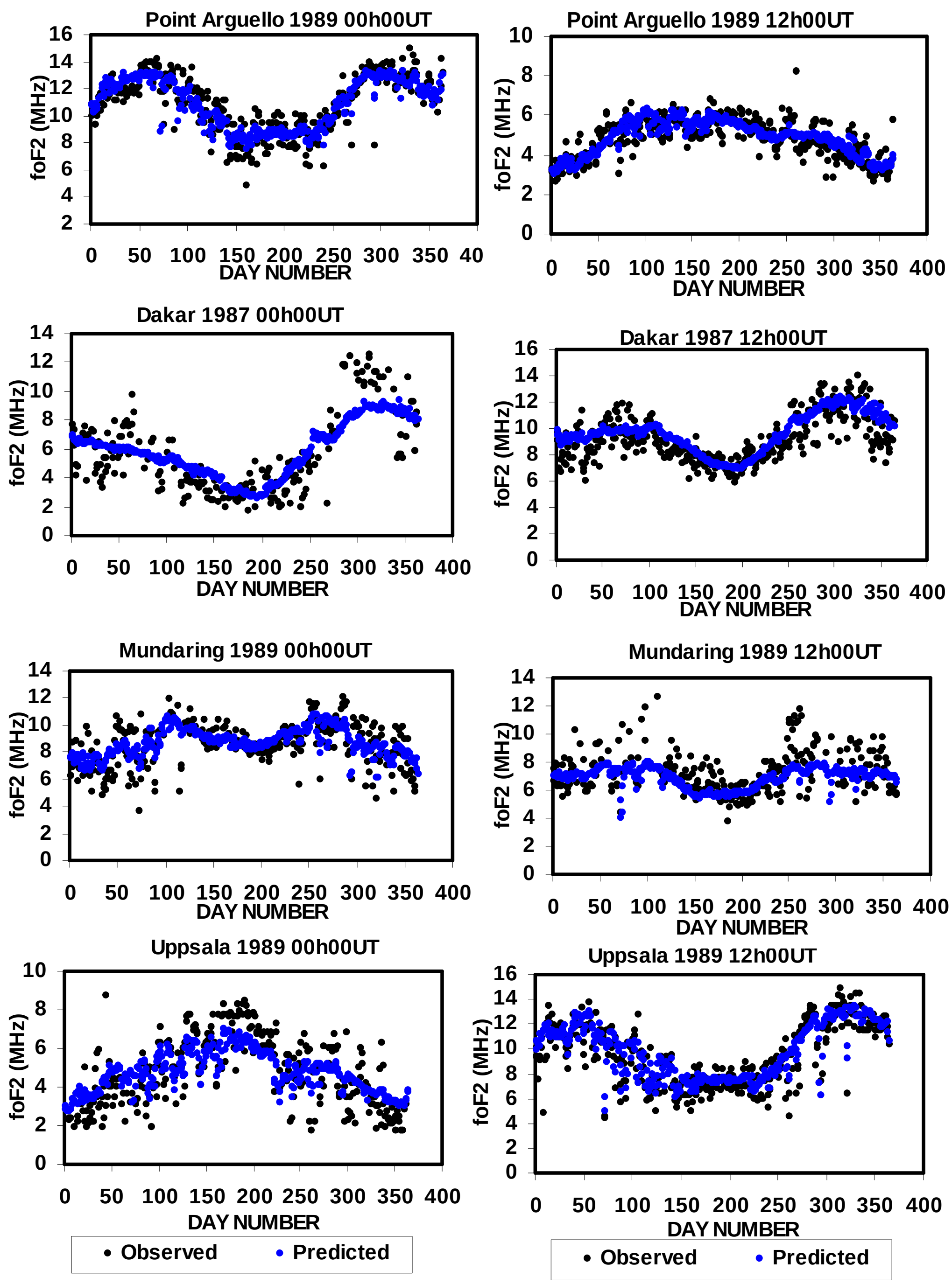

Figure 3-47a. Samples of comparisons of the seasonal variation between measured (observed) and NRTNN near-real time foF2 model predicted values at 00h00UT and 12h00UT for selected verification stations (outside training period) for the year indicated.

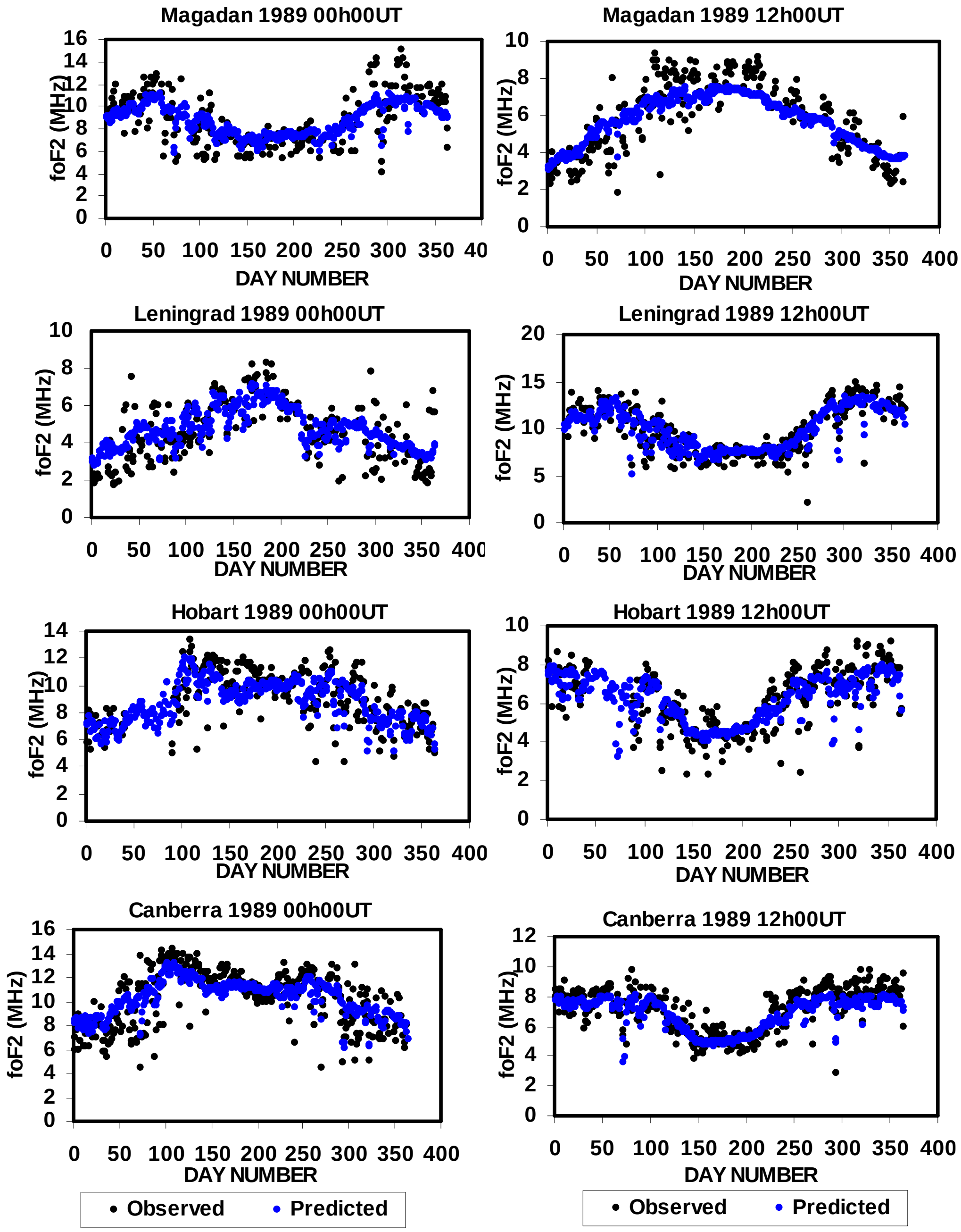

Figure 3-47b. Samples of comparisons of the seasonal variation between measured (observed) and NRTNN near-real time foF2 model predicted values at 00h00UT and 12h00UT for selected verification stations (outside training period) for the year indicated.

3.6.7 Conclusion

In this section, an attempt has been made to apply NNs to the development of a global near-real time foF2 empirical model. From the results it is evident that in addition to the geophysical information from any geographic location, recent past observations of foF2 from these four selected stations (Port Stanley, Grahamstown, Boulder and Dourbes) could be used as inputs to a NN for the purpose of near-real time foF2 predictions. This reveals that short-term foF2 information at the control locations can be used to determine the behaviour of foF2 at another location on the globe. However, it is important to mention here that there could be an improvement on this work if data from more stations are included in the training process. Also, for the model to be effectively utilized, recent observations of foF2 from these four stations must be available in real time. Therefore, it is my intention to continuously update this model as more data are made available from other ionospheric stations.

The next chapter discusses comparisons of results obtained from the foF2 and M(3000)F2 models (sections 3.3 and 3.4 respectively) with the IRI model and observed values at some high latitude stations. This is required in order to assess how well the models are applicable to this region of the ionosphere that is known to be unpredictable due to the effects of thermospheric winds which limit the accuracy of foF2 predictions.

Chapter 4

4 Comparisons of the foF2 NN and M(3000)F2 NN models with the IRI model at high latitude stations

4.1 Introduction

Various researchers (Muldrew and Vickrey, 1982; Rino et al., 1983; Hargreaves et al., 1985a, 1985b; Hanuise, 1983) have shown that high latitudes are the most variable regions of the ionosphere. The production of ionization in the low and mid latitudes is almost entirely by extreme ultra-violet (EUV) and X-ray radiations from the sun (Rishbeth and Garriott, 1969; Hargreaves, 1979), with additional control by electromagnetic forces at low latitudes arising from the horizontal alignment of geomagnetic fields over the magnetic equator. In addition to the production of ionization by EUV and X-ray radiations, the high latitude is greatly controlled by the sporadic nature of the solar and auroral activity (Rishbeth and Garriott, 1969; Hargreaves, 1979; McNamara, 1991; Hunsucker and Hargreaves, 2003). This is due to the fact that the high latitude is generally more accessible to the energetic particle emissions from the sun that produces additional ionization. As a result, due to the effects of thermospheric neutral winds, the high latitude is more complex, and predictions of ionospheric parameters such as foF2 and M(3000)F2 in this region are usually not possible (Rishbeth and Garrott, 1969; Hunsucker and Hargreaves, 2003). Because of this complex nature, a number of the existing global models of foF2 and M(3000)F2 are lacking realistic predictions at the high latitudes. The most widely used among these models is the IRI model. A comprehensive review of the performance of HF prediction models at high latitudes can be found in Hunsucker and Hargreaves (2003). For the purpose of validation of the predictive ability of the neural network based foF2 and M(3000)F2 models developed in this research at the high latitudes, I have made use of the IRI model as a standard model for comparison. The main objective is to determine how well the NN models (foF2 and M(3000)F2 NN models) could be used at the high latitude regions of the ionosphere for HF prediction purposes. The next two sections are focused on the comparisons of the foF2 NN and M(3000)F2 models predictions with the IRI model predictions and the observed values at a few selected high latitude stations based on the availability of data.

4.2 foF2 NN

This section compares results obtained by the NN2 model (i.e. final foF2 NN model discussed in section 3.3) with the IRI model (URSI and CCIR coefficients) and the observed values from selected high latitude stations. The RMS error differences between the observed and predicted values of foF2 by the URSI, CCIR and NN2 models are as shown in Table 23. These verification stations were not included in any form in the training of the NN2 model. It can be observed from the RMSE differences that the NN2 model results compare favourably with the IRI model. This is clearly illustrated in the bar graph of Figure 4-1. The test carried out here illustrates that the NN2 model could also be equally employed for the purpose of foF2 predictions at high latitudes within the limit of these errors. Therefore, it is evident from the results that a trained NN can properly capture the complex irregularity nature of the high latitudes due to the effects of the sporadic solar and auroral activity in these regions. Figures 4-2 and 4-3 illustrate the diurnal and seasonal variations of the NN2 model foF2 predictions and comparisons with the IRI model (URSI and CCIR) predictions and the observed values at a few selected high latitude stations. It can be observed from these figures that both the NN2 model and the IRI model predictions follow the general trend of the foF2 variations in this region. An exception is the Byrd Station where the NN2 model prediction error is relatively larger than that of both the URSI and CCIR. This is clearly shown in Figure 4-2 (Byrd Station) where the NN2 model overestimates the foF2 values at 18h00UT in 1960. Despite this, these comparisons suggest that the NN techniques can successfully be used as a tool for the global foF2 model, even at the high latitudes.

Table 23. The foF2 RMSE differences at selected verification stations at high latitudes.

S/N	Station name	Long °N	Lat °E	RMSE (MHz)			Period
				URSI	CCIR	NN2	
1	Thule/Qanaq	77.5	290.8	1.486	1.506	1.435	1959
2	College	64.9	212.2	1.311	1.447	1.247	1991
3	Yakutsk	62.0	129.6	1.569	1.523	1.393	1959
4	Magadan	60.0	151.0	1.619	1.603	1.538	1991
5	Davis	-68.6	77.9	1.731	1.792	1.786	1991
6	Syowa Base	-69.0	39.6	1.410	1.474	1.330	1980
7	Bryd Station	-80.0	240.0	1.298	1.206	1.523	1960

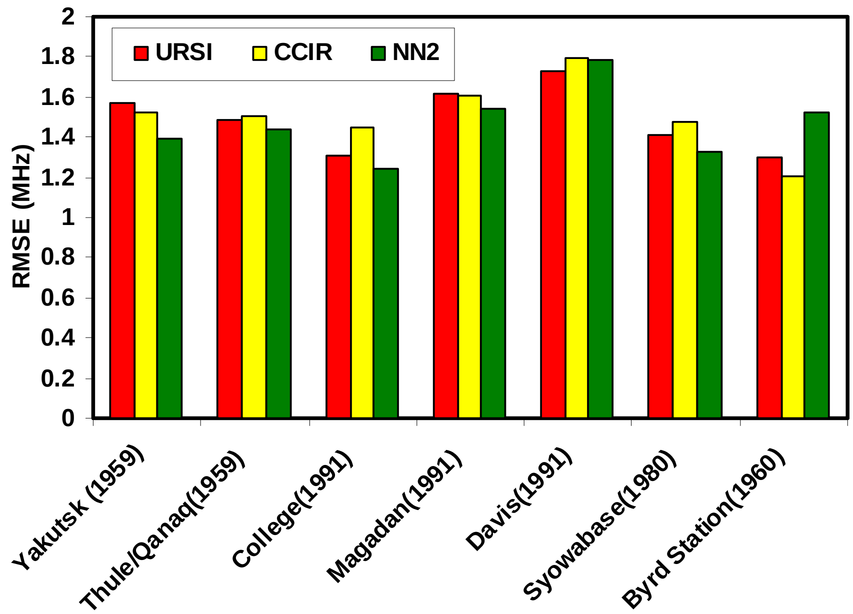

Figure 4-1. Bar graph illustrating the RMS error differences between measured and the URSI, CCIR and NN2 predictions for all daily hourly foF2 values for a few selected stations at high latitude for the period indicated.

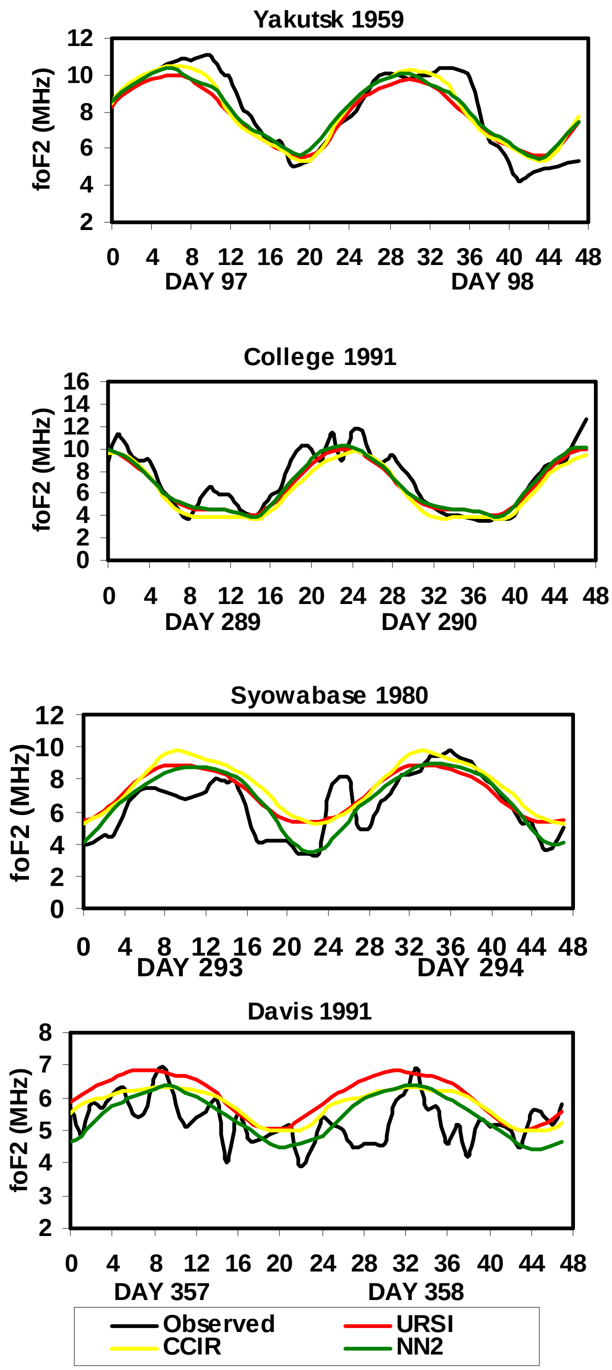

Figure 4-2. Examples of diurnal variations of the NN2 foF2 predicted values with the IRI model (URSI and CCIR) predictions and observed values for 2 consecutive days starting at 00h00UT on the first of the days shown at selected high latitude stations.

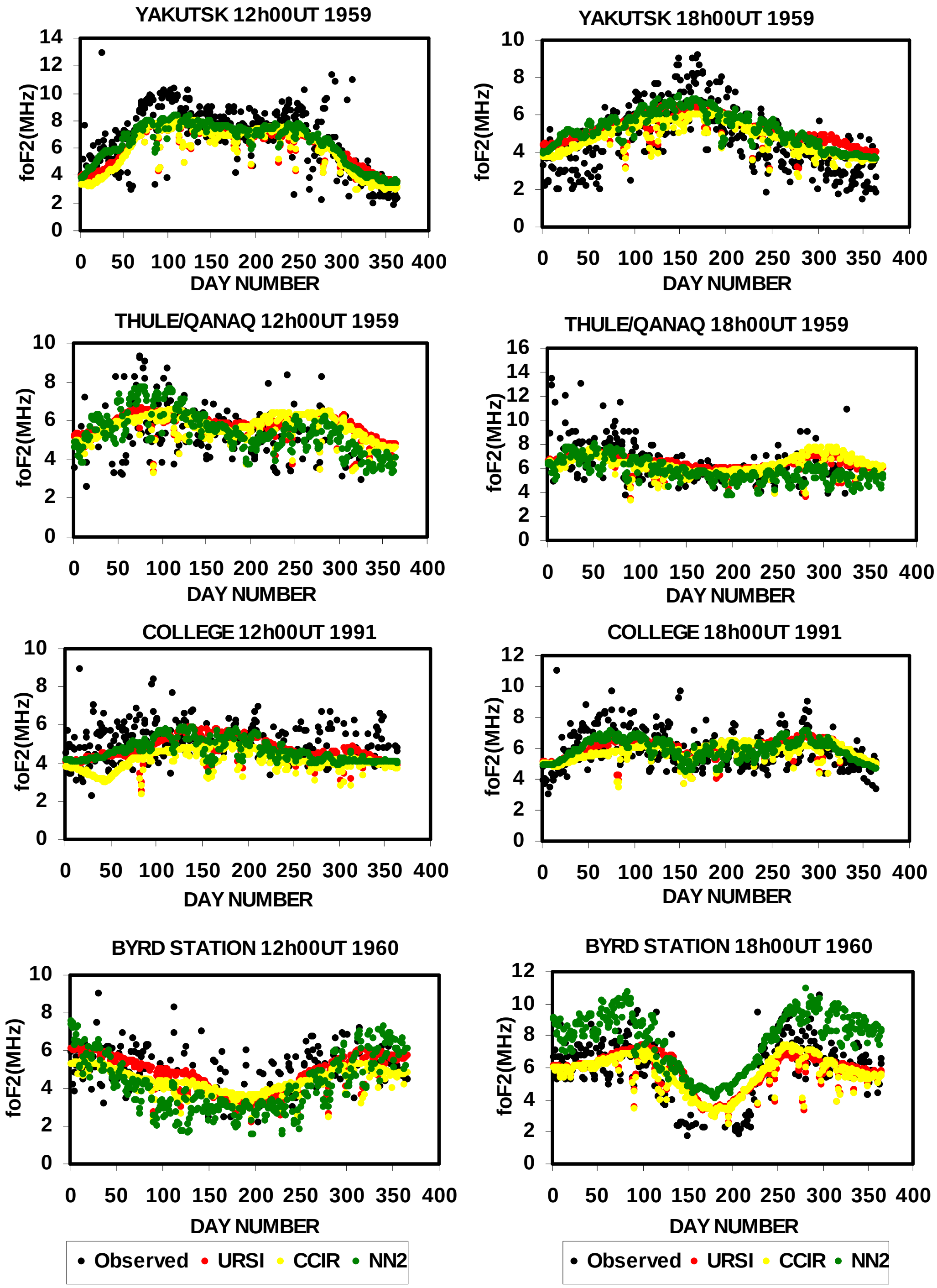

Figure 4-3a. Examples of seasonal comparisons between the NN2 foF2 model prediction, the IRI model (URSI and CCIR), and observed values at a few selected high latitude stations at 12h00UT and 18h00UT during the year indicated.

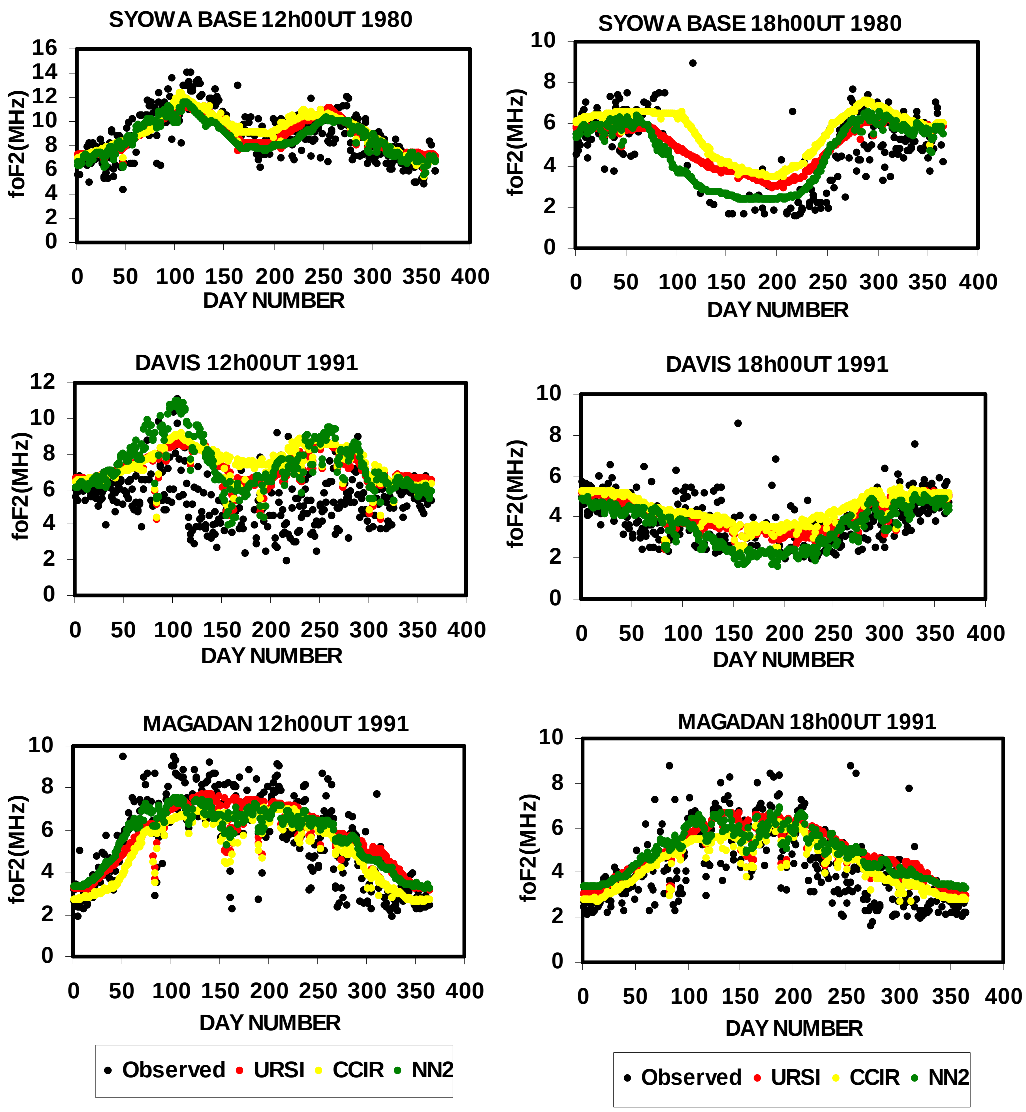

Figure 4-3b. Examples of seasonal comparisons between the NN2 foF2 model prediction, the IRI model (URSI and CCIR), and observed values at a few selected high latitude stations at 12h00UT and 18h00UT during the year indicated.

4.3 M(3000)F2 NN

Similar comparisons between the M(3000)F2 model (i.e. NNM model) predictions with the IRI model (CCIR M(3000)F2 model) predictions and observed values from a few selected high latitude stations have been carried out here. Table 24 shows a list of a few verification stations (not included in the training of the NNM model) and the error differences between the observed values of M(3000)F2 and the NNM and IRI model predictions. The results from the error Table 24 show that there are cases where the IRI model performance is relatively better than the NNM model, and vice versa. These differences are small and can be clearly seen from the bar graph illustration of Figure 4-4. Typical examples of diurnal variations between the NNM model and the IRI model predictions with the observed values from four stations are as shown in Figure 4-5. Similar comparisons of seasonal behaviour between the observed, the NNM model and the IRI model predicted values of M(3000)F2 are illustrated by Figures 4-6(a, b and c). These graphs have the same variations in time with the observed values. From these results it is evident that the application of the NN techniques to ionospheric predictions in the high latitude region is highly promising.

Table 24. The M(3000)F2 RMSE differences at selected verification stations at high latitudes.

S/N	Station	Lat ^{o}N	Long ^{o}E	RMSE (MHz)		Year
				IRI	NNM	
1	Thule/Qanaq	77.50	290.8	0.261	0.258	1959
2	Thule/Qanaq	77.50	290.8	0.211	0.257	1964
3	Barrow	71.30	203.2	0.245	0.248	1959
4	Barrow	71.30	203.2	0.228	0.230	1964
5	Yakutsk	62.00	129.6	0.175	0.163	1959
6	Yakutsk	62.00	129.6	0.171	0.165	1964
7	Casey	-66.20	110.5	0.268	0.272	1991
8	Davis	-68.60	77.9	0.272	0.281	1991
9	Davis	-68.60	77.9	0.371	0.345	1993
10	Syowa Base	-69.00	39.6	0.245	0.230	1979
11	Byrd Station	-80.00	240.0	0.222	0.302	1959

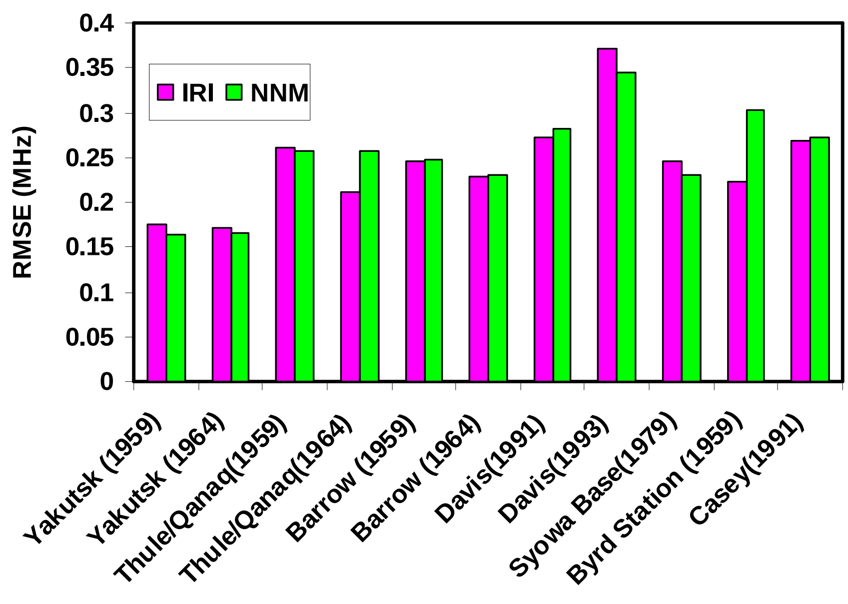

Figure 4-4. Bar graph illustrating the RMS error differences between measured and the IRI and NNM model predictions for all daily hourly values of M(3000)F2 for a few selected stations at high latitude for the period indicated.

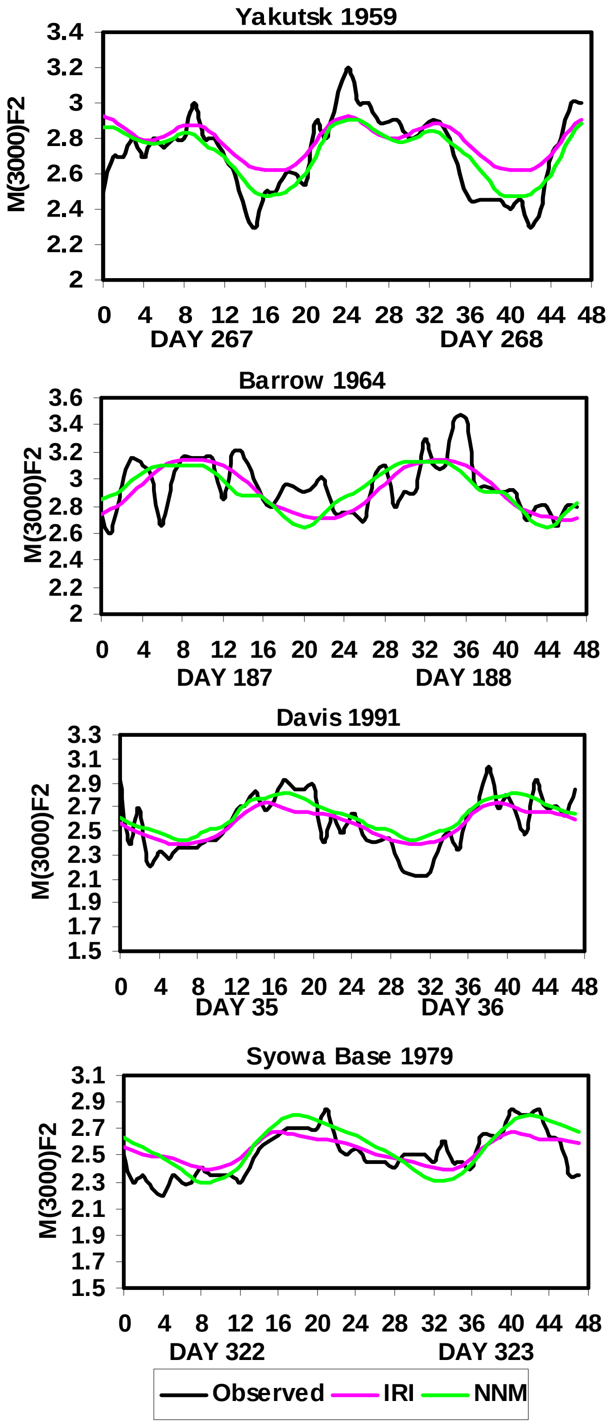

Figure 4-5. Examples of diurnal variations of the NNM M(3000)F2 predicted values with the IRI model predictions and observed values for 2 consecutive days starting at 00h00UT on the first of the days shown at selected high latitude stations.

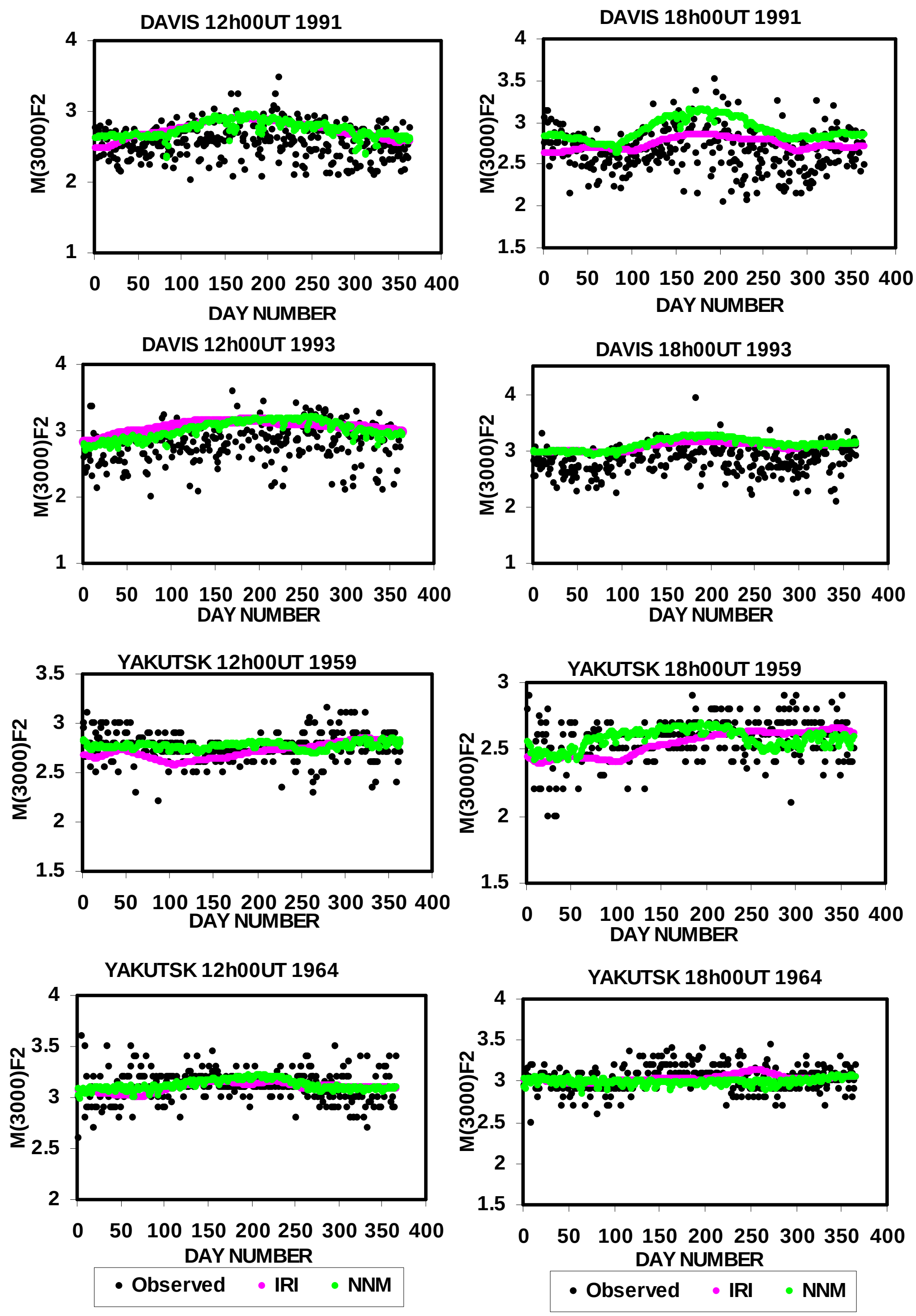

Figure 4-6a. Examples of comparisons of seasonal variations of the NNM M(3000)F2 model predictions with the IRI model and observed values at a few selected high latitude stations at 12h00UT and 18h00UT during the year indicated.

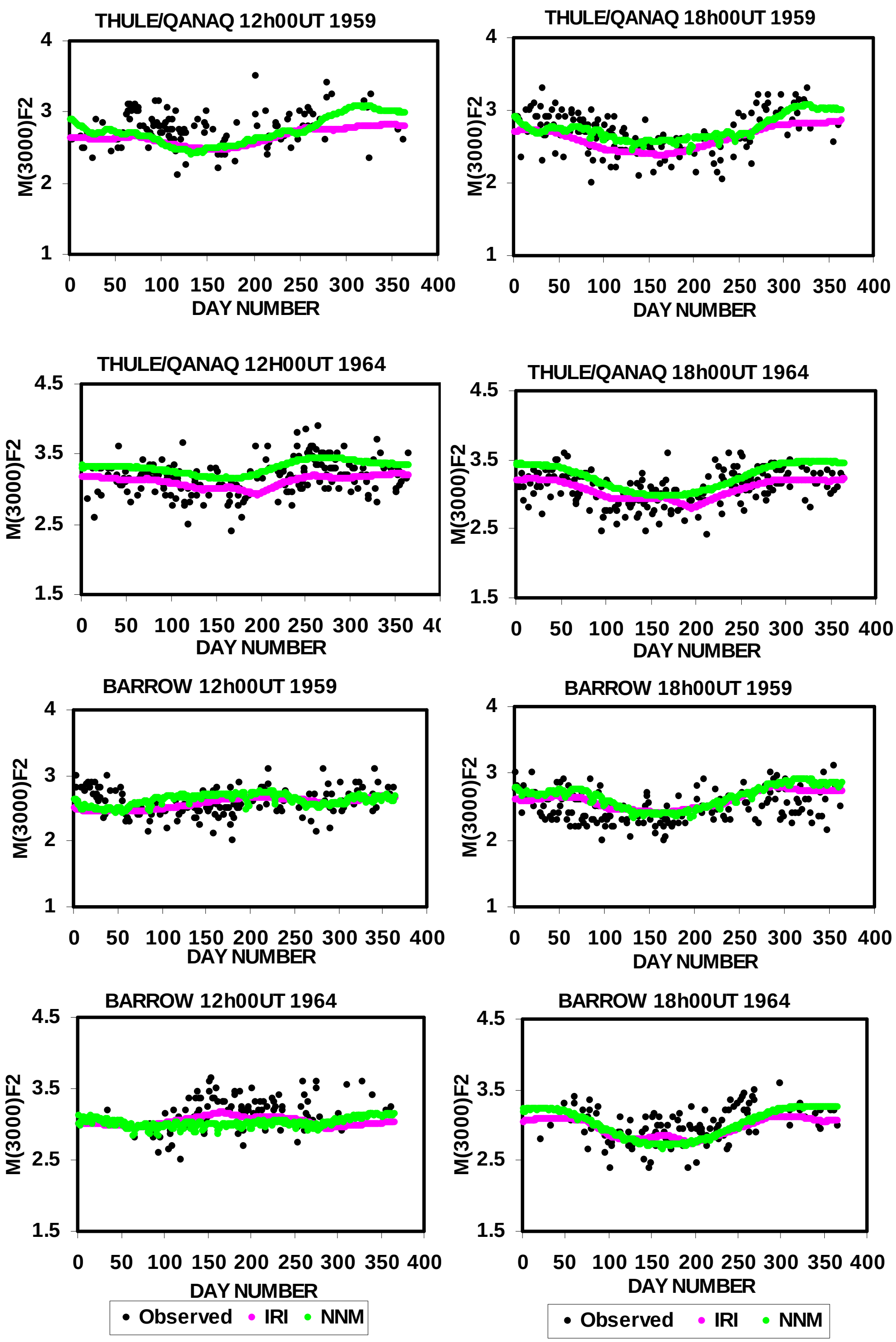

Figure 4-6b. Examples of comparisons of seasonal variations of the NNM M(3000)F2 model predictions with the IRI model and observed values at a few selected high latitude stations at 12h00UT and 18h00UT during the year indicated.

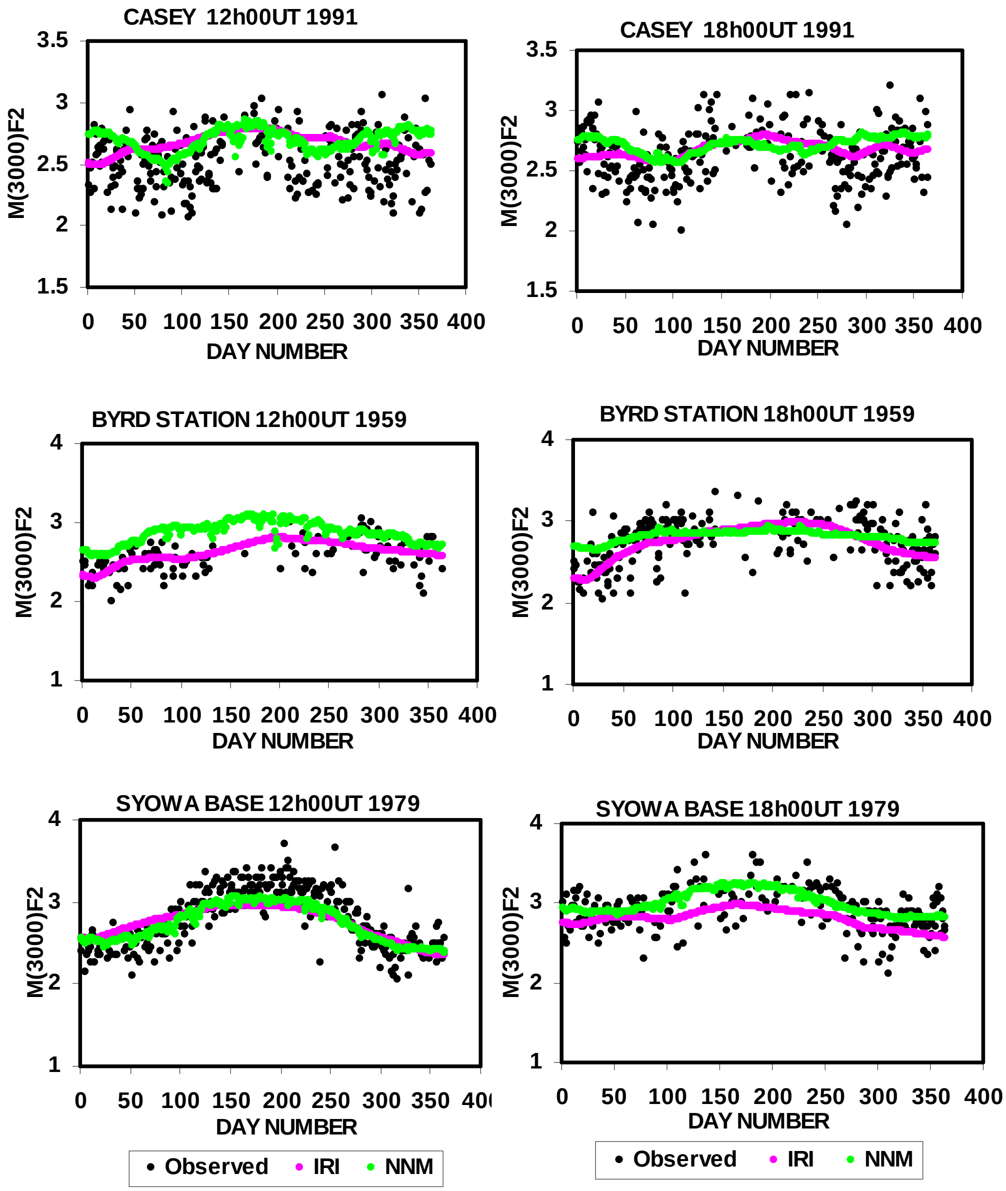

Figure 4-6c. Examples of comparisons of seasonal variations of the NNM M(3000)F2 model predictions with the IRI model and observed values at a few selected high latitude stations at 12h00UT and 18h00UT during the year indicated.

4.4 Conclusion

The results presented in this chapter, which compare favourably with the IRI model, serve to illustrate the potential of a NN based empirical model for *spatial* and *temporal* modeling of the foF2 and M(3000)F2 ionospheric parameters at high latitude regions. Despite the fact that the verification stations were not included in the training of the NN models, a close inspection of the graphs of diurnal and seasonal variations of Figures 3-49, 3-50, 3-52 and 3-53 shows that the model (NN2 and NNM models) predictions closely follow the measurement variations. This indicates that the NN models have been able to model the irregularities of the high latitudes due to the effects of thermospheric neutral winds. There could be an improvement over the performance of the present NN models if more data from the high latitude regions are included in the training process.

Chapter 5 Conclusion

5.1 Summary

In this thesis I have described the development of a neural network (NN) based global empirical model for the F2 region peak electron density using extended geophysically relevant inputs. Although various groups (discussed in the main text) have applied the NN technique to station and regional specific ionospheric prediction problems, this work is the first of its kind from a global perspective. The ability of the NN to deal with non-linear behaviour has been employed for modeling non-linear dynamical processes (both in space and time) associated with the F2 region of the ionosphere on a global scale. The results presented in this work, which compare favourably with the IRI model, successfully demonstrate the potential of NNs for *spatial* and *temporal* modeling of the ionospheric parameters foF2 and M(3000)F2 globally. Also, based on the results obtained and coupled with efforts being made by various researchers (discussed in the main text), it is evident that the NN technique could be an alternative to classical methods for solving ionospheric prediction problems. Four different models have been developed in this work. These are the foF2 NN model, M(3000)F2 NN model, short-term foF2 NN model and a near-real time foF2 NN model.

It should be made clear at this point that the aim of this research was not to criticise the IRI model, but rather to demonstrate the potential of NNs for predictive purposes in the field of the ionosphere as an alternative to the classical methods. As explained earlier in the text, there are a few cases where each of the methods (i.e. the IRI and NN based models) performs better than the other for specific stations. This indicates that the end user of these models has alternatives from which to choose for predictive purposes.

The results obtained from sections 3.5 (short-term foF2 NN model) and section 3.6 (near-real time foF2 NN model) reveal that, in addition to the *temporal* and *spatial* input variables discussed in section 3.2.3, short-term forecasting of foF2 is much improved by including past observations of foF2 itself. Again, it is evident from the results obtained in section 3.6 that there is correlation between measured foF2 values at different locations. Comparisons of the foF2 NN model and M(3000)F2 NN model predictions with that of the IRI model and observed values at a few selected high latitude stations suggest that the NN technique can successfully be employed to model the complex irregularities associated with the high latitude regions.

5.2 Limitations of the present work

There are a few limitations that should be taken into account when using these models. Firstly, the accuracy of the models, especially the foF2 and M(3000)F2 models, at high latitudes is not as good as in the low and mid latitude regions. This is probably due to the fact that a limited dataset from high latitudes was used in the training process of these models, as well as high level of variability associated with this region of the ionosphere. But the results obtained at a few selected stations at high latitudes (Chapter 4) suggest that the models can equally be used to the same extent as that of the IRI model in these regions. Secondly, one major limitation of the short-term foF2 NN model (i.e. foF2 up to 5 hours ahead forecast) is that it cannot be used at locations where there are no records of past observations of foF2 values. This is because the model requires recent past observations of foF2 at any target geographic location as inputs. Apart from this, the model can be used successfully at any location where this information is available. In the case of the near-real time foF2 model, recent past observations of foF2 from the four selected control stations (i.e. Port Stanley, Grahamstown, Boulder and Dourbes) must be made available in real time for the model to be effectively utilized. In spite of these limitations, the models developed can be used successfully for the global predictions of foF2 and M(3000)F2 within the limit of errors enumerated in the text.

5.3 Implementation and future work

Future work includes the software development of the models into an implementation form and the updating of the models as more data becomes available. A block diagram of all the components that contribute to the four models (i.e. foF2 NN model, M(3000)F2 NN model, short-term foF2 NN model and near-real time foF2 NN model) is shown in Figure 5-1. This block diagram illustrates how the future implementation of these models would make them available to an end-user. Initially, the user would specify which of the 4 available models should be utilized for the required task. The inputs required would be displayed on the user guide interface. In the case of the foF2 and M(3000)F2 models, the models require the year, day number (DN), geographic latitude (θ), geographic longitude (λ), and hour in Universal Time (UT) (e.g. year=1999, DN=120, Lat=33, Long=200, HR=12h00UT) as inputs. The user has the option to enter values of solar index (R2) and magnetic index (A16) as inputs, otherwise values of R2 and A16 are determined using data that is provided in additional files (Look-up Tables). If the user chooses the option to forecast foF2 values up to 5 hours in advance, the model requires 4 past recent observations of foF2 (i.e. F_{-3}, F_{-2}, F_{-1}, F_0) from that target location in addition to year, day number (DN), geographic latitude (θ), geographic longitude (λ), and hour in

Universal Time (UT) as inputs. Note that F_0 corresponds to the current foF2 from that target location. The model then generates F_{+1}, F_{+2}, F_{+3}, F_{+4}, and F_{+5} as outputs corresponding to 5 values of F2 critical frequencies ahead of current foF2 respectively.

The implementation of the near-real time foF2 NN model depends on the availability of past recent observations of foF2 from the control stations (Port Stanley, Grahamstown, Boulder and Dourbes) in real time. The user can only have control over the geographic coordinates (latitude and longitude) in case the user requires prediction for a particular region of the globe. Every other geophysical input will be provided online. The outputs of the near-real time foF2 model will be in the form of a contour map, which displays foF2 at every location across the entire globe. This is one of the major tasks in the implementation since a solid agreement between the managements of all the four control ionosonde stations (Port Stanley, Grahamstown, Boulder and Dourbes) is required as regards availability of data in real time.

This thesis has described the development of a NN based global ionospheric model for the F2 peak maximum electron density (foF2) and propagation factor M(3000)F2. Based on the results obtained in this research and the comparison made with the IRI model (URSI and CCIR coefficients), these results justify consideration of this technique for global ionospheric prediction models. I believe that, after consideration by the IRI community, these models will prove to be valuable to both the HF communication and worldwide ionospheric communities.

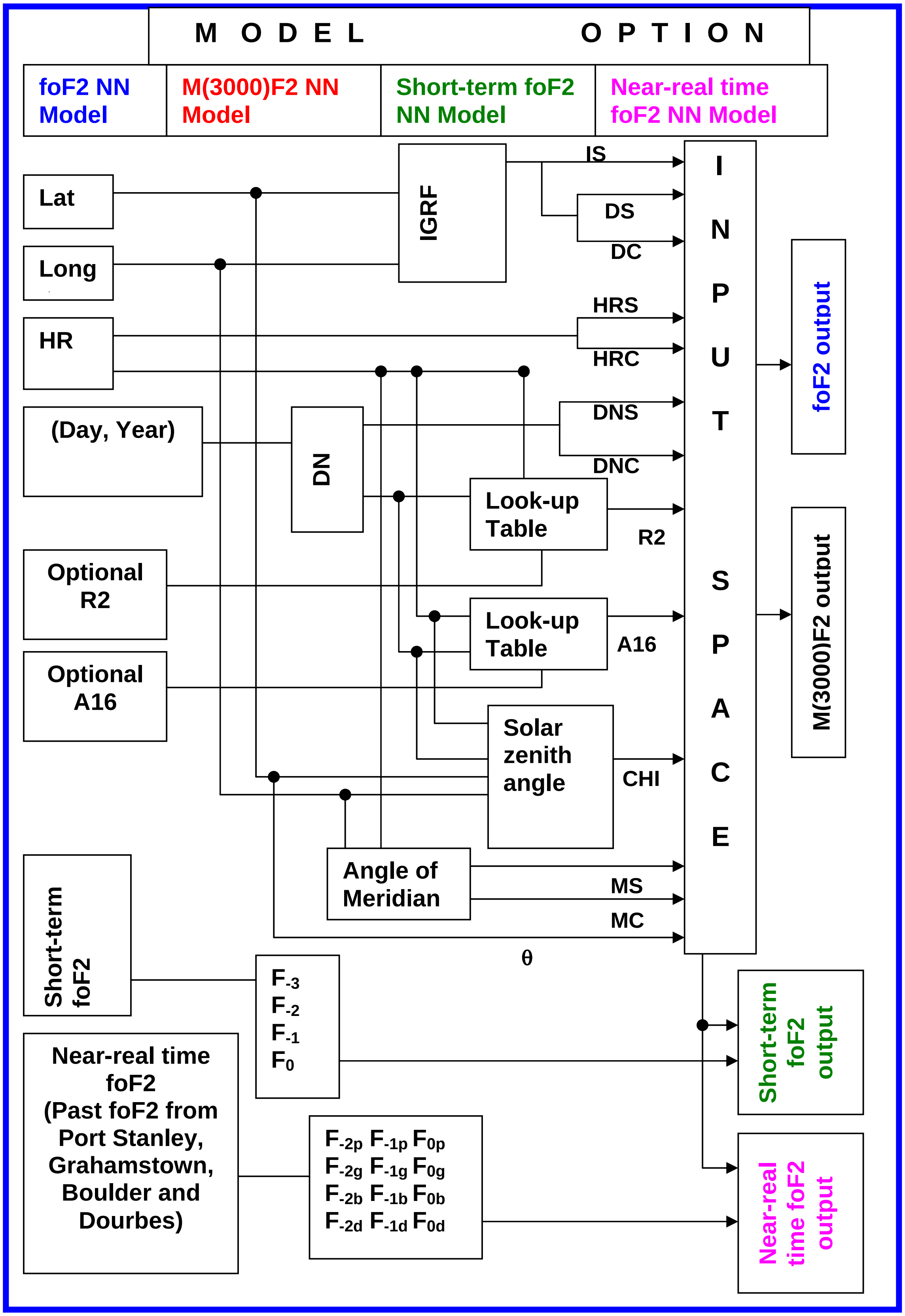

Figure 5-1. A block diagram of the proposed model implementation.

References

Adeniyi J.O., Bilitza D., Radicella S.M., Willoughby A.A., Equatorial F2-peak parameters in the IRI model, *Adv. Space. Res.* 31, 507-512, 2003.

Altinay O., Tulunay E., Tulunay Y. Forecasting of ionospheric critical frequency using neural networks, *Geophys. Res. Lett.* 24, 1467-1470, 1997.

Anderson D., Fuller-Rowell T.J., Space Environment Topics, Space Environment Center (SEC) at URL http://www.sel.noaa.gov/Info/Iono.pdf, 1999. (Accessed on February 2005).

Appleton F.R.S., Studies of the F2 layer in the ionosphere, *J. Atmos. Terr. Phys*. 1, 106-113, 1950.

Balan N., Bailey G.J., Jenkins B., Rao P.B., Moffett R.J., Variations of ionospheric ionisation and related solar fluxes during an intense solar cycle, *J. Geophys. Res*., 99(A2), 2243-2253, 1994.

Barghausen A.F., Finney J.W., Proctor L.L., Schultz L.D., Predicting long-term operational parameters of high-frequency sky-wave telecommunications systems, ESSA Tech. Rep., ERL-110-ITS-78, 1969.

Bent R.B., Lepofsky J.R., Llewellyn S.K., Schmid P.G., Ionospheric range-rate effect in satellite-to-satellite tracking, in: Soicher, H. (Ed), Operational Modelling of the Aerospace Propagation Environment, *Vol. I. AGARD conference Proceedings,* Vol. 230, 9-1 – 9-15, 1978.

Berry M.J.A., and Linoff G., Data Mining Techniques for Marketing, Sales, and Customer Support, New York: John Wiley & Sons, 1997.

Bilitza D., Sheikh N.N., Eyfrig R., A global model for the height of the F-2peak using M3000 values from the CCIR numerical maps. Telecommun. J. 46, 549-553, 1979.

Bilitza, D., International Reference Ionosphere 2000. *Radio Sci*. 36, 261 – 275, 2001.

Bilitza, D., International Reference Ionosphere 1990, *National Science Data Center, Report* 90-22, Greenbelt, Maryland, USA, 1990.

Bilitza D., Bhardwaj S., Koblinsky C., Improved IRI predictions for the GEOSAT time period, *Adv. Space Res*. 20,1755-1760, 1997.

Bilitza D., The importance of EUV indices for the International Reference Ionosphere. *Phys. Chem. Earth(c)*. 25, 515-521, 2000.

Bilitza D., Ionospheric models for radio propagations studies, in *The Review of Radio Science* 1999-2002, 625-679, IEEE Press, Piscataway, N.J. 2002.

Bilitza D., 35 years of International Reference Ionosphere – Karl Rawer's legacy, *Adv. Space Res*. 2, 283-287, 2004.

Bradley P.A., Dudeney J.R., A simple model of the vertical distribution of electron concentration in the ionosphere, *J. Atmos. Terr. Phys*. 35, 2131-2146, 1973.

Bradley P.A. Mapping the critical frequency of the F2 layer: Part 1 – requirements and development to around 1980. *Adv. Space Res.,* 10, 47-56, 1990.

Bradley P.A., Indices of ionospheric response to solar-cycle epoch, *Adv. Space Res.* 13, 25-28, 1993.

Bradley P.A., PRIME, Prediction and retrospective ionospheric modeling over Europe Final Reports to project COST238, Rutherford Appleton Laboratory, Chilton, Didcot, UK, 1999.

Bradley P.A., Stanislawska, I., Juchnikowski, G. Perspectives on updated foF2 maps for IRI. *Adv. Space Res.* 34, 2067-2074, 2004.

Bremer J., Ionospheric trends in mid-latitudes as a possible indicator of the atmospheric greenhouse effect. *J. Atmos. Terr. Phys.*, 54, 1505-1511, 1992.

Cander, LjR., Lamming, X. Neural networks in ionospheric prediction and short-term forecasting, *10th International Conference on Antennas and Propagation, 14-17 April 1997, Edinburgh, IEEE Conference Publication,* 496. 2.27-2.30, 1997.

Challinor R.A., Eccles D., Longitudinal variations of the mid-latitude ionosphere produced by neutral–air winds –I, Neutral-air winds and the ionosphere drifts in the northern and southern hemispheres, *J. Atmos. Terr. Phys.* 33, 363-369, 1971.

Chen Y.I., Liu J.Y., Chen S.C., Statistical investigation of the saturation effect on sunspot on the ionospheric foF2, *Phys. Chem. Earth(C),* 25, 359-362, 2000.

Ching B.K., Chiu Y.T., A phenomenological model of global ionospheric electron density in the E-, F1- and F2-regions, *J. Atmos. Terr. Phys*. 35, 1615-1630, 1973.

Chiu Y.T., An improved phenomenological model of ionospheric density, *J. Atmos. Terr. Phys*. 37, 1563-1570, 1975.

Derong L., Tsu-Shuan C., Zhang Yi., A constructive algorithm for feedforward neutral networks with incremental training, *IEEE. Trans. Circuit Syst*. 49, 1876-1879, 2002.

Dougherty J.P., On the influence of horizontal motion of the neutral air on the diffusion equation of the F-region, *J. Atmos. Terr. Phys*., 20, 167-176, 1961.

Duncan R.A., F-regions seasonal and magnetic-storm behaviour, *J. Atmos. Terr. Phys*. 31, 59-70, 1969.

Eyfrig R., The effect of the magnetic declination on the F2-layer, *Ann. Géophys*. 19, 102-117, 1963.

Fausett L. Fundamentals of Neural Networks, Prentice-Hall International Inc., 1994.

Field P.R., Rishbeth H., The response of the ionospheric F2-layer to geomagnetic activity: an analysis of worldwide data, *J. Atmos. Solar-Terr. Phys.* 59, 163-180, 1997.

Forbes J.M., Scott E.P., Xiaoli Z., Variability of the ionosphere, *J. Atmos. Solar- Terr. Phys.* 62, 685-693, 2000.

Fox M.W., McNamara L.F., Improved World-Wide Maps of Monthly Median of foF2, *J. Atmos. Terr. Phys.*, 50, 1077-1086, 1988.

Francis N.M., Brown A.G., Akram A., Cannon P.S., Broomhead D.S., Non-linear prediction of the ionospheric parameter foF2, in *Proceedings of the second International Workshop on Artificial Intelligence applications in Solar-terrestrial Physics,* ESA, WPP-148 Proceedings., edited by I. Sandahl and E. Jonsson, 219-223, European Space Agency, Paris, 1998.

Fuller-Rowell T.J., Araujo-Pradere E., Codrescu M.V., An empirical ionospheric storm-time correction model, *Adv. Space Res*. 25, 139-146, 2000.

Fuller-Rowell T.J., Codrescu M.V., Moffett R.J., Quegan S., On the seasonal response of the thermosphere and ionosphere to geomagnetic storms, *J. Geophys. Res.* 101, 2343-2353, 1996.

Gupta J.K., Lakha S., Long term ionospheric electron content variations over Delhi, *Ann. Geophysica.* 18, 1636-1644, 2001.

Hanbaba, Improved quality of service in ionospheric telecommunication systems planning and operation, Final Report to Project COST251, Space Research Centre, Warsaw, Poland, 1999.

Hanuise C., High-latitude ionospheric irregularities: review of recent radar results, *Radio Sci* . 18, 1093-1121, 1983.

Hargreaves J.K., The upper Atmospheric and Solar-Terrestrial Relations, an introduction to the aerospace environment, *Van Nostrand Reinhold Company*, New York, 1979.

Hargreaves J.K., Burns C.J., Kirkwood S.C., EISCAT Studies of F-region irregularities using beam scanning, *Radio Sci.* 20, 745-754 1985a.

Hargreaves J.K., Burns C.J., Kirkwood S.C., Irregular structures in the high-latitude F-region observed using the EISCAT incoherent scatter radar. *Proc. AGARD Conference* 382 (Fairbanks, Alaska), 1985b.

Haykin, S. Neural Networks: A Comprehensive Foundation, Macmillan, Indianapolis, Indiana, 1994.

Hecht-Nielsen R., Neurocomputing, Reading, M.A: Addison-Wesley, 1990.

Hermandez J.V., Tajima T., Horton W., Neural net forecasting for geomagnetic activity, *Geophys. Res. Lett.* 20, 2707, 1993.

Hirose Y., Yamashita K., Hijiya S., Back-propagation algorithm which varies the number of hidden units, *Neural Netw*. 4, 61-66, 1991.

Houminer Z., BennettnJ.A., Dyson P.L., Real-time ionospheric model updating, *J. Electr. Electron. Eng.* 13, 99-104, 1993.

Hunsucker R.D., Hargreaves J.K., The high-latitude ionosphere and its effects on radio propagation, Cambridge University Press, 2003.

Jones W.B., Obitts D.L. Global representation of annual and solar cycle variation of foF2 monthly median 1954-1958, U.S. Institute for Telecommunication Science, Research Report OT/ITSRR 3, National Technical Information Service, COM 75-11143/AS, Springfield, Virginia, 1970.

Jones W.B., Gallet R.M., The representation of diurnal and geographic variations of ionospheric data by numerical methods, *Telecommun. J.* 29,129-149, 1962.

Jones W.B., Gallet R.M., The representation of diurnal and geographic variations of ionospheric data by numerical methods, *Telecommun. J.* 32, 18-28, 1965.

Kane R.P., Solar cycle variation of foF2, *J. Atmos. Terr. Phys*. 54, 1201-1205, 1992.

King J.W., Smith P.A., The seasonal anomaly in the behaviour of the F2-layer critical frequency, *J. Atmos. Terr. Phys*. 30, 1707-1713, 1968.

King J.W., Kohl H., Pratt R., The effect of atmospheric winds on the height of the F2-layer peak at middle and high latitudes, *J. Atmos. Terr. Phys*. 29, 1529-1539, 1967.

King J.W., Slater A.J., Errors in predicted values of foF2, and hmF2 compared with the observed day-to-day variability, *Telecommun. J.* 40, 766, 1973.

Kohl H., King J.W., Eccles D., Some effects of neutral air winds on the ionospheric F-layer, *J. Atmosph. Terr. Phys*. 30, 1733-1744, 1968.

Kohl H., King J.W., Atmospheric winds between 100 and 700 km and their effects on the ionosphere, *J. Atmos. Terr. Phys*. 29, 1045-1062, 1967.

Kouris S.S., Bradley P.A., Dominici P., Solar-cycle variation of the daily foF2 and M(3000)F2, *Ann Geophysicae*, 16 1039-1042, 1998.

Kumluca A., Tulunay E., Tulunay Y., Relative significance of inputs to a neural network, in *Engineering Applications of Neural Networks,* 361-364, Systeemi tekniikan seura ry, Abo, Finland, 1997.

Kumluca A., Tulunay E., Topalli I., Temporal and spatial forecasting of ionospheric critical frequency using neural networks. *Radio Sci*., 34, 1497-1506, 1999.

Lamming X., Cander LjR. Monthly median foF2 modelling COST 251 Area by neural networks. *Phys. Chem. Earth (c).* 24, 349-354, 1999.

Leftin M., Ostrow S.M., Preston C., Numerical maps of the monthly median HF, F2 for solar cycle minimum and maximum, ERL Technical Memo #69, Boulder Colorado, 1967.

Liu J.Y., Chen Y.I., Lin J.S., Statistical investigation of the saturation effect in the ionospheric foF2 versus sunspot, solar radio noise, and solar EUV radiation. *J. Geophys. Res*., 108(A2), 1067, doi: 10.1029/2001JA007543, 2003.

Liu L., Wan W., Ning B., Statistical modeling of ionospheric foF2 over Wuhan. *Radio Sci*., 39, RS2013, doi:10.1029/2003RS003005, 2004.

Lundstedt H., Wintoft P., Prediction of magnetic storms from solar wind data with the use of neural networks, *Ann. Geophys.* 12, 19-24, 1994.

McClelland J.L., Rumelhart D.E., Exploration in parallel distributed processing, Cambridge, M.A: MIT Press, 1988.

McCulloch W.W., Pitts W., A logical Calculus of ides imminent in nervous activity. *Bull. Math. Biophys*., 5, 115-133, 1943.

McKinnell L.A., A new empirical model for the peak ionospheric electron density using neural networks. MSc. Thesis, Rhodes University, Grahamstown, South Africa, 1996.

McKinnell L.A., Poole A.W.V. The development of a neural network based short-term foF2 forecast program, *Phys. Chem. Earth (c).* 25, 287-290, 2000.

McKinnell L.A., Poole A.W.V. Ionospheric variability and electron density profile studies with neural networks, *Adv. Space Res.,* 27, 83-90, 2001.

McKinnell L.A., A neural network based ionospheric model for the bottomside electron density profile over Grahamstown, South Africa, *PhD Thesis,* Rhodes University, Grahamstown, South Africa*, 2002*.

McNamara L.F., *Radio amateurs guide to the ionosphere*, Krieger Publishing Company, 1994.

Mikhailov S.K., Mikhailov V.V., Skoblin M.G., A method for foF2 and M(3000)F2 instantaneous mapping over Europe (MQMF2-Inst Model). In: P. Bradley and B.A. de la Morena (eds), *Proceedings of the COST238/PRIME Workshop*, El Arenosillo, Spain, 1994.

Millward G.H., Rishbeth H., Fuller-Rowell T.J., Aylward A.D., Quegan S., Moffett R.J., Ionospheric F2- layer seasonal and semiannual variations, *J. Geophy. Res.* 101, 5149-5156, 1996.

Minsky M., and Papert S., Perceptrons, Cambridge, MA: MIT Press, 1969.

Muldrew D.B., Vickrey J.F., High-atitude F region enhancements observed simultaneously with ISIS 1 and the Chatanika rader, J. Geophys. Res. 87, 8263-8272 , 1982.

Nisbet J.S. On the construction and use of a simple ionospheric model, *Radio Sci.,* 6, 437 – 464. 1971.

Obrou O.K., Bilitza D., Adeniyi J.O., Radicella S.M., Equatorial F2-layer peak hight and correlation with vertical ion drift and M(3000)F2, *Adv. Space Res.* 31, 513-520, 2003.

Poole A.W.V., McKinnell L.A. On the predictability of foF2 using neural networks. *Radio Sci.,* 35, 225-234, 2000.

Poole, A.W.V., Poole, M. Long-term trends in foF2 over Grahamstown using neural networks, *Annals of Geophysics,* 45, 155-161, 2002.

Rao M.S.V., Rao R.S., The hysteresis variation in F2-layer parameters, *J. Atmos. Terr. Phys*. 31, 1119-1126, 1969.

Richards P.G., Seasonal and solar cycle variations of the ionospheric peak electron density: Comparison of measured and models, *J. Geophys. Res.*, 106(A12), 12803-12819, 2001.

Richard S., Belehaki A., Burešovă D., Cander Lj., Kutiev I., Pietrella M., Stanisławska I., Stankov S., Tsagouri I., Tulunay Y., Zolesi B. Nowcasting, forecasting and warning for ionospheric propagation: tools and methods. *Ann. Geophys*., 47, 957-983. 2004.

Rino C.L., Livingston R.C., Tsunoda R.T., Robinson R.M., Vickrey J.F., Senior C., Cousins M.D., Owen J., Recent studies of the structure and morphology of auroral-zone F-region irregularities, *Radio Sci*. 18, 1167- 1180, 1983.

Rishbeth H., Setty C.S.G.K., The F-layer at sunrise, *J. Atmos. Terr. Phys*. 20, 263-276, 1961.

Rishbeth H., Garriott O.K., Introduction to ionospheric physics, Academic press, New York and London, 1969.

Rishbeth H., Mendillo M., Patterns of F2-layer variability, *J. Atmos. Solar- Terr. Phys.* 63, 1661-1680, 2001.

Rishbeth H., How the thermospheric composition affects the ionospheric F2-layer. *J. Atmos. Solar-Terr. Phys*. 60, 1385-1402, 1998.

Rishbeth H., The effect of winds on the ionospheric F2-peak, *J. Atmos. Terr. Phys*. 29, 225-238, 1967.

Rishbeth H., Thermospheric winds and the F-region: A review, *J. Atmos. Terr. Phys*. 34, 1-47, 1972.

Rodger A.S., Wrenn G.L., Rishbeth H., Geomagnetic storms in the Antarctic F-region. II. Physical interpretation, *J. Atmos. Terr. Phys*. 51, 851-866, 1989.

Rosenblatt F., The Perceptron: A Probabilistic Model for Information Storage and Organization in the Brain, Psychological Review 65, 386-408, 1959.

Rumelhart, D.E., Hinton G.E., Williams R.J., Learning representations by back-propagating error, Nature, 323, 533-536, 1986b.

Rush C.M., An ionospheric observation network for use in short-term propagation predictions. *Telecommun. J*. 43, 544-549, 1975.

Rush C.M., Pokempner M., Anderson D.N., Stewart F.G., Perry J., Improving ionospheric maps using theoretically derived values of foF2, *Radio Sci*., 28, 95-107, 1983.

Rush C.M., Pokempner M., Anderson D.N., Stewart, F.G., Perry J. Maps of foF2 derived from observations and theoretical data, *Radio Sci*., 19, 1083-1097, 1984.

Rush C.M., Fox M., Bilitza D., Davies K., McNamara L., Stewart F., PoKempner M. Ionospheric Mapping: An Update of foF2 Coefficients, *Telecomm. J*., 56, 179-182, 1989.

Russell C.T., On the heliographic latitude dependence of the interplanetary magnetic field as deduced from the 22-year cycle of geomagnetic activity, *Geophys. Res. Lett*. 1, 11-12, 1974.

Russell C.T., Mulligan T., The 22-year variation of geomagnetic activity: Implications for the polar magnetic field of the sun, *Geophys. Res. Lett.* 22, 3287-3288, 1995.

Sethi N.K., Goel M.K., Mahajan K.K., Solar cycle variations of foF2 from IGY to 1990. *Ann. Geophysicae,* 20, 1677-1685, 2002.

Shimazaki T., World-wide daily variations in the height of the maximum electron density of the ionospheric F2-layer*, J. Radio Res. Lab.* 2, 85-97, 1955.

Smith P.A., King J.W., Long-term relationships between sunspots, solar faculae and the ionosphere, *J. Atmos. Terr. Phys*. 43, 1057-1063, 1981.

Titheridge J.E., Buonsanto M.J., Annual variations in the electron content and height of the F layer in the northern and southern hemispheres, related to neutral compositions, *J. Atmos. Terr. Phys*. 45, 683-696, 1983.

SNNS, Stuttgart Neural Network Simulator user manual, version 4.2, University of Stuttgart, Institute for Parallel and Distributed High Performace Systems, (IPVR), 1995a.

SNNS, Stuttgart Neural Network Simulator, retrieved 1998, at URL http://www-ra.informatik.uni-tuebingen.de/SNNS/, 1995b.

Titheridge J.E., Winds in the ionosphere - A review, *J. Atmos. Terr. Phys*. 57, 1681-1714, 1995.

Torr M.R., Torr D.G., The seasonal behaviour of the F2-layer of the ionosphere, *J. Atmos. Terr. Phys*. 35, 2237-2251, 1973.

Torr M.R., Torr D.G., Richards P.G., Causes of the F region winter anomaly, *Geophys. Res. Lett*. 7, 301-304, 1980.

Trísková L., Chum J., Hysteresis in dependence of foF2 solar indices, Adv. Space Res. 18 145-148, 1996.

Tulunay Y., An attempt to model the influence of the trough on HF communication by using neural networks. *Radio Sci.* 36, 1027-1041, 2001.

Tulunay E, Özkaptan C., Tulunay Y. Temporal and spatial forecasting of the foF2 values up to twenty four hours in advance, *Phys. Chem. Earth(c)*. 25, 281-285, 2000.

Widrow B., and Hoff M.E., Adaptive Switching Circuits, IRE WESCON Convention Record, 4, 96-104, 1960.

Williscroft L.A., Poole A.W.V., Neural networks, foF2, sunspot and magnetic activity, *Geophys. Res. Lett*., 23, 3659-3662, 1996.

Wintoft P., Twenty-four hour predictions of foF2 using neural networks, *Radio Sci.,* 35, 395-408, 2000.

Wintoft P., Cander LjR., Short-term prediction of foF2 using time delay neural networks, *Phys. Chem. Earth (c).* 24, 343-347, 1999.

Wintoft P., Cander LjR. Ionospheric foF2 storm forecasting using neural networks. *Phys. Chem. Earth (c).* 25, 267-273, 2000.

Wrenn G.L., Rodger A.S., Rishbeth H., Geomagnetic storms in the Antarctic F-region. I. Diurnal and seasonal patterns for main phase effects, *J. Atmos. Terr. Phys*. 49, 901-913, 1987

Wright J.W., The F-region seasonal anomaly, *J. Geophys. Res*. 68, 4379-4381, 1963.

Wu J.G., Lundstedt H., Prediction of geomagnetic storms from solar wind data using Elman recurrent neural networks, *Geophys. Res. Lett.* 23 319-322, 1996.

Zakharov I.G., Tyrnov O.F., Short-term critical frequency variations and their predictions in the Multitude ionospheric F2 region, *Phys. Chem. Earth*, 24, 371-374, 1999.

Xenos T.D., Neural-network-based prediction techniques for single station modelling and regional mapping of the foF2 M(3000)F2 ionospheric characteristics, *Nonlinear Proc. Geophys*., 9, 477-486, 2002.

Zolesi B., Cander LjR., Evolution of the ionospheric mapping and modelling during the last four decades. *Fisica de la Tierra* 12, 127-154, 2000.

Zolesi B., Cander LjR., Advances in regional mapping over Europe, *Ann. Geofi.* 41, 827-842, 1998.